Characterisation and Modelling of Indoor and Short-Range MIMO Communications

Michail Matthaiou

A thesis submitted for the degree of Doctor of Philosophy.
The University of Edinburgh.
November 2008

Abstract

Over the last decade, we have witnessed the rapid evolution of Multiple-Input Multiple-Output (MIMO) systems which promise to break the frontiers of conventional architectures and deliver high throughput by employing more than one element at the transmitter (Tx) and receiver (Rx) in order to exploit the spatial domain. This is achieved by transmitting simultaneous data streams from different elements which impinge on the Rx with ideally unique spatial signatures as a result of the propagation paths' interactions with the surrounding environment. This thesis is oriented to the statistical characterisation and modelling of MIMO systems and particularly of indoor and short-range channels which lend themselves a plethora of modern applications, such as wireless local networks (WLANs), peer-to-peer and vehicular communications.

The contributions of the thesis are detailed below. Firstly, an indoor channel model is proposed which decorrelates the full spatial correlation matrix of a 5.2 GHz measured MIMO channel and thereafter assigns the Nakagami-m distribution on the resulting uncorrelated eigenmodes. The choice of the flexible Nakagami-m density was found to better fit the measured data compared to the commonly used Rayleigh and Ricean distributions. In fact, the proposed scheme captures the spatial variations of the measured channel reasonably well and systematically outperforms two known analytical models in terms of information theory and link-level performance.

The second contribution introduces an array processing scheme, namely the three-dimensional (3D) frequency domain Space Alternating Generalised Expectation Maximisation (FD-SAGE) algorithm for jointly extracting the dominant paths' parameters. The scheme exhibits a satisfactory robustness in a synthetic environment even for closely separated sources and is applicable to any array geometry as long as its manifold is known. The algorithm is further applied to the same set of raw data so that different global spatial parameters of interest are determined; these are the multipath clustering, azimuth spreads and inter-dependency of the spatial domains.

The third contribution covers the case of short-range communications which have nowadays emerged as a hot topic in the area of wireless networks. The main focus is on dual-branch MIMO Ricean systems for which a design methodology to achieve maximum capacities in the presence of Line-of-Sight (LoS) components is proposed. Moreover, a statistical eigenanalysis of these configurations is performed and novel closed-formulae for the marginal eigenvalue and condition number statistics are derived. These formulae are further used to develop an adaptive detector (AD) whose aim is to reduce the feasibility cost and complexity of Maximum Likelihood (ML)-based MIMO receivers.

Finally, a tractable novel upper bound on the ergodic capacity of the above mentioned MIMO systems is presented which relies on a fundamental power constraint. The bound is sufficiently tight and applicable for arbitrary rank of the mean channel matrix, Signal-to-Noise ratio (SNR) and takes the effects of spatial correlation at both ends into account. More importantly, it includes previously reported capacity bounds as special cases.

Declaration of originality

I hereby declare that the research recorded in this thesis and the thesis itself was composed and originated entirely by myself in the School of Engineering and Electronics at The University of Edinburgh.

The software used to perform all the computer simulations was written entirely by myself with the following exception

- The routines used for cluster identification through the non-parametric Kernel Density Estimate technique were legally obtained from [1].

Michail Matthaiou
November 2008

Acknowledgements

"I am digging my way to something,
to something better."
- James Hetfield -

When I was accepted as a Ph.D. student at the University of Edinburgh in the summer of 2005, I knew I had to go through a very long and lonely path and sometimes overcome my limits. Now, as this journey has almost reached its final destination I would like to explore this opportunity and express my deepest gratitude to a number of people who have provided me with invaluable help over these last three years. First of all, I am truly indebted to my supervisor Dr. David Laurenson for his priceless help and guidance over the course of my research and for proof-reading this thesis. His wise suggestions have always helped me and most of them have gone into the thesis.

Equally important was the enthusiasm and endless support I received from Dr. John Thompson, who provided me with access to the results of propagation measurements carried out in Vienna at a very critical part of my research and also peer-reviewed a great part of this thesis.

I would like to thank Dr. Yannis Kopsinis and Dr. Athanasia Tsertou for not only sharing the same office with me but also for always being by my side. Sometimes their sound advice and support was more than I could handle. Without their support, the work would have never reached the quality presented here.

My sincere thanks goes to my dear friend and colleague Dr. Ioannis Sarris, formerly of Bristol University, for his continuous help since the very beginning and for a number of stimulating technical discussions.

I am also grateful to Dr. Nima Razavi-Ghods and Prof. Sana Salous from Durham University for the joint research and measurement campaigns we carried out together. The support provided by my second supervisor, Dr. Cheng-Xiang Wang, from Heriot-Watt University during the final part of my work is greatly acknowledged as well. Moreover, I am frankly thankful to Prof. Akbar Sayeed from Winsconsin-Madison University for all the long discussions on MIMO channel modelling and the results presented in Chapter 6.

The financial aid I received from Engineering and Physical Sciences Research Council (EPSRC) as well as from the Joint Research Institute (JRI), which is part of the Edinburgh Research Partnership, is also strongly appreciated. In this aspect, I would like to thank Prof. Steve McLaughlin for his guidance during the application stage and also for offering me a generous funding.

During the last three years here in Edinburgh, I had the fortune to have some people around me that made this period probably one of the most interesting in my life. Just a few of the names are Colin M., Dimitra V., Eirini K., Elias A., Giorgos A., Giorgos K., Luis B., Mary C., Marianthi A., Simon L., Steve D., Theodora K. and many more. All my long-time friends back in Greece deserve warm thanks as well but unfortunately the list is too long to name all of them!

Lastly, and most importantly, I wish to thank my parents, Katerina and Antoni, my sister Anny and my grandmother Mary for reasons that words fall short in describing.

This thesis is dedicated to my mother for being my main source of inspiration and for her boundless love. I hope I have not disappointed you...

Michail Matthaiou
Edinburgh, November 2008.

Contents

List of figures

List of tables

Acronyms and abbreviations

2D	two-dimensional
3D	three-dimensional
3GPP	3rd Generation Partnership Project
AAU	Aalborg University
AD	Adaptive Detector
AIC	Akaike Information Criterion
AoA	Azimuth of Arrival
AoD	Azimuth of Departure
APS	Angular Power Spectrum
BER	Bit Error Rate
BLAST	Bell Laboratories Layered Space-Time
BRAN	Broadband Radio Access Network
BS	Base Station
CCDF	Complementary Cumulative Distribution Function
CDF	Cumulative Distribution Function
COST	COoperation in the field of Scientific and Technical research
CR	Cramèr Rao
CSI	Channel State Information
DFT	Discrete Fourier Transform
DML	Deterministic Maximum Likelihood
DoA	Direction of Arrival
DoD	Direction of Departure
DSRC	Dedicated Short Range Communications
EM	Expectation Maximisation
ESPRIT	Estimation of Signal Parameter via Rotational Invariance Technique
ETSI	European Telecommunications Standards Institute
FB	Forward Backward
FD	Frequency Domain
FD-SAGE	Frequency-Domain SAGE

FT	Fourier Transform
GO	Geometrical Optics
GSCM	Geometry-based Stochastic Channel Model
HIPERLAN	HIgh PErformance Radio LAN
HR	High-Rank
IEEE	Institute of Electrical and Electronics Engineers
i.i.d.	independent and identically distributed
IST	Information Society Technology
ITS	Intelligent Transportation System
KDE	Kernel Density Estimate
KLT	Karhunen-Loève Transform
LoS	Line-of-Sight
LR	Low-Rank
MDL	Minimum Descriptive Length
MIMO	Multiple-Input Multiple-Output
ML	Maximum Likelihood
MMSE	Minimum Mean Squared Error
MPC	Multipath Component
MSE	Mean Squared Error
MT	Mobile Terminal
MUSIC	MUltiple Signal Classification
NLoS	Non Line-of-Sight
OFDM	Orthogonal Frequency Division Multiplexing
OLoS	Obstructed Line-of-Sight
OSIC	Ordered Successive Interference Cancellation
PDF	Probability Density Function
PDP	Power Delay Profile
PIC	Parallel Interference Cancellation
Pl	Path loss
RARE	Rank Reduction Estimator
r-RARE	root-RARE
s-RARE	spectral-RARE
RF	Radio Frequency

rms	root mean squared
RMSE	Root Mean Squared Error
RMUSIC	Root MUSIC
RT	Ray Tracing
RV	Random Variable
Rx	Receiver
SAGE	Space Alternating Generalised Expectation-Maximisation
SATURN	Smart Antenna Technology in Universal Broadband Wireless Networks
SCM	Spatial Channel Model
SCME	Spatial Channel Model-Extended
SIC	Serial Interference Cancellation
SIMO	Single-Input Multiple-Output
SISO	Single-Input Single-Output
SM	Spatial Multiplexing
SML	Stochastic Maximum Likelihood
SNR	Signal-to-Noise Ratio
SS	Spatial Smoothing
std	standard deviation
SV	Saleh Valenzuela
ToA	Time of Arrival
TUV	Technical University of Vienna
Tx	Transmitter
UCA	Uniform Circular Array
ULA	Uniform Linear Array
VCR	Virtual Channel Representation
VTR	Vehicle-to-Roadside
VTV	Vehicle-to-Vehicle
WHO	World Health Organisation
Wi-Fi	Wireless Fidelity
WINNER	Wireless World Initiative New Radio
WLAN	Wireless Local Area Network
WiMAX	Worldwide Interoperability for Microwave Access
ZF	Zero Forcing

List of symbols

$\odot$	element-wise (Schur-Hadamard) product
$\otimes$	Kronecker product
$\mathbf{0}_{m\times n}$	$(M \times N)$ all-zero matrix
$\mathbf{1}_{m\times n}$	$(M \times N)$ all-one matrix
$\mathbf{a}_r(\phi_{r,\ell})$	receive steering vector at azimuth $\phi_{r,\ell}$
$\mathbf{a}_t(\phi_{t,\ell})$	transmit steering vector at azimuth $\phi_{t,\ell}$
$\mathbf{A}_r$	receive steering matrix
$\mathbf{A}_t$	transmit steering matrix
$\widetilde{\mathbf{A}}_r$	independent receive DFT matrix
$\widetilde{\mathbf{A}}_t$	independent transmit DFT matrix
b	peak amplitude of the LoS signal
$\mathbf{B}_L$	diagonal matrix of the L path gains
C	instantaneous channel capacity
C_r	Rayleigh criterion to find surface roughness
$\overline{C}$	ergodic capacity
$\overline{C}_{max}$	maximum ergodic capacity
$\overline{C}_{min}$	minimum ergodic capacity
d	distance
d_0	reference path loss distance
d_r	inter-element distance at the receive array
d_t	inter-element distance at the transmit array
$\mathbf{D}(f)$	delay matrix of the ME model
D_r	extent of receive near-field scatterers from the x-axis
D_t	extent of transmit near-field scatterers from the x-axis
D_x	displacement on the x-axis
D_y	displacement on the y-axis
f	frequency index
f_k	k-th frequency bin of the channel frequency response
$f(r)$	hat function

$g[k]$	fading variations of the k-eigenmode
$G_r(\mathbf{\Omega}_r)$	receive antenna pattern in the 3D space
$G_t(\mathbf{\Omega}_t)$	transmit antenna pattern in the 3D space
h_k	smooth parameter of the KDE technique on the kth dimension
$h\left(\overrightarrow{r_t}, \overrightarrow{r_r}, \tau, \Omega_t, \Omega_r\right)$	distance-variant double directional channel impulse response
$h\left(t, \tau, \Omega_t, \Omega_r\right)$	time-variant double directional channel impulse response
$H(A\|B)$	conditional entropy between RVs A and B
$\mathbf{H}^{\dagger}$	Moore-Penrose pseudoinverse
$\mathbf{H}_{\text{DS}}$	Distributed scatterers model
$\mathbf{H}_{\text{finite}}$	Finite scatterers model
$\mathbf{H}_{\text{L}}$	deterministic LoS matrix
$\mathbf{H}_{\text{ME}}$	Maximum entropy model
$\mathbf{H}_{\text{mod}}$	Nakagami fading model
$\mathbf{H}_{\text{struct}}$	Structured channel model
$\mathbf{H}_{\text{virt}}$	Virtual channel representation model
$\mathbf{H}_{\text{w}}$	complex white Gaussian matrix
$\mathbf{H}_{\text{weichsel}}$	Weichselberger model
$\mathbf{H}(t, \tau)$	time-delay channel impulse response matrix
$\mathbf{H}(f, m, n)$	double directional-frequency dependent channel transfer function
$\mathcal{CN}(\mu, \sigma^2)$	complex Gaussian variable with mean μ and variance σ^2
$\mathcal{CN}(\mathbf{X}, \mathbf{Y})$	complex normally distributed matrix with mean $\mathbf{X}$ and covariance $\mathbf{Y}$
$\mathbf{I}_M$	$(M \times M)$ identity matrix
$I\left(\mathbf{x}; \mathbf{y}\right)$	mutual information between input $\mathbf{x}$ and output $\mathbf{y}$
K	Ricean K-factor
$\mathcal{K}(\cdot)$	kernel function for the KDE technique
K_c	number of clusters
K_s	subset of finite terms in an infinite double summation
L	number of impinging paths
L_c	number of paths within a cluster
$L_k^n(x)$	generalized k-th order Laguerre polynomial
m	Nakagami-m fading parameter
M	number of receive elements
n_p	path loss factor

$\mathbf{n}(t)$	time domain noise signal vector
N	number of transmit elements
$\widetilde{\mathcal{N}}(\mu, \sigma^2)$	circularly symmetric complex Gaussian variable with mean μ and variance σ^2
N_f	number of frequency bins
N_0	noise power
N_p	sample points in the KDE technique
N_s	subset of finite terms in an infinite double summation
$\mathbf{N}(k)$	frequency domain noise vector
p_ℓ	non-negative noise coefficient of the ℓ-th path in the SAGE algorithm
$p(r)$	PDF of the fading envelope
$\mathcal{P}(a, x)$	regularised gamma function
$P_{\phi_r}(\cdot)$	receive power azimuth spectrum
$P_{\phi_t}(\cdot)$	transmit power azimuth spectrum
$P_{k,l}(x)$	polynomial of order $k - l$ in x
P_r	received power
P_t	transmit power
P_0	received power at a known reference distance
$\mathbf{P}^r(t)$	diagonal received power matrix of the ME model
$\mathbf{P}^t(t)$	diagonal transmit power matrix of the ME model
$\mathcal{CQ}()$	complex non-central quadratic form distribution
Q	constellation size of a modulation technique
$\mathbf{Q}$	input covariance matrix
r	fading envelope
$\overrightarrow{r_r}$	position of receiver in the 3D space
$\overrightarrow{r_t}$	position of transmitter in the 3D space
$\mathbf{R}_{\mathbf{H}}$	full spatial correlation matrix
$\mathbf{R}_r$	receive correlation matrix
$\mathbf{R}_t$	transmit correlation matrix
$\mathbf{R}_{\sigma_r, d_r}$	deterministic spatial correlation matrix seen from the receiver
$\mathbf{R}_{\sigma_S, 2D_r/S}$	deterministic spatial correlation matrix seen from the virtual array
$\mathbf{R}_{\sigma_t, d_t}$	deterministic spatial correlation matrix seen from the transmitter
s_1	inter-element distance at the transmit 2-element ULA
s_2	inter-element distance at the receive 2-element ULA

S	number of near-field scatterers
S_t	number of near-field scatterers at the transmit side
S_r	number of near-field scatterers at the receive side
$\mathbf{S}(\theta_\ell)$	data signal of the ℓ-th path
t	time index
T	cluster time of arrival
$\mathbf{T}$	MIMO LoS correlation matrix
$\mathbf{u}_k$	k-th eigenvector of the full spatial correlation matrix
$\mathbf{U}$	periodic multi-frequency transmit test signal
$\mathbf{U}_r$	receive eigenbasis
$\mathbf{U}_t$	transmit eigenbasis
w_k	k-th largest eigenvalue of the scaled MIMO correlation matrix
$\widetilde{w_k}$	k-th largest eigenvalue of the MIMO correlation matrix
$\mathbf{w}$	vector containing the Wishart matrix eigenvalues
$\widetilde{\mathbf{w}}$	MMSE detector test vector
$\mathbf{W}$	scaled MIMO correlation matrix
$\widetilde{\mathbf{W}}$	MIMO correlation matrix
$\mathcal{W}$	power coupling matrix of the structured model
$\mathcal{CW}()$	complex non-central Wishart distribution
$\mathbf{x}(t)$	time-domain transmit signal vector
$\hat{\mathbf{x}}$	estimated transmit signal vector
$\mathbf{y}(t)$	time-domain received signal vector
$\mathbf{Y}_\ell$	complete data of the ℓ-th path
z	condition number of a dual complex Wishart matrix
$z\left(\tau, \phi_r, \phi_t; \mathbf{Y}_\ell\right)$	cost function of the FD-SAGE algorithm
$\mathbf{Z}^+$	set of positive integers
β	MPC complex path gain
$\mathbf{\Gamma}_\ell(t)$	full polarimetric matrix of the ℓ-th path
δ_R	receive correlation coefficient
δ_T	transmit correlation coefficient
ϵ	offset of an ergodic capacity upper bound
θ	axis rotation angle around the y axis
θ_ℓ	channel parameter vector for the ℓ-path

$\mathbf{\Theta}(t, f)$	scattering matrix of the ME model
λ	carrier wavelength
λ_1, λ_2	eigenvalues of the non-centrality matrix $\mathbf{\Omega}$
λ_k	k-th eigenvalue of the full spatial correlation matrix
$\boldsymbol{\lambda}$	vector containing the LoS MIMO matrix eigenvalues
$\boldsymbol{\lambda}_r$	vector with the eigenvalues of the receive correlation matrix
$\boldsymbol{\lambda}_t$	vector with the eigenvalues of the transmit correlation matrix
$\mathbf{\Lambda}_r$	diagonal matrix with the eigenvalues of the receive correlation matrix
$\mathbf{\Lambda}_t$	diagonal matrix with the eigenvalues of the transmit correlation matrix
$\mathbf{M}$	mean channel matric of a MIMO Ricean system
$\overrightarrow{\nu_r}$	speed of the receiver
$\overrightarrow{\nu_t}$	speed of the transmitter
ρ	received SNR
ρ_{ϕ_t,ϕ_r}	spatial correlation coefficient between azimuth spreads
σ^2	variance of a RV
σ_r	angular spread at the receiver
σ_s	angular spread of a virtual array
σ_t	angular spread at the transmitter
$\mathbf{\Sigma}$	correlation matrix of a dual Wishart matrix
τ	MPC time of arrival
ϕ_r	azimuth of arrival
$\phi_{r,rms}$	rms azimuth spread at the receive side
$\overline{\phi}_{t,rms}$	mean azimuth spread at the receive side
ϕ_t	azimuth of departure
$\phi_{t,rms}$	rms azimuth spread at the transmit side
$\overline{\phi}_{t,rms}$	mean azimuth spread at the transmit side
Φ_r	mean cluster azimuth of arrival
Φ_t	mean cluster azimuth of departure
ψ_r	elevation direction of arrival
ψ_t	elevation direction of departure
Ω	average power of Nakagami-m
$\mathbf{\Omega}_r$	receive spatial angle vector in the 3D space
Ω_r	direction of arrival in the 3D space

$\mathbf{\Omega}_t$	transmit spatial angle vector in the 3D space
Ω_t	direction of departure in the 3D space
$\mathbf{\Omega}$	centrality matrix of a dual Wishart matrix
$\mathbf{\Omega}_{\text{virt}}$	power coupling matrix of the VCR model
$\widetilde{\mathbf{\Omega}}_{\text{virt}}$	element-wise square root of $\mathbf{\Omega}_{\text{virt}}$
$\mathbf{\Omega}_{\text{weichsel}}$	power coupling matrix of the Weichselberger model
$\widetilde{\mathbf{\Omega}}_{\text{weichsel}}$	element-wise square root of $\mathbf{\Omega}_{\text{weichsel}}$
$[\cdot]^*$	complex conjugate operation
$[\cdot]^H$	Hermitian transposition
$[\cdot]^\dagger$	pseudo-inverse operation
$[\cdot]^T$	transposition operation
$E\{\cdot\}$	expectation operation
std$\{\cdot\}$	standard deviation operation
$\mathrm{vec}(\cdot)$	vectorisation operation
$\det(\cdot)$	determinant of a matrix
$\|\cdot\|_F$	Frobenius norm of a matrix
$\mathrm{tr}(\cdot)$	trace of a matrix
$\delta(\cdot)$	Dirac delta function
${}_0F_1(;)$	classical hypergeometric function
${}_2F_1(,;;)$	Gaussian hypergeometric function
${}_f\widetilde{F}_g(.,.;.,.)$	complex hypergeometric function of two matrix arguments
$\gamma(a,x)$	lower incomplete gamma function
$\Gamma(\cdot)$	Gamma function
$\arg\max_x g(x)$	maximising argument of the function $g(x)$
$\arg\min_x g(x)$	minimising argument of the function $g(x)$
$I_q(\cdot)$	modified Bessel function of first kind and qth order
$Q_{p,q}(y,z)$	Nutall Q-function
$Q(y,z)$	Marcum Q-function
$\cos(\cdot)$	cosine function
$\exp(\cdot)$	exponential function
$\log_2(\cdot)$	logarithmic function with base 2
$\sin(\cdot)$	sine function
$\mathbf{U}(\cdot)$	unit step function

Chapter 1
Introduction

The rapid advances of wireless communications over the last decades in conjunction with the design of upcoming mobile networks have necessitated the comprehensive understanding of the dynamic radio propagation mechanisms and characteristics. This demanding task can normally be accomplished by conducting radio channel measurements followed by the extraction of the path's parameters and the development of accurate channel models. On these grounds, the first goal of this thesis is the propagation modelling of modern indoor radio systems operating at the 5 GHz band. The second goal is related to short-range communications and particularly with the development of high throughput optimised architectures as well as with the investigation of the most important eigencharacteristics and derivation of novel ergodic capacity bounds. This introductory chapter covers the state-of-the art in the area of wireless communications and, further, addresses the open research challenges that have constituted the key motivations for the present Ph.D. work. Section 1.1 discusses the evolution of wireless communications with a view to the limitations of traditional configurations and the benefits of employing multiple antennas at both terminals. Section 1.2 explores the latest advances in indoor communications while Section 1.3 is dedicated to short-range propagation and potential future applications. Section 1.4 summarises the author's contributions to the field of multi-antenna systems. Finally, Section 1.5 gives a general outline of the remainder of the thesis.

1.1 Evolution of wireless communication technology

When Guglielmo Marconi back in 1901 signalled the letter "S" across the Atlantic, from England to Newfoundland, he never envisaged what his invention could lead to. The evolution of wireless communications continued through the years fostered by the development of semiconductor technology, advances in integrated circuit technology and the research in information theory as well as in digital signal processing, in the continuing search for higher system capacity, improved usability and bandwidth efficiency. In the near future, wireless networks are expected to provide a plethora of high-quality services (data, voice, video, networking) between different users and multiple sources of information; ultimately, the convergence between

decentralised wired and wireless technologies (subnetworks) will allow operators or content providers, and eventually customers, to enjoy the complete functionalities and resources of the network towards the direction of ubiquitous communications. This means that users will be able to receive the same service through different access networks regardless of the devices they will be utilising.

Many communication systems nowadays are based on conventional Single-Input Single-Output (SISO) architectures, where both the transmitter (Tx) and receiver (Rx) are equipped with a single antenna. However, irrespective of the modulation and coding scheme employed, it has been shown that for a finite bandwidth and given Signal-to-Noise Ratio (SNR), these systems set a fundamental upper limit on the data rate (usually referred to as *channel capacity*) and thus are inconvenient to support the future demanding applications. Throughout this thesis, capacity is adopted as the appropriate metric for quantifying the performance of wireless systems; in general, channel capacity refers to the maximum achievable data rate that can be transmitted over the channel with asymptotically small error probability. From an information theory point of view, Shannon defines channel capacity as the maximum of *mutual information*[1] [2].

A considerable number of researchers over the globe support that the solution for high throughput resides in the use of millimetre wave frequencies (60 GHz and beyond) because of the massive bandwidth available for dense wireless local communications (7 GHz of unlicensed spectrum) and the lower interference levels [3]. Another very significant motivation for exploiting this band is the fact that the wavelength becomes very short at such high frequencies, leading to devices of reduced size and making feasible the integration of many antennas and transceivers into a single chip. Nevertheless, this technology is still expensive due to the extreme accuracy required for constructing small-scale radio frequency (RF) equipment and for developing sophisticated signal processing algorithms; what's more, most current commercial applications are located at the microwave band. Recently, there has been an increasing design interest to decrease the feasibility cost of today's 60 GHz technology by using cheap, low-power silicon germanium chips [4]. In any case though, due to the excessive path loss (quadratic increase with frequency) and the oxygen absorption present at 60 GHz (10–15 dB/km), most practical platforms deploy high-gain directive antennas that rule out multipath propagation by focusing energy on a certain direction, specifically intended for fixed point-to-point applications with a coverage area of a few meters (< 10 m).

[1] This definition is valid for the usual case of memoryless channels, i.e. each channel realisation is independent of the previous one.

The most promising candidates for fulfilling the increasing demand for enhanced data rates within a fixed limited bandwidth are the so-called Multiple-Input Multiple-Output (MIMO) systems which make use of multiple antenna elements at both the Tx and Rx. It has been theoretically shown that these systems offer benefits which go far beyond those of traditional configurations by fully exploiting the scattering environment; in fact, under specific propagation conditions, i.e. high multipath richness, MIMO capacity grows linearly with the minimum number of transmit and receive antennas [5, 6]. This capacity boost is achieved by the simultaneous transmission in time and within the same frequency interval of orthogonal, non-interfering data streams which are conveyed through the established spatial subchannels between the two ends. The differentiation at the Rx happens in the spatial domain and is possible since each multipath impinging on it has experienced a series of complex propagation interactions with the surrounding environment and therefore carries a unique spatial signature. Given this high practical importance of MIMO technology, the key motivation of this thesis is to study in depth the performance of indoor and short-range MIMO systems that are expected to support forthcoming high-speed (well above 100 Mbits/s) Wireless Local Area Networks (WLANs).

1.2 Indoor wireless communications

The first part of the thesis focuses on the area of indoor communications which has been extensively explored over the last decades following the increasing demand for high-speed data transmission over medium ranges. Current indoor WLAN systems operate mainly at the 2.4 and 5.2 GHz bands as standardised by either the Institute of Electrical and Electronics Engineers (IEEE) 802.11 protocol or its European counterpart, namely the HIgh PErformance Radio LAN (HIPERLAN) protocol defined by the European Telecommunications Standards Institute (ETSI) Broadband Radio Access Network (BRAN). In detail, the IEEE 802.11a protocol operates at 5.2 GHz and is able to deliver data rates as high as 54 Mbits/s within the operation range of a so-called hotspot or access point (approximately 35 m in an indoor propagation environment)[2] [7]. Likewise, the IEEE 802.11n consensus standard, which is currently under development and due to be finalised in June 2009, has also specified the usage of this band for WLAN applications introducing the application of MIMO technology along with a wider operation bandwidth (40 MHz instead of 20 MHz as in IEEE 802.11a). The objectives of this protocol are a raw data rate of up to 600 Mbits/s (when four elements are employed at both

[2] Please note that this technology is widely known as Wireless Fidelity (Wi-Fi).

IEEE protocol	Carrier frequency	Channel bandwidth	Maximum data rate	Indoor oper. range
802.11a	5 GHz	20 MHz	54 Mbits/s	35 m
802.11b	2.4 GHz	20 MHz	11 Mbits/s	38 m
802.11g	2.4 GHz	20 MHz	54 Mbits/s	38 m
802.11n	2.4/5 GHz	40 MHz	600 Mbits/s	70 m

Table 1.1: *Basic characteristics of the IEEE 802.11 family of protocols.*

ends) along with a coverage radius of approximately 70 m [8]; some experts claim that these revolutionary benefits will eventually convince the majority of modern commercial users to abandon cable access networks technology. The main specifications of the most known IEEE 802.11 protocols are tabulated in Table 1.1.

Apart from WLAN services, a new innovative technology promises to replace last-mile wired-access networks and provide broadband Internet to emerging markets that have no broadband access. With a theoretical maximum data rate of 75 Mbits/s and maximum transmission range of 50 Km, the Worldwide Interoperability for Microwave Access (WiMAX) protocol is regarded as an economically viable solution for seamless long-range delivery of information. The associated IEEE 802.16d standard, finalised in 2004 for the 2–11 GHz frequency band, is suitable for fixed wireless access but lacks mobility support [9]. Since then, various amendments were proposed which evolved to the latest IEEE 802.16e standard, aiming to support nomadic mobility [10]. This mobile WiMAX scheme is planning to use MIMO technology to improve coverage and exploit the Non Line-of-Sight (NLoS) propagation that exists in the vast majority of practical radio channels. Interestingly, most countries allow higher power output levels in the upper 5 GHz band (5.725–5.850 GHz) than in the lower 5 GHz bands, making the former more attractive to WiMAX applications. Though originally designed for point-to-multipoint topologies in which a base station (BS) distributes traffic to many subscriber stations mounted on rooftops, WiMAX is also anticipated to provide users with broadband connectivity over huge indoor areas such as transportation halls, shopping malls, airport lounges and many more; this is the key difference between WiMAX and the 802.11 hotspots which offer a moderate coverage and are convenient for allowing a home or office PC to connect to the Web [11].

1.3 Short-range wireless communications

The second part of this thesis covers the area of short-range communications where the two ends are not spaced far apart and the link is dominated by a non-fading deterministic Line-of-Sight (LoS) component. While the conventional applications include peer-to-peer communications, fixed wireless access and Bluetooth, an emerging technology has recently attracted considerable research and industry interest. This is the field of vehicular on-the-road communications which hold the promise of great improvements in both the efficiency of the transport systems and the safety of all road users.

The automotive industry strives decisively to develop a novel WLAN technology suitable for vehicle-to-vehicle (VTV) and vehicle-to-roadside (VTR) channels. The so-called Dedicated Short-Range Communications (DSRC) protocol is designed to work in parallel with cellular communications by providing high data rates with a low latency between vehicles and from vehicles to fixed infrastructure units. The official spectrum allocation for DSRC was completed in 1999 by the American Federal Communication Commission which designated 75 MHz of bandwidth, partitioned into seven 10 MHz channels, at the 5.9 GHz Intelligent Transportation System (ITS) frequency band. It has also being standardised as the IEEE 802.11p protocol (due to be ratified in April 2009) which is essentially an amendment of the IEEE 802.11a protocol adjusted for low overhead operations in the DSRC spectrum [12]. Apart from the DSRC bandwidth that is half of the 802.11a bandwidth, the remaining physical layer specifications, such as the modulation scheme, frame structure and training sequences, are almost identical [13]. Nevertheless, while IEEE 802.11a has been designed for indoor WLAN applications in a low-mobility environment, IEEE 802.11p is expected to operate over time-selective channels where vehicles are moving with speeds as high as 120 miles/h and offer a wider coverage of up to 1000 m.

The DSRC applications are usually classified into safety and non-safety with higher priority being given to the former category following the steadily increasing need for zero-accident road journeys and minimisation of the tremendous cost caused by traffic collisions. In 2006, road accidents accounted for 39,000 deaths within Europe while in the U.K. alone this number was 3,172. According to the World Health Organisation (WHO), road accidents cause the death of 1.2 million people annually worldwide, making it the seventh biggest killing cause in the world, while by 2020 road deaths are predicted to become the third killing cause. Road traffic injuries cost low-income and middle-income countries between 1% and 2% of their gross

national product which represents more than the total development aid received by these countries [14]. While different factors contribute to vehicle crashes, such as mechanical problems and bad weather, driver behaviour is considered to be the leading cause of more than 90 percent of all road accidents. In fact, the inability of drivers to react fast to emergency situations can potentially cause chain collisions where an initial crash is followed by secondary crashes [15]. This is the main reason behind extending ITS technology to safety applications that include among others: intersection collision avoidance, road status reports, alerts for approaching emergency vehicles and lane departure, forward obstacle detection and avoidance as well as sudden halt warnings.

Apart from safety applications, a variety of more demanding applications have emerged which range from high-speed networking and video streaming to mobile commerce and Web surfing. Due to the high spectral efficiency requirements these applications impose, the use of multiple antenna elements seems sensible, thereby bringing MIMO technology to the field of vehicular communications. An illustrative graph showing the future of vehicular communications with full availability, connectivity, flexibility, and transparency between road users is seen in Fig. 1.1.

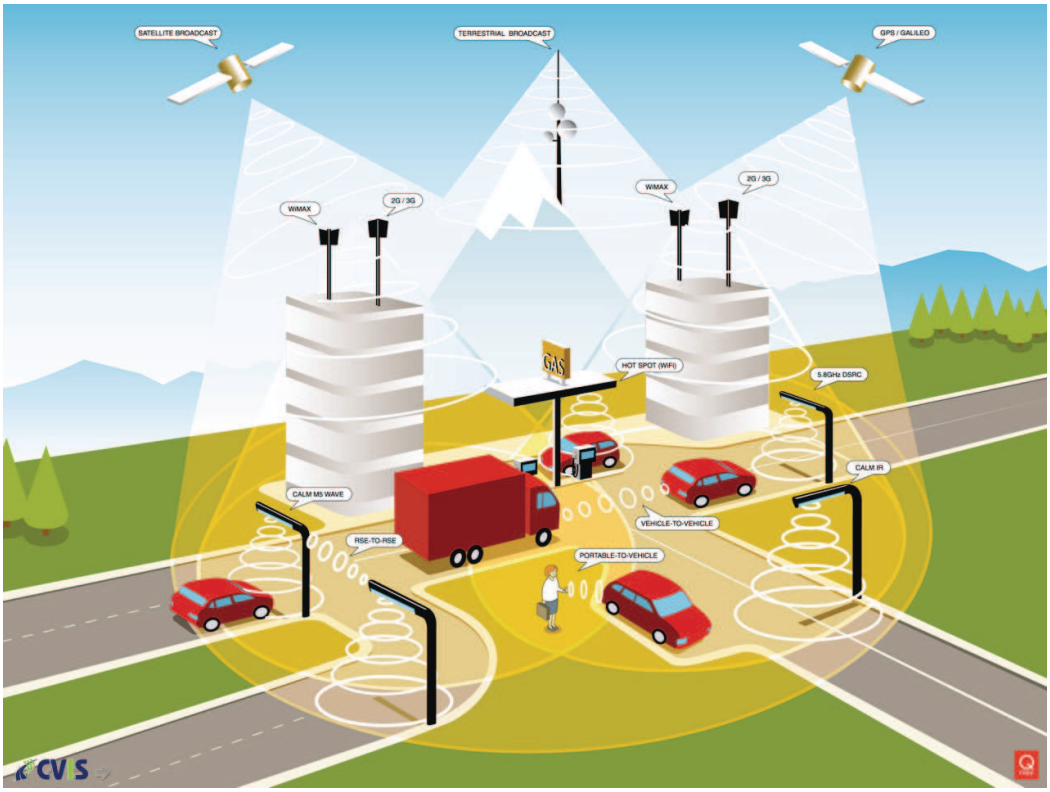

Figure 1.1: *A future deployment scenario of vehicular communications (courtesy of [16]).*

1.4 Key contributions

The main contributions of this work are now summarised as follows:

- A novel statistical-based indoor channel model that captures the fading variations of each spatial eigenmode separately and assigns the flexible Nakagami-m distribution to each of them [17, 18]. The model yields an excellent fit with a set of measured data and systematically outperforms two analytical reference models that have recently been proposed in the corresponding literature.

- A powerful unconstrained technique for generating independent Nakagami-m envelope deviates for arbitrary values of the corresponding shape parameters. The method is constructed upon the well known *rejection/acceptance* technique and overcomes the deficiencies of all similar techniques and in parallel offers a remarkable accuracy [19].

- A new maximum likelihood (ML) high-resolution array processing technique namely, the three-dimensional (3D) frequency domain-Space Alternating Generalised Expectation Maximisation (FD-SAGE) algorithm is devised for estimating the multipath parameters in both temporal and spatial domains [20]. The scheme is further used to characterise an indoor MIMO channel by means of clustering, azimuth dispersion and inter-dependency of the spatial domains [21].

- For the case of dual-branch[3] VTR MIMO Ricean configurations, a maximum near-field[4] LoS capacity criterion is formulated as a function of the carrier wavelength, transmit-receive separation distance and inter-element spacings. The capacity of systems that follow this criterion is not only benefited by the presence of strong LoS components but is normally greater than the capacity offered by the usual Rayleigh channels [22].

- Taking into account the high practical usability of dual MIMO Ricean systems (small setup size and low implementation cost), a detailed statistical eigenanalysis is carried out and novel closed-form formulae are derived for the eigenvalue and condition number densities [23]. These expressions are subsequently used to construct an adaptive detec-

[3] Throughout the thesis, the term *dual-branch* or simply *dual* will stand for MIMO systems with two transmit and two receive antenna elements.

[4] Hereafter, the term *near-field* will express the close-in region of an antenna where the angular distribution is dependent upon the distance from the source and the waves are propagating as spherical wavefronts. On the contrary, the *far-field* is the region outside the near-field where the angular distribution is independent of the distance from the source and the waves are propagating as plane wavefronts.

tor (AD) which switches between the robust but computationally expensive ML and the suboptimal Zero Forcing (ZF) detector [24].

- A novel ergodic capacity upper bound for dual double-correlated MIMO Ricean systems is derived based on a fundamental power constraint; the bound is applicable for arbitrary rank of the deterministic mean channel matrix and arbitrary SNR and, more importantly, includes previously reported analytical bounds as special cases [25]. The tightness of the bound is also analytically determined for asymptotically low and high SNRs.

1.5 Organisation of the thesis

An outline of the remainder of this thesis is given in this section.

Chapter 2 covers the principles of wireless propagation and subsequently presents the fundamental properties of the promising MIMO technology. Moreover, the area of channel modelling is reviewed while the main characteristics of each model are highlighted. A categorisation of all models, with regard to which features the model's designer intends to reconstruct, is also performed.

Chapter 3 proposes a novel spatial channel model based on the *Karhunen-Loève Transform* (KLT) which is validated through a set of measurement data at the carrier frequency of 5.2 GHz. The scheme decomposes the MIMO correlation matrix and assigns a Nakagami-m fading distribution to each resulting uncorrelated eigenmode. The model's performance is assessed by means of mutual information and link-level performance where its superiority, in comparison with two reference models, is clearly demonstrated.

Chapter 4 introduces an array processing algorithm for extracting multipath channel parameters. In particular, the 3D FD-SAGE algorithm is employed in conjunction with the serial interference cancellation (SIC) technique to identify the dominant paths and estimate their key parameters. Apart from validating the scheme robustness in a synthetic environment, a detailed characterisation of the previously mentioned measured channel is conducted in the double directional domain using the SAGE framework.

Chapter 5 suggests a straightforward criterion for achieving high VTR MIMO capacities in the presence of a LoS component. The sensitivity of the proposed configuration is investigated under optimal and suboptimal positioning and orientation conditions. Secondly, the eigenstatistics

of dual MIMO Ricean channels are analytically assessed and closed-form formulae are derived which are validated through Monte-Carlo simulations. These statistical results are finally applied to the detection stage of MIMO receivers so that an AD is developed that can minimise the implementation cost and complexity of most practical ML-based testbeds.

Chapter 6 derives a novel upper bound on the ergodic capacity of dual spatially correlated MIMO Ricean systems that includes previously reported bounds as special cases. Apart from being remarkably simple and efficient, the bound is applicable for any arbitrary rank of the LoS component and system SNR. Its tightness is analytically evaluated and asymptotic closed-form expressions for the error of the bound are presented which are verified through Monte-Carlo simulations.

Chapter 7 forms a summary of the most important conclusions drawn from this thesis and proposes several research paths for future work.

Chapter 2
MIMO wireless systems and background of channel modelling

The medium responsible for the transmission and reception of information signals between two antennas in space is widely known as the wireless propagation channel. According to [26], there is a key difference between the radio channel and the propagation channel. In particular, the latter does not take into account the antenna patterns and this means that isotropic antennas are assumed at both sides. The radio channel though includes both array responses and therefore is described by a non-directional channel response. In this chapter, the fundamental concepts and background for statistically modelling a MIMO propagation channel are assessed. The remainder of this chapter is organised as follows: Section 2.1 presents a summary of the basic multipath propagation mechanisms and manifestations experienced in typical wireless channels. In Section 2.3, the foundations of MIMO technology are outlined along with an investigation of the trade-offs between MIMO features. Also, a brief derivation of the very useful capacity formula is presented. In Section 2.4, the principles of multi-dimensional channel modelling are introduced with a view to double directional propagation. Section 2.5 focuses on the current state-of-the-art in the area of MIMO channel modelling; classification of the channel models into relevant categories is also provided along with the key characteristics of each model. Finally, Section 2.6 concludes the chapter and summarises the key findings.

2.1 Basic multipath propagation mechanisms

In a wireless channel, the interaction of the transmitted signal with the physical environment as it travels towards the Rx creates multiple propagated wavefronts; a phenomenon usually referred to as *multipath propagation*. Multipath propagation occurs due to three basic mechanisms, namely *reflection*, *diffraction*, and *scattering*. In Fig. 2.1, an illustrative figure shows the mechanisms causing multipath effects in an indoor environment. The impact of each of these mechanisms on the received signal is outlined below.

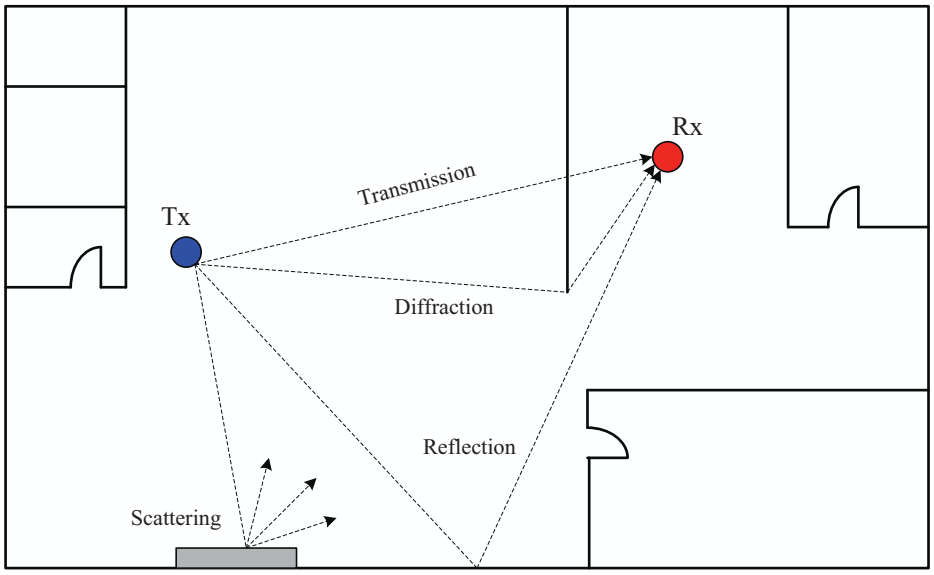

Figure 2.1: *Basic propagation mechanisms in an indoor wireless channel.*

Transmission corresponds to the direct route between the Tx and Rx; if this is unobstructed, free-space LoS propagation takes place. In the case of obstructed-LoS (OLoS) transmission through walls and ceilings, it has been found that the penetration loss, as defined by Rice in [27], is a function of the construction materials of a building, building orientation with respect to the Tx, internal layout, floor height and the percentage of windows in a building [28]. The main effect of OLoS transmission is that the direct component power is much closer to the power of the diffracted and reflected components.

Reflection occurs when a propagating electromagnetic wave impinges upon a surface with dimensions much larger than the wavelength λ of the wave. In an outdoor environment, reflections are created by the surface of the earth and buildings while in an indoor environment, reflections are mostly caused by floors, walls, ceilings and furniture [29]. The roughness of surface defines the type of reflection according to:

- *Specular reflection* occurs when the surface is smooth and ideally infinite. The incoming wave splits up into reflected and transmitted (refracted) waves whose magnitudes can be computed via Fresnel's formulae. The main characteristic of specular reflection is that the directions of the incident and reflected waves are the same with respect to the surface normal on the same plane. While there are no perfectly flat and infinite surfaces, specular reflection is a good approximation if the surface is sufficiently large in wavelengths (i.e. larger than the cross-section of the first Fresnel zone) and not too rough compared to λ.

- *Diffuse reflection* occurs when the surface has a degree of roughness and this causes the incoming ray to be spread in a broad range of non-specular directions and further reduces the energy in the specular direction. The severity of diffuse scattering is dependent on both the surface roughness and incidence angle. A critical surface roughness C_r is determined by the Rayleigh criterion which is given as [30]

$$C_r = \frac{4\pi\sigma\cos\theta}{\lambda} \tag{2.1}$$

where σ is the standard deviation of the surface irregularities and θ is the angle of incidence with respect to the normal of the surface. In general, the surface is considered to be smooth and thus specular reflection dominates when $C_r < 0.1$; in such a case, waves reflected from the surface encounter only small relative phase shift with respect to each other. For $C_r > 10$ though, highly diffuse reflection dominates and the specularly reflected wave is small enough to be neglected given that waves reflected from the surface exhibit a relatively large phase shift. An illustrative graph showing the different types of reflection can be seen in Fig. 2.2.

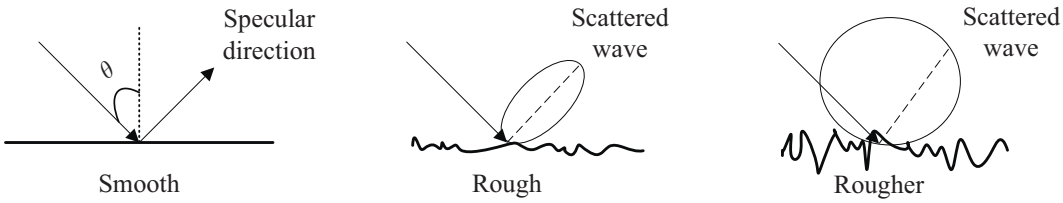

Figure 2.2: *The effect of surface roughness on the type of reflection (adopted from [30]).*

Diffraction occurs when a radio path is obstructed by either a surface that has sharp irregularities (edges) or a dense body with dimensions that are large compared to λ, causing secondary waves to be formed behind the obstructing body [29]. This phenomenon originates from Huygen's principle which states that all points on a wavefront act as point sources of secondary wavelets; these wavelets are eventually combined to produce a new wavefront in the direction of propagation [29, 30]. Diffraction is often termed shadowing because the diffracted field can reach the Rx even when shadowed by an impenetrable obstruction [31]. In outdoor environments, diffraction usually occurs via propagation around hills or over rooftops while in the indoor environment, diffraction normally occurs via propagation around door openings and corners. The power loss associated with this propagation effect is usually very high compared to that of reflection.

Scattering occurs when a radio wave impinges on any surface with dimensions of the order of λ or less, causing the reflected energy to spread out in all directions. In an urban environment, typical obstructions that yield scattering are foliage, lamp posts and road signs while in indoor environments the primary scatterers are walls and furniture [29]. Henceforth, the term scatterer will describe any obstacle that causes a change to the direction of a propagating wavefront.

2.2 Basic multipath propagation manifestations

At this point, the reader is reminded that multipath propagation can also be characterised by means of *path loss* (Pl) and *fading*. A brief description of these phenomena is provided below.

2.2.1 Path loss

Path loss can be defined as the ratio of the received to transmitted power. In fact, it expresses the diminution of the received power P_r with distance d as

$$P_r(d) = P_0 \left(\frac{d}{d_0} \right)^{-n_p} \tag{2.2}$$

where n_p is the so-called Pl factor and P_0 the reference power, dependent on the transmitted power, frequency and antenna gains, at a known distance d_0. For free-space propagation, $n_p = 2$ but becomes larger for other more complicated cases. In general, the more cluttered an environment is the higher the value of n_p. The Pl also depends on the operating frequency; the authors in [32] compared the path losses for 1.7 GHz and 60 GHz and showed that the difference is greater than 45 dB. The difference in P_0 (31 dB) partially explains the result. The rest of the difference is due to the higher penetration loss of materials and the stronger reflections and diffractions at higher frequencies. An excellent review of Pl models can be found in [33, 34].

2.2.2 Slow and fast fading

The superposition of all impinging waves at the Rx gives rise to fluctuations in the amplitude and phase of the received signal, commonly known as multipath fading, which is also distance dependent. A further classification can be made in two categories namely *large scale* (or *slow fading* or sometimes *shadowing*) and *small scale fading* (or *fast fading*).

Large scale fading refers to the slow long-term variation of the local mean signal strength as a mobile terminal (MT) moves over tens of wavelengths. The term shadowing is indicative since typically these changes are due to the changes in visibility or the appearance/disappearance of shadowing objects on the signal paths. In outdoor environments, it is mainly caused by prominent terrain contours (for instance hills, forests, buildings) while in indoor propagation, it occurs due to the blocking effects of large objects such as walls and furniture [31]. The envelope of a slow-fading signal has been found to follow a log-normal distribution especially in outdoor environments [29].

Small scale fading expresses the dramatic short-term changes in the signal envelope as a MT moves over small distances. This rapid fluctuation can be attributed to the incoherent summation of a large number of independent rays coming from all directions with random phases (as a result of different path lengths) which can add either constructively or destructively. Fig. 2.3 illustrates an example of the path loss, small and large scale fading phenomena as a function of the distance travelled by a MT.

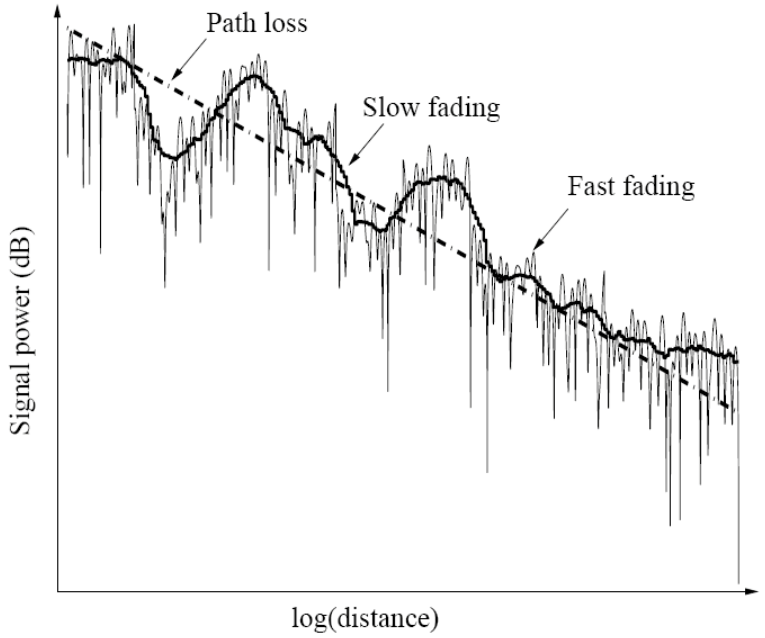

Figure 2.3: *Fading manifestations vs the distance travelled by a MT (courtesy of [35]).*

For the statistical description of fast fading envelopes, three main distributions have been proposed, namely Rayleigh, Ricean and Nakagami-m. Rayleigh fading can model multipath situations when there is no direct LoS between the Tx and Rx and the incoming waves have approximately equal amplitudes. The probability density function (PDF) of the signal's envelope

r is then given by [36]

$$p(r) = \frac{r}{\sigma^2} \exp\left(-\frac{r^2}{2\sigma^2}\right), \quad r \geq 0 \tag{2.3}$$

where $E\left\{r^2\right\} = 2\sigma^2$ is the distance-average power of the received signal. For the rest of the thesis, the notation $E\left\{\cdot\right\}$ will refer to the expectation operation. Under these conditions the phase of the received signal is uniformly distributed in $[0, 2\pi)$. In practice, however, there is occasionally a dominant incoming wave which can be either a LoS component or a strong specular wavefront. In such a case, the envelope of the received signal follows the Ricean distribution according to [36]

$$p(r) = \frac{r}{\sigma^2} \exp\left(-\frac{r^2 + b^2}{2\sigma^2}\right) I_0\left(\frac{br}{\sigma^2}\right), \quad r \geq 0, A \geq 0 \tag{2.4}$$

with b being the peak amplitude of the dominant signal and $I_0(\cdot)$ the modified Bessel function of first kind and zero order. The Ricean K-factor controls the ratio of powers of the free-space signal and the scattered waves, i.e. $K = b^2/2\sigma^2$; when $K = 0$ the Ricean distribution degenerates to a Rayleigh distribution.

The Nakagami-m distribution [37] has also attracted considerable research interest since it yields a satisfactory fit for various measured channels over a wide range of frequency bands [38, 39]. The corresponding PDF is

$$p(r) = \frac{2}{\Gamma(m)} \left(\frac{m}{\Omega}\right)^m r^{2m-1} e^{-mr^2/\Omega}, \quad r \geq 0 \tag{2.5}$$

where $\Gamma(\cdot)$ expressing the Gamma function and $\Omega = E\left\{r^2\right\} \geq 0$ is the average power. The Nakagami fading figure m, indicating the severity of fading, is determined as

$$m = \frac{\Omega^2}{E\left\{(r^2 - \Omega)^2\right\}} \geq \frac{1}{2}. \tag{2.6}$$

Both Ricean and Nakagami-m distributions have two shape parameters and behave approximately equivalently near their mean value. When $m = 1$ the Nakagami distribution reduces to Rayleigh distribution while for $m = 0.5$ it reduces to the one-sided Gaussian distribution.

2.2.3 Flat and frequency-selective fading

Another distinction is usually made to the type of fading with regard to the so-called *coherence channel bandwidth*. The coherence bandwidth, which is inversely related to the time delay spread of the channel, indicates the minimum frequency separation at which the attenuation of the amplitudes of two frequency components becomes decorrelated. The decorrelation is usually defined as the point where the correlation coefficient between the fading envelopes at the two frequencies is reduced from unity to 0.9 or 0.5.

On this basis, *flat fading* occurs when the coherence bandwidth is larger than the bandwidth of the signal. Therefore, all frequency components of the signal will experience the same magnitude of fading. On the other hand, *frequency-selective fading* occurs when the coherence bandwidth of the channel is smaller or of the order of the bandwidth of the signal. Under these circumstances, two frequency components that are far apart experience substantially different attenuations.

2.3 Fundamentals of MIMO technology

2.3.1 Background of MIMO systems

The potential of employing multiple antennas at both ends of a radio link in order to improve the channel throughput was sparked by the pioneering work of Winters in 1987 [40]. Surprisingly, it was not until mid-90s that two breakthrough papers by Foschini [5] and Telatar [6] separately investigated this promising technology in detail. Both authors showed that MIMO systems have the unique ability to turn multipath propagation, usually regarded as a serious hindrance in wireless communications, into an advantage for increasing the spectral efficiency. Under independent Rayleigh fading conditions, MIMO systems offer a linear capacity increase that is proportional to the minimum number of receive M and transmit N antenna elements, i.e. $\min\{M, N\}$.

The boost in spectral efficiency offered by an ideal MIMO system was firstly demonstrated in [5], where an architecture called BLAST[1] along with a reconstruction algorithm and a coding/decoding scheme were devised. The most attractive feature of MIMO systems is their ability to simultaneously transmit individual (orthogonal) data streams from each antenna el-

[1] BLAST: Bell Labs Layered Space Time.

ement; in the literature, this feature is widely known as *spatial multiplexing* (SM) [41]. The number of orthogonal multiplexed streams depends on the spatial properties of the surrounding environment and is upper limited by $\min\{M, N\}$.

Another feature of MIMO systems is *spatial diversity* which is a means to combat fading by exploiting multiple uncorrelated replicas of the transmitted signal. Diversity occurs when the antenna spacing is high enough so that independent signal paths are created, resulting in a reduced variation of the received signal's power. Diversity reduces the probability that all branches are in a deep fade simultaneously and thus it enhances the error rate performance (channel hardening). MIMO techniques permit the spatial diversity to be exploited at both sides of the radio link with the maximal diversity gain being MN.

However, there is an inherent trade-off between SM and spatial diversity. This means that increasing the diversity advantage comes at the expense of decreasing the SM gain, and vice versa. In fact, the authors in [42] showed that the diversity-multiplexing trade-off achievable by a system is a more fundamental measure of its performance than just its maximal diversity gain or its maximal multiplexing gain alone. Generally, the optimal trade-off is determined by system requirements such as the desired data rate and reliability of transmission. High data rates can be achieved by employing multiplexing to full extent while high reliability benefits from diversity [43].

Smart antenna systems, which use an antenna array at a single end, make use of *beamforming* in order to increase the average SNR and suppress interference from other users by steering energy into desired directions. Likewise, for MIMO systems beamforming may be applied at the Tx and/or the Rx side. The more directive a channel is the higher its beamforming gain. For pure LoS conditions with only one path present, the maximal beamforming gain MN is obtained, albeit at the expense of an increased spatial correlation that diminishes the beneficial effects of spatial diversity. Finally, it should be underlined that full beamforming excludes full diversity or multiplexing and the same is true for full diversity and beamforming/multiplexing; however, full multiplexing excludes beamforming whereas it only reduces diversity.

2.3.2 General structure of MIMO systems

Let us now consider a general MIMO system equipped with N transmit and $M \leq N$ receive antenna elements. For such a scenario, the transmitted signal $\mathbf{x}(t) \in \mathbb{C}^{N\times 1}$ can be modelled as a signal vector

$$\mathbf{x}(t) = [x_1(t), x_2(t) \ldots, x_N(t)]^T \tag{2.7}$$

where $x_n(t)$ is the signal emitted by the n-th transmit antenna element and $[\cdot]^T$ denotes transposition. Similarly, the received signal vector $\mathbf{y}(t) \in \mathbb{C}^{M\times 1}$ is modelled as

$$\mathbf{y}(t) = [y_1(t), y_2(t) \ldots, y_M(t)]^T . \tag{2.8}$$

Then, the input-output complex relationship can be succinctly written as

$$\mathbf{y}(t) = \left[\sqrt{\frac{\rho}{N}} \int_{\tau} \mathbf{H}(t,\tau)\mathbf{x}(t-\tau)d\tau\right] + \mathbf{n}(t) \tag{2.9}$$

where ρ is the average SNR per branch at the Rx and $\mathbf{n}(t)$ is the noise plus interference term. The elements of the channel impulse response matrix $\mathbf{H}(t,\tau) \in \mathbb{C}^{M\times N}$ describe the response between the m-th receive and the n-th transmit element. The channel matrix, containing all complex response coefficients, is then written as

$$\mathbf{H}(t,\tau) = \begin{bmatrix} h_{11}(t,\tau) & h_{12}(t,\tau) & \cdots & h_{1N}(t,\tau) \\ h_{21}(t,\tau) & h_{22}(t,\tau) & \cdots & h_{2N}(t,\tau) \\ \vdots & \vdots & \ddots & \vdots \\ h_{M1}(t,\tau) & h_{M2}(t,\tau) & \cdots & h_{MN}(t,\tau) \end{bmatrix} \tag{2.10}$$

where τ corresponds to the delay index. For the flat-fading case, where the channel is non-zero only for $\tau = 0$, (2.9) becomes

$$\mathbf{y}(t) = \sqrt{\frac{\rho}{N}}\mathbf{H}(t)\mathbf{x}(t) + \mathbf{n}(t). \tag{2.11}$$

2.3.3 MIMO capacity

For the derivation of MIMO capacity formula, let us consider the case where the Tx is constrained to its total power P_t regardless of the number of antennas, i.e.

$$\mathrm{tr}(\mathbf{Q}) \leq P_t \tag{2.12}$$

where $\mathbf{Q} = E\left\{\mathbf{x}\mathbf{x}^H\right\}$ is the input covariance matrix, $[\cdot]^H$ denotes the Hermitian transpose and $\mathrm{tr}(\cdot)$ returns the trace of a matrix. The common assumption that the elements of $\mathbf{n}(t)$ are independent and identically distributed (i.i.d.) $\sim \mathcal{CN}(0,1)$ complex variables is introduced and then the noise covariance matrix $E\left\{\mathbf{n}\mathbf{n}^H\right\} = \mathbf{I}_M$, with $\mathbf{I}_M$ the $(M \times M)$ identity matrix.

As was remarked in the introductory chapter, for memoryless channels, capacity represents the maximum mutual information. Following (2.11), the mutual information $I\left(\mathbf{x};(\mathbf{y},\mathbf{H})\right)$ between the input $\mathbf{x}$ and the output $\mathbf{y}$ can be written as[2]

$$I\left(\mathbf{x};(\mathbf{y},\mathbf{H})\right) = H\left(\mathbf{y}|\mathbf{H}\right) - H\left(\mathbf{y}|\mathbf{x},\mathbf{H}\right) = H\left(\mathbf{y}|\mathbf{H}\right) - H\left(\mathbf{n}|\mathbf{H}\right). \tag{2.13}$$

In general, $H(A|B)$ stands for the conditional entropy between the random variables (RVs) A and B. Given a covariance matrix $\mathbf{Q}$, circularly symmetric complex Gaussian variables[3] are entropy maximisers and therefore it is sensible to assign this distribution[4] to the input signal $\mathbf{x}$ [6]. Then, the received signal is in turn a circularly symmetric complex Gaussian variable with covariance matrix $E\left\{\mathbf{y}\mathbf{y}^H\right\} = \frac{\rho}{N}\mathbf{H}\mathbf{Q}\mathbf{H}^H + \mathbf{I}_M$. Substituting this relationship into (2.13), the mutual information of a random MIMO channel becomes

$$I = \log_2\left(\det\left(\frac{\rho}{N}\mathbf{H}\mathbf{Q}\mathbf{H}^H + \mathbf{I}_M\right)\right). \tag{2.14}$$

Hence, the instantaneous capacity C of an $(M \times N)$ MIMO channel with Gaussian inputs is [6]

$$C = \max_{\mathbf{Q}\geq 0;\ \mathrm{tr}(\mathbf{Q})\leq P_t} \log_2\left(\det\left(\frac{\rho}{N}\mathbf{H}\mathbf{Q}\mathbf{H}^H + \mathbf{I}_M\right)\right) \tag{2.15}$$

where the maximisation is performed over a set of positive and semi-definite Hermitian matrices

[2] Note that the channel is fully described with input $\mathbf{x}$ and output $(\mathbf{y},\mathbf{H}) = (\mathbf{H}\mathbf{x}+\mathbf{n},\mathbf{H})$.

[3] A circularly symmetric complex Gaussian variable z, denoted by $z \sim \tilde{\mathcal{N}}(0,\sigma^2)$, is a complex RV $z = x + jy$ where both x and y are i.i.d. $\sim \mathcal{N}(0,\sigma^2/2)$.

[4] The differential entropy of a complex Gaussian vector $\mathbf{x}$ with covariance $\mathbf{Q}$ is given by $\log_2(\det(\pi e\mathbf{Q})$.

$\mathbf{Q}$ satisfying (2.12). The ergodic capacity (or the expectation of C) then reads

$$\overline{C} = \max_{\mathbf{Q}\geq 0;\ \mathrm{tr}(\mathbf{Q})\leq P_t} E_{\mathbf{H}} \left\{ \log_2 \left(\det \left(\frac{\rho}{N} \mathbf{H}\mathbf{Q}\mathbf{H}^H + \mathbf{I}_M \right) \right) \right\} \tag{2.16}$$

where the expectation is taken with respect to the random channel matrix $\mathbf{H}$. To the best of the author's knowledge, no explicit closed-form solution for the maximisation over $\mathbf{Q}$ exists in the literature. In his seminal work though, Telatar showed that when the channel matrix has i.i.d. $\sim \widetilde{\mathcal{N}}(0,1)$ entries and no channel state information (CSI) is available at the Tx, it is optimal to use a uniform power distribution with a transmit covariance matrix $\mathbf{Q} = \mathbf{I}_N$. Under these conditions, a Rayleigh fading channel is modelled with sufficient physical separation between the transmit and receive antenna elements. This approach results in the well known formula for the ergodic MIMO capacity [5, 6]

$$\overline{C} = E_{\mathbf{H}} \left\{ \log_2 \left(\det \left(\mathbf{I}_M + \frac{\rho}{N} \mathbf{H}\mathbf{H}^H \right) \right) \right\}. \tag{2.17}$$

For the remainder of this thesis, the above equation will be used[5]. However, it should be made clear that this formula is based on the isotropic property of the i.i.d. complex Gaussian $\mathbf{H}$ where the ergodic capacity is achieved with covariance matrix identity. There is a misconception on this issue since many researchers define the ergodic capacity, irrespective of the distribution of the channel matrix, according to (2.16). This discrepancy can be attributed to the difficulty in deriving the optimum matrix $\mathbf{Q}$ when the channel is not i.i.d. complex Gaussian [44].

The ergodic capacity is evidently maximised when $E\left\{\mathbf{H}\mathbf{H}^H\right\} = N\mathbf{I}_M$. In physical terms, this corresponds to a system with orthogonal MIMO subchannels and a capacity equivalent to that of M independent SISO channels as

$$\overline{C}_{max} = M \log_2(1+\rho). \tag{2.18}$$

On the other hand, the minimum ergodic capacity is obtained for $E\left\{\mathbf{H}\mathbf{H}^H\right\} = N\mathbf{1}_M$, where $\mathbf{1}_M$ is an $(M \times M)$ all-one matrix. This corresponds to an entirely correlated MIMO system and the associated capacity is equivalent to that of a Single-Input Multiple-Output (SIMO) system

$$\overline{C}_{min} = \log_2(1+M\rho). \tag{2.19}$$

[5]When $M \geq N$, M should be replaced with N and $\mathbf{H}\mathbf{H}^H$ with $\mathbf{H}^H\mathbf{H}$. This holds true thanks to the fundamental determinant property $\det(\mathbf{I}+\mathbf{A}\mathbf{B}) = \det(\mathbf{I}+\mathbf{B}\mathbf{A})$.

In order to get a solid insight into the advantages of MIMO systems, a graph showing the complementary cumulative distribution functions (CCDFs) of capacity, for different numbers of Tx/Rx elements and a fixed SNR $\rho = 20$ dB, is depicted in Fig. 2.4. The channel matrix is assumed to have i.i.d. Rayleigh fading entries. Clearly, capacity exhibits a linear increase with the number of antenna elements thereby validating the aforementioned theoretical background. Finally, when perfect CSI is available at both ends, smarter allocation strategies have been proposed, like the *water filling* theorem so as to maximise capacity [45]. The main concept behind this scheme is to allocate the highest amount of power to the strongest spatial subchannels. An investigation of MIMO capacity bounds, under different assumptions about the available CSI at both the Rx and Tx, can be found in [46, 47].

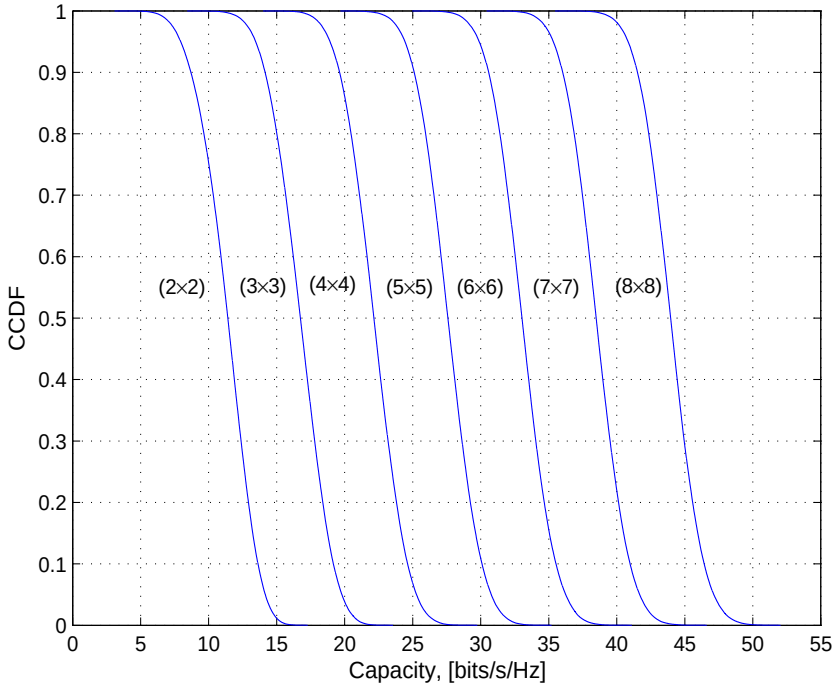

Figure 2.4: *Capacity CCDFs of different i.i.d. Rayleigh MIMO channels.*

2.4 Multi-dimensional channel modelling

In MIMO channels, the selectivity in time and frequency domains comes with the selectivity in a third dimension, that is space. Taking into account that the angular (spatial) distribution of energy is a key issue when modelling MIMO channels, we end up with the so-called *double*

directional description. The terms double directional indicate that the spatial characterisation is carried out at both ends of the link whereas a non-directional model accounts merely for the temporal spreading.

2.4.1 Principles of double directional propagation

In Fig. 2.5, a rich scattering MIMO channel consisting of multiple propagation paths is shown.

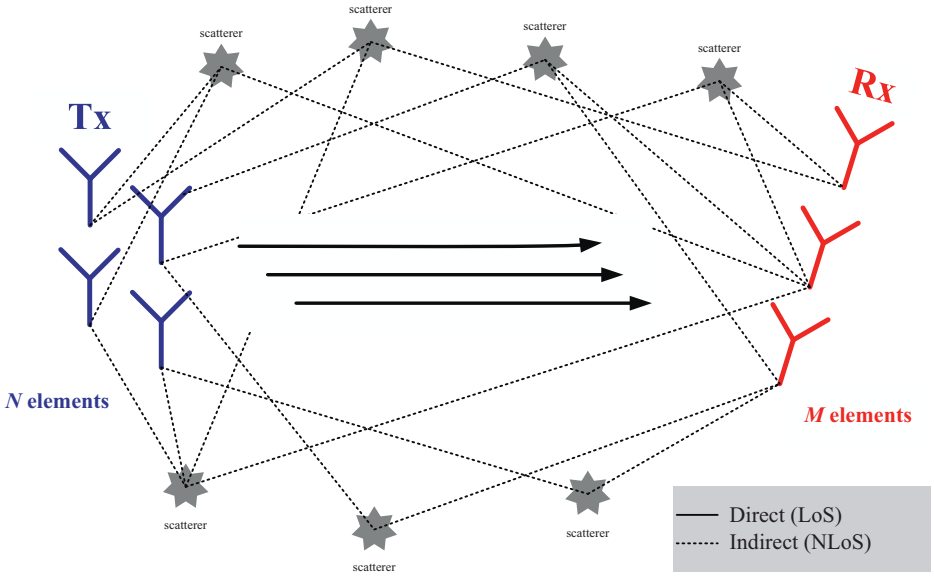

Figure 2.5: *The concept of double directional propagation in MIMO channels.*

In general, each multipath component (MPC) can be identified by means of its Time of Arrival (ToA), Direction of Arrival (DoA), Direction of Departure (DoD) and complex amplitude. Then, the communication between a Tx located at $\overrightarrow{r_t}$ and a Rx located at $\overrightarrow{r_r}$ in the 3D space may be expressed as the superposition of L impinging paths, leading to the *double directional impulse response* [26, 48]

$$h\left(\overrightarrow{r_t}, \overrightarrow{r_r}, \tau, \Omega_t, \Omega_r\right) = \sum_{\ell=1}^{L} \beta_\ell \delta(\tau - \tau_\ell)\delta(\mathbf{\Omega}_t - \Omega_{t,\ell})\delta(\mathbf{\Omega}_r - \Omega_{r,\ell}). \tag{2.20}$$

In the above equation, β_ℓ, τ_ℓ, $\Omega_{t,\ell}$, $\Omega_{r,\ell}$ are the complex amplitude, ToA, DoA, DoD of the ℓ-th MPC respectively and $\delta(\cdot)$ is the delta Dirac function. For the sake of simplicity, the polarisation selectivity has been excluded from the analysis. The spatial angle $\mathbf{\Omega}_t$ is uniquely

determined by the azimuth ϕ_t and elevation ψ_t which are the spherical coordinates on a sphere of unit radius[6],

$$\mathbf{\Omega}_t \triangleq [\cos(\phi_t)\sin(\psi_t), \sin(\phi_t)\sin(\psi_t), \cos(\psi_t)]^T . \tag{2.21}$$

In realistic wireless channels though, the positions of both the Tx and/or Rx and surrounding scatterers are not fixed but may change with time. This also causes the disappearance of MPCs and the appearance of new interactions. In this light, a more general version of (2.20) can be obtained for time-variant channels where the number of MPCs as well the corresponding parameters are varying with time

$$h\left(t, \tau, \Omega_t, \Omega_r\right) = \sum_{\ell=1}^{L(t)} \beta_\ell(t)\delta(\tau - \tau_\ell(t))\delta(\mathbf{\Omega}_t - \Omega_{t,\ell}(t))\delta(\mathbf{\Omega}_r - \Omega_{r,\ell}(t)). \tag{2.22}$$

Following the distinction between the radio and propagation channel as defined in [26], we can easily conjecture that (2.22), which describes the latter, assumes isotropic radiators at both ends of the link.

2.4.2 Double directional propagation and MIMO channel matrix

While the double directional response (2.20) is indicative of the underlying propagation mechanisms, the MIMO channel matrix can describe the responses between each pair of transmit and receive elements given a specific antenna configuration and bandwidth. A direct conjunction (for time-invariant channels) between these two frameworks is achieved via the relationship [49]

$$h_{ij}(\tau) = \int_{\mathbf{\Omega}_t}\int_{\mathbf{\Omega}_r}\int_{\tau'} h\left(\overrightarrow{r_t}^{(j)}, \overrightarrow{r_r}^{(i)}, \tau', \mathbf{\Omega}_t, \mathbf{\Omega}_r\right) G_t(\mathbf{\Omega}_t) \\ G_r(\mathbf{\Omega}_r) f(\tau - \tau') d\tau' d\mathbf{\Omega}_r d\mathbf{\Omega}_t \tag{2.23}$$

where $\overrightarrow{r_t}^{(j)}$ expresses the j-th transmit element coordinates and $G_t(\mathbf{\Omega}_t)$ is the transmit antenna pattern. The same notation holds for the receive side through the subscript $(\cdot)_r$. Finally, $f(\tau)$ is the combined impulse response of both antennas. From (2.23), the reader sees that the impulse response needs to be known between all possible pairs of transmit and receive elements [49].

[6]The DoA $\mathbf{\Omega}_r$ is defined likewise.

2.5 Review of MIMO channel models

In recent years, the area of MIMO channel modelling has gained extensive research interest since an accurate model can in principle predict the propagation mechanisms and ultimately make possible the integration of MIMO technology into real-life applications. This section provides a survey of the most important developments in the area of MIMO channel modelling. Following the concept in [50], channel models are classified into *physical* and *analytical* models. The former are independent of antenna configurations (antenna pattern, number of antenna elements, array geometry, polarisation) and system bandwidth while analytical models characterise the channel impulse response between individual transmit and receive antennas in a mathematical way without explicitly accounting for wave propagation.

2.5.1 Physical models

Physical models are supported by the principles of electromagnetic wave propagation and originate from the early days of cellular radio when only the signal amplitude distributions and Doppler spreads could be investigated. Following the rapid evolution of wireless communications, these models became far more sophisticated in order to encompass additional features such as the time delay spread, angular statistics, joint distributions between delay/angular domains and many more. In any case though, the great majority of them are built upon the fundamental principles of cellular radio models [51]. Physical models can be further classified into *deterministic*, *geometry-based stochastic* and *non-geometrical stochastic* models [49, 50].

2.5.1.1 Deterministic physical models

In deterministic models, the environment (positions of Tx, Rx and scatterers) is prescribed in a fixed (deterministic) way and thereafter the fundamental Maxwell's equations are solved using one of the widely known methods of electromagnetism (Method of Moments, Finite Difference Time Domain Method, Finite Element Method). Naturally, the accuracy of deterministic models is strongly dependent on the accuracy and detail of the site-specific representation of the propagation medium. The main drawback of deterministic models is that they require large amounts of computer resources (both memory and processing time) if different channel situations are to be studied, as well as a detailed description of simulation environments that is often time-consuming and impractical.

The most known deterministic models are the ray tracing (RT) algorithms [52, 53], constructed upon the Geometrical Optics (GO) theory in order to account for the signal's interactions with the surrounding environment. RT techniques try to assess the propagation characteristics such as path loss, reflection, diffraction and scattering. GO theory relies on the so-called ray approximation which is valid when the wavelengths of the propagating waves are much smaller than the dimensions of the environment obstacles; this is the case for most urban propagation problems. The ray approximation suggests that multipath propagation can be expressed as a tube of rays, each of them corresponding to a piece-wise linear path connecting two terminals [50]. In RT algorithms, the positions of both terminals as well as the maximum number of successive interactions, usually referred to as the prediction order, are specified by the user. Apart from the environment's geometry, the electromagnetic parameters of materials and the speeds of moving objects (cars, buses) also need to be inserted as input parameters to the model at the generic iteration. Yet, RT models are only representative of the considered environment and thus, multiple runs are required to obtain a comprehensive set of different propagation environments.

2.5.1.2 Geometry-based stochastic physical models

The plethora of geometry-based stochastic channel models (GSCMs) makes the detailed description of them a non-trivial task. Hence, the focus will be on the most innovative models (some dating back to 70s) given that the majority of the rest are actually variations of them. In a GSCM, the location of the scatterers is chosen stochastically assuming a certain PDF and the model is derived from the position of the scatterers by applying the fundamental laws of reflection, diffraction and scattering. The main GSCM advantages were summarised in [54] as

- An immediate projection onto physical reality is available since the important parameters (like scatterer locations) are usually determined according to simple geometrical considerations.
- Most effects are implicitly reproduced; for instance, small scale fading is created by the superposition of waves from individual scatterers while DoA and delay drifts caused by MT movement are implicitly included.
- All information rests a priori in the distribution of scatterers; hence, dependencies of the power delay profile (PDP) and angular power spectrum (APS) do not further complicate the model.

- Tx/Rx and scatterer movement as well as shadowing and the (dis)appearance of propagation paths can be easily implemented; this allows for inclusion of long-term channel correlations in a straightforward way.

An initial modelling approach was introduced by Lee in 1973 [55] who suggested the even placement of scatterers on a circle (ring) around the MT to predict the spatial correlation between signals received by two sensors. This approach is valid when the BS is elevated and not obstructed by local scattering, as usually occurs in macrocells. Since then, different extensions have been proposed with the most significant reported in [56, 57]. The simplicity and easy implementation of the one-ring model makes it remarkably elegant; hence, it has also been applied to multi-antenna element systems, as a number of recent publications indicates [58–61]. The extension to account for frequency-selective MIMO channels, and thus enable the accurate simulation of the highly promising Orthogonal Frequency Division Multiplexing (OFDM) MIMO systems, was recently published in [62]. A uniformly distributed disk of scatterers around the MT is another model describing scattering especially in macrocellular environments where the BS antenna is mounted above rooftops and thus no scattering occurs from locations near it. The idea of placing the scatterers within a circle was motivated by Jakes' work [63] and adopted by many research groups which subsequently extracted the Doppler spectrum [64], joint ToA/DoA distribution [51], APS [65] and finally the delay spread and DoA distribution [66]. Different types of scatterer distributions, such as Rayleigh [67] and one-sided Gaussian [68], have also been reported.

If a microcellular environment is to be examined then the uniform placement of scatterers within an ellipse, whose foci are the BS and the MT, yields an enhanced fit [69]. Under these conditions, antenna heights are relatively low and therefore scattering is likely to occur in the vicinity of both the BS and MT. A space-time generalisation of this model for SIMO channels can be found in [70] while the extension to wideband MIMO channels in [71]. It should be pointed out that both one-disk and elliptical models allow for a path-loss exponent to be defined so that scatterers with longer delays suffer larger attenuation. However, they are both deficient for indoor environments where the scatterers are distributed all over the 3D volume and thus it is impossible to obtain any information about their distribution and further multiple (rather than single) reflections occur [72].

It is also worth noting a special class of GSCMs, namely the two-ring models which are appropriate for mobile-to-mobile communications especially when neither the Tx nor the Rx are

elevated but both are surrounded by a large number of local scatterers. Early work on SISO systems is outlined in [73, 74] while further work on MIMO systems, focusing on either the space-time correlation or space-time-frequency correlation functions, can be respectively found in [75, 76] and [77, 78]. A geometrical two-ring model for two MTs, separated by distance d and moving with velocities $\overrightarrow{\nu_t}$ and $\overrightarrow{\nu_r}$ respectively, is shown in Fig. 2.6.

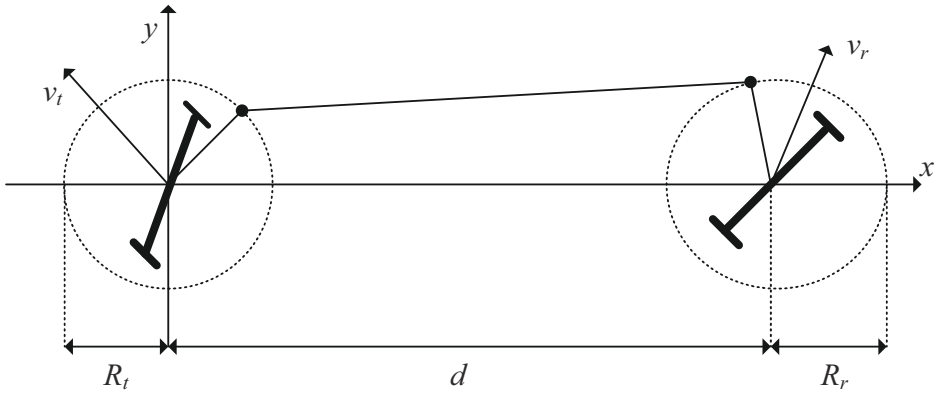

Figure 2.6: *The geometrical two-ring model for a* 2×2 *MIMO channel with local scatterers distributed on rings with radii* R_t *and* R_r.

All the above considerations (apart from the two-ring model) are based on the assumption that only single scattering occurs. In physical reality though, multiple-scattering is prevalent especially for micro- and picocells; for instance, in microcells most of energy is waveguided through street canyons exhibiting multiple reflections just as in indoor environments [54]. A potential solution lies in the use of *equivalent scatterers* whose positions and pathloss are chosen appropriately to artificially generate a certain delay and DoA [79]. While this alternative is sufficiently effective for SISO antenna systems, it becomes complicated for MIMO where once the location of a scatterer is fixed (with respect to the desired parameters of an impinging path), the DoD from the Tx is implicitly described as well [50]. On these grounds, Molisch devised a generic model for outdoor microcells and macrocells by combining stochastic placement of scatterers with simplified semi-RT to simulate the double scattering and a mixed geometrical/stochastic process to account for waveguiding and diffraction [80]. As a matter of fact, the model, which is substantially based on the European Cooperation in the field of Scientific and Technical research (COST) 259 directional channel model [81], embodies a wide variety of propagation effects, namely, LoS propagation, single and double scattering, scattering via far clusters, waveguiding, roof-edge diffraction, large-scale variations and moving scatterers.

2.5.1.3 Non-geometrical stochastic physical models

The non-geometric stochastic models describe paths from Tx to Rx by statistical parameters only, without reference to the geometry of the physical environment. They are also named empirical models since they are based on experimental data. In general, they are very useful for a posteriori simulation purposes [82]. A further distinction is usually made with respect to the clustering of MPCs as follows.

Extended Saleh-Valenzuela model: The first comprehensive statistical channel model, specifically for an indoor multipath environment, was proposed by Saleh and Valenzuela (SV) in [83]. The authors observed that MPCs tend to arrive at the Rx in clusters or bundles. Hereafter, clusters are defined as an accumulation of MPCs with similar temporal and angular characteristics, namely ToAs, Azimuth of Arrivals (AoAs) and Azimuth of Departures (AoDs). The formation of clusters is related to the building structure while the MPCs within a cluster are formed by multiple reflections from objects in the vicinity of the Tx and Rx. Both the power of MPCs within a cluster as well as the average cluster power follow an exponential decay over time. Moreover, the arrival times were described by two Poisson processes corresponding to the arrival time of clusters and of MPCs within clusters.

The SV model was later extended into the spatial domain for SISO and dynamic SIMO channels by Spencer [84] and Chong *et al.* [85], respectively. While the authors in [84] assumed that the spatial and temporal domains are independent the authors in [85] showed that this assumption is invalid for LoS scenarios; in such an environment, paths arriving at the Rx with short delays have a relatively large angular range whereas paths arriving with longer delays have angles very similar to the LoS direction thereby leading to the dependency of the two domains. A key conclusion drawn from both models is that MPCs within a cluster follow a Laplacian distribution. A further extension to the SV model for the MIMO case was accomplished by Wallace and Jensen in [86]. From experimental data, the authors observed clustering phenomena at both ends of the link. Then, the narrowband double directional impulse response, arising from K_c clusters and L_c MPCs within a cluster, can be succinctly written as

$$h\left(\phi_t, \phi_r\right) = \frac{1}{\sqrt{L_c K_c}} \sum_{\ell=0}^{L_c-1} \sum_{k=0}^{K_c-1} \beta_{k\ell} \delta(\phi_t - \Phi_{t,k} - \phi_{t,k\ell}) \delta(\phi_r - \Phi_{r,k} - \phi_{r,k\ell}) \qquad (2.24)$$

where Φ_t and Φ_r are the mean transmit and receive azimuthal angles within the k-th cluster; $\phi_{t,k\ell}$ and $\phi_{r,k\ell}$ are the transmit and receive angle of the ℓ-th MPC in the k-th cluster respectively,

which also has a complex amplitude given by $\beta_{k\ell}$. The average-ray power in each cluster was assumed to be constant so that $\beta_{k\ell} = \mathcal{N}(0, |\beta_\ell^2|)$. In addition, the mean DoD and DoA (cluster centres) are uniformly distributed over $(0, 2\pi)$ while a zero-mean Laplacian PDF with standard deviation σ is assigned to the MPCs within each cluster at both ends

$$p(\phi_{k\ell}) = \frac{1}{\sqrt{2}\sigma} e^{-|\sqrt{2}\phi_{k\ell}/\sigma|}. \tag{2.25}$$

If a wideband model is desired, (2.24) can be simply rewritten as

$$h(\tau, \phi_t, \phi_r) = \frac{1}{\sqrt{L_c K_c}} \sum_{\ell=0}^{L_c-1} \sum_{k=0}^{K_c-1} \beta_{k\ell} \delta(\tau - T_k - \tau_{k\ell}) \delta(\phi_t - \Phi_{t,k} - \phi_{t,k\ell}) \times \delta(\phi_r - \Phi_{r,k} - \phi_{r,k\ell}) \tag{2.26}$$

where T_k is the arrival time of the k-th cluster (determined by a Poisson process) and $\tau_{k\ell}$ is the arrival time of the ℓ-th MPC measured from the beginning of cluster k (determined by a second Poisson process). It is noteworthy that the study of clustering effects in temporal and spatial domains is nowadays regarded as a hot topic in wireless communications. The papers cited above as well as the results presented in [87], which demonstrated the harmful impact of clustering on channel capacity, triggered a great amount of interest for these topics. Numerous publications have been documented dealing with cluster identification and cluster distributions, most of them by the groups at Technical University of Vienna (TUV) and Aalborg University (AAU); the interested readers are referred to [88–91] among others.

Zwick model: Zwick *et al.* [72] investigated an indoor channel which is basically characterised by reflections rather than diffuse scattering and the number of significant MPCs is higher. Their model disproves the formation of clusters when the operation bandwidth is high, based on the experience drawn from previous measurements (see [72] and references therein). The key equation of the model reads for the directional, time-variant frequency-dependent response as

$$\mathbf{H}(t, f, \mathbf{\Omega}_t, \mathbf{\Omega}_r) = \sum_{\ell=1}^{L(t)} \mathbf{\Gamma}_\ell(t) e^{-j2\pi f \tau_\ell(t)} \delta(\mathbf{\Omega}_t - \Omega_{t,\ell}(t)) \delta(\mathbf{\Omega}_r - \Omega_{r,\ell}(t)) \tag{2.27}$$

where $\mathbf{\Gamma}_\ell(t)$ is the full polarimetric matrix whose entries contain the losses and depolarisation of all scattering processes (reflections, transmissions, diffractions, etc.) of the ℓ-th wave. The rest of notation is consistent to that of (2.22). The channel response between all transmit and receive elements can be easily obtained by introducing the phase shifts of all MPCs, according to

the relative position of the antenna elements. Furthermore, the appearance and disappearance of paths over time is modelled by a genetic marked Poisson process. Once a MPC has been generated (birth) its properties are updated until it dies off (death). Deterministic ray tracing tools are employed for producing the huge data sets required for the statistical evaluation of the model parameters [92, 93]. The main mpdel's advantage is that it enables the transition between LoS and OLoS configurations in an easy manner by modelling the LoS component separately from all other MPCs. Consequently, all environments can be modelled using the same framework instead of employing different burdensome techniques. However, the relatively large number of frequency-dependent site-specific parameters that need to be defined and the fact that the time-dispersion of each separate MPC is neglected are the main drawbacks of this model.

2.5.2 Analytical models

In the previous section, physical models were studied; nevertheless, it turns out that for system design, MIMO simulations and design of space-time codes, analytical models are preferred as they are able to capture the channel matrix from a mathematical viewpoint.

2.5.2.1 Correlation-based analytical models

The correlation-based analytical models have been constructed upon the first and second order statistics of a MIMO channel. According to [94], the full spatial correlation matrix

$$\mathbf{R_H} \triangleq E_{\mathbf{H}} \left\{ \mathrm{vec}\left(\mathbf{H}\right) \mathrm{vec}(\mathbf{H})^H \right\} \in \mathbb{C}^{MN \times MN} \tag{2.28}$$

where $\mathrm{vec}(\cdot)$ stacks the columns of a matrix into a vector, can completely describe the spatial behaviour of the MIMO channel since it contains the mutual correlation complex values between all channel matrix elements. The one-sided correlation matrices are also defined as

$$\mathbf{R}_t \triangleq E_{\mathbf{H}} \left\{ \left(\mathbf{H}^H \mathbf{H}\right)^T \right\} \in \mathbb{C}^{N \times N} \tag{2.29}$$

$$\mathbf{R}_r \triangleq E_{\mathbf{H}} \left\{ \mathbf{H}\mathbf{H}^H \right\} \in \mathbb{C}^{M \times M}. \tag{2.30}$$

A direct physical interpretation of the elements of $\mathbf{R_H}$ is not possible though and thus different approximations of $\mathbf{R_H}$ have been proposed that rely either on a separability assumption between the transmit/receive correlation matrices or on a decomposition in the eigen/beam-space.

I.i.d. Rayleigh model: The i.i.d. Rayleigh model was the initial scheme for assessing the performance of MIMO channels and went on to become the most common analytical tool for the design of space-time codes. The entries of the channel matrix are assumed to be i.i.d. zero-mean complex Gaussian variables with unit variance, thereby corresponding to a spatially white MIMO channel. These channels occur when the antenna spacings and/or the the angular spreads are high enough to induce independent fading (zero spatial correlation) and a large number of multipaths impinge on the Rx from all directions; then, the correlation matrix becomes proportional to the identity matrix. In practice though, the spatial subchannels are rarely uncorrelated due to the limited angular spreads and array sizes.

In the same way, the presence of a strong LoS coherent component may violate the assumption of Rayleigh fading causing the channel statistics to be Ricean distributed instead. In this case, the channel matrix consists of a spatially deterministic specular component $\mathbf{H}_{\mathrm{L}}$, which contains the free-space responses between all antenna duets, and a random Rayleigh-distributed component $\mathbf{H}_{\mathrm{w}}$ which accounts for the scattered signals. The LoS MIMO channel model then reads as [95]

$$\mathbf{H} = \sqrt{\frac{K}{K+1}}\mathbf{H}_{\mathrm{L}} + \sqrt{\frac{1}{K+1}}\mathbf{H}_{\mathrm{w}}. \tag{2.31}$$

Kronecker model: The so-called Kronecker model was evaluated by the group at AAU as a contribution to the IST-SATURN[7] initiative to model narrowband NLoS propagation [94]. The extension of the narrowband model to the wideband case was performed in [96] where the authors assumed that the delay bins in the PDP are independent and thus applied the Kronecker model to each tap. The model simply claims that the spatial correlation matrix can be well approximated by the Kronecker product of the one-sided correlation matrices according to

$$\mathbf{R}_{\mathbf{H}} = \frac{1}{\mathrm{tr}(\mathbf{R}_r)}\mathbf{R}_t \otimes \mathbf{R}_r \tag{2.32}$$

where $\otimes$ returns the Kronecker product of two matrices. Then, it is trivial to show that the channel matrix may be modelled as

$$\mathbf{H}_{\text{kron}} = \frac{1}{\sqrt{\mathrm{tr}(\mathbf{R}_r)}}\mathbf{R}_r^{1/2}\mathbf{H}_{\mathrm{w}}\left(\mathbf{R}_t^{1/2}\right)^T \tag{2.33}$$

where $(\cdot)^{1/2}$ denotes any matrix square root fulfilling $\mathbf{R}_r^{1/2}\left(\mathbf{R}_r^{1/2}\right)^H = \mathbf{R}_r$. Yu *et al.* [96],

[7] Information Society Technology-Smart Antenna Technology in Universal Broadband Wireless Networks.

have proved that for systems with three or less transmit and receive antennas, aggregate statistics, like average capacity, can be precisely predicted. Given its simplicity (operations on vec $(\mathbf{H})$ are replaced by matrix manipulations on $\mathbf{H}$) and the fact that it allows for independent array optimisation at Tx and Rx, the scheme has become popular for MIMO simulations. However, Kronecker models enforce the spatial correlation properties at both ends to be separable; that is all DoDs couple into all DoAs with the same power profile, and vice versa. Then, the joint APS is assumed to be the product of the DoA and DoD power spectra, which produces artifact paths lying at the vertical and horizontal intersections of the real DoD and DoA spectral peaks [97]. These artifacts increase the apparent diversity but decrease the apparent capacity since they take away energy from all real paths that do not lie at the intersection points so that the overall power is kept constant. These undesired implications of the Kronecker model can be clearly seen in Fig. 2.7 where both the normalised measured and modelled angular power spectra of an 8×8 indoor MIMO channel at 5.2 GHz have been plotted, with receive and transmit inter-element spacings of 0.5λ and 0.4λ respectively (a detailed discussion on the investigated measurement campaign is given in Section 3.1). When larger antenna arrays are used (improved angular resolution) the model's performance is significantly impaired [97, 98].

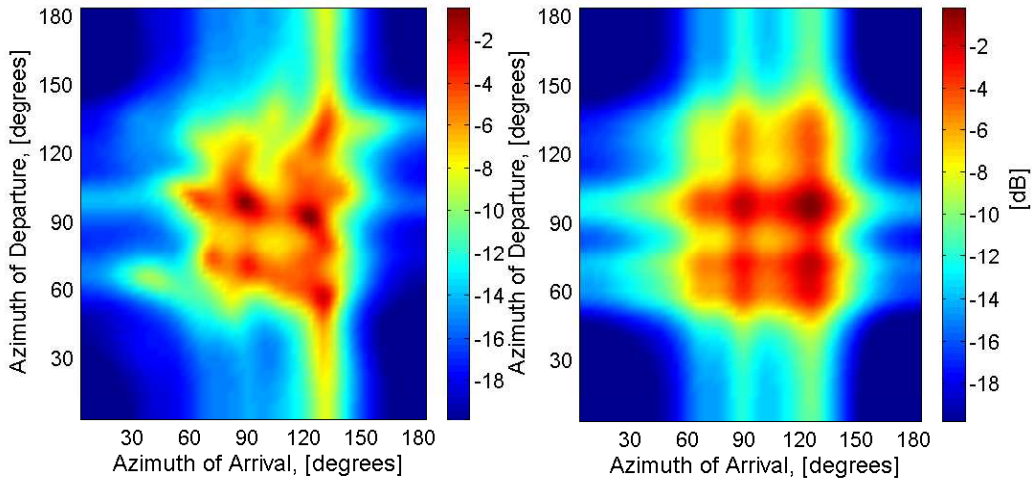

Figure 2.7: *Joint angular power spectrum for a measured (left) and a synthetic MIMO channel based on the Kronecker model (right).*

Weichselberger model: The so-called Weichselberger (or eigenbeam) model alleviates the deficiencies of the Kronecker model by considering the joint correlation structure of both ends and consequently the average coupling between the spatial subchannels is effectively mod-

elled [99]. This implies that the correlation properties at the Tx and Rx are modelled jointly. The eigenvalue decomposition of the transmit and receive correlation matrices yields

$$\mathbf{R}_t = \mathbf{U}_t \mathbf{\Lambda}_t \mathbf{U}_t^H \tag{2.34}$$

$$\mathbf{R}_r = \mathbf{U}_r \mathbf{\Lambda}_r \mathbf{U}_r^H \tag{2.35}$$

where $\mathbf{\Lambda}_t$ is a diagonal matrix containing the positive, real-valued eigenvalues of $\mathbf{R}_t$ and the columns of the unitary eigenbasis $\mathbf{U}_t$ correspond to the eigenvectors at the Tx. The same nomenclature holds for the Rx side. The coupling between the two ends is determined by the power coupling matrix $\mathbf{\Omega}_{\text{weichsel}}$ whose positive and real-valued coefficients $\omega_{\text{weichsel},m,n}$ specify the mean amount of energy coupled from the n-th transmit eigenvector to the m-th receive eigenvector. The structure of $\mathbf{\Omega}_{\text{weichsel}}$ is heavily dependent on the spatial arrangement of scatterers and determines all the fundamental features of a MIMO channel, i.e. number of multiplexed data streams, degree of diversity and beamforming gain. An excellent description of how the structure of Ω_{weichsel} is related to the surrounding spatial environment exists in [99]. Mathematically speaking, the power coupling matrix can be directly obtained from the transfer matrix $\mathbf{H}$ as

$$\mathbf{\Omega}_{\text{weichsel}} = E_{\mathbf{H}} \left\{ \left(\mathbf{U}_r^H \mathbf{H} \mathbf{U}_t^* \right) \odot \left(\mathbf{U}_r^T \mathbf{H}^* \mathbf{U}_t \right) \right\} \tag{2.36}$$

where $\odot$ returns the element-wise Schur Hadamard multiplication. Assuming that the eigenbasis at the Rx is independent of the transmit weights and vice versa, the key formula of the model reads as

$$\mathbf{H}_{\text{weichsel}} = \mathbf{U}_r \left(\widetilde{\mathbf{\Omega}}_{\text{weichsel}} \odot \mathbf{H}_{\text{w}} \right) \mathbf{U}_t^T \tag{2.37}$$

where $\widetilde{\mathbf{\Omega}}_{\text{weichsel}}$ expresses the element-wise square root of $\mathbf{\Omega}_{\text{weichsel}}$. While the model necessitates the spatial eigenbases at one side to be always the same for any spatial weight at the other side, the eigenvalues may differ. Despite the fact that the eigenbases are undoubtedly influenced by the spatial structure of the transmit signals, the less restrictive assumption for the eigenvalues improves drastically the attained accuracy. The Kronecker model is intuitively considered as a special case of the sophisticated Weichselberger framework obtained with the rank-1 coupling matrix $\mathbf{\Omega}_{\text{weichsel}} = \boldsymbol{\lambda}_r \boldsymbol{\lambda}_t^T$, where $\boldsymbol{\lambda}_t$ and $\boldsymbol{\lambda}_r$ are vectorised versions of $\mathbf{\Lambda}_t$ and $\mathbf{\Lambda}_r$, respectively.

Apart from its increased complexity, the main drawback of the Weichselberger scheme lies in the estimation of the joint APS since the multipath environment is occasionally not rendered

accurately; this may lead to a rather blurred version of the APS. Although more robust than the Kronecker model with systems employing more than four antennas, the model still faces difficulties in capturing the spatial variations [98]. This shortcoming is again illustrated by plotting the measured and modelled joint APS for a different measurement scenario (see Fig. 2.8).

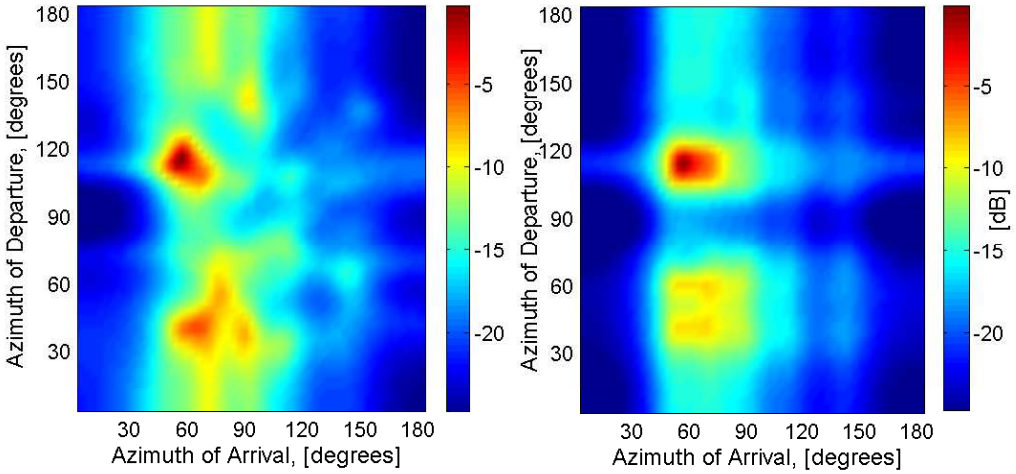

Figure 2.8: *Joint angular power spectrum for a measured (left) and a synthetic MIMO channel based on the Weichselberger model (right).*

Structured model: To the best of the author's knowledge, this is the latest analytical MIMO channel model and in essence represents an extension of the Weichselberger model to three dimensions, namely the receive-transmit-delay space [100]. It is based on the notion of structured vector modes, initially introduced in [43], and recasts the MIMO channel matrix as a tensor to account for correlation in all domains and especially between delay bins in the PDP. Assuming N_f delay bins, the model's key equation is given by

$$\mathbf{H}_{\text{struct}} = \mathcal{W} \times_1 \mathbf{U}_r \times_2 \mathbf{U}_t \times_3 \mathbf{U}_d \tag{2.38}$$

where $\mathbf{U}_d$ is the eigenbasis of the delay correlation matrix, $\mathcal{W} \in \mathbb{C}^{M \times N \times N_f}$ is a tensor whose entries reflect the wideband power coupling between the two ends and $\mathcal{A} \times_n \mathbf{M}$ denotes the n-th mode tensor product between a tensor $\mathcal{A} \in \mathbb{C}^{I_1 \times I_2 \cdots \times I_n \times \cdots I_N}$ and a matrix $\mathbf{M} \in \mathbb{C}^{J_n \times I_n}$. Similar to the Weichselberger model, the structured model does not assume independence between scatterers at the Tx and Rx and hence it systematically outperforms the Kronecker model as two different measurement campaigns revealed [100]. The model yields also a greater robustness as its estimated capacity error remains relatively unchanged as the array sizes get larger.

2.5.2.2 Propagation-based analytical models

Virtual channel representation: The so-called virtual channel representation (VCR) is a tractable linear model, valid for uniform linear arrays (ULAs), initially prompted by the limited resolution in the spatial signal space[8] [101]. The main idea is that the finite number of antennas represent nonetheless a discrete sampling in the aperture domains which are directly related to the angular domains via a Fourier transform (FT). The use of FT explains why the model can be applied merely to ULA configurations as the sampling needs to be uniform in the aperture domains [82]. The angular range at both ends is partitioned into fixed, predefined directions which are determined by the spatial resolution, that is the size and inter-element spacings of the arrays. Please note that the latter characteristic affects also the degree of mutual coupling which distorts the array response and needs to be minimised using an array perturbation matrix [102]. The model is virtual in the sense that it does not represent the real directions but only the contribution of the channel to those fixed directions. The key formula of the model reads as

$$\mathbf{H}_{\text{virt}} = \widetilde{\mathbf{A}}_r \left(\widetilde{\mathbf{\Omega}}_{\text{virt}} \odot \mathbf{H}_{\text{w}} \right) \widetilde{\mathbf{A}}_t^T \tag{2.39}$$

where $\widetilde{\mathbf{A}}_r$ and $\widetilde{\mathbf{A}}_t$ are the channel independent discrete Fourier transform (DFT) matrices of size $(M \times M)$ and $(N \times N)$ respectively. The columns of these orthonormal matrices constitute steering vectors into the directions of virtual angles. As anticipated, $\widetilde{\mathbf{\Omega}}_{\text{virt}}$ is again the element-wise square root of a $(M \times N)$ matrix $\mathbf{\Omega}_{\text{virt}}$ whose entries reflect the power coupling between the n-th virtual transmit angle and the m-th receive virtual angle. In this case, the coupling matrix is obtained through (2.36), by using the predefined DFT matrices $\widetilde{\mathbf{A}}_r$ and $\widetilde{\mathbf{A}}_t$ instead of the eigenbases $\mathbf{U}_r$ and $\mathbf{U}_t$ respectively. The author emphasises that the VCR and the Weichselberger models represent in essence different perspectives of the modelling domain; the former is modelled in beamspace while the latter in eigenspace.

Its straightforward geometrical projection makes the model rather appealing while the structure of $\widetilde{\mathbf{\Omega}}_{\text{virt}}$ provides an insightful interpretation of the scattering effects on the multiplexing gain and level of diversity. The VCR model yields a better fit in terms of joint APS compared to Kronecker and Weichselberger schemes, particularly for a high number of antenna elements (enhanced spatial resolution and therefore higher number of steering directions) [49]. However, it struggles considerably when it comes to measure the ergodic and outage mutual information metrics; this is a side-effect of the abrupt spatial partition. To be more precise, the underlying

[8] Note that the VCR model might be qualified as correlation-based as well.

model assumption of uncorrelated fading is problematic since any scatterer lying between two virtual angles is anticipated to induce correlated fading due to sidelobe effects. In the worst case scenario, a MPC at the middle of a fixed partition is modelled by four equal-powered, independently-fading components and we eventually end up with more MPCs than the measured channel really has [49]. To sum up, the VCR does not distinguish between scatterers which are separated by less than the angular resolution.

Finite scatterers model: The main motivation for developing this model has been the theory of double directional propagation, as described in Section 2.4. Assuming narrowband transmission, that is the signal bandwidth is narrow compared with the overall coherence bandwidth of the channel, the delay of each path can be disregarded. Then, the channel response is the superposition of a finite number of L waves each connected to a specific AoA, AoD and complex amplitude. Following (2.20), the channel matrix reads as [103]

$$\mathbf{H}_{\text{finite}} = \sum_{\ell=1}^{L} \mathbf{a}_r(\phi_{r,\ell})\beta_\ell \mathbf{a}_t^H(\phi_{t,\ell}) = \mathbf{A}_r \mathbf{B}_L \mathbf{A}_t^H. \tag{2.40}$$

In the above equation, $\mathbf{a}_r(\phi_{r,\ell})$ and $\mathbf{a}_t(\phi_{t,\ell})$ are the steering vectors at Rx and Tx corresponding to the ℓ-th MPC. By concatenating the steering vectors for all DoAs (DoDs), the $(M \times L)$ matrix $\mathbf{A}_r$ (or the $(N \times L)$ matrix $\mathbf{A}_t$) is obtained. The diagonal matrix $\mathbf{B}_L = \text{diag}(\beta_1, \beta_2, \ldots, \beta_L)$ contains the complex gains of all paths.

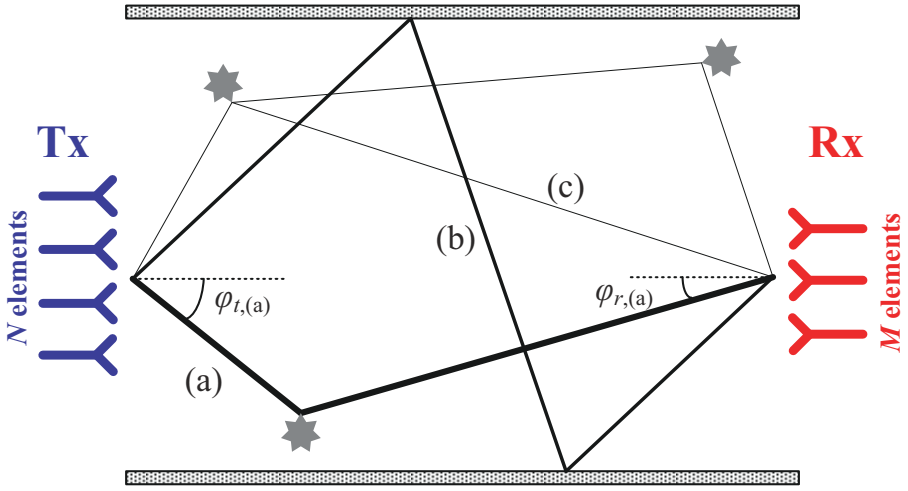

Figure 2.9: *Illustration of the finite scatterers model showing examples of (a) single scattered paths, (b) doubly reflected paths, and (c) split components.*

The finite scatterers model not only accounts for single and doubly scattered components (paths

(a) and (b) respectively in Fig. 2.9) but also for split components (path (c) in Fig. 2.9) which may have a single AoD but subsequently split, resulting in two or more AoAs (and vice versa). Therefore, it may be regarded as a generalised version of most GSCMs which can deal only with single and doubly scattered components [79, 80]. The derivation of (2.40) was based on the assumption that the transmit and receive elements are ideal uncoupled isotropic radiators. Deviations from these unrealistic conditions can be easily investigated by multiplying with appropriate transformation matrices [104]. Summarising, the main differences compared with the VCR model are:

- The finite scatterers model allows for arbitrary number of AoDs and AoAs regardless of the number of transmit and receive antenna elements.
- It can be applied to any antenna geometry (after appropriate manipulations) and thus it is not restricted to single-polarised ULAs.
- The model is not linear in $\phi_{r,\ell}$ and $\phi_{t,\ell}$.

Distributed scatterers model: The so-called distributed scatterers model was developed to assess the performance of outdoor MIMO systems and suggest guidelines for achieving subchannel orthogonality and hence high channel capacity [105]. Both the Tx and Rx are surrounded by a set of S actual near-field scatterers whose extent from the horizontal axis is denoted as D_t and D_r respectively. The value of S is assumed to be large enough to induce random fading while the arrangement of scatterers follows no certain pattern. Moreover, the angular spreads of the reflected waves are σ_t and σ_r. The inter-element distance at Tx and Rx is expressed as d_t and d_r; the scatterers at the receive side can be seen as a virtual array of S elements between the Tx and Rx with an average element spacing $2D_r/S$. The propagation scenario described above has been plotted in Fig. 2.10.

The MIMO channel transfer function is then given by

$$\mathbf{H}_{\text{DS}} = \frac{1}{\sqrt{S}} \mathbf{R}^{1/2}_{\sigma_r,d_r} \mathbf{H}_{\text{w},r} \mathbf{R}^{1/2}_{\sigma_S,2D_r/S} \mathbf{H}_{\text{w},t} \mathbf{R}^{1/2}_{\sigma_t,d_t} \tag{2.41}$$

where $\frac{1}{\sqrt{S}}$ is a normalisation factor and $\mathbf{H}_{\text{w},r}$, $\mathbf{H}_{\text{w},t}$ are i.i.d. Rayleigh fading matrices of size $(M \times S)$ and $(S \times N)$, respectively whereas σ_S is the angular spread for the virtual array

$$\tan(\sigma_S/2) = D_t/R. \tag{2.42}$$

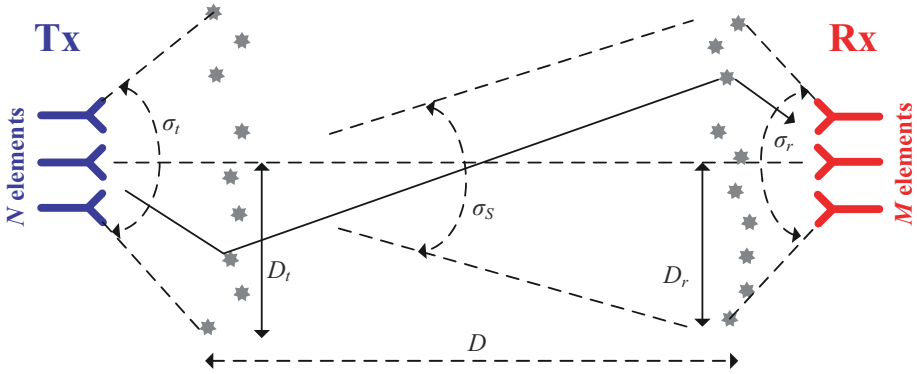

Figure 2.10: *Illustration of the distributed scatterers model showing the angular spreads.*

The deterministic matrices $\mathbf{R}_{\sigma_t,d_t}$, $\mathbf{R}_{\sigma_S,2D_r/S}$, $\mathbf{R}_{\sigma_r,d_r}$ control the spatial correlation seen from the Tx, virtual array and the Rx, respectively. The degree of correlation is governed by the angular spread and inter-element distance since high angular spreads and element separations reduce correlation leading to high-rank (HR) channel matrices. If the correlation matrix at one end is low-rank (LR), then from (2.41) the MIMO channel is also LR. The opposite though is not always true. In some cases, fading may be uncorrelated at both sides of the link, i.e. $\mathbf{R}_{\sigma_t,d_t} = \mathbf{I}_N$ and $\mathbf{R}_{\sigma_r,d_r} = \mathbf{I}_M$ but the MIMO channel rank remains poor. This unusual phenomenon is known as the *keyhole* effect. Conceptually, the rank of the channel matrix is by definition determined by the rank of the correlation matrix of the virtual array $\mathbf{R}_{\sigma_S,2D_r/S}$. When the distance D is large compared to the product of D_t and D_r the channel rank eventually drops. This may occur in specific roof-top diffraction scenarios where a vertical-base antenna is employed. Other physical examples of keyholes include a spatial keyhole in a metal screen, a modal keyhole in a waveguide or a hallway where only one mode is present [106]. Under these circumstances, the elements of the channel matrix are distributed according to a double Rayleigh distribution which fades twice as often as a standard Rayleigh distribution [105].

Maximum entropy model: This model was developed on the grounds of statistical inference in order to attribute a joint probability distribution to the channel transfer matrix. By using the theorem of maximum entropy the authors in [44] demonstrated that a modelling framework can be easily created out of the state of knowledge available. The choice of distribution with the greatest entropy, and only this, guarantees that unknown information is not introduced. For expressing the prior knowledge statistically and estimating the parameters of the model, the principles of Bayesian probability theory were also employed. In order to achieve consistency, regardless of the application of the model, the following axiom was defined:

If the prior information $\mathbf{I_1}$ *which is the basis for channel model* $\mathbf{H_1}$ *is equivalent to the prior information* $\mathbf{I_2}$ *of channel model* $\mathbf{H_2}$*, then both models must be assigned the same probability distribution* $f(\mathbf{H_1}) = f(\mathbf{H_2})$.

This axiom originates from the fundamental principle that if a problem can be solved in more than one way the outcomes should be consistent. In its broadest version, the model assumes knowledge of the following

- Number of stationary scatterers at the transmit and receive side S_t and S_r respectively.
- Velocities of Tx and Rx $\overrightarrow{\nu_t}$ and $\overrightarrow{\nu_r}$ respectively.
- AoD from transmit antenna i to scatterer j denoted as $\phi_{t,ij}$ and carrying power P_{ij}^t.
- AoA from scatterer i to receive antenna j denoted as $\phi_{r,ij}$ and carrying power P_{ij}^r.
- The $S_r \times S_t$ delay matrix linking each DoA to each DoD, written as

$$\mathbf{D}(f) = \begin{bmatrix} e^{-j2\pi f\tau_{1,1}} & e^{-j2\pi f\tau_{1,2}} & \dots & e^{-j2\pi f\tau_{1,S_t}} \\ e^{-j2\pi f\tau_{2,1}} & e^{-j2\pi f\tau_{2,2}} & \dots & e^{-j2\pi f\tau_{2,S_t}} \\ \vdots & \vdots & \ddots & \vdots \\ e^{-j2\pi f\tau_{S_r,1}} & e^{-j2\pi f\tau_{S_r,2}} & \dots & e^{-j2\pi f\tau_{S_r,S_t}} \end{bmatrix} \tag{2.43}$$

The response of a time-variant frequency selective MIMO channel then has the following structure

$$\mathbf{H}_{\text{ME}}(t,f) = \frac{1}{\sqrt{S_r S_t}} \mathbf{A}_r(t,f) \mathbf{P}^{r\frac{1}{2}}(t) \left(\mathbf{\Theta}(t,f) \odot \mathbf{D}(f)\right) \mathbf{P}^{t\frac{1}{2}}(t) \mathbf{A}_t(t,f). \tag{2.44}$$

with $\mathbf{P}^{r\frac{1}{2}}(t) = \text{diag}\left(\sqrt{P_1(t)}, \dots, \sqrt{P_{S_r}(t)}\right)$ being the received power matrix and in accordance $\mathbf{P}^{t\frac{1}{2}}(t) = \text{diag}\left(\sqrt{P_1(t)}, \dots, \sqrt{P_{S_t}(t)}\right)$ is the transmit power matrix. It was shown that a Gaussian i.i.d. distribution with zero mean and unity variance should be assigned to $\mathbf{\Theta}(t,f)$ since it is the solution of the consistency argument and maximises entropy.

The goodness of this model was tested using the data from both a wideband outdoor and an indoor measurement campaign, performed at frequencies of 2.1 GHz and 5.2 GHz with a bandwidth of 100 MHz. The model yields a satisfactory compliance in terms of capacity especially at 2.1 GHz. The main advantage of this approach is its flexibility since every new piece of information on the environment can be straightforwardly incorporated in a consistent way.

2.5.3 Standardised models

A brief review of the most important standardised models, established by several international organisations, is now provided. The aim to give the reader a view of recent and ongoing channel modelling activities. It should be noted though, that these models are not intended to enhance understanding of MIMO propagation characteristics.

2.5.3.1 3GPP spatial channel model

The 3rd Generation Partnership Project (3GPP) system-level spatial channel model (SCM) has been designed for the simulation of third-generation networks in urban and suburban macrocells as well as in urban microcells. It is noteworthy that a link-level SCM has also being developed for the purpose of calibration, where taps with different delays are assumed independent and can be fully characterised by their spatial parameters, i.e. angular spread, APS, AoA/AoD [107]. The model structure and simulation methodology are identical for all these environments but the input parameters, like delay spread, angular spreads and so forth, are different [50]. The provided implementation is a tap-delay line model where each tap consists of several subpaths which share the same delay but have different directions of arrival and departure. Adding up these different subpaths (which all have deterministic amplitudes but random phases) leads to Rayleigh or Ricean fading. In [107], a parameter table has been given which lists all the important parameters, such as number and power of paths and subpaths and spatial parameters. The system bandwidth is normally assumed to be 5 MHz, but an extension to larger bandwidths was proposed in [108], where a wideband SCM is adopted.

The core of the link-level 3GPP MIMO model is a Kronecker model which provides a direct link between the rank of $\mathbf{R_H}$ and capacity and, more importantly, requires a low number of input parameters [109]. It also introduces spatial and spatio-temporal separability at all three levels, namely cluster, link and system levels. On the other hand, the SCM [108] was also proposed by the 3GPP for both link- and system-level simulations. In [110] though, it was shown that SCM shows the spatial separability at the link and system levels, but not at the cluster level since its spatial correlation is related to the joint AoA/AoD distribution. Likewise, the spatio-temporal separability is observed for the SCM only at the system level. To summarise, the simpler Kronecker model can capture only the average spatio-temporal properties of MIMO channels while SCM, though more complex, provides a deeper insight into the variations of different MIMO realisations.

2.5.3.2 IEEE 802.11n channel models

This set of models, developed by the High Throughpout Task Group within the IEEE 802.11n Working Group, have been designed for indoor WLANs at both 2 and 5 GHz with an operating bandwidth of 100 MHz [111]. They essentially represent an improved and standardised version of the SV model with overlapping clusters in the delay domain [82]. Six canonical environments (A to F) are modelled including, flat-fading, residential, small office, typical office, large office and large open space. For each of the six environments, the TGn model specifies a different set of simulation settings. Typically, the number of clusters varies from 2 to 6 for different indoor scenarios while the overall root mean squared (rms) delay spread ranges between 0 (flat-fading) and 150 ns.

In general, these models are a combination of the Kronecker approach along with the cluster modeling framework as given in [83, 84]. More specifically, at each time instant, l, the full spatial correlation matrix, $\mathbf{R}_{\mathbf{H}}^{l}$, is approximated using (2.32); the correlation matrices at each delay tap, $\mathbf{R}_{t}^{l}$ and $\mathbf{R}_{r}^{l}$, are obtained by the APS and angular spreads at the Tx and Rx, respectively. In order to determine the latter two characteristics, the results of [83, 85] have been adopted and, consequently, the APS of the l-th tap is modelled by a Laplacian distribution whose spread is equal to the cluster spread. This is consistent with the results presented in [112], where it was clearly demonstrated that the instantaneous tap azimuth spread is slightly less than the cluster spread with the difference becoming smaller as the channel bandwidth decreases. On a similar basis, taps are assigned a truncated Laplacian distribution with the mean AoA and AoD being uniformly distributed over $[0, 2\pi)$. The cluster azimuth spread is normally selected in the range $20°$–$40°$ and is correlated with the delay spread. The temporal channel variations are characterised by means of the Doppler spectrum, which consists of a ”bell-shaped” part with low Doppler frequency and an optional additional ”horn” peak at a larger Doppler frequency. The latter is caused by vehicle movements which mostly occur in large-space environments (model F). As additional options, path-loss modeling and polarisations have also been treated in [111].

2.5.3.3 WINNER channel model

The IST-Wireless World Initiative New Radio (WINNER) project has been developed by a consortium of 41 partners which aimed to define radio interface technologies needed for a ubiquitous radio system concept as well as radio network topologies and deployment concepts for the provision of a ubiquitous coverage area [113]. The model is inherently related to 3GPP

but a wider bandwidth of up to 100 MHz is used in both 2 and 5 GHz frequency ranges. This is achieved through the SCM-Extended (SCME) model by introducing the so-called intracluster delay spread, which is zero in the original SCM [114]. The model covers six different indoor and outdoor propagation environments, particularly, indoor small office, indoor large hall, urban microcell, urban small macrocell, suburban macrocell and rural [115] with the key parameters of each environment being extracted from several real-life measurement campaigns.

The modelling approach is based on a generic sum-of-sinusoids model where the double directional characteristics, delay, polarisation and complex amplitude of each MPC are considered. The clusters are defined independently in DoA and DoD domains and this assumption significantly simplifies parameter extraction and coefficient generation [115]. The key model's features are the modelling of cross-correlation between large scale parameters (i.e. delay spread, AoA/AoD spread and lognormal shadowing), the inclusion of polarisation effects via a (2×2) polarimetric matrix and finally, the consideration of elevation in indoor environments [50]. A more detailed discussion on the model characteristics along with a MATLAB implementation of it are available in [113].

2.5.3.4 COST 259/273/2100 channel models

The COST project is a European research initiative which includes COST 259 (1996–2000) in the field of "Flexible personalised wireless communications" [81] and similarly COST 273 (2001–2005) in the field of "Towards mobile broadband multimedia networks" [116]. Both subprojects aimed to develop efficient and generalised radio channel models suitable for modern MIMO communications. It should be noted that 3GPP and IEEE 802.11n can be regarded as special cases of COST models (though with different parameter settings) [50].

According to [50], the COST 259 directional model was the first model which explicitly investigated the complex relationships between BS-MT distance, delay dispersion and angular spread. The model relies on the key notions of *external* and *global parameters*. The former are fixed for a simulation run and include the following features of the simulation environments among others: frequency band, average BS-MT distance, average height of BS and MT antennas and average building heights and separations. The latter parameters must be extracted by exhaustive real-life measurement trials since their scope is to describe the propagation conditions of each *radio environment*; in fact, they are sets of pdfs and/or statistical moments of the stochastic parameters. For instance, the number of visible clusters is normally modelled via a

Poisson process. More importantly, global parameters provide necessary information for the appropriate design of communication systems with regard to practical issues like modulation scheme, burst length, coding scheme etc. We also refer to *local parameters* which are basically random realisations of the global parameters and are assumed to remain constant within a small local area of the order of tens of λ; therefore they can only describe the instantaneous channel conditions. The main advantage of the COST 259 model is that it can handle the continuous motion of the MT across different radio environments and return as output the double directional impulse response, as the one given in (2.20). A thorough discussion on the most important aspects of the COST 259 model can be found in [117]. On the other hand, there are two fundamental deficiencies of the COST 259 framework. The first one is the assumption of stationary scatterers which implies that time variations are attributed only to the MT movement. Secondly, delay attenuations are modelled as complex Gaussian RVs which, in practice, means that a relatively high number of MPCs should be present at each delay bin.

The COST 273 approach represents an extended version of the COST 259 one since 18 different radio environments are now considered (compared to 13) including some scenarios of high practical interest nowadays, such as peer-to-peer communications and fixed wireless access. The COST 273 employs the same generic channel model for all types of environments that is also identical to that of COST 259 for macrocells; this is a significant distinction to the COST 259 model, which used different generic models for pico-, micro- and macrocells. The simulation parameters have also been updated to comply with the observations drawn from a plethora of recently available double directional MIMO campaigns [116]. The key methodology of COST 273 is to model the mean angles and delays of clusters by geometrical considerations, while the intracluster spreads and small scale fading may be expressed by either a geometrical approach or a tapped delay line representation. However, a significant discrepancy exists when it comes down to the modelling of multiple interactions. Under these circumstances, the concept of *twin clusters* is introduced so that each cluster is divided into a cluster corresponding to the BS side and one at the MT. The angular dispersion at BS and MT are independently modelled while the two clusters have the same scatterer distributions and long-term behaviours (twins). These two representations are connected via a so-called *stochastic cluster link delay*, which is the same for all scatterers within a cluster. This link delay guarantees realistic path delays while the placement of the cluster is defined by the angular cluster statistics as seen from the BS and MT, respectively [50].

The latest COST initiative, is the COST 2100 project (2006–2010) in the field of "Pervasive mobile & ambient wireless communications" [118] which aims, among others, to bring together various aspects of mobile-to-mobile communications to support future telematics applications, such as improved navigation mechanisms and infotainment services [119, 120]. Other subworking groups explore the design of compact antenna systems for terminals, localisation in ultra-wideband systems, and establishment of reference channel models that will include diffuse scattering interactions and investigate the temporal behaviour caused by moving scatterers [118].

2.6 Summary

The goal of this chapter has been twofold. Firstly, the basic characteristics of radio propagation were described as they are essential in order to comprehend the nature of wireless channels. As anticipated, MIMO channels are also governed by these well known mechanisms with the only difference lying in the reciprocity of propagation (double directional) due to the multiple antenna elements at both sides of the radio link. Secondly, taking into account that practical measurements are cumbersome and unique for each environment, the main focus was on channel models that are tractable statistical tools for capturing multipath propagation and interactions with the surrounding environment. Apart from reviewing the area of channel modelling, the author classified models with regard to which feature the designer intends to capture (double-directional propagation or impulse response) and determined the models' limitations. To sum up, this chapter outlines the scope and represents a stepping stone for the remainder of the thesis.

Chapter 3
Stochastic modelling of MIMO channels using the spatial eigenmodes

In the previous chapter, the author reviewed the most important analytical MIMO channel models whose disadvantages necessitate the development of a more general framework able to capture the spatial activity with finer detail. This chapter presents a new stochastic indoor model, which originates from the widely known KLT, and is constructed upon the eigendecomposition of the full correlation matrix. It is shown that the channel matrix can be modelled by the superposition of the spatial eigenmodes experiencing independent Nakagami-m fading. The model is derived based on measurement data collected at a carrier frequency of 5.2 GHz in an indoor environment under a range of propagation conditions. The Nakagami-m distribution offers a good fit with the measured data and furthermore it is more flexible compared to the commonly employed Rayleigh distribution. The remainder of this chapter is organised as follows: In Section 3.1, a MIMO measurement campaign carried out in an office environment is described. Section 3.2 outlines the foundations of the new analytical model and offers a physical interpretation of the spatial parameters that comprise it. In Section 3.3, the choice of the Nakagami-m distribution for modelling the fluctuations of the measured envelopes is clarified. In Section 3.4, a novel method for generating independent Nakagami-m deviates based on the rejection/acceptance technique is proposed. The goodness and efficiency of the proposed method are subsequently demonstrated in depth. In Section 3.5, the performance of the stochastic model is evaluated using the measured data and compared with two well known analytical models reported in the literature. Finally, Section 3.6 concludes the chapter and summarises the key findings.

3.1 Indoor measurement campaign

An indoor measurement campaign was carried out in the Electrical Engineering Building within TUV, in an area with many office partitions (highly cluttered environment). The heart of the

measurement setup was the RUSK ATM MEDAV vector channel sounder operating at a centre frequency of 5.2 GHz [121]. The sounder was probed at 193 equi-spaced frequency bins covering the 120 MHz of operating bandwidth with a dynamic range of typically 35 dB. The two ends were synchronised via an optical fibre [43, 49]. The measurements were repeated at 128 temporal snapshots in order to enhance the output SNR. The channel had to be static during one such snapshot and for this reason the campaign was conducted at night to ensure stationarity. By averaging over all snapshots the receive SNR was increased by $10 \cdot \log(128) = 21$ dB theoretically to values up to 50-60 dB; however, the signal discrimination ability remains limited by the dynamic range of the sounder.

The Rx was mounted on a wooden tripod at a height of 1.5 m and employed a ULA of eight vertically-polarised printed dipoles with an inter-element distance of $d_r = 0.4\lambda$. Two dummy elements were also used. Each single antenna had a 3 dB azimuth beamwidth of about 120°. Prior to any DoA estimation process, the physical receive array was fully calibrated in order to remove the undesired effects of electromagnetic mutual coupling between the antenna elements, amplification errors, non-identical element responses and other array imperfections and this was accomplished using the method described in [102]. At the Tx, an omni-directional sleeve antenna was moved on a 10×20 rectangular grid with element spacings of $d_t = 0.5\lambda$. By considering a virtual eight-element ULA on each row, a total number of $13 \times 10 = 130$ spatial realisations of the 8×8 MIMO transfer matrix is acquired. Hence, a total set of $130 \times 193 = 25,090$ space and frequency realisations per measurement scenario was obtained. For the present study, 24 different Rx locations were investigated in several offices while the Tx was positioned at a fixed position in the hallway. In order to acquire the whole azimuth domain activity, the Rx was steered to three different broadside directions spaced by 120° (D1, D2 and D3) leading to the generation of 72 data sets, i.e. combinations of Rx positions and directions. Hereafter, each data set will be denoted via the Rx location and broadside direction, e.g. 2D3. Please note that most office rooms were sparsely furnished with wooden and metal furniture (computers, chairs, tables). The doors between the hallway and the rooms were also wooden or glass-filled [49]. The measurement layout along with the Rx locations are depicted in Fig. 3.1.

3.2 Derivation of the spatial MIMO channel model

Prior to pursuing the statistical description of a new analytical model, it would be wise to justify the reason behind developing one more scheme in an already saturated area. At this

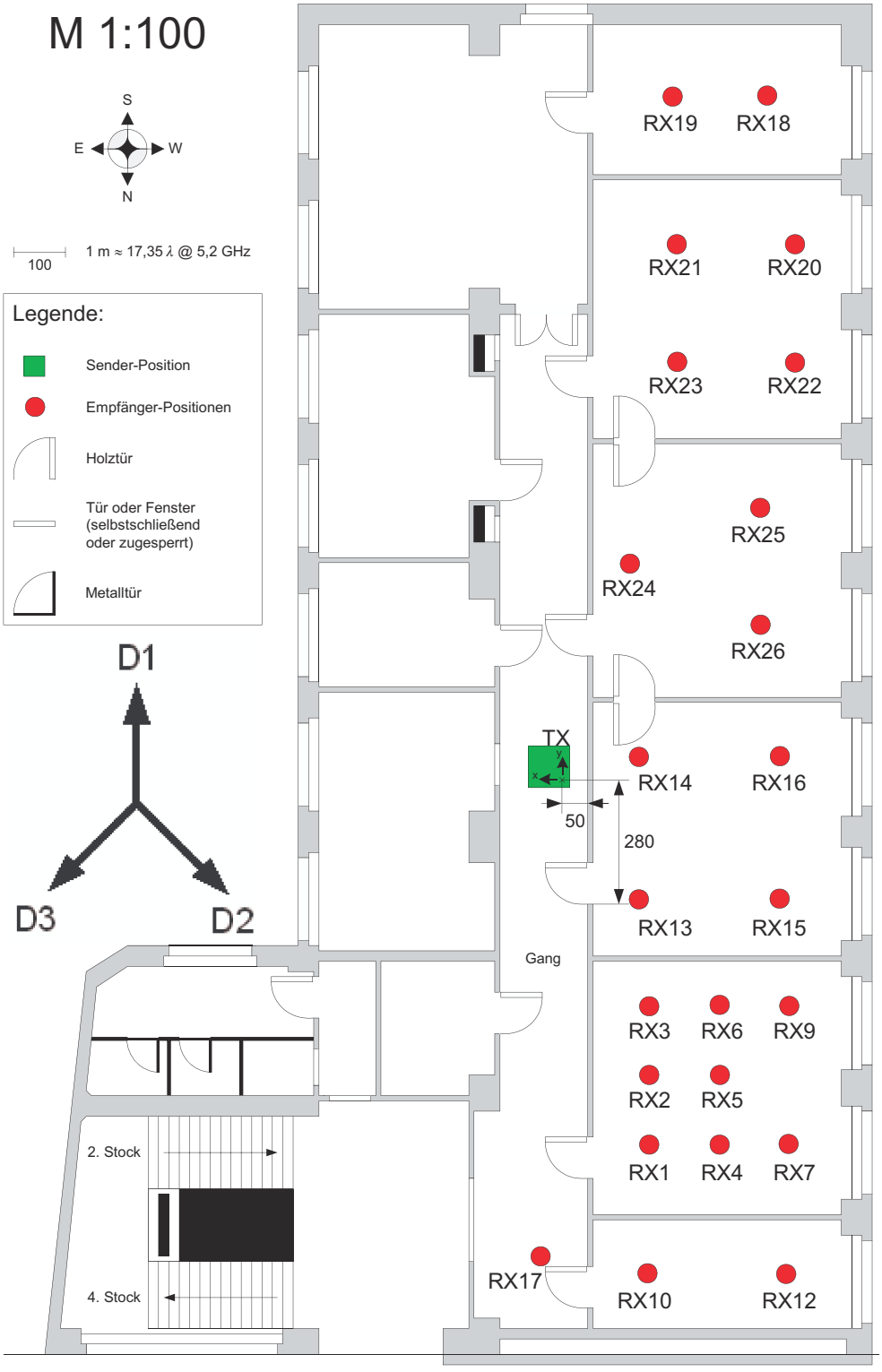

Figure 3.1: *Layout of the measurement environment and Rx locations (taken from [49]).*

point, the reader should be reminded that a common assumption for constructing a correlation-based model is that the channel follows a zero-mean complex Gaussian distribution; then, the second-order statistics suffice for its spatial description. In such a case, any channel realisation can be generated by the full spatial correlation matrix (equivalent to the covariance matrix) according to

$$\mathrm{vec}\left(\mathbf{H}\right) = \mathbf{R}_{\mathbf{H}}^{1/2}\mathrm{vec}\left(\mathbf{H}_{\mathrm{w}}\right). \tag{3.1}$$

This model is a valid formalism only when the channel statistics are jointly Gaussian though this rarely holds in practice. A potential solution for capturing the non-normality is to decorrelate the spatial subchannels and model the marginal behaviour of each decorrelated subchannel separately. This approach is essentially a KLT which has been extensively used in numerous applications that span image compression to seismology and computer graphics in order to decorrelate multi-element data using the eigendecomposition of the correlation matrix [122]. At a next stage, the assumption of Rayleigh fading may be relaxed by assigning a different fading distribution.

Let's assume now a flat-fading MIMO channel with N transmit and M receive antenna elements. The eigendecomposition of $\mathbf{R}_{\mathbf{H}}$, defined in (2.28), into a sum of rank-1 matrices is given by

$$\mathbf{R}_{\mathbf{H}} = \sum_{k=1}^{MN} \lambda_k \mathbf{u}_k \mathbf{u}_k^H \tag{3.2}$$

where λ_k are the real non-zero ordered eigenvalues $(\lambda_1 \geq \lambda_2 \geq \ldots \geq \lambda_{MN} \geq 0)$ and $\mathbf{u}_k$ contain the corresponding eigenvectors which are by definition mutually orthogonal and have unit norm. The number of non-zero eigenvalues determines also the rank of $\mathbf{R}_{\mathbf{H}}$ which is upper bounded by MN. The eigenvector $\mathbf{u}_k$ can be reshaped column-wise into the matrix $\mathbf{U}_k = \mathrm{unvec}\left(\mathbf{u}_k\right) \in \mathbb{C}^{M\times N}$ which will be referred to hereafter as the k-th *eigenmode*. From a physical viewpoint, eigenvalues specify the degree of diversity offered by the channel while eigenmodes, commonly representing a linear combination of propagation paths, are indicative of the SM ability [99]. Likewise, the channel matrix may be modelled as

$$\mathbf{H}_{\mathrm{mod}} = \sum_{k=1}^{MN} g[k]\sqrt{\lambda_k}\mathbf{U}_k. \tag{3.3}$$

From (3.3), it can be readily inferred that the PDF of $g[k]$ expresses the fading variations of the channel. In fact, the fading coefficients $g[k]$ are i.i.d. complex RVs satisfying the key

relationship $E_g\{g[m]g^*[n]\} = \delta_{mn}$, where δ_{mn} is the Kronecker delta function. The validity of (3.3) can be easily checked by calculating the correlation matrix of $\mathbf{H}_{\text{mod}}$ as

$$\begin{aligned} E_g\left\{\text{vec}(\mathbf{H}_{\text{mod}})\text{vec}(\mathbf{H}_{\text{mod}})^H\right\} &= \sum_{k=1}^{MN}\sum_{n=1}^{MN}\sqrt{\lambda_k}\sqrt{\lambda_n}\mathbf{u}_k\mathbf{u}_n^H E_g\{g[k]g^*[n]\} \\ &= \sum_{k=1}^{MN}\lambda_k\mathbf{u}_k\mathbf{u}_k^H \equiv \mathbf{R}_{\mathbf{H}}. \end{aligned} \tag{3.4}$$

It should be noted that the second-order moment of the fading coefficients $g[k]$ is assumed to be the same for all k so that the eigenvalues λ_k reflect the power of each eigenmode.

3.3 Nakagami-m fading characteristics

The resulting uncorrelated eigenmodes of the proposed channel model (3.3) are now assigned a Nakagami-m fading process that, as was mentioned in Chapter 2, yields a satisfactory fit with empirical data for various measured channels. The normalised (unity power) Nakagami-m PDF of the fading envelope r is given by

$$p(r) = \frac{2}{\Gamma(m)}m^m r^{2m-1}e^{-mr^2}, \quad r \geq 0. \tag{3.5}$$

The Nakagami fading figure $m[k]$ ($1 \leq k \leq MN$) is estimated directly from the measured data according to

$$\begin{aligned} m[k] &= \frac{E\left\{\left|\mathbf{u}_k^H\text{vec}(\mathbf{H})\right|^2\right\}^2}{E\left\{\left\{\left|\mathbf{u}_k^H\text{vec}(\mathbf{H})\right|^2 - E\left\{\left|\mathbf{u}_k^H\text{vec}(\mathbf{H})\right|^2\right\}\right\}^2\right\}} \\ &= \frac{\lambda_k^2}{E\left\{\left\{\left|\mathbf{u}_k^H\text{vec}(\mathbf{H})\right|^2 - \lambda_k\right\}^2\right\}} \geq \frac{1}{2}. \end{aligned} \tag{3.6}$$

An example indicating the excellent fit of the Nakagami-m distribution with the distribution of a measured fading envelope is depicted in Fig. 3.2 (location 1D3). Please note that the parameters of the Ricean fit were obtained by directly applying a ML estimator to the raw data. This aggregate statistical metric shows the poor match of the commonly used Rayleigh distribution while the Ricean distribution fits reasonably well except in the tails of the measured data. Similar trends were observed at most of the considered cases. To further justify the choice of the

	average	std	min	max	smallest MSE
Rayleigh	2.38×10^{-4}	1.72×10^{-3}	5.59×10^{-7}	5.32×10^{-2}	5.79 (%)
Ricean	4.95×10^{-5}	1.28×10^{-4}	5.53×10^{-7}	4.72×10^{-3}	21.81 (%)
Nakagami-m	3.81×10^{-5}	1.23×10^{-4}	4.65×10^{-7}	4.18×10^{-3}	72.40 (%)

Table 3.1: *MSE characteristics of three CDF fitting distributions.*

Nakagami-m distribution, the Mean Squared Error (MSE) of these three candidate cumulative distribution function (CDF) fits across the whole data set, has been computed; the key characteristics are tabulated in Table 3.1. The acronym std stands for the standard deviation of a RV. The average and standard deviation measures indicate that the Nakagami-m fit yields a rather good accuracy and substantially outperforms the Rayleigh fit by an order of one magnitude while it remains robust and experiences the lowest maximum MSE. On the basis of which distribution best fits the measured data set, the smallest MSE occurs at 72.40% of the cases when a Nakagami-m fit is employed thereby confirming its improved performance compared to the other two reference distributions (right-hand column of Table 3.1).

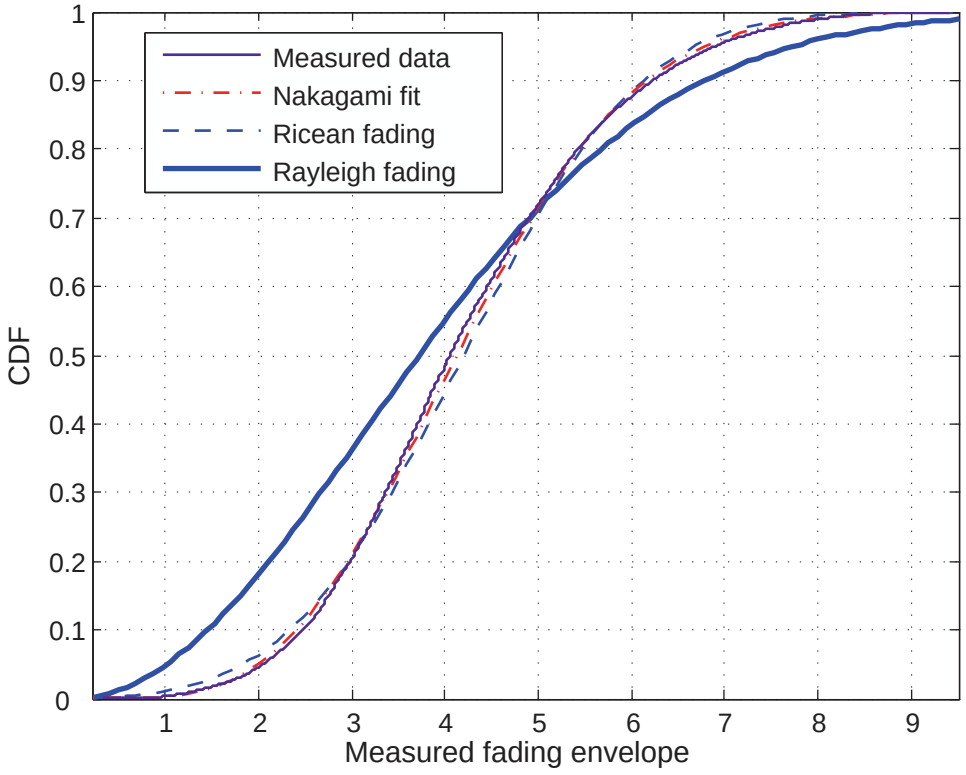

Figure 3.2: *CDF of a measured fading envelope in comparison with Nakagami-m, Rayleigh and Ricean distributions (location 1D3).*

3.4 Generation of independent Nakagami-m envelope deviates

This section suggests an unconstrained method for the generation of independent Nakagami-m envelope deviates based on the *rejection/acceptance technique* [123]. Please note that the generation of independent Nakagami-m RVs may in general offer an insight into the characterisation of practical systems operating in slowly varying Nakagami-m fading environments. Surprisingly, few results have been reported covering the computer simulation of independent Nakagami-m fading [36, 124, 125].

The so-called *brute force method* [36] considers the square root of a sum of squares of p zero-mean identically distributed Gaussian RVs and leads to a Nakagami distribution with $m = p/2$; yet, this scheme is limited to integer and half-integer values of m. The authors in [124] showed that the product of a square-root beta process and a complex Gaussian process forms an accurate approach but unfortunately is valid only for values of $m < 1$. The *inverse method* proposed in [125] is sufficiently accurate for arbitrary values of m but requires the computation of a different set of coefficients for each m value.

The initial attempt to apply the rejection/acceptance method in order to generate independent Nakagami-m samples was recently addressed in [126] but lacks a uniform approach for the whole range of m values. In particular, the authors suggest the use of either the folded-Gaussian ($0.5 \leq m \leq 1.0$) or the Gaussian ($m \geq 1.0$) PDFs as hat functions, resulting in the achieved efficiency being strongly dependent on the corresponding interval (65.75% and 66.67% respectively); an additional option to select different constants (which were determined empirically) enchanced the efficiency for particular ranges of m (see Tables I and II in [126]). This was achieved by applying the rejection scheme only in the confined region $0 \leq x \leq 4\Omega$ since for high values of the envelope r and $m \geq 1$ the tails of the considered scaled Gaussian PDF may fall below the tails of the Nakagami-m PDF. In this light, a simple technique with no constraints on the range of shape parameters is proposed in this section which overcomes the inadequacies of the above mentioned schemes and yields an excellent accuracy.

3.4.1 Rejection method

The rejection method requires the selection of a comparison function (usually referred to as the hat function) $f(r)$ that has finite area and satisfies the inequality $f(r) \geq p(r)$ with $p(r)$ being the original PDF. In the present case, a second-order inverse polynomial function is proposed

as the hat function and therefore

$$p(r) = \frac{2}{\Gamma(m)} \left(\frac{m}{\Omega}\right)^m r^{2m-1} e^{-mr^2/\Omega} \tag{3.7}$$

$$f(r) = \frac{A\sqrt{\Omega}}{\Omega - B\sqrt{\Omega}r + r^2}. \tag{3.8}$$

An illustrative graph of the two functions under investigation is shown in Fig. 3.3.

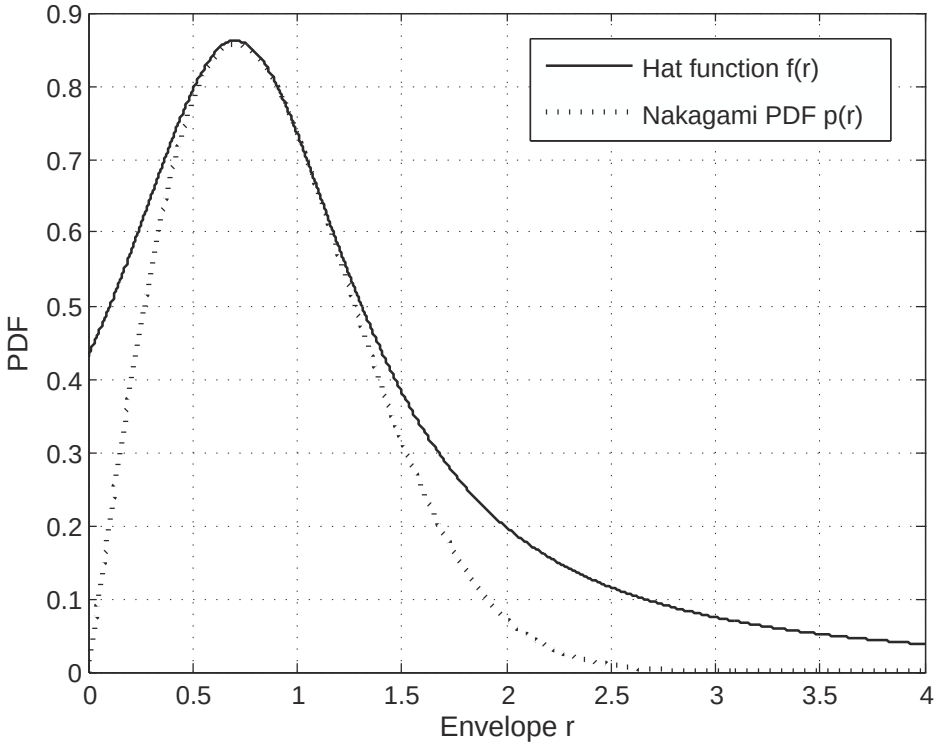

Figure 3.3: *Rejection method for generating random Nakagami-m deviates using an inverse polynomial function.*

The determination of A and B is an inter-dependent problem which can be solved with an iteration method. Taking into account that the maxima of (3.7) and (3.8) should coincide[1], it is trivial to show that $B = 2\sqrt{\frac{2m-1}{2m}}$. The scaling factor, A, is set such that the curves intersect at a single point, $r = r_{min}$, without crossing (minimum distance). In other words,

$$\frac{A\sqrt{\Omega}}{\Omega - B\sqrt{\Omega}r_{min} + r_{min}^2} = p(r_{min}) \Rightarrow \tag{3.9}$$

$$A = \frac{\Omega - B\sqrt{\Omega}r_{min} + r_{min}^2}{\sqrt{\Omega}} p(r_{min}). \tag{3.10}$$

[1]The maximum of a Nakagami PDF occurs at $r = \sqrt{\frac{2m-1}{2m}}$ and that of the hat function at $r = B/2$.

In order to find the position of minimum distance between the two curves, the derivative of their difference needs to be set equal to zero which results in the following equation

$$\lim_{r \to r_{min}} \frac{d}{dr} \left(f(r) - p(r) \right) = 0 \tag{3.11}$$

or

$$\lim_{r \to r_{min}} \frac{d}{dr} \left(\frac{\left(\Omega - B\sqrt{\Omega} r_{min} + r_{min}^2 \right) p(r_{min})}{\Omega - B\sqrt{\Omega} r + r^2} - p(r) \right) = 0. \tag{3.12}$$

For the ease of computation, the above equation is written in a more compact form

$$\lim_{r \to r_{min}} \frac{d}{dr} \left(\frac{a(r_{min}) p(r_{min})}{a(r)} - p(r) \right) = 0 \tag{3.13}$$

where $a(r) = \Omega - B\sqrt{\Omega} r + r^2$. Then, it is trivial to show that

$$\frac{d}{dr} a(r) = 2r - B\sqrt{\Omega} \tag{3.14}$$

$$\frac{d}{dr} p(r) = \frac{p(r)}{r} \left[(2m-1) - \frac{2mr^2}{\Omega} \right]. \tag{3.15}$$

After some easy manipulations of (3.13), we end up with

$$p(r_{min}) \lim_{r \to r_{min}} \frac{d}{dr} a(r) = -a(r_{min}) p(r_{min}) \left(\frac{(2m-1) - 2mr_{min}^2/\Omega}{r} \right) \Rightarrow \tag{3.16}$$

$$\lim_{r \to r_{min}} \frac{d}{dr} a(r) = -a(r_{min}) \left[(2m-1) - \frac{2mr^2}{\Omega} \right] \Rightarrow \tag{3.17}$$

$$r_{min} \left(2r_{min} - B\sqrt{\Omega} \right) = \left(\Omega - B\sqrt{\Omega} r_{min} + r_{min}^2 \right) \left(\frac{2mr_{min}^2}{\Omega} - (2m-1) \right) \Rightarrow \tag{3.18}$$

$$\frac{2mr_{min}^4}{\Omega} - 2mBr_{min}^3/\sqrt{\Omega} - r_{min}^2 + 2mBr_{min}\sqrt{\Omega} + (1-2m)\,\Omega = 0 \Rightarrow \tag{3.19}$$

$$\left(r_{min} - \sqrt{\Omega} \right) \left(r_{min} + \sqrt{\Omega} \right) \left(\frac{2mr_{min}^2}{\Omega} - \frac{2mBr_{min}}{\sqrt{\Omega}} + 2m - 1 \right) = 0. \tag{3.20}$$

The last quadratic term of the product has a discriminant always equal to zero, which results in a negative value for A for all $m \geq 2/3$. This, however, makes the hat function negative since the denominator in (3.8) is always positive. Hence, only one valid positive solution exists at $r_{min} = \sqrt{\Omega}$. Substituting the above solution into (3.10), the following relationship comes up

$$A = (2 - B) \frac{2m^m}{\Gamma(m)} e^{-m} > 0. \tag{3.21}$$

For the generation of independent samples from (3.8) the inverse method is introduced [123]; firstly, the indefinite integral of (3.8) is computed returning the closed-form function

$$u = \int f(r)dr = \frac{2A\tan^{-1}\left(\frac{\frac{2r}{\sqrt{\Omega}}-B}{\sqrt{4-B^2}}\right)}{\sqrt{4-B^2}}. \tag{3.22}$$

A random sample of r is now generated via the inverse function of (3.22) which reads as

$$r = \frac{\sqrt{\Omega}}{2}\left(\sqrt{4-B^2}\tan\left(\frac{u\sqrt{4-B^2}}{2A}\right)+B\right) \tag{3.23}$$

with u denoting a RV distributed uniformly in the range $\left[\frac{2A\tan^{-1}\left(\frac{-B}{\sqrt{4-B^2}}\right)}{\sqrt{4-B^2}}, \frac{A\pi}{\sqrt{4-B^2}}\right]$.

The above limits express respectively the minimum and maximum of (3.22) for $r \in [0, +\infty)$, and define also the efficiency of the rejection method; in fact, their difference represents by definition the area below $f(r)$. The generated sample r is accepted only if a random sample, uniformly distributed in the area under $f(r)$, lies also under $p(r)$. The pseudocode employed throughout the rejection scheme is summarised in Algorithm 1.

Algorithm 1 Rejection method for generating Nakagami-m deviates

1: Determine the values of A and B of the hat function with an iterative procedure.
2: **for** $i = 1$ to Number of samples **do**
3: Generate a uniform RV u in $\left[\frac{2A\tan^{-1}\left(\frac{-B}{\sqrt{4-B^2}}\right)}{\sqrt{4-B^2}}, \frac{A\pi}{\sqrt{4-B^2}}\right]$.
4: Generate a sample of r according to (3.23).
5: Estimate the value of the hat function $f(r)$ through (3.8).
6: Estimate the value of the Nakagami PDF $p(r)$ through (3.7).
7: Generate a uniform RV u' in the total area under $f(r)$, i.e. $[0, f(r)]$.
8: **if** $u' < p(r)$ **then**
9: accept r
10: **else**
11: reject r
12: **end if**
13: **end for**

3.4.2 Performance evaluation

After generating 2^{20} random samples of r using (3.23), the algorithm's performance was tested from different perspectives. In Fig. 3.4, the theoretical and simulated Nakagami-m PDFs are depicted for four different values of m assuming $\Omega = 1$; the attained accuracy is remarkably high, thereby verifying the choice of the rejection scheme as a powerful and straightforward technique for generating random deviates.

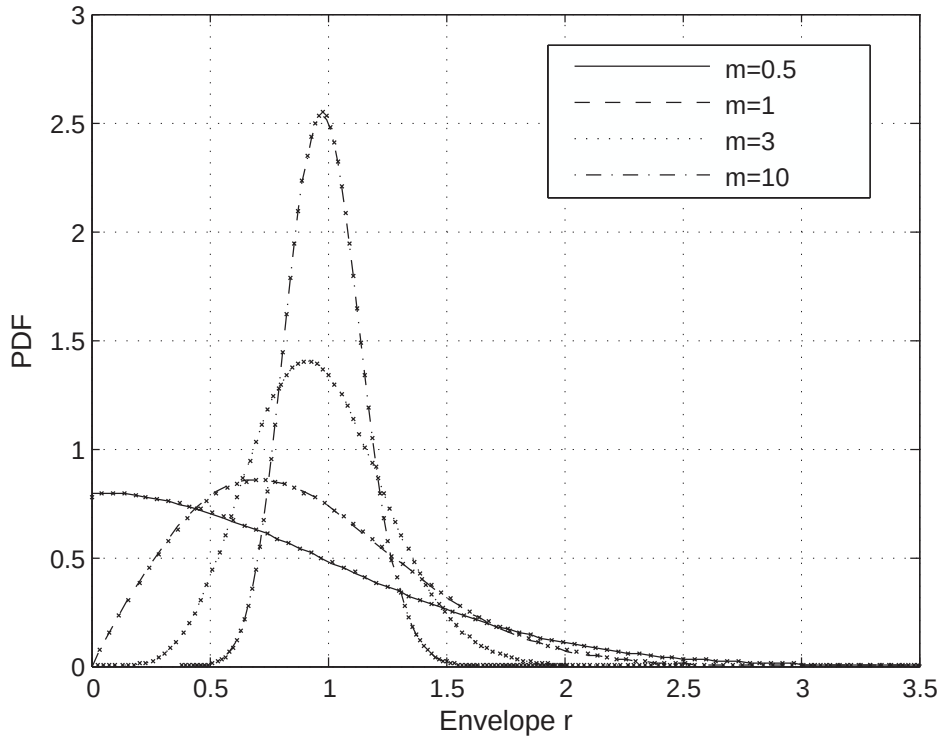

Figure 3.4: *Theoretical (curves) and simulated (stars) Nakagami-m PDFs for four arbitrary values of m using the rejection method ($\Omega = 1$).*

As far as the method's efficiency is concerned, this is directly related to the value of the m parameter. For high values of m, the tails of (3.7) decay faster than those of (3.8); this means that the relative difference between the two functions under comparison grows and this causes the achieved efficiency to decrease. In any case though, the efficiency in the common range of interest ($0.5 \leq m \leq 2.5$) rests above 65%, as Fig. 3.5 indicates.

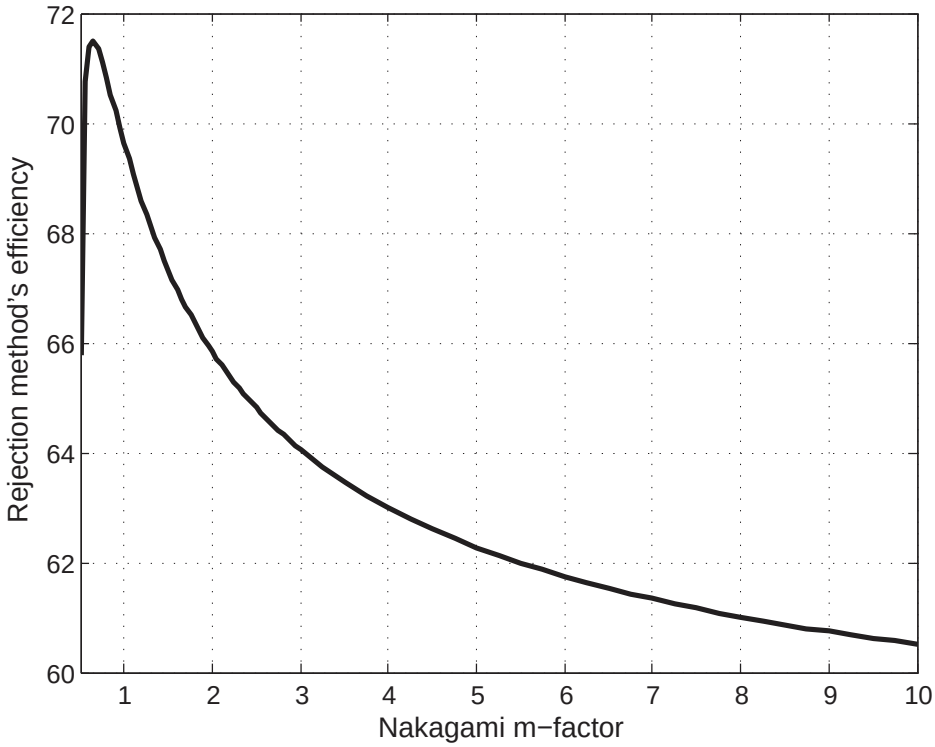

Figure 3.5: *Efficiency of the rejection method as a function of the m factor.*

3.5 MIMO channel model validation

The indoor campaign described in Section 3.1 provided the necessary amount of data for validating the analytical MIMO model of (3.3). The model is assessed by means of information theory as well as link-level performance. The measured correlation matrix is firstly computed using all space and frequency realisations and thereafter decomposed in order to obtain the spatial eigenmodes; as a next step, $25,090$ synthetic channel realisations are generated according to (3.3) so that the measured and simulated ensembles are the same[2]. It should be noted that the spatial fading coefficients were generated according to $g[k] = r[k] \exp(j\phi[k])$, where $\phi[k]$ is a random phase distributed uniformly in $[0, 2\pi)$. The uniform phase assumption was found to be valid even for large values of the m-factor (i.e. non-Rayleigh conditions) and thanks to its intrinsic simplicity was incorporated throughout the analysis.

[2]It was found that a further increase in the ensemble size did not significantly affect the variance of the estimators.

3.5.1 Information theory performance

A common policy in the capacity analysis of all measured MIMO channels is to remove the path-loss effects and have unity energy on average [96]. In practice, a system with perfect power control is simulated whose performance is assessed independently of the average SNR. On this basis, both ensembles are normalised so that the constraint $E\left\{\|\mathbf{H}\|_F^2\right\} = MN$ is fulfilled, where $\|\cdot\|_F$ corresponds to the Frobenius norm. The instantaneous capacity, assuming perfect CSI at the Rx but no knowledge at the Tx, reads

$$C = \log_2\left(\det\left(\mathbf{I}_M + \frac{\rho}{N}\mathbf{H}\mathbf{H}^H\right)\right) \quad \text{(bits/s/Hz)} \tag{3.24}$$

and the ergodic capacity is evaluated following (2.17). The SNR ρ was set equal to 20 dB to ensure that is well below the measured SNR after being averaged across all the temporal snapshots. The expectation operation was performed on either the measured data or the fading realisations of $g[k]$. In Fig. 3.6, three different models are compared, namely the Nakagami, Weichselberger and VCR models; the modelled ergodic capacity is plotted against the measured ergodic capacity for each of the 72 scenarios under investigation.

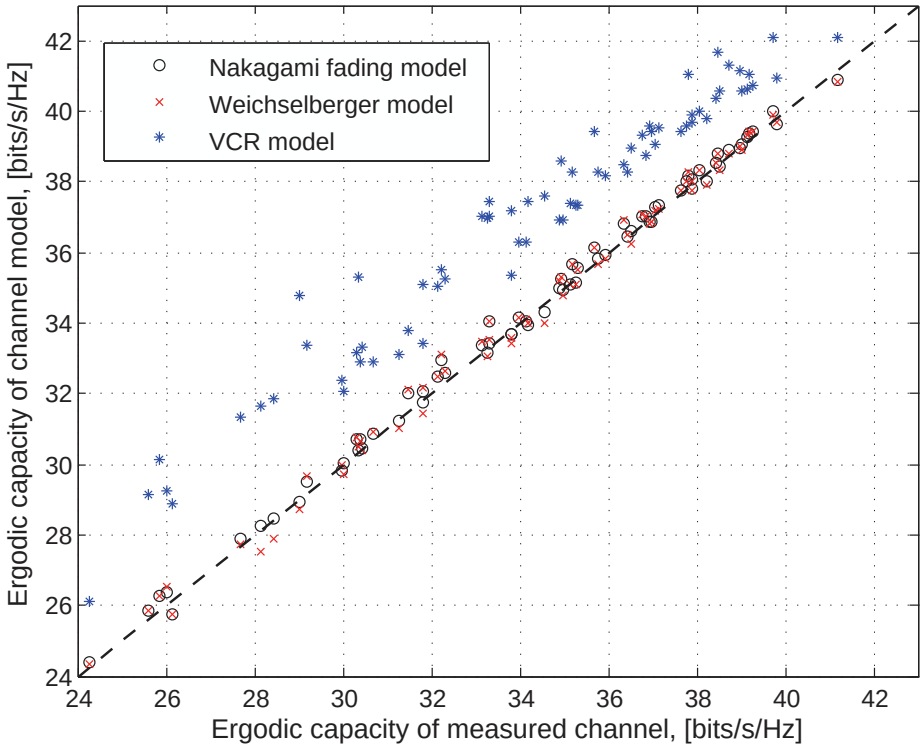

Figure 3.6: *Ergodic capacity for three different channel models versus measured ergodic capacity. The dashed line corresponds to the points of no modelling error.*

Please note that the Kronecker model has not been included in the following analysis since it is a special case of the Weichselberger model and yields an inferior performance for the great majority of cases [43, 49, 98]. From this figure, it is clearly observable that the proposed model holds a smaller modeling error than the Weichselberger model, whose mismatch increases with decreasing capacity, for all the scenarios under investigation; in particular, a 2.2 dB improvement was achieved in the MSE from -9.72 to -11.93 dB. The VCR model systematically overestimates the modelled capacity as a result of the artificial generation of MPCs discussed in Chapter 2; in this case, the MSE is as high as 8.81 dB disclosing the rather poor fit of the specific model. These results are in reasonable agreement with those presented in [49, 98]. The good fit of the Nakagami model can be partially attributed to the presence of strong OLoS components at the majority of Rx locations due to its inherent higher flexibility compared to the more restricted Rayleigh and Ricean distributions. In other words, for the corresponding eigenmodes $m > 1$ and therefore the fluctuations of the signal strength reduce compared to Rayleigh fading.

Traditionally, the ergodic capacity is a metric of the amount of average error-free information transmitted; however, a key issue in the design of multi-antenna systems is the outage capacity usually regarded as a more fair measure of the probability of successful transmission within a given time frame. The $q\%$ outage capacity $C_{out,q}$ is the capacity that is guaranteed in $(100-q)\%$ of the cases

$$Prob\left[C < C_{out,q}\right] = q\%. \tag{3.25}$$

In order to calculate the outage capacity a precise knowledge of the CDF of the RV C is required. For a specific Rx location (22D1) the measured and modelled capacity CDFs are plotted in Fig. 3.7 where it is shown that the Nakagami fading model yields the best fit; at the 10% outage capacity the proposed scheme deviates by 1.64 bits/s/Hz while the Weichselberger and the VCR models by 2.36 and 3.91 bits/s/Hz respectively. In addition, the slope of the capacity CDF is directly related to the notion of diversity, i.e. the reliability of the radio link for a given confidence interval. All modelled curves are steeper than the measured curve, thereby overestimating the achieved diversity, but the proposed model remains sufficiently robust and offers the best accuracy again. Similar conclusions can be drawn from the whole set of data after estimating the 10% outage capacity (see Fig. 3.8).

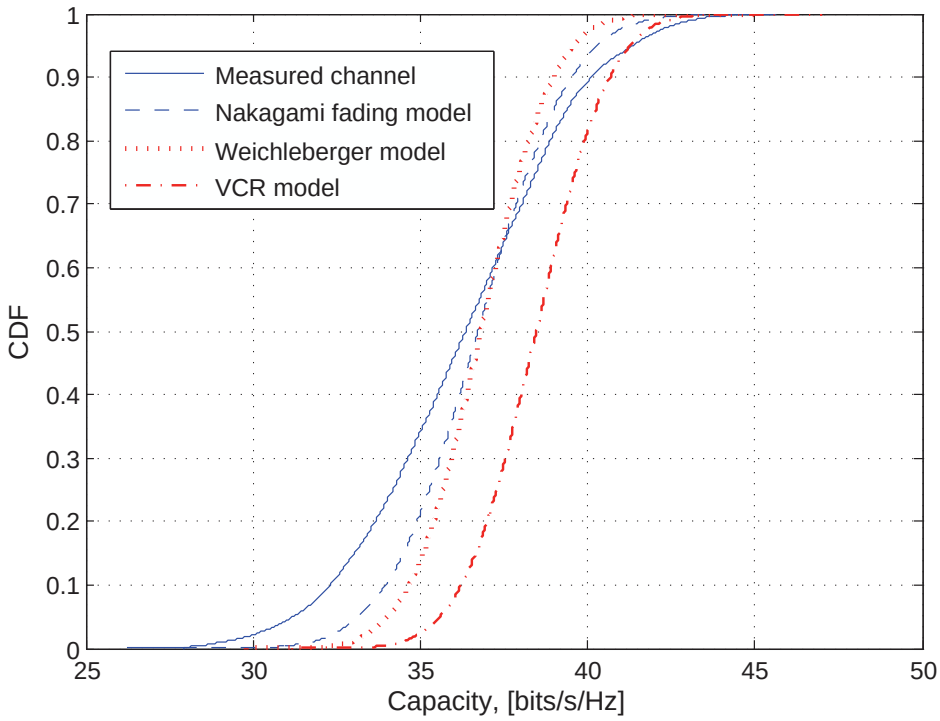

Figure 3.7: *Capacity CDFs for a measured and modelled channels (location 22D1).*

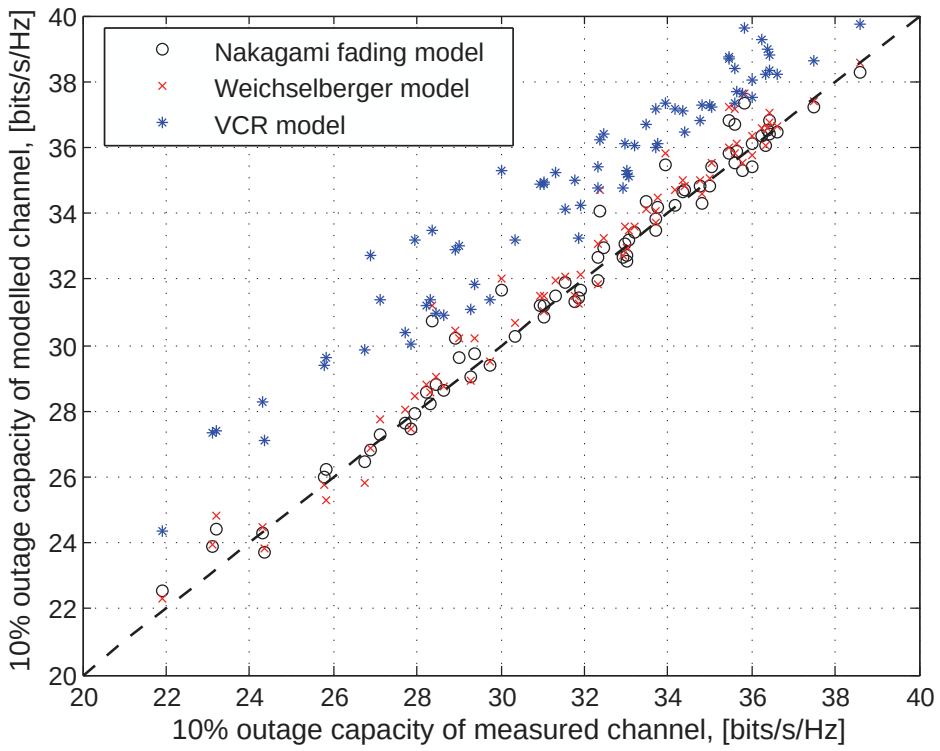

Figure 3.8: *10% outage capacity for three different channel models versus measured outage capacity. The dashed line corresponds to the points of no modelling error.*

In terms of the estimation MSE, the performance gain is 2.21 dB from -1.65 dB to -3.86 dB compared to the model implemented by Weichselberger. As anticipated, the predefined steering angular directions make the VCR framework unable to capture MPCs lying between them and this gives rise to overestimated statistics. In this case, the MSE is 9.83 dB demonstrating a dramatic degradation of 13.69 dB compared to the Nakagami scheme.

3.5.2 Link-level performance

The analysis presented in the previous section was based on an information theory approach which used channel capacity as a criterion for testing the goodness of fit for all MIMO models. In order to conduct a concise comparison study though, the models' performance should be investigated from a link-level perspective as well. Assuming a SM transmission strategy, a linear Minimum Mean Squared Error (MMSE) detector is considered which can minimise the overall error caused by noise and mutual interference[2]. The uncoded transmitted signal is modulated using BPSK (Binary Phase Shift Keying) modulation. Referring back to the input-output MIMO relationship (2.11), the estimated transmit signal vector $\hat{\mathbf{x}}$ is [128]

$$\hat{\mathbf{x}} = \widetilde{\mathbf{w}} \cdot \mathbf{y}, \text{ where } \widetilde{\mathbf{w}} = \arg\min_{\mathbf{w}} E\left\{ \|\mathbf{w}\mathbf{y} - \mathbf{x}\|^2 \right\} \tag{3.26}$$

and thus the following closed-form expression is obtained

$$\hat{\mathbf{x}} = \mathbf{H}^H \left(\mathbf{H}\mathbf{H}^H + N_0 \mathbf{I}_M \right)^{-1} \cdot \mathbf{y} \tag{3.27}$$

where N_0 is the noise power. The Bit Error Rate (BER) is measured by counting the number of erroneously detected symbols and divide this number with the total number of transmitted symbols, assuming that the entries of the noise term are $\sim \widetilde{\mathcal{N}}(0,1)$ RVs. The BER curves for a single measurement scenario (location 15D3), in which the dominant eigenmode has an m-factor equal to 5.3, are depicted in Fig. 3.9. All channel models tend to underestimate the BER with the proposed model yielding an enhanced accuracy, especially in the high SNR region. For instance, performance gains of 6% at 20 dB, of 12% at 30 dB and of more than 28% at 35 dB over the Weilscelberger scheme were noticed. The VCR fails to approximate the empirical BER leading to an irreducible underestimation.

[2] A more detailed discussion on SM detection algorithms is given in Chapter 5.

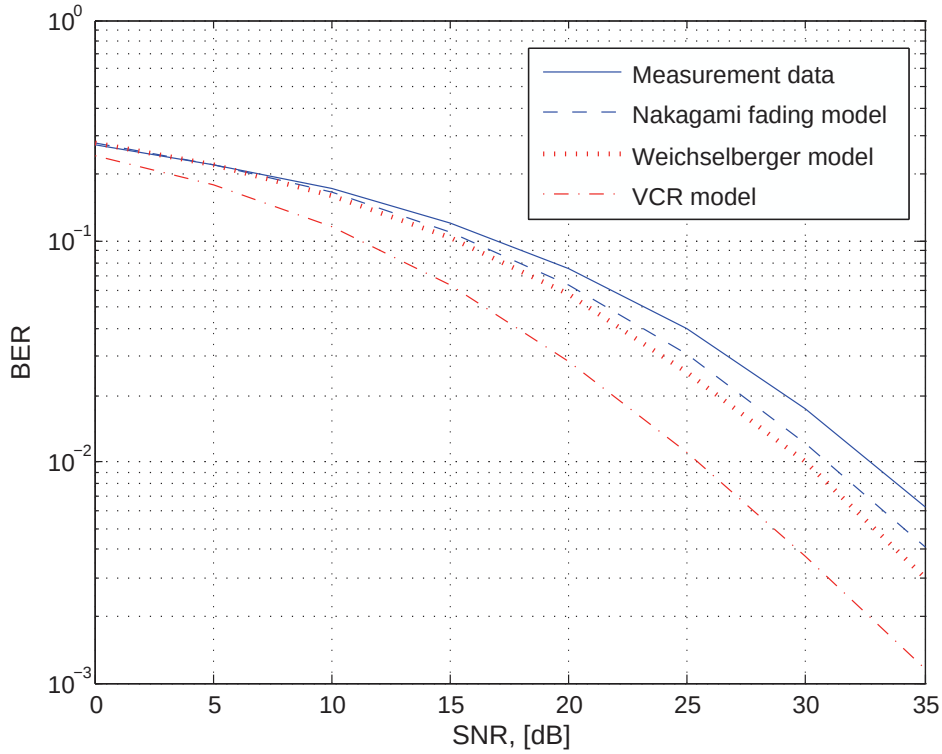

Figure 3.9: *BER performance of measured and modelled channels (location 15D3).*

The so-called BER mismatch is finally explored at a target SNR of 20 dB against the Nakagami m-factor of the dominant eigenmode (c.f. Fig. 3.10). In general, the BER mismatch is defined as the absolute difference between the measured and the modelled BER at a predefined target SNR. Please note that while there is no dependency between the m-factor and the Weichselberger/VCR models, their direct mapping offers a deeper insight into the estimation accuracy of all schemes as a function of the critical parameter m. To this end, a key observation to be made is that the distribution of the m values clearly confirms the assumption of Nakagami fading while a significant portion of them lies well beyond the typical unity value. The proposed model has again a superior performance, compared to the Weichselberger scheme, for the vast majority of measured scenarios (68 out of 72 scenarios) with the MSEs being 2.24×10^{-5} and 4.47×10^{-5} respectively, expressing a 3 dB improvement. Once again, the VCR model deviates significantly from the actual BER and the output MSE is larger by more than an order of magnitude (7.96×10^{-4}). It is noteworthy that the relative difference of models' estimators is higher when more than one eigenmode experiences purely Nakagami fading ($m > 2$).

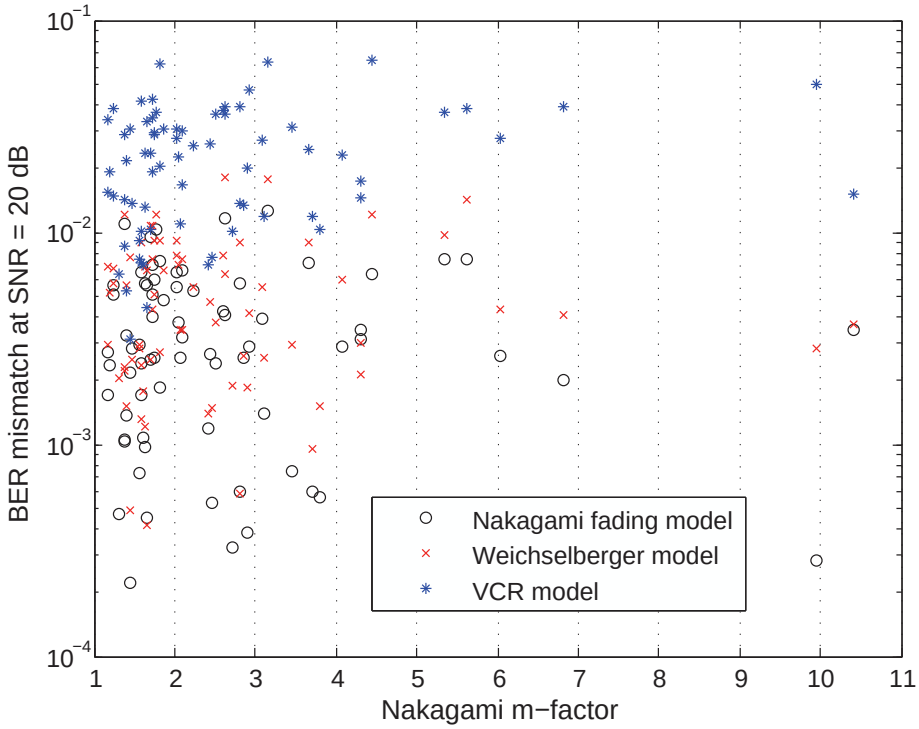

Figure 3.10: *BER mismatch at a target SNR of 20 dB against the Nakagami m-factor of the dominant eigenmode.*

3.6 Summary

In this chapter, a novel spatial-based analytical model has been devised using the data from an indoor measurement campaign conducted at 5.2 GHz. Following the formalism of the KLT, the scheme decorrelates the spatial subchannels and models their marginal behaviour separately. This approach not only provides a reasonable physical interpretation but also relaxes the stringent condition of joint Gaussian channel statistics. A deeper analysis of the measured data revealed that the fading envelopes of the vast majority of the spatial eigenmodes follow a Nakagami-m distribution rather than a Rayleigh or Ricean distribution. For the generation of Nakagami-m RVs the rejection technique is introduced with a second-order inverse polynomial function serving as the hat function. The method is accurate for arbitrary values of m and Ω, thus indicating its high flexibility. By assigning the independent Nakagami-m fading process on each eigenmode, the performance of the proposed scheme was tested from two different perspectives (information theory and link-level) and compared it with the sophisticated Weichselberger and suboptimal VCR models. It was shown that the Nakagami model outperforms the former by approximately 2.2 dB in the case of ergodic and outage capacity and by 3 dB in

terms of BER mismatch. On the other hand, the VCR yields a rather poor fit in all cases leading to intolerable errors.

The only disadvantage of the proposed scheme lies in its increased complexity burden which is generally a crucial issue in the choice of the most appropriate channel model. While the VCR and the Weichselberger models require respectively $MN = 64$ and $MN + M(M - 1) + N(N - 1) = 176$ real parameters to be specified, the complexity order of the Nakagami scheme is equal to that of the full correlation model, i.e. $(MN)^2 = 4096$. However, in terms of processing time a modest increase of 45% was observed on a 3.2 GHz Pentium, making the model rather appealing when an enhanced accuracy is desired. For example, if a MIMO Rx is to be simulated for a quasi-static[3] channel with reasonable data packet lengths ($\gg 1$ symbol), the proposed channel model can be applied to generate the channel for each separate frame and increase drastically the achieved accuracy without a significant sacrifice in the simulation time. Ultimately, the scheme can be deployed as a framework for describing different scenarios operating at the 5 GHz frequency band, e.g. WLANs, fixed wireless and peer-to-peer communications. It can also be used as a tractable tool for the simulation of MIMO systems, design of space-time codes and construction of optimum spatial filtering at both ends.

[3] A *quasi-static* channel is wide sense stationary, i.e. its statistics remain constant during the entire transmission. In general, the quasi-static channel assumption is a good model for users that are stationary or moving very slowly relative to the rate of communication.

Chapter 4
A high-resolution array processing algorithm for channel characterisation

For the construction of efficient physical channel models as well as the optimum design and realistic performance evaluation of multi-antenna systems, a detailed knowledge of the statistical distributions of the multipath parameters is required. This involves multi-dimensional practical measurement trials followed by the joint extraction of different propagation characteristics in the corresponding domains, i.e. ToA, DoA, DoD, Doppler frequency, polarisation, complex path gain, etc. This is usually accomplished by high-resolution array signal processing algorithms applied directly to the raw measurement data. In this chapter, a ML frequency domain estimation algorithm is devised, namely the 3D FD-SAGE algorithm which can reliably characterise a wireless channel. The scheme is based on a SIC strategy for both detecting the paths and estimating their corresponding parameters. The remainder of the chapter is organised as follows: Section 4.1 covers the most known parameter estimation algorithms that have been reported over the last decades. Section 4.2 elaborates on the fundamentals of the Expectation-Maximisation (EM) and SAGE algorithms as well as on their applications to channel characterisation. In Section 4.3, the kernel of the 3D FD-SAGE algorithm is discussed for a far-field propagation scenario where a finite number of plane waves impinge on the Rx. The algorithm's performance is evaluated in Section 4.4 for a synthetic environment and in Section 4.5 for a measured environment. In Section 4.6, the intrinsic deficiencies of the SAGE framework are addressed. Finally, Section 4.7 concludes the chapter and summarises the key findings.

4.1 Parameter estimation techniques

The quintessential goal of channel characterisation is the identification of MPCs in conjunction with the estimation of their parameters in both temporal and spatial domains. As a further step, we can obtain a geometrical projection of the signal's interactions with the surrounding environment and thereafter work out the dominant propagation mechanisms. The computation

of the paths' parameters implies the use of parameter estimation techniques which are globally classified into two main categories namely, *spectral-based* and *parametric methods* [129].

4.1.1 Spectral-based methods

The key idea is to generate the spectrum of the parameter under investigation and then the locations of the discrete peaks are recorded as the parameter estimates. The main advantage of these techniques is that they are simple and require no extensive memory requirements. The spectral-based techniques can be further classified into *beamforming techniques* and *subspace-based methods*. The classical definition of beamforming states that an array should be steered in one direction at a time so that the output power is measured; the steering locations which result in maximum power yield the parameter estimates, e.g. AoA. Different beamforming schemes have been implemented with the most known and straightforward being the *Bartlett* or *conventional* beamformer [130] and the *Capon's beamformer* [131]. While both schemes (and their alternatives) are reasonably simple their performance is strongly dependent on the array aperture and the system SNR. In highly scattered environments with correlated sources, they fail to capture all multipath activity. The author points out that two signals are correlated when their correlation coefficient is non-zero while they are coherent when their correlation coefficient is one. According to [129], two signals are coherent if one is a scaled and delayed version of the other.

These intrinsic deficiencies of beamforming techniques may be partially eliminated through the use of subspace methods. These methods rely on the decomposition of the input covariance matrix into a signal and a noise subspace and the most well known scheme is MUltiple SIgnal Classification (MUSIC) algorithm [132, 133], which outperforms the beamformers and satisfies the two basic criteria of estimation theory: *consistency*[1] and *efficiency*[2]. Although the MUSIC spatial spectrum is not a true spectrum, it exhibits peaks in the vicinity of the true DOAs. A comprehensive analysis of the algorithm's performance can be found in [134]. A performance measure of Bartlett, Capon's and MUSIC methods can be seen in Fig 4.1, where the normalised spectra generated by these methods are shown. A ULA with five elements and inter-element distance equal to $\lambda/2$ was used in the simulation and the SNR was set to 20 dB. The true directions of arrival are -10° and 0°.

[1] An estimate is consistent if it converges to the correct value when the number of observations tends to infinity.
[2] An estimator is statistically efficient if it asymptotically attains the Cramér-Rao (CR) lower bound.

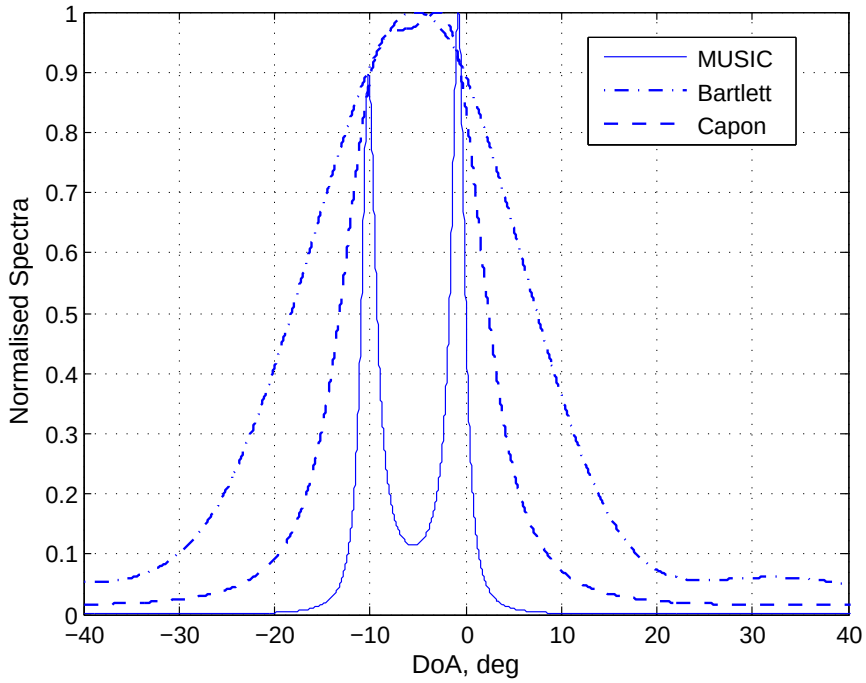

Figure 4.1: *Normalised power spectra of Bartlett (dash-dotted), Capon (dashed) and MUSIC (solid) methods vs DoA. The true directions of arrival are* $-10°$ *and* $0°$.

Undoubtedly, Bartlett and Capon's beamformers fail to resolve both signals; MUSIC though returns two distinct peaks. The crucial advantage of MUSIC is that, in contrast to beamformers, it yields statistically consistent estimates. On the other hand, the performance enhancement of MUSIC is achieved at a considerable cost in computational burden as the search is carried out across the whole parameter space. Moreover, when the amount of data or the SNR is low it can hardly resolve closely spaced signals. In the limiting case of coherent signals, MUSIC's advantages vanish and the estimates are inconsistent. A potential solution for mitigating the undesired effects of correlated signals lies in the *forward-backward* averaging (FB) [135] or *spatial smoothing* (SS) [136] techniques. Their key concept is to split the array into a number of overlapping subarrays which induce a random phase modulation and hence decorrelate the signals. Nevertheless, these techniques are practically applicable only to ULA geometries and further they inevitably reduce the effective aperture of the array since the subarrays are smaller than the original array [129].

4.1.2 Parametric methods

The shortcomings of spectral-based techniques dictated the development of the more robust parametric methods which directly estimate the parameter of interest without first computing a spectrum, albeit at the expense of an intensive complexity. This is a result of the multi-dimensional search required to determine the paths' parameters. A classification is usually made for parametric techniques into *subspace-based approximations* and *ML methods* [129].

4.1.2.1 Subspace-based approximations

The subspace-based methods constitute the first class in the family of parametric methods; they offer similar statistical performance as ML methods but are less complex. In the specific case of ULAs, high-resolution algorithms can be directly applied leading to an enhanced accuracy. A brief overview of the most important techniques in now provided.

ESPRIT: Since its formal derivation in 1985 [137], the so-called Estimation of Signal Parameters via Rotational Invariance Techniques (ESPRIT) algorithm has been widely deployed for DoA estimation, harmonic analysis, frequency estimation, delay estimation, and combinations thereof [138]. The scheme may be considered as a counterpart of the MUSIC algorithm expanded in the signal subspace rather than in the noise subspace. Moreover, it is more robust and far less complex since the solution is essentially given in closed form and no numerical search through all possible steering vectors is needed. On the contrary, the ESPRIT estimators are unbiased only if the antenna arrays used fulfil the strict condition of two identical and translationally invariant subarrays (shift-invariance) and hence the scheme is applicable to certain topologies (in practice ULAs and their combinations). If different configurations are to be employed, such as circular arrays, special modifications need to be performed in order to transform the circular array into a virtual array with uniform linear structure. Furthermore, it is noted that like MUSIC, ESPRIT cannot handle correlated paths. Pre-processing techniques, as the ones reported above for the MUSIC algorithm, are required.

Unitary ESPRIT: The so-called Unitary ESPRIT [139] is applicable to specific array geometries, namely centro-symmetric arrays[3], and is based on the transformation of the complex data matrix to a real matrix of the same size and involves only real-valued calculations throughout. The resulting algorithm performs better in terms of correlated sources compared to the conven-

[3] An array is called centro-symmetric if its element locations are symmetric with respect to the centroid and the complex radiation characteristics of paired elements are the same.

tional ESPRIT algorithm, but when more two correlated sources are present it fails to maintain the rank of the signal covariance matrix and hence, a SS technique is still required.

Root MUSIC: The Root-MUSIC (RMUSIC) is basically a polynomial-rooting version of the conventional MUSIC algorithm [140]. When only small samples are available, RMUSIC yields a superior performance and also has a lower failure rate for closely spaced sources. Likewise, the algorithm was initially applied only to ULA configurations although recently a novel scheme was introduced which processes the data in the element-space domain and is applicable for any array geometry. The so-called Element-Space RMUSIC algorithm provides asymptotically optimal AoA estimation and has very good statistical performance [141].

RARE: The rank reduction estimator (RARE) is a relatively new eigenspace-based estimation method for multi-dimensional harmonic retrieval problems. Two variants have been developed so far, namely the root RARE (r-RARE) [142] and the spectral RARE (s-RARE) [143]. The former exploits its rooting-based implementation and the rich Vandermode structure in the measurement data to improve the estimation performance. Also, the r-RARE is a search-free algorithm and thus its computational cost is substantially lower than that of the s-RARE. However, both schemes are susceptible to array orientation errors which noticeably deteriorate the output accuracy. This problem has been addressed in [144] where the proposed modified RARE is more robust in terms of DoA estimation and exhibits a performance close to the CR bound.

4.1.2.2 ML methods

In general, ML techniques, which are built upon the statistical properties of the ray paths, are optimal and experience a superior performance even in the low SNR region or when the data ensemble is small. In addition, they offer a high degree of robustness and flexibility with regard to the array geometry they can be applied to. Two different assumptions about the transmit signals lead to two different versions which are outlined below [129].

Deterministic ML: The deterministic ML (DML) method poses no assumptions about the ray paths. The complex gains are modelled as arbitrary deterministic sequences while the noise as a stationary Gaussian white random process. Then, the estimated parameters are obtained by solving a multi-dimensional minimisation problem which is usually computationally expensive.

Stochastic ML: The stochastic ML (SML) method models the complex path gains as stationary, temporally white Gaussian RVs. It is interesting to note that the model is applicable even if

the signal waveforms are not Gaussian but still requires an exhaustive numerical search while it shows a better accuracy than the corresponding DML method (see [129] and references therein), with the difference being pronounced for small numbers of antenna elements, low SNR and highly correlated signals.

4.2 Principles of the EM and SAGE algorithms

4.2.1 The EM algorithm

One of the most known DML approaches is the EM algorithm which was initially formulated by Dempster *et al.* in [145] as a general method for maximising likelihood functions that arise in various statistical estimation problems. The EM algorithm supplements the observed measurements which are *incomplete* or have missing values with a *complete data* space whose relationship to the parameter space facilitates estimation. An EM scheme is comprised of two steps: an Expectation step (E-step) and a Maximisation step (M-step); the former calculates the expectation of the complete-data log-likelihood, using the current estimate of the parameters and conditioned upon the observations, while the latter maximises the expectation with respect to all the unknown parameters. These two steps are iterated until convergence is reached.

4.2.2 The SAGE algorithm

The main motivation for introducing the SAGE algorithm is the slow convergence rate of the classical EM scheme due to its simultaneous update procedure [146]. The SAGE algorithm generalises the idea of data augmentation to simplify computations of EM algorithm and improve the convergence rate [147]. This is done by breaking down the sequential maximisation problem into several smaller ones and using EM to update the parameter subset associated with each reduced problem while keeping the estimates of the remaining parameters fixed. Still, the derivation of the algorithm relies on the key notions of *complete (unobservable)* and *incomplete (observable)* data. However, the mapping from complete to incomplete data is allowed to be random rather than deterministic as occurs within the EM [145]. To sum up, the SAGE algorithm yields a faster convergence rate along with a reduced complexity. Last but far from least, a crucial advantage of both the EM and SAGE schemes is that they can be applied to any arbitrary antenna geometry provided that the array manifold is fully available and further require no spatial smoothing for resolving correlated sources.

4.2.3 Application to the problem of channel characterisation

The original application of the EM algorithm for estimating the parameters of superimposed signals in white Gaussian noise can be found in [149]. The application of the SAGE algorithm to the problem of channel characterisation was originally investigated by Fleury *et al.* in [150] and [151], where time-invariant and time-variant SIMO channels respectively were studied. Their study was performed exclusively in the time domain and the sounding signal consisted of an infinite train of rectangular pulses modulated by a pseudo-noise sequence. An extension to MIMO systems has been presented in [152]. In this case, both ends of the link were equipped with RF switches whose timing structure was selected so that the MIMO sub-channels are sounded sequentially. This technique reduces hardware costs and effort for system calibration. The overall sounding of the propagation channel was performed in a time-division multiplexed mode. The broadest version of these schemes can be found in [153], where the authors considered an extra selectivity domain, i.e. polarisation.

On the other hand, the main motivation for applying the SAGE algorithm in the FD can be attributed to the operation of the commonly used RUSK vector channel sounders of MEDAV company [121]. In such a case, the Tx is probed by a multi-tone frequency excitation signal and the sounder output represents the complex frequency response. The initial development of the FD-SAGE algorithm has been presented in [154] for a dynamic indoor SIMO channel where the Rx was in motion. However, this model did not account for angular spread at the transmit side. In this thesis, the aforementioned approach in this thesis has been extended to encompass the double directional information.

4.3 The 3D FD-SAGE algorithm

The general problem of interest is stated as follows. Let's assume a finite number, L, of specular wavefronts impinging on the Rx, i.e. all signal sources as well as the scatterers are located in the corresponding far-field regions. The transmitted signal model is assumed to be narrowband and thus time delays between elements of the arrays can be approximated by phase shifts. For the sake of simplicity, only horizontal propagation is considered and therefore the elevation angle is discarded. This assumption does not have a significant impact on the estimation of azimuth as long as the elevation is confined within $\pm 40^{\circ}$ [150]; in fact, the elevation incidence is very likely to lie within this range when the Tx and Rx are mounted at the same heights. Under these

conditions, the channel transfer function can be modelled as (similar to (2.40))

$$\mathbf{H}(f,m,n) = \sum_{\ell=1}^{L} \beta_\ell \mathbf{a}_r(\phi_{r,\ell})\mathbf{a}_t^T(\phi_{t,\ell}) \exp\left(-j2\pi\tau_\ell f\right) \tag{4.1}$$

with f, m, n representing the selectivity in frequency, receive and transmit spatial domains respectively. For clarity, the spatial dependency is dropped and all the path parameters are concatenated in a vector $\theta_\ell \triangleq [\tau_\ell, \phi_{r,\ell}, \phi_{t,\ell}, \beta_\ell]$. By considering N_f frequency bins, the noise-corrupted transfer function at the k-th frequency bin with $1 \leq k \leq N_f$, is given as

$$\mathbf{H}(k) = \sum_{\ell=1}^{L} \mathbf{S}(k;\theta_\ell) + \mathbf{N}(k). \tag{4.2}$$

In the above equation, the elements of the $(M \times N)$ matrix $\mathbf{N}(k)$ are independent complex zero-mean white Gaussian noise processes with unit spectral height. The contribution of each path reads as

$$\mathbf{S}(k;\theta_\ell) = \beta_\ell \mathbf{a}_r(\phi_{r,\ell})\mathbf{a}_t^T(\phi_{t,\ell}) \exp\left(-j2\pi\tau_\ell f_k\right). \tag{4.3}$$

Referring to (4.2) the channel response, $\mathbf{H}(k)$, is identified as the incomplete data and is related to the complete data, $\mathbf{Y}_\ell(k)$, according to

$$\mathbf{H}(k) = \sum_{\ell=1}^{L} \mathbf{Y}_\ell(k) \tag{4.4}$$

where

$$\mathbf{Y}_\ell(k) = \mathbf{S}(k;\theta_\ell) + p_\ell \mathbf{N}_\ell(k) \quad \ell = 1, \ldots, L. \tag{4.5}$$

In the SAGE context, it is optimal to set $p_\ell = 1$ since empirical evidence shows that this choice leads to a fast convergence of the algorithm even in the early iteration steps [146, 151]. During the E-step the complete data of the ℓ-th path is estimated; this can be done using either the Parallel Interference Cancellation (PIC) or the SIC scheme. Although the former is commonly used in conjunction with the SAGE algorithm in the time domain, the latter yields more stable and robust performance in the frequency domain [154]. The main concept of the SIC technique is to order the waves with respect to their received power in a descending order; thereafter, paths are estimated and cancelled successively from the received channel response. By doing that, the effects of interference caused by the strong MPCs are removed, otherwise they are likely to lead to inaccurate estimates for the low power MPCs. When the multipath activity is high, the

PIC scheme can be unstable and diverge from the solution, especially in low SNR scenarios. Furthermore, the PIC scheme is laborious since it requires the whole set of waves in order to compute the updated estimates. The E-step of the 3D FD-SAGE algorithm then becomes

$$\widehat{\mathbf{Y}}_\ell(k;\hat{\theta}') = \mathbf{H}(k) - \sum_{\ell'=1}^{\ell-1} \mathbf{S}(k;\hat{\theta}'_{\ell'}). \tag{4.6}$$

The coordinate wise updating procedure for obtaining the parameters $\hat{\theta}''$ of each wave based on all previous estimates $\hat{\theta}'$ reads as (M-step)

$$\hat{\tau}''_\ell = \arg\max_{\tau} \left\{ \left| z(\tau, \hat{\phi}'_{r,\ell}, \hat{\phi}'_{t,\ell}; \widehat{\mathbf{Y}}_\ell(k;\hat{\theta}') \right|^2 \right\} \tag{4.7}$$

$$\hat{\phi}''_{r,\ell} = \arg\max_{\phi_r} \left\{ \left| z(\hat{\tau}''_\ell, \phi_r, \hat{\phi}'_{t,\ell}; \widehat{\mathbf{Y}}_\ell(k;\hat{\theta}') \right|^2 \right\} \tag{4.8}$$

$$\hat{\phi}''_{t,\ell} = \arg\max_{\phi_t} \left\{ \left| z(\hat{\tau}''_\ell, \hat{\phi}''_{r,\ell}, \phi_t; \widehat{\mathbf{Y}}_\ell(k;\hat{\theta}') \right|^2 \right\} \tag{4.9}$$

$$\hat{\beta}''_\ell = \frac{1}{M \cdot N \cdot N_f} \cdot z\left(\hat{\tau}''_\ell, \hat{\phi}''_{r,\ell}, \hat{\phi}''_{t,\ell}; \widehat{\mathbf{Y}}_\ell(k;\hat{\theta}') \right) \tag{4.10}$$

where $z\left(\tau, \phi_r, \phi_t; \mathbf{Y}_\ell\right)$ is the so-called cost (or correlation) function; in general, the cost function originates from the fundamental concept of ML techniques while at each optimisation stage its peak corresponds to the expected parameter value [146]. In the present case, it is given by

$$\begin{aligned} z\left(\tau, \phi_r, \phi_t; \mathbf{Y}_\ell\right) &\triangleq \mathbf{a}_r^H(\phi_r)\mathbf{U}^* \odot \mathbf{Y}_\ell \mathbf{a}_t^*(\phi_t) \\ &= \mathbf{a}_r^H(\phi_r) \sum_{k=1}^{N_f} e^{j2\pi\tau f_k} \odot \mathbf{Y}_\ell(k) \mathbf{a}_t^*(\phi_t). \end{aligned} \tag{4.11}$$

The term $\mathbf{U}^*$ expresses the conjugate of the calibrated periodic multi-tone frequency excitation signal [121]. The execution of this update process once defines one iteration cycle of the 3D FD-SAGE algorithm while at the μ-th iteration step the parameters of the path $\ell = \mu \text{mod}(L)+1$ are re-estimated. The parameter estimates are sequentially and cyclically updated until convergence is attained. The complex amplitude is then computed as the output signal normalised by the total energy. As for any other iteration method, the algorithm converges when the difference between two successive estimators becomes smaller than a predefined threshold. Typical thresholds of 0.5 ns and 0.1° for the delay and angular domains have respectively been used, as sufficiently small iteration steps.

4.3.1 Initialisation of the SAGE algorithm

It is well established that the convergence of any iteration technique to a global maximum is strongly dependent upon the initial conditions. Again, the initialisation procedure is based on a successive cancellation scheme with the iteration step μ ranging from $\{-(L-1),\ldots,0\}$. By starting with the pre-initial setting $\hat{\theta}' = [0,\ldots,0]$ for $\ell = 1,\ldots L$, the initial estimates for the ToA and AoA were computed according to

$$\hat{\tau}_{\ell}'' = \arg\max_{\tau} \left\{ \sum_{m=1}^{M} \sum_{n=1}^{N} \left| \sum_{k=1}^{N_f} e^{j2\pi\tau f_k} \widehat{\mathbf{Y}}_{\ell,m,n}(k;\hat{\theta}'') \right|^2 \right\} \tag{4.12}$$

$$\hat{\phi}_{r,\ell}'' = \arg\max_{\phi_r} \left\{ \sum_{n=1}^{N} \left| \mathbf{a}_r^H(\phi_r) \sum_{k=1}^{N_f} e^{j2\pi\hat{\tau}_{\ell}'' f_k} \widehat{\mathbf{Y}}_{\ell,n}(k;\hat{\theta}'') \right|^2 \right\} \tag{4.13}$$

It should be underlined that at the initialisation of the ℓ-th wave the estimates related to $\ell' \geq \ell$ remain equal to 0, i.e. $\hat{\theta}' = [\hat{\theta}_1',\ldots,\hat{\theta}_{\ell-1}',0,\ldots,0]$. From (4.12) and (4.13) it can be conjectured that the ToA is calculated via coherent summation across all antenna elements while the AoA via coherent summation across only the transmit elements.

4.3.2 Determination of the model order-SIC technique

A critical issue in the area of parameter estimation algorithms is the determination of the model order or, in other words, the number of impinging signals that lie above the noise floor. This is widely referred to as the detection problem and has been extensively addressed over the last decades. Two information theoretic criteria are usually deployed thanks to their simplicity: the Akaike information criterion (AIC) [155] and the minimum descriptive length (MDL) [156]. The main drawback of these schemes is that they almost collapse when highly correlated signals are present. Further, they are mostly applicable to scenarios where the number of signals is less than the number of antenna elements. In realistic wireless channels though, both assumptions are usually violated. The same observations infer from [26], where real-life MIMO measurement data was used and it turned out that these information theoretic criteria are insufficient.

In order to circumvent these constraints, the detection problem has been incorporated within the initialisation stage; the SIC technique is applied until the detected paths have power levels relative to the strongest path below a threshold. This can either be a constant value for synthetic environments or the dynamic range of the sounder for measured channels.

4.4 Performance evaluation of the 3D FD-SAGE algorithm

The performance of the 3D FD-SAGE algorithm is firstly evaluated in a synthetic environment by means of Monte-Carlo simulations. Here a predefined number of impinging plane waves with known parameters is used. For generating a rich scattering propagation scenario, a high number of MPCs and an extended delay range to account for the multiple long-delayed echoes are needed. The Tx employed a ULA with $M = 8$ elements with an inter-element distance of $d_t = \lambda/2$ while the Rx an eight-element Uniform Circular Array (UCA) with a radius of $\lambda/2$. For these two configurations, the array responses are

$$\mathbf{a}_r(\phi_r) = \left[\exp\left(j\pi\cos(\phi_r)\right), \ldots, \exp\left(j\pi\cos\left(\phi_r - \frac{2\pi(M-1)}{M}\right)\right)\right]^T \quad (4.14)$$

$$\mathbf{a}_t(\phi_t) = \left[1, \exp\left(j2\pi d_t\cos(\phi_t)\right), \ldots, \exp\left(j2\pi d_t(N-1)\cos(\phi_t)\right)\right]^T \quad (4.15)$$

The number of frequency bins was set equal to $N_f = 193$ with an operating bandwith of 240 MHz to provide a satisfactory resolution in the temporal domain (4.16 ns). The complex amplitude, β_ℓ, was assumed to be an independent zero-mean complex Gaussian RV while the ToA, τ_ℓ, was randomly and independently chosen from a uniform distribution in $[0, 800]$ ns; similarly, the azimuth DoA, $\phi_{r,\ell}$, and DoD, $\phi_{t,\ell}$, were chosen from a uniform distribution in $[0, 180]^\circ$. Finally, white complex Gaussian noise was added to the transfer matrix, according to (4.2) with an input SNR of 20 dB. The actual as well as the estimated paths' parameters are tabulated in Table 4.1 and Table 4.2, respectively. It is evident that the algorithm yields a remarkable accuracy for the great majority of paths. As anticipated, paths will be precisely estimated only when their characteristics differ by the intrinsic resolution of the corresponding domain. The ToA estimates are more precise than the angular estimates due to the increased resolution of the temporal domain; this accounts also for the lobes of the temporal cost functions to be narrower and is also consistent with the results presented in [148, 154].

Apart from the operating SNR, the algorithm's performance is heavily dependent on the number of paths lying within the dynamic range. For higher values of L the arrays fail to accurately capture all MPCs due to their finite aperture. To further justify this statement, the root-mean squared errors (RMSE) of all the paths' parameters as a function of L has been computed with the results being shown in Table 4.3.

Path no. ℓ	Actual ToA, τ_ℓ [ns]	Actual AoA, $\phi_{r,\ell}$ [°]	Actual AoD, $\phi_{t,\ell}$ [°]	Actual power, $\lvert\beta_\ell\rvert^2$ [dB]
1	515.45	35.05	107.08	-21.69
2	302.88	40.66	47.19	-23.16
3	649.26	30.72	108.51	-24.42
4	426.26	40.97	128.01	-24.72
5	280.58	78.42	39.91	-25.23
6	751.20	55.99	21.13	-27.90
7	700.75	166.20	53.41	-28.33
8	440.12	77.43	57.38	-29.77
9	497.98	33.26	76.35	-31.69
10	469.63	162.87	91.41	-31.93
11	166.19	176.35	15.39	-32.61
12	240.99	78.99	47.24	-34.21
13	376.73	20.01	144.18	-36.06
14	184.39	46.45	5.25	-38.90
15	675.44	73.56	167.19	-41.85

Table 4.1: *Actual channel parameters for $L = 15$ paths.*

Path no. ℓ	Estimated ToA, $\hat{\tau}_\ell$ [ns]	Estimated AoA, $\hat{\phi}_{r,\ell}$ [°]	Estimated AoD, $\hat{\phi}_{t,\ell}$ [°]	Estimated power, $\lvert\hat{\beta}_\ell\rvert^2$ [dB]
1	515.53	35.06	107.01	-21.75
2	302.84	40.82	47.18	-23.13
3	649.25	30.68	108.49	-24.41
4	426.24	40.92	128.00	-24.71
5	280.56	78.42	39.88	-25.22
6	751.17	55.93	21.13	-27.88
7	700.74	166.16	53.38	-28.32
8	440.14	77.45	57.39	-29.76
9	497.99	33.18	76.24	-31.71
10	469.62	162.76	91.45	-31.96
11	166.18	175.77	15.54	-32.60
12	240.97	78.97	47.32	-34.22
13	376.75	20.11	144.14	-36.04
14	184.37	46.31	4.04	-38.84
15	675.47	73.58	166.85	-41.94

Table 4.2: *The 3D FD-SAGE estimated channel parameters for $L = 15$ paths.*

No. of paths, L	RMSE ToA, [ns]	RMSE AoA, [°]	RMSE AoD, [°]
10	0.07	0.34	0.91
20	0.13	0.85	1.36
30	1.73	2.67	8.12
40	12.5	5.04	9.51
50	47.3	14.6	19.4

Table 4.3: *RMSEs of simulated SAGE parameters.*

4.5 Channel characterisation in the double directional domain

The performance of the 3D FD-SAGE algorithm is now assessed by post-processing the raw data obtained from the indoor measurement campaign described in Section 3.1. While the algorithm has been developed on the joint spatio/temporal domain, the limited sounder's delay resolution of 8.3 ns allows a very limited path separation (i.e. path length difference equals 2.49 m or approximately 43 wavelengths at 5.2 GHz) in the delay domain and therefore only the joint AoA/AoD domain is investigated.

Following [88], 150 random realisations of the measured (8×8) channel transfer matrix $\mathbf{H}$ were selected and for each realisation the SAGE algorithm is executed. This value not only allows a fair comparison with the results presented in [88] but also satisfies the tradeoff between a low computational burden and a sufficiently large subset of the data ensemble (25,090 realisations in total). Besides, a further increase in the subset size was found to lead to no dramatic changes in the final estimation results (less than 0.5° in all cases).

At the initialisation stage, the SIC technique was employed until the signal's power became smaller than -20 dB relative to the strongest peak so that all dominant MPCs in the received signal could be extracted. Please note that the study presented in the following section is performed in terms of multipath clustering, azimuth dispersions and inter-dependency between the azimuth domains.

4.5.1 Cluster identification

The next step of channel characterisation involved cluster identification on the joint AoA/AoD spatial domain based on the SAGE estimates. Unfortunately, the widely used clustering algorithms require that the number of clusters is specified by the user which is inappropriate in

the considered case [157]. As in [85], the author resorted to the use of non-parametric kernel density estimates (KDEs), which are flexible and robust, for jointly identifying the clusters. In general, KDE techniques are employed for associating a smooth non-parametric estimate of the unknown PDF with an arbitrary collection of observations. For bivariate data points, the two dimensional (2-D) KDE $\widehat{f}(x_1, x_2)$ is given by

$$\widehat{f}(x_1, x_2) = \frac{1}{N_p} \sum_{i=1}^{N_p} \frac{1}{h_1 h_2} \mathcal{K}\left(\frac{x_1 - x_{1,i}}{h_1}, \frac{x_2 - x_{2,i}}{h_2} \right) \tag{4.16}$$

where N_p denotes the number of random observations, $\mathcal{K}(x, y)$ is the kernel function and h_1 and h_2 are the kernel widths (or bandwidths) of the two dimensions. The smoothness of the estimator is primarily determined by the selection of the kernel widths and also by the choice of the kernel function. For the ease of computation, a bivariate Gaussian kernel function is introduced where

$$\mathcal{K}(x_1, x_2) = \frac{1}{2\pi} \exp\left\{ -\frac{x_1^2 + x_2^2}{2} \right\}. \tag{4.17}$$

The concept of bandwidth selection has recently gained considerable attention since if the values of h_1 and h_2 are too large, we end up with oversmoothing phenomena which remove the key features of the underlying distribution. An excellent review of the most frequently used methods can be found in [158]. While there is no overall best method for automatic bandwidth selection, the direct-plug-in (DPI) method, originally proposed in [159], was adopted due to the following advantages

- It yields optimal asymptotic performance, that is the asymptotic rate is $N_p^{-1/2}$.
- For large sample sizes the strength of the plug-in estimator grows.

On the other hand, a potential disadvantage rests in the intrinsic sensitivity of the PI bandwidth to the choice of the so-called auxiliary bandwidths which may result in bias instability [160]. Taking into account that the weaker components may have negligible influence on the calculation of statistical spreads but can introduce unavoidable errors when calculating PDFs such as for the number of clusters, only the $N_p = 1000$ AoA/AoD pairs exhibiting the largest gain amplitudes were used through the cluster identification process. In order to get an understanding of the identification process[4], a scatter plot showing the joint AoA/AoD SAGE estimates is depicted in Fig. 4.2(a) (location 24D2). The corresponding joint density plot after being

[4]The software implementation of KDE was obtained from [1].

processed by the two-dimensional (2D) KDE technique can be seen in Fig. 4.2(b) with the circles corresponding to the identified clusters. The reader can observe that clusters become far more obvious after the KDE procedure and can be easily determined by visual inspection. The estimated number of clusters is tabulated in Table 4.4 (columns 2-4); a mean number of 6.875 is found compared to 8.8 in [88]. This difference can be attributed to the constraint of no overlapping clusters imposed by the authors therein which is relaxed in the present work. This limitation may generally lead to an overestimation of the number of clusters since in realistic channels clusters are not always clearly separated and therefore they are likely to overlap.

4.5.2 Global parameters of the spatial domains

In this section, the main focus is on the global spatial parameters and the effects these have on the ergodic capacity. The first comprehensive study of azimuth dispersion can be found in [161] and its extension in [162]. The authors considered different outdoor scenarios and examined the level of temporal and azimuth dispersion as well as the degree of correlation between them. Similar work was also reported in [163], [164] and [165]. However, all these studies were limited to the joint spatio-temporal dispersion and therefore disregarded the spatial activity at the transmit side. Recently, the dispersion experienced at the Tx in an outdoor-to-indoor channel has been addressed [166], but the authors focused on the intra-cluster (within clusters) properties which implies that the formulation of a broader channel description was beyond their scope.

4.5.2.1 Angular dispersion

It is widely known that the beneficial effects of MIMO technology can be severely limited by spatial correlation at both ends of the radio link, that is the signal correlation between the antenna elements [59]. The degree of spatial correlation is inversely related to the spatial dispersion usually characterised by the rms azimuth spread, i.e. the root second central moment of the APS

$$\phi_{t,rms} = \sqrt{\frac{\sum_{\ell=1}^{L} P_{\phi_t}(\ell) \cdot \phi_t(\ell)^2}{\sum_{\ell=1}^{L} P_{\phi_t}(\ell)} - \frac{\left(\sum_{\ell=1}^{L} P_{\phi_t}(\ell) \cdot \phi_t(\ell)\right)^2}{\left(\sum_{\ell=1}^{L} P_{\phi_t}(\ell)\right)^2}} \tag{4.18}$$

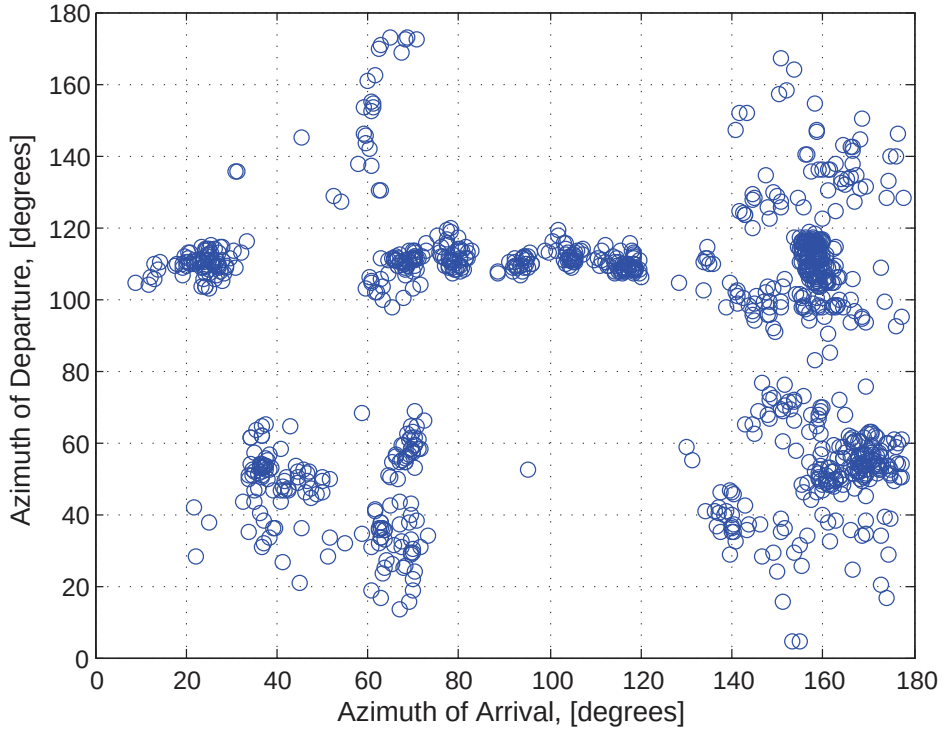

(a) Scatter plot of MPCs AoA-AoD as obtained from the SAGE algorithm.

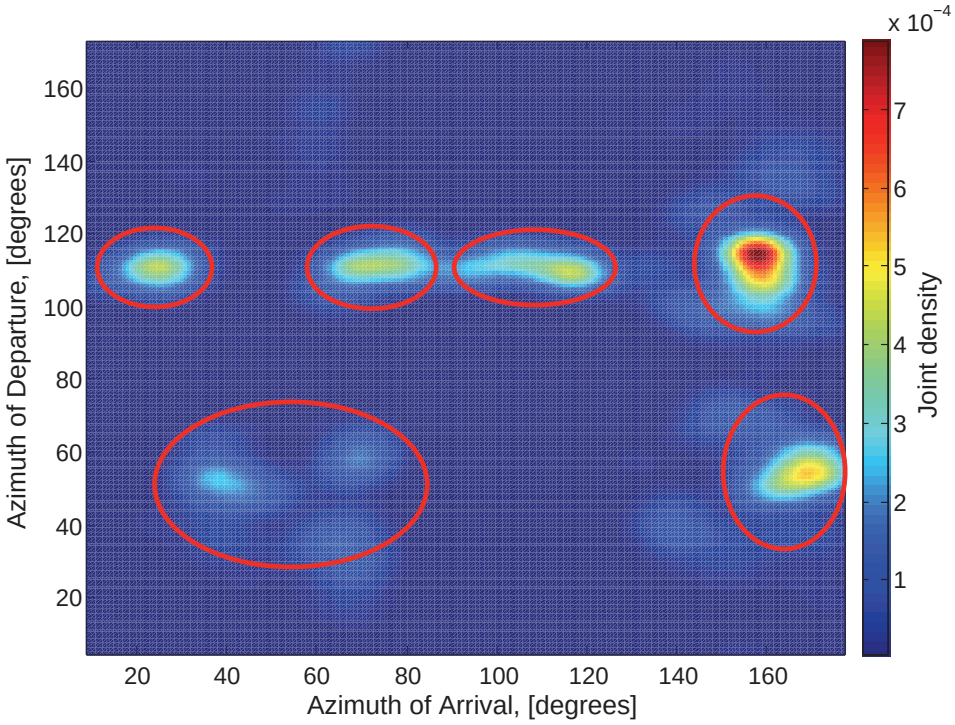

(b) Joint density distribution after being processed by the 2-D KDE with the red circles showing the identified clusters.

Figure 4.2: *Cluster identification using the 2-D KDE procedure (location 24D2).*

where $P_{\phi_t}(\ell)$ is the power of the ℓ-th MPC in the transmit APS. The same notation holds for the receive side. The obtained CDFs for a LoS (17D1) and an NLoS (16D2) location can be seen in Fig. 4.3(a) and Fig. 4.3(b), respectively. A lognormal distribution is fitted to the empirical data and plotted for comparison since it was found that it yields an accurate match for the great majority of the considered scenarios. This implies that the azimuth spread can be directly described by the density

$$f(x) = \frac{1}{x\sigma_t\sqrt{2\pi}} \exp\left(-\frac{(\ln x - \mu_t)}{2\sigma_t^2}\right) \tag{4.19}$$

where $\mu_t = E\{\ln(\phi_{t,rms})\}$ and $\sigma_t = \text{std}\{\ln(\phi_{t,rms})\}$. It should be remembered that the lognormal distribution is also adopted by different standardisation bodies, such as 3GPP and COST 273, as an effective means to model global azimuth spreads [107, 116].

From Fig. 4.3, the reader can notice the excellent fit for the AoA spread while the AoD spread exhibits a slight deviation from the lognormal CDF, especially for the NLoS case. This can be attributed to the so-called transmit bimodal angular distribution which occurs at all Tx locations close to the Rx (locations 13-16) and violates the single mode assumption that lies behind the power normality on the exponential scale. In physical terms, the OLoS component and the back-wall reflections contribute to the creation of two separate regions (modes) across the transmit spatial domain; this phenomenon is clearly illustrated in Fig. 4.4 where an AoD histogram for location 14D3 has been plotted. At the Rx though, due to the highly cluttered environment in which it is situated, this effect becomes very weak and therefore the AoAs are more evenly distributed across the azimuth domain.

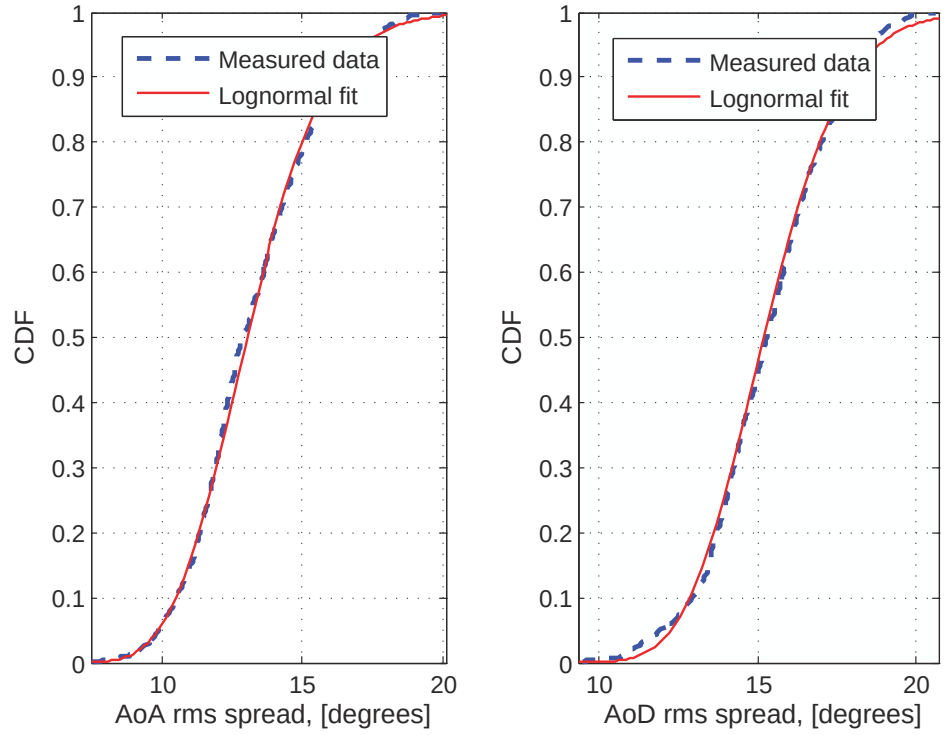

(a) LoS location (17D1).

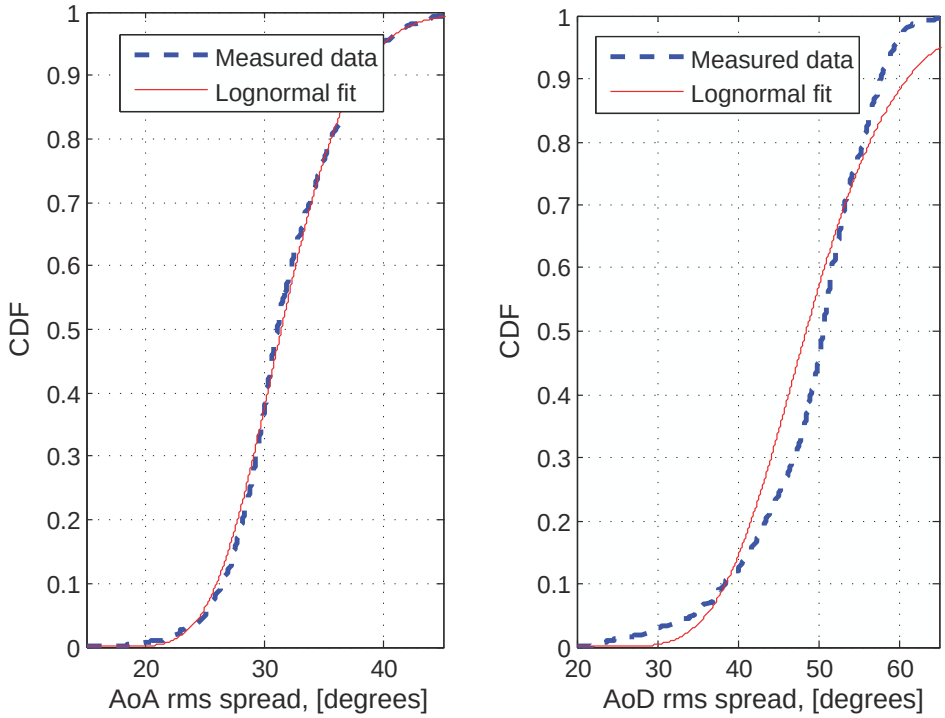

(b) NLoS location close to the Rx (16D2).

Figure 4.3: *Empirical azimuth rms spreads and best fit lognormal distributions for two different Rx locations.*

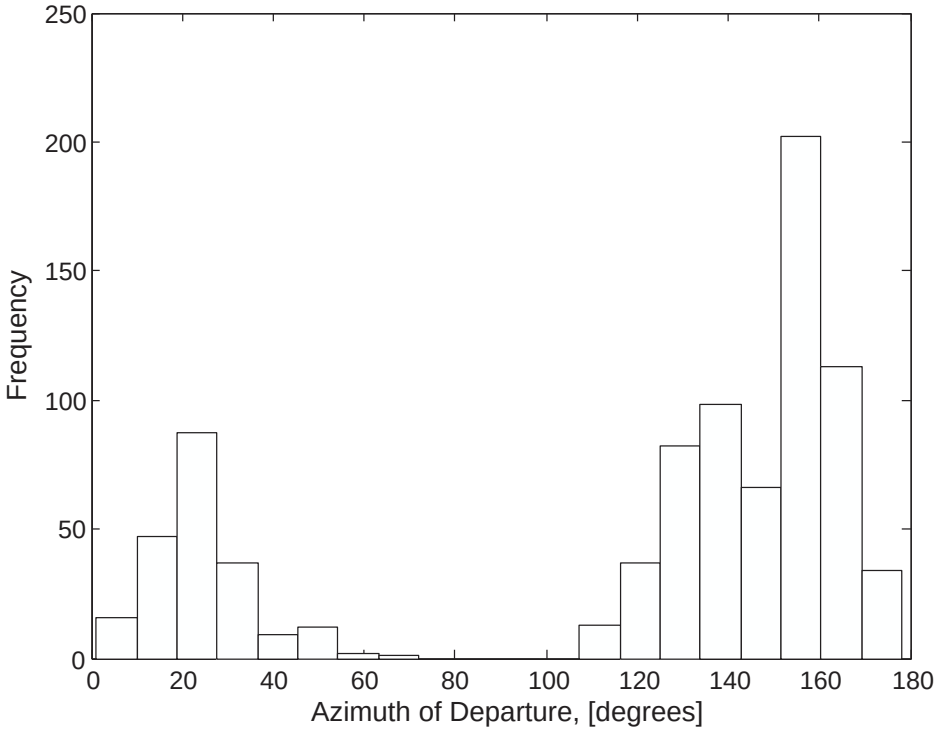

Figure 4.4: *Histogram of measured AoDs for location 14D3 showing the bimodal distribution across the transmit azimuth domain.*

4.5.2.2 Correlation between the angular domains

A correlation study was also performed in order to investigate whether the mechanisms leading to spatial dispersion at the two ends are similar. The spatial correlation coefficient between the azimuth spreads was calculated for each measurement scenario according to

$$\rho_{\phi_t,\phi_r} = \left| \frac{\sum_{p=1}^{150} \left(\phi_{t,rms}(p) - \overline{\phi}_{t,rms}\right)\left(\phi_{r,rms}(p) - \overline{\phi}_{r,rms}\right)}{\sqrt{\sum_{p=1}^{150} \left(\phi_{t,rms}(p) - \overline{\phi}_{t,rms}\right)^2 \sum_{p=1}^{150} \left(\phi_{r,rms}(p) - \overline{\phi}_{r,rms}\right)^2}} \right|, \quad \rho_{\phi_t,\phi_r} \in [0,1] \quad (4.20)$$

where $\overline{\phi}_{t,rms}$, $\overline{\phi}_{r,rms}$ are the average values of the transmit and receive azimuth spreads respectively. All obtained values are shown in Table 4.4 (columns 5-13). Analysis of the measurement results revealed a high correlation at LoS (17) and OLoS locations (13D1, 14D3, 23D3, 24D3) where the Tx-Rx distance is low and the Tx faces the Rx[5]. This is anticipated since the direct dominant component is followed by multiple reflections which all follow a similar route thereby

[5]For illustrative purposes, the values obtained at LoS locations are depicted in heavy-gray coloured cells while the Tx facing the Rx cases in light-gray coloured cells.

leading to a high correlation. The dependency of the spatial domains in the LoS case can be regarded as a counterpart of the high correlation between the spatio-temporal domains (again under LoS conditions) as documented in [85, 165] (for more details please see Section 2.5.1.3). On the contrary, at the vast majority of NLoS locations the dominant path vanishes and the degree of correlation is relatively low; under these circumstances, the propagation mechanisms have become far more complex (multiple-order reflection, diffraction and scattering) and the impinging paths follow different routes reducing the dependency of the two domains.

As far as the mean azimuth spread is concerned, a number of interesting conclusions can been drawn. Firstly, the LoS and OLoS locations exhibit the lowest dispersion, indicating a lower spatial decorrelation, as the dominant paths mask the scattered waves making them lie within the noise region; that is, the lower power paths are not observable and hence did not contribute to the global azimuth spread. The Rx locations in the vicinity of the outer wall (such as 9D1, 12D1, 16D1, 18D1, 18D2, 20D1, 22D1, 22D2, 25D2) yield very high values of AoA spread because of the weak high-order waves which bounce off the surrounding walls. For the AoD dispersion, its large values at locations 14-16 are due to the bimodal energy distribution as was previously mentioned. In general, the receive azimuth spread is higher than the transmit spread at 51 out of the 72 considered scenarios (71.8% of the cases). The AoA spread ranges between 11 and 56 degrees whereas the AoD spread between 10 and 51 degrees. One explanation suggests that the transmitted energy is confined within a region around the direct Tx-Rx path while the received multipath activity is spread over the whole azimuth domain. This means that the transmitted waves create a single or at most two clusters under the bimodal conditions and hence the values of the transmit spread are normally lower than those of the receive spread. In any case though, the obtained values are well above the ones reported in the corresponding literature from measurements at a base station mounted above rooftops [161, 162]; this is a direct consequence of the low antenna heights and closer proximity of local scatterers.

4.5.2.3 Effects on ergodic capacity

In Fig. 4.5 and Fig. 4.6, the ergodic capacity, as calculated by (2.17), has been plotted against the spatial parameters of interest, i.e. the azimuth spreads and the correlation coefficient between them. Normally, low angular spreads cause a decrease in MIMO capacity since they diminish the advantages of multipath propagation causing the rank-deficiency of the channel matrix [59]. Clearly, a consistent observation can be made for the measured data set under investigation; the

Rx	No. of clusters			$\overline{\phi}_{r,rms}$ [°]			$\overline{\phi}_{t,rms}$ [°]			ρ_{ϕ_t,ϕ_r}		
locat.	D1	D2	D3	D1	D2	D3	D1	D2	D3	D1	D2	D3
1	4	6	5	21.9	44.2	26.2	23.3	21.2	22.5	0.13	0.17	0.36
2	6	6	7	21.0	46.9	29.8	28.6	23.7	19.7	0.08	0.35	0.57
3	5	8	7	15.3	42.3	44.4	28.3	23.3	30.3	0.17	0.21	0.11
4	5	8	8	30.4	50.2	26.2	26.3	26.2	19.6	0.27	0.01	0.58
5	6	7	6	11.4	45.2	35.0	32.3	27.4	26.9	0.25	0.11	0.23
6	6	7	7	40.1	40.8	29.5	28.1	24.8	23.9	0.42	0.19	0.48
7	6	7	9	34.2	39.9	27.5	31.3	24.8	23.3	0.06	0.52	0.56
9	7	8	8	50.8	33.9	27.8	31.1	25.1	26.1	0.21	0.26	0.21
10	8	6	10	21.4	52.6	37.3	20.3	17.2	17.5	0.52	0.30	0.12
12	7	7	8	43.4	19.1	19.5	17.9	17.0	15.7	0.23	0.14	0.32
13	7	7	7	11.6	54.6	50.1	17.0	45.6	31.8	0.61	0.22	0.25
14	7	8	7	27.2	47.1	13.0	45.3	51.2	33.8	0.53	0.05	0.51
15	7	7	6	29.8	37.0	27.8	40.6	47.8	42.5	0.33	0.03	0.15
16	9	6	7	45.1	31.4	23.6	47.1	48.5	49.3	0.42	0.16	0.18
17	9	5	6	13.0	35.2	31.4	14.9	11.0	10.2	0.65	0.42	0.47
18	7	7	9	56.8	49.0	30.3	15.4	12.4	16.3	0.35	0.66	0.40
19	4	10	4	26.5	51.5	31.1	14.5	15.6	11.2	0.58	0.37	0.63
20	5	7	7	42.6	34.3	23.3	25.8	22.6	27.2	0.11	0.48	0.12
21	10	9	4	33.9	43.2	21.3	22.9	27.8	26.0	0.03	0.33	0.34
22	5	9	9	43.3	47.6	30.1	22.6	26.2	24.6	0.14	0.15	0.12
23	9	8	9	40.3	43.5	26.1	21.1	25.4	23.7	0.33	0.03	0.70
24	7	6	4	40.8	39.4	15.2	33.6	29.3	28.2	0.23	0.31	0.79
25	5	7	3	34.1	46.9	21.2	34.0	39.6	38.1	0.38	0.17	0.22
26	5	8	8	40.8	37.1	24.0	31.8	37.9	39.1	0.41	0.04	0.34

Table 4.4: *Spatial characteristics at all Rx locations and orientations. The heavy and light-gray colored cells correspond to LoS and OLoS locations respectively.*

effects of azimuth spread on capacity are more pronounced at the receive side where $\overline{\phi}_{r,rms}$ and $\overline{C}$ behave in a more correlated way than $\overline{\phi}_{t,rms}$ and $\overline{C}$ do. From a statistical viewpoint, the correlation between $\overline{\phi}_{r,rms}$ and $\overline{C}$ is 0.5518 while between $\overline{\phi}_{t,rms}$ and $\overline{C}$ is 0.1574.

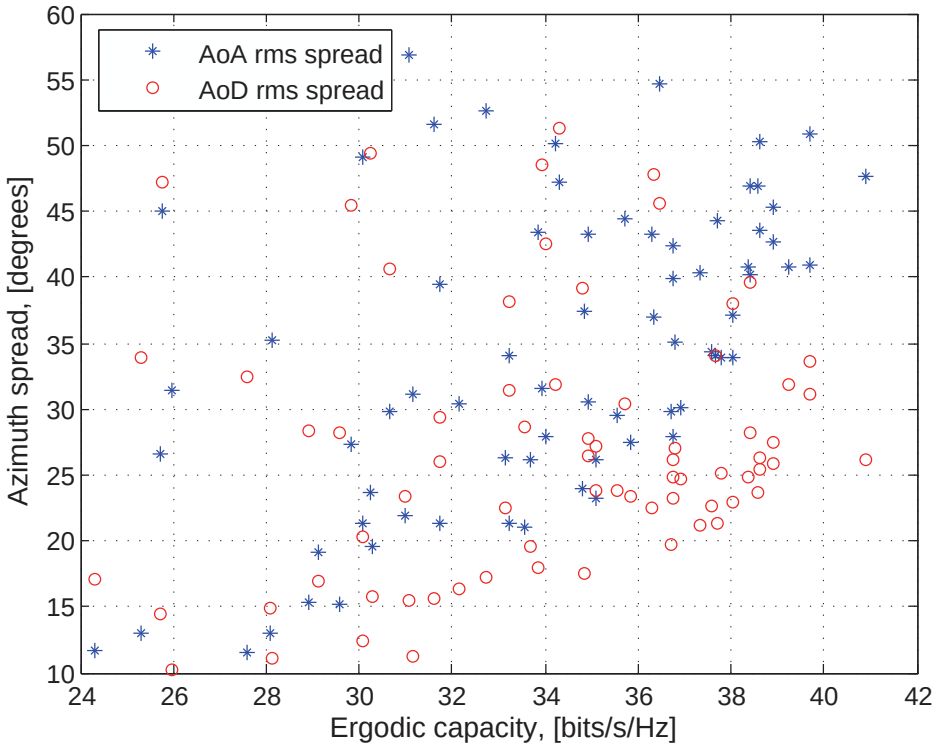

Figure 4.5: *Ergodic capacity as a function of the mean rms azimuth spreads* $\overline{\phi}_{t,rms}$ *and* $\overline{\phi}_{r,rms}$.

This trend may be attributed to the fact that the values of transmit azimuth spreads are slightly misleading due to either the bimodal distribution or near-field scattering effects which artificially increase them. This means that high transmit spreads are not always indicative of high multipath activity and therefore do not always lead to larger MIMO capacities. Similarly, an increase in dependency between the spatial domains leads to a decrease in the ergodic capacity. The relatively small number of deviations from this general trend can be attributed to strong OLoS components which raise the total received power level but, at the same time, contribute to a high degree of correlation. For practical systems, large angular spreads have a beneficial effect on MIMO capacity by enriching the SM potential (higher number of orthogonal subchannels) while independence of the two angular domains leads to an improvement in the spatial diversity of the MIMO link (high reliability).

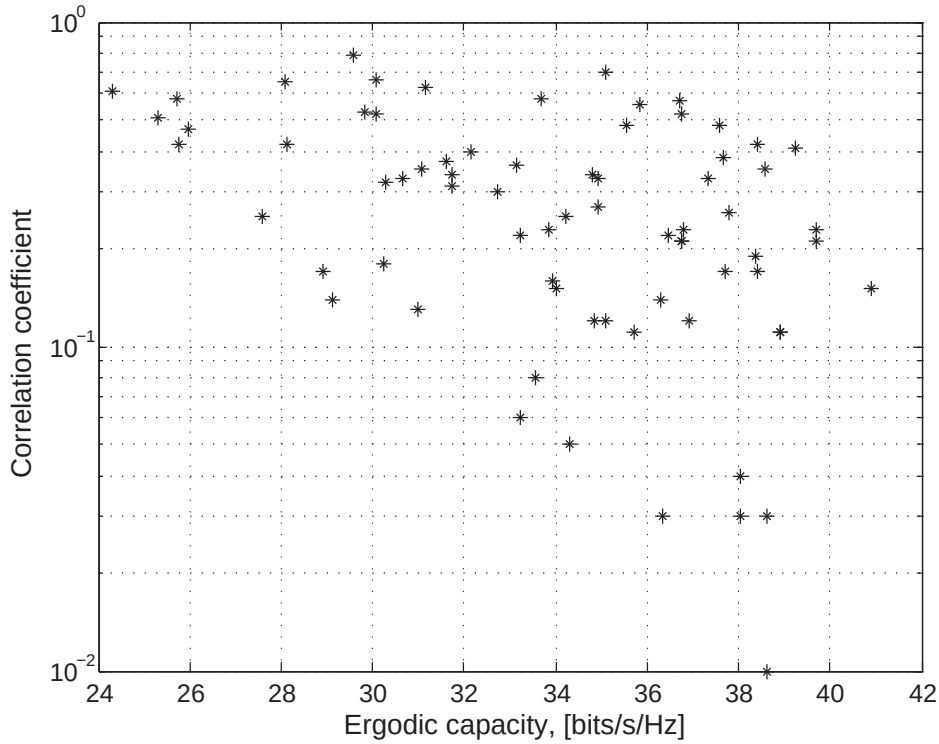

Figure 4.6: *Ergodic capacity as a function of the spatial correlation coefficient* ρ_{ϕ_t,ϕ_r}.

4.6 Limitations of the SAGE algorithm

So far, only the advantages offered by the SAGE algorithm have been addressed. However, there are some concomitant deficiencies of this framework which are summarised below. The first shortcoming lies in the identification of the diffuse scattering phenomena which occur when the MPCs are closely distributed around a local region forming a cluster of rays with very similar temporal characteristics and small angular spread. The author restates herein the fundamental point-source assumption which suggests that the radio channel can be regarded as the superposition of a finite number of specular propagation paths. However, realistic radio channels contain not only concentrated propagation paths, but also an amount of MPCs resulting from distributed diffuse scattering. When the size of the cluster is smaller than the resolution of the corresponding domain, the MPCs within a cluster can not be resolved and only the nominal direction is tracked; when the cluster size is larger than the intrinsic system's resolution, only a few dominant MPCs will be identified. In both cases though, the contributions of MPCs within a cluster are not fully removed and thus the update process is prone to interference from residual energy from the detected components (error propagation) [167].

The alleviation of this problem has been addressed separately in [168], where it was shown that the direction estimates are RVs whose distribution depends only on the angular spread of the diffuse scattering, and in [169], where a multivariate circular complex normal distribution was assigned to the diffuse scattered paths. The authors therein suggest the use of the so-called RIMAX algorithm [170, 171] which is essentially an iterative ML parameter estimation scheme based on both multi-dimensional conjugate gradient search and sequential parameter update. In comparison with SAGE, its complexity is drastically reduced especially if the number of paths is smaller than the number of samples and, furthermore, the convergence speed is enhanced as the parameter-wise search is replaced by the faster nonlinear gradient search [116]. The estimation results are the deterministic multi-dimensional parameters of the specular propagation paths as well as the parameters of a simplified model for the diffuse scattered MPCs. The Enhanced SAGE (E-SAGE) scheme is an alternative which estimates only the nominal parameters of the cluster and its spreads [172]. However, the parameters for each of the MPCs within a cluster cannot be estimated due to the limited fundamental resolution of the algorithm. This technique yields better phantom path discrimination as it takes the spread of each cluster into account when implementing the E-step and therefore the relative power difference between the strongest path and the phantom paths is increased (enhanced signal cancellation).

The assumption of far-field conditions may not be always met in practice especially for terminals mounted at low heights (for instance in peer-to-peer communications). In this case, local scatterers are more densely distributed around the terminals leading to near-field scattering, i.e. spherical instead of plane waves are created. In a similar manner, plane waves impinging on a sharp edge are expected to propagate as cylindrical diffracted wavefronts in the 3D space. Due to the high power loss associated with this propagation mechanism though (see Section 2.1), its impact on the performance of estimation algorithms becomes significant only when the diffracting body is in the Rx's vicinity.

From a computational point of view, a limitation exists in the SIC technique which is subject to interference from the uncancelled $\ell + 1$ path as well as the residual components from the previous paths that are not totally removed from the total response. This may lead to inaccurate estimates due to power imbalance. Finally, the complexity level of the SAGE scheme, particularly that of the M-step, necessitates the use of more efficient approaches as the one described in [173]. Due to the iterative nature of the algorithm, applying it to the estimation of superimposed signals can be time consuming and impractical. The long processing time whilst

awaiting convergence, especially in multi-dimensional problems, turns out to be the main algorithm's drawback.

4.7 Summary

The design and performance planning of MIMO systems poses a prerequisite, that is the precise knowledge of the multipath parameters in different selectivity domains. In this chapter, a new multi-dimensional version of the FD-SAGE algorithm has been presented. The channel model under consideration consists of an finite number of plane waves whose temporal and angular parameters need to be defined in the frequency domain. The SIC technique has been incorporated in both the initialisation and the estimation stages, following previous studies which demonstrated its higher reliability compared to the PIC approach in the frequency domain. By generating a synthetic environment the performance of the SAGE algorithm was tested; apart from its excellent accuracy, the scheme offers a high degree of flexibility for any antenna geometry and plus it remains robust in the presence of correlated sources in contrast to the majority of array signal processing algorithms. Nevertheless, paths are resolved only when their characteristics differ by the intrinsic resolution of the temporal and spatial domains.

Using a set of raw measurement data, a detailed characterisation of an indoor MIMO channel was also carried out in the joint AoA/AoD domain. Lower dispersion and higher correlation occur when a LoS is present or when the Tx faces the Rx and the distance between them is low (OLoS propagation) while for NLoS Rx locations, the dispersion is larger and in turn the two spatial domains are decorrelated. The transmit bimodal angular distribution is another interesting phenomenon that artificially increases the AoD spread at Rx locations close to the Tx. The common belief that high angular spreads contribute to high MIMO capacities was verified while the independence of the two azimuth domains seems to have a positive impact on capacity performance.

Finally, the fundamental limitations of the SAGE framework were addressed in the last part of this chapter since they should always be taken into account in the physical interpretation of the algorithm's output. Summarising, this sophisticated version of the SAGE algorithm can be used to work out the propagation conditions of most practical wireless channels and ultimately aid the planning of multiple-antenna systems.

Chapter 5
Statistical characterisation of dual-branch MIMO Ricean systems

While the previous two chapters were devoted to the modelling and characterisation of indoor MIMO systems, the present chapter covers the area of short-range communications which have recently emerged as a hot topic in the area of wireless networks. In the interesting case of VTR propagation, the presence of a LoS component is highly likely especially if the road traffic is sparse and hence there are no obstacles between the two ends; this means that the fading statistics of the channel matrix entries are not Rayleigh but Ricean instead. The first aim of this chapter is to devise a dual-branch architecture able to deliver high MIMO throughput under these LoS conditions. Secondly, a detailed statistical eigenanalysis of these dual-branch MIMO architectures is performed, based on the principles of random matrix theory. The outputs of this analysis are thereafter used to construct an AD that offers a drastic reduction in the complexity and implementation cost of practical MIMO receivers. The remainder of the chapter is organised as follows: In Section 5.1, a design methodology for LoS-optimised MIMO systems is proposed that overcomes the problem of reduced multiplexing gain in LoS conditions with the derived criterion being adapted to a VTR propagation scenario. Section 5.2 elaborates on the eigenvalue and condition number statistical properties of dual-branch MIMO Ricean systems for which closed-form formulae are derived and validated via Monte-Carlo simulations. Section 5.3 exploits these analytical results to develop the aforementioned AD for the usual case of SM-MIMO systems. Finally, Section 5.4 concludes the chapter and summarises the key findings.

5.1 LoS-optimised MIMO systems for VTR communications

While it is greatly accepted that a single LoS path is optimal for SISO systems since it enhances their performance with respect to multipath conditions, these results can not be straightforwardly extended to the MIMO case. Generally, LoS propagation limits the beneficial effects

of MIMO technology because the channel matrix is normally rank deficient due to the linear dependence of the LoS' rays phases on the receive elements. In detail, it has been found that in most LoS scenarios the communication subchannels have almost identical responses and the differentiation of the received signals at the MIMO detector becomes difficult due to the reduced multiplexing gain between the different pairs of transmit and receive elements [174–176]. Consequently, an unavoidably high percentage of erroneously detected transmitted signals occurs. Over the last years though, research in the field of short-range communications revealed that high capacities are still achievable in LoS by appropriate positioning of the antenna elements so that the LoS rays become orthogonal [177–179]. This means that subchannel orthogonality, which is a key condition for capacity maximisation, can be achieved as long as special antenna geometries are employed at both the Tx and Rx [105]. The main disadvantage of the above cited papers though, is the fact that they were tied to fixed communication systems where both terminals are static. Thus, in this section, these results are extended to account for the case of DSRC where a moving car is communicating with a fixed roadside unit; under these circumstances, a LoS-optimised architecture is devised assuming that both ends are equipped with two-element ULAs. The model's equation for MIMO Ricean channels (2.31) is now rewritten for the sake of continuity

$$\mathbf{H} = \sqrt{\frac{K}{K+1}}\mathbf{H}_{\mathrm{L}} + \sqrt{\frac{1}{K+1}}\mathbf{H}_{\mathrm{w}}. \tag{5.1}$$

In the case of free-space propagation, the complex entries of the deterministic component $\mathbf{H}_{\mathrm{L}}$ are of the form $e^{-jkd_{m,n}}/d_{m,n}$, where $k = 2\pi/\lambda$ is the wavenumber corresponding to the carrier wavelength λ and $d_{m,n}$ is the distance between a receive element $m \in \{1,2\}$ and a transmit element $n \in \{1,2\}$. Assuming, without loss of generality, isotropic radiators and negligible differences in the path-losses the normalised free-space matrix component becomes

$$\mathbf{H}_{\mathrm{L}} = \begin{bmatrix} e^{-jkd_{1,1}} & e^{-jkd_{1,2}} \\ e^{-jkd_{2,1}} & e^{-jkd_{2,2}} \end{bmatrix}. \tag{5.2}$$

5.1.1 Maximum LoS MIMO capacity criteria

For a purely deterministic channel ($\mathbf{H} = \mathbf{H}_{\mathrm{L}}$), the instantaneous capacity is also deterministic and depends exclusively on the distances between the antenna elements whereas the corre-

sponding formula is

$$C = \log_2 \left(\det \left(\mathbf{I}_2 + \frac{\rho}{2} \mathbf{H}_{\mathrm{L}} \mathbf{H}_{\mathrm{L}}^{\mathrm{H}} \right) \right). \tag{5.3}$$

As was indicated in Section 2.3.3, the instantaneous capacity is maximised when $\mathbf{H}\mathbf{H}^H = 2\mathbf{I}_2$. For the deterministic case, that is the eigenvalues of the LoS correlation matrix $\mathbf{T} = \mathbf{H}_{\mathrm{L}}\mathbf{H}_{\mathrm{L}}^H$ become equal and therefore we end up with perfectly orthogonal MIMO spatial subchannels, i.e. full-rank matrix. In [178], it was shown that this condition is satisfied when

$$|d_{1,1} - d_{2,1} + d_{2,2} - d_{1,2}| = (2r+1)\frac{\lambda}{2}, \;\; r \in \mathbf{Z}^+ \tag{5.4}$$

where $\mathbf{Z}^+$ is the set of positive integers. In physical terms, the authors therein concluded that the sum of path differences $(d_{1,1} - d_{2,1})$ and $(d_{2,2} - d_{1,2})$ needs to be an odd integer multiple of a half wavelength. While the capacity maximisation criterion (5.4) is expressed as a function of distances between the antenna elements, in practice is awkward since it disregards the array geometries and orientations. A more tractable criterion can be derived by considering the geometry depicted in Fig. 5.1 which is basically a top view of the propagation scenario under consideration, with the car moving on a straight trajectory along the y-axis and both arrays being placed perpendicular to the ground. The distance between the two arrays on the x and y axes are respectively dx and dy whereas the constant height difference is given as dz. A side view of the same scenario is illustrated in Fig. 5.2; an axis rotation by an angle θ has been conducted around the y-axis in order to make the array origins lie on the same axis and ease the post-processing. The coordinates of all elements with regard to the new coordinate system $x'yz'$ have also been included. The inter-element distances are respectively s_1 at the Tx and s_2 at the Rx. The distance between the first element of each array is

$$D = \sqrt{dx^2 + dy^2 + dz^2} \tag{5.5}$$

while the rotation angle θ can be defined as

$$\cos\theta = \frac{\sqrt{dx^2 + dy^2}}{D} \tag{5.6}$$

$$\sin\theta = \frac{dz}{D}. \tag{5.7}$$

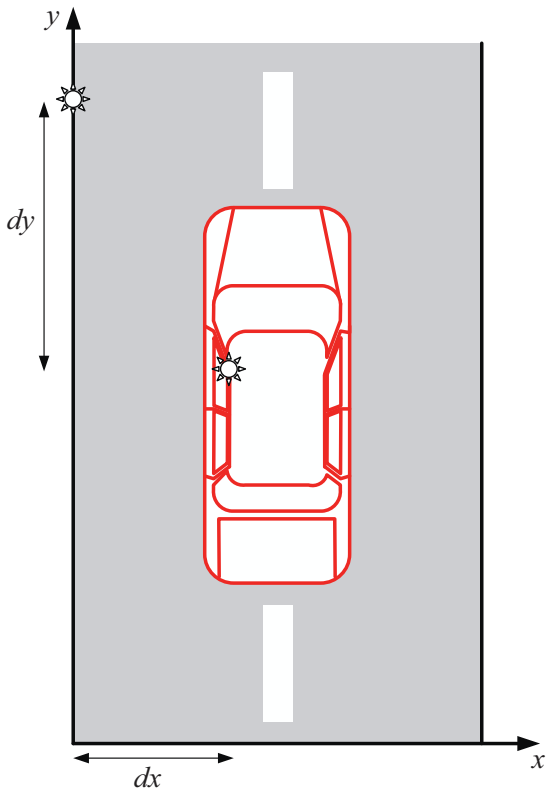

Figure 5.1: *Top view of a vehicle-to-roadside propagation scenario.*

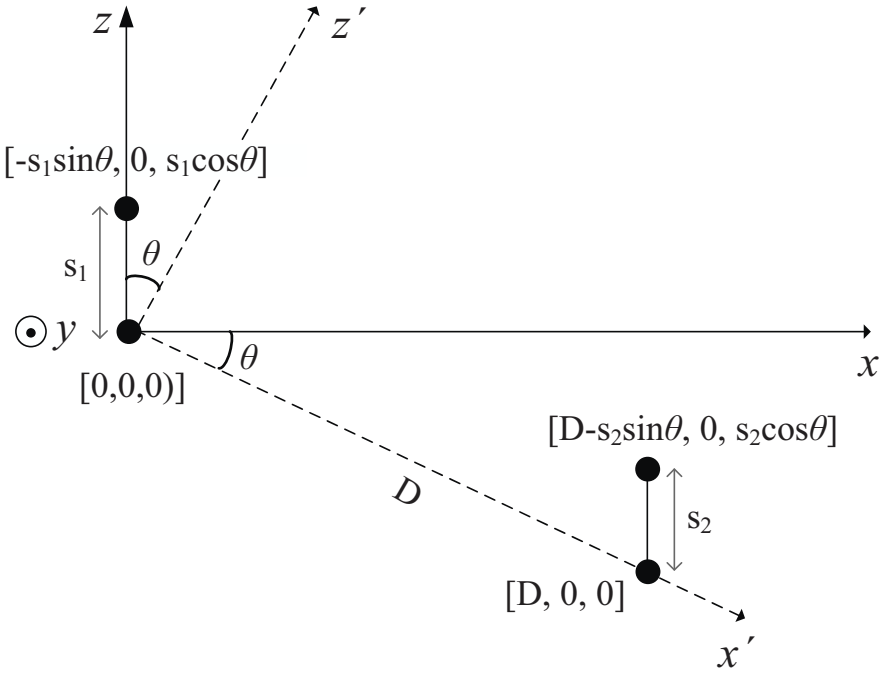

Figure 5.2: *Side view of a vehicle-to-roadside propagation scenario with 2-element ULAs at both ends.*

The Euclidean distances between all antenna pairs are given by

$$d_{1,1} = D \tag{5.8}$$

$$d_{1,2} = \sqrt{(D + s_1 \sin\theta)^2 + (s_1 \cos\theta)^2} \tag{5.9}$$

$$d_{2,1} = \sqrt{(D - s_2 \sin\theta)^2 + (s_2 \cos\theta)^2} \tag{5.10}$$

$$d_{2,2} = \sqrt{(D + (s_1 - s_2)\sin\theta)^2 + ((s_1 - s_2)\cos\theta)^2}. \tag{5.11}$$

As a next step, a Taylor series approximation is introduced in order to simplify the above set of equations

$$\begin{aligned} \sqrt{(D+\mu)^2 + \nu^2} &= (D+\mu)\sqrt{1 + \frac{\nu^2}{(D+\mu)^2}} \\ &\approx (D+\mu) + \frac{\nu^2}{2(D+\mu)}. \end{aligned} \tag{5.12}$$

This approach is sufficiently accurate as long as $(D+\mu)^2 \gg \nu$; this holds true for all practical systems where D is of order of meters while s_1, s_2 are typically of order of centimetres. Then, the Euclidean distances become

$$d_{1,1} = D \tag{5.13}$$

$$d_{1,2} \approx D + s_1 \sin\theta + \frac{(s_1 \cos\theta)^2}{2(D + s_1 \sin\theta)} \tag{5.14}$$

$$d_{2,1} \approx D - s_2 \sin\theta + \frac{(s_2 \cos\theta)^2}{2(D - s_2 \sin\theta)} \tag{5.15}$$

$$d_{2,2} \approx D + (s_1 - s_2)\sin\theta + \frac{((s_1 - s_2)\cos\theta)^2}{2(D + (s_1 - s_2)\sin\theta)}. \tag{5.16}$$

A further simplification is easily achieved if the denominators in (5.14)–(5.16) are approximated by $2D$. Once more, the error introduced is negligible. By replacing (5.13) and modified (5.14)–(5.16) into (5.4), the simplified maximum capacity criterion can be written as

$$s_1 s_2 \approx \lambda \left(r + \frac{1}{2}\right) \frac{D}{\cos^2\theta}, \quad r \in \mathbf{Z}^+. \tag{5.17}$$

This formula is now a function of the inter-element distances, Tx-Rx distance, orientation of the arrays and carrier frequency. In general, larger distance requires larger antenna spacings while higher frequency requires smaller antenna spacings. For fixed frequency and Tx-Rx distance, the arrays can be designed so that subchannel orthogonality is attained.

5.1.2 Capacity variations

Although the derived criterion is simple, it does not take into account possible deviations from the optimum values which are always present in realistic propagation environments due to either design inaccuracies or positioning displacements. What's more, most practical applications are designed to operate within a coverage area rather than between fixed points. In this section, the capacity of configurations fulfilling the criterion (5.17) is tested under a range of more practical conditions, such as the displacements from optimal positions and the presence of multipath scattering.

5.1.2.1 Displacement effects

For the assumed scenario, the receive array is not fixed at a specific position but its location changes constantly with the car motion. The performance of the proposed scheme is firstly evaluated by means of displacement from an optimal point within an area of interest. Let's assume the optimal point to occur when $dx = 5$ m, $dy = 0$ and $dz = 2$ m ($D_{\text{opt}} = 5.3852$ m and $\theta_{\text{opt}} = 21.8°$). These are typical values of a short-range peer-to-peer propagation scenario where one terminal is mounted well below rooftops. The carrier ITS frequency is 5.9 GHz and the SNR ρ is set to 20 dB. Using the solution of equal inter-element spacing, the minimum optimal spacing for the full-rank model (i.e. the solution of (5.17) for $r = 0$) returns $s_1 = s_2 = 39.85$ cm. At this point, capacity reaches its maximum value which is $C_{\text{max}} = 2\log_2(1+\rho) = 13.32$ bits/s/Hz. The LoS component of this optimised configuration is[1]

$$\mathbf{H}_{\text{L}}^{opt} = \begin{bmatrix} 0.8384 + j0.5451 & 0.9074 - j0.4202 \\ 0.0160 - j0.9999 & 0.8384 + j0.5451 \end{bmatrix}. \tag{5.18}$$

with the two eigenvalues of $\mathbf{T}^{opt}$ being equal to 2. The sensitivity of the proposed orientation to displacements from the optimal point on the $x-y$ plane can now be addressed. The considered area is determined as $0 \leq D_x \leq 15$ m and $-50 \leq D_y \leq 50$ m where D_x, D_y are the displacements on the corresponding axes. The variations of capacity are illustrated in Fig. 5.3. It is easily seen that the system capacity is highly sensitive to displacements in the direction of y-axis whereas it seems to be less susceptible to displacements in the direction of x-axis (smaller dynamic range). As anticipated, when the car is passing by the infrastructure unit ($D_y = 0$) the largest capacity values are observed. For the range $-20 \leq D_y \leq 20$ m, which

[1]The subscripts *opt*, *subopt* and *conv* respectively stand for optimal, suboptimal and conventional configurations.

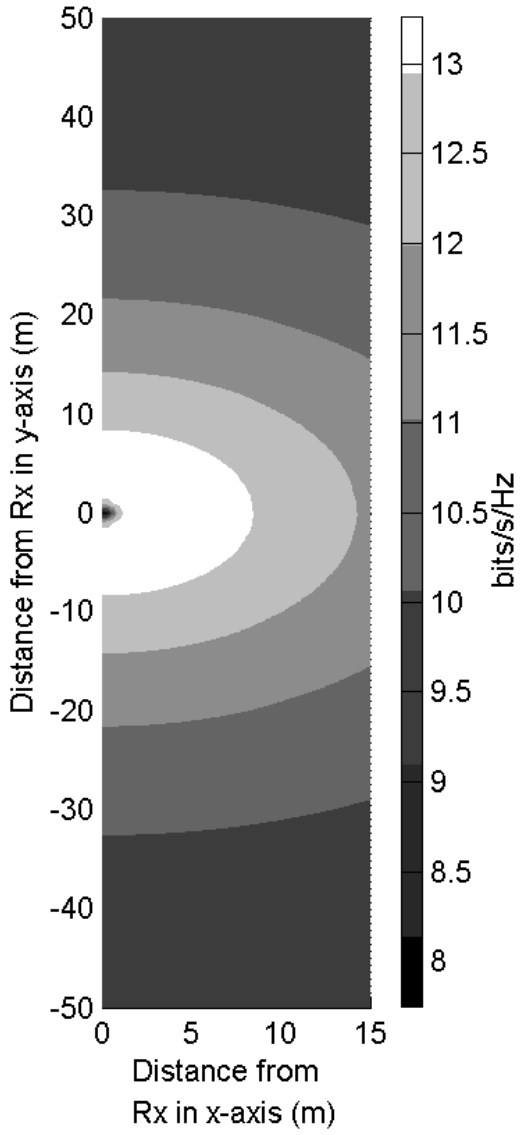

Figure 5.3: *Capacity variation against displacement on the $x - y$ plane.*

corresponds to a total area of $40 \times 15 = 600$ m^2, the proposed scheme delivers high capacities and outperforms the i.i.d. Rayleigh system which yields an ergodic capacity of 11.4 bits/s/Hz at the same operating SNR.

5.1.2.2 Scattering effects

So far, only a deterministic channel has been considered and for this reason free-space propagation is the only propagation mechanism. This assumption is fairly valid for short ranges where the LoS component is expected to dominate over the scattered paths (high K-factor). In practice though, some degree of scattering is always present due to the interaction of the transmitted signal with the physical environment as it travels towards the Rx. For a multipath MIMO channel, the channel matrix $\mathbf{H}$ becomes a stochastic fading process making capacity become a RV as well. A total set of 50,000 Monte-Carlo realisations of $\mathbf{H}$ is acquired from (5.1) using the same fixed optimum settings for the LoS matrix $\mathbf{H}_{\mathrm{L}}^{opt}$ as before. The effects of the K-factor on channel capacity are depicted in Fig. 5.4(a). For the specific full-rank geometry, the monotonic capacity increase with the K-factor as well as the enhanced diversity performance (steeper CDF curves) are of paramount significance. In fact, this behaviour contradicts the common belief that higher K-factors, which induce stronger deterministic components, lead to higher correlation and thus lower capacity; in strong LoS conditions the proposed configuration systematically outperforms most conventional architectures. These results are in line with those presented in [177–179]. To shed some light on this phenomenon, a conventional LR architecture with $s_1 = s_2 = 0.5\lambda$ and arrays in the far-field region, is also examined. This implies that the LoS signals propagate as plane wavefronts whose phases are highly correlated and therefore $\mathbf{H}\mathbf{H}^H = 2\mathbf{1}_2$. The LoS matrix component then becomes

$$\mathbf{H}_{\mathrm{L}}^{conv} = \begin{bmatrix} 0.8384 + j0.5451 & 0.8272 - j0.5618 \\ -0.1653 + j0.9862 & 0.8384 + j0.5451 \end{bmatrix}. \tag{5.19}$$

whereas the eigenvalues of $\mathbf{T}^{conv}$ are $(4, 4, 08 \times 10^{-5})$. A completely inverse trend is now observed in Fig. 5.4(b) with the presence of a LoS path cancelling off the MIMO advantages. In the low K-factor regime though, the capacity performance of both systems becomes identical while in the limit ($K \to -\infty$ dB) the LoS component vanishes and we end up with a pure i.i.d. Rayleigh channel, regardless of the antenna element positions. On the other hand, in the limit ($K \to \infty$ dB), the conventional configuration degenerates into a single-path MIMO link.

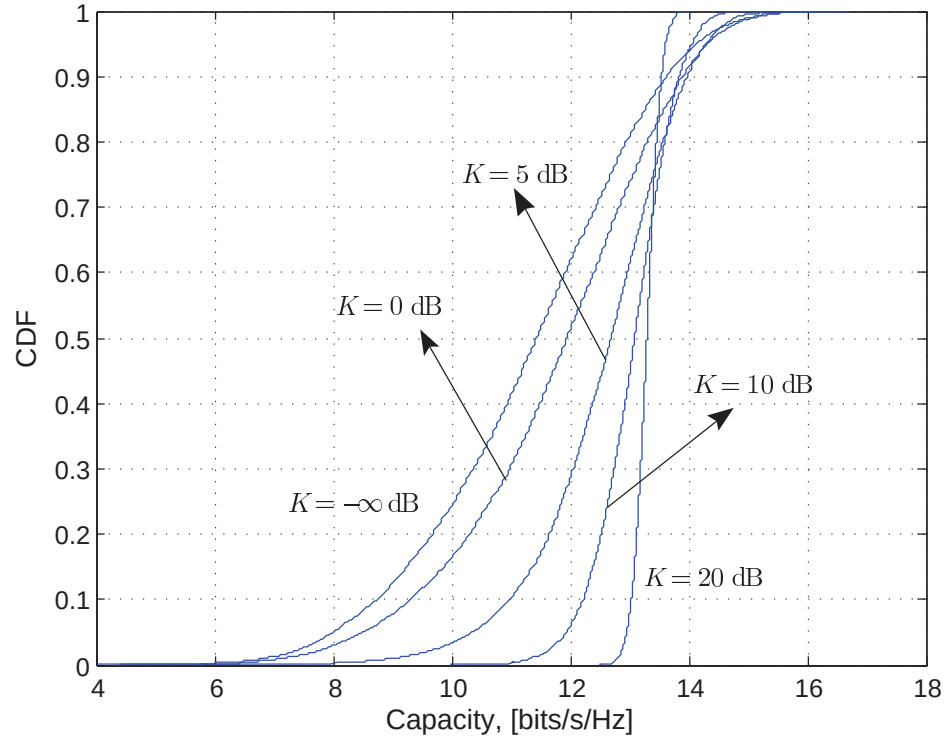

(a) Optimised configuration.

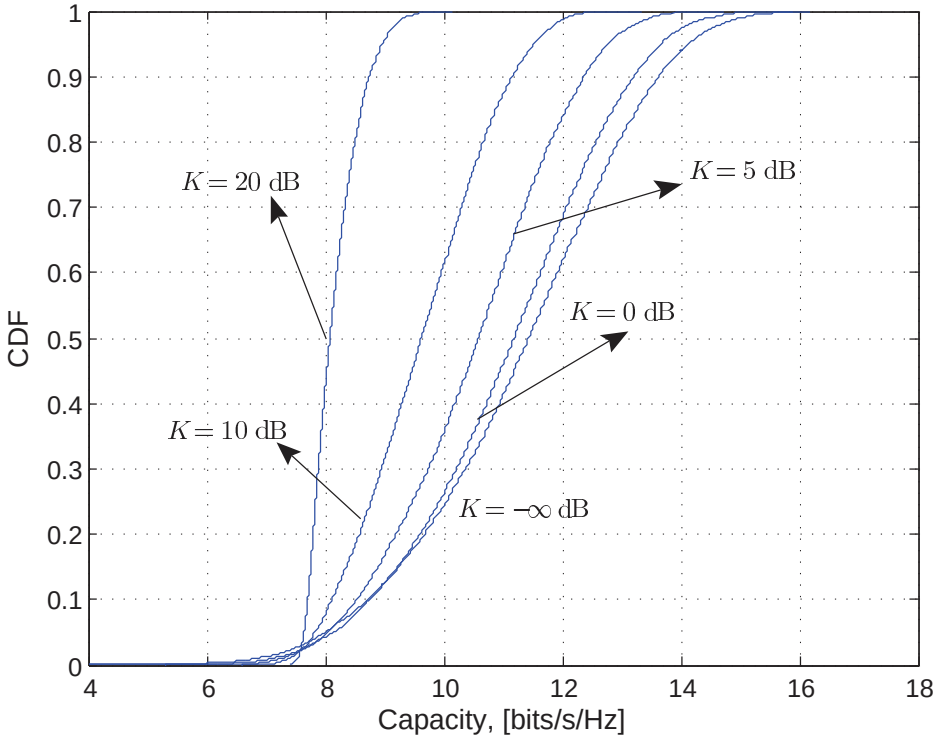

(b) Conventional configuration.

Figure 5.4: *Capacity CDFs of two stochastic MIMO channels ($\rho = 20$ dB).*

As a next step, the dynamic evolution of capacity is studied again for different values of the K-factor and the obtained results are shown in Fig. 5.5. As the K-factor increases the dynamic range of capacity increases too; for $K \geq 10$ dB the ergodic channel capacity is able to reach its maximum value and becomes more robust to displacements from optimum locations. On the other hand, for $K \leq 0$ dB the system performance is unaffected by the car motion and also gets closer to the ergodic Rayleigh capacity which implies that the benefits of LoS-optimised arrays are minimised.

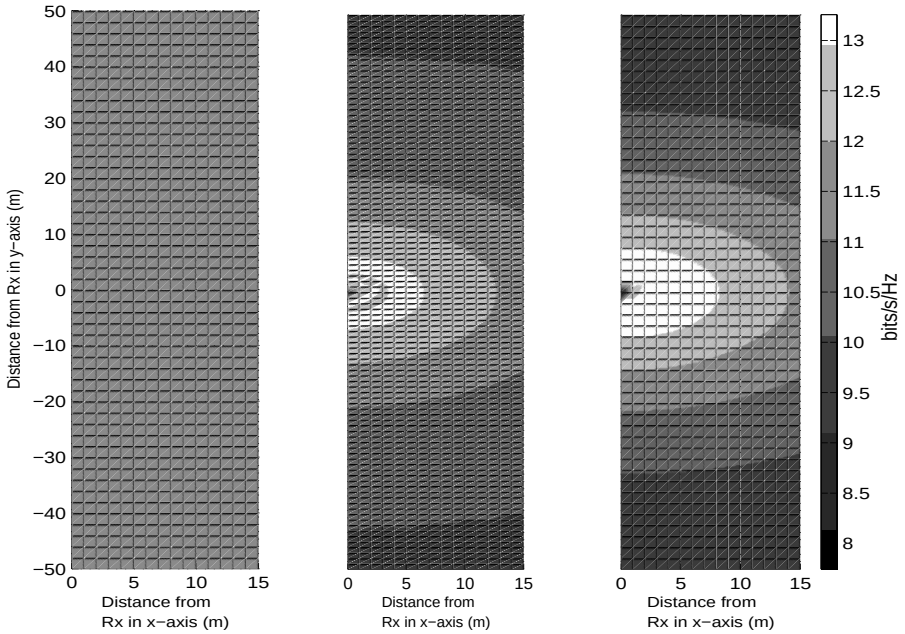

(a) $K = 0$ dB (b) $K = 10$ dB (c) $K = 20$ dB

Figure 5.5: *Sensitivity of ergodic capacity to displacements on the $x - y$ plane for different values of the K-factor.*

5.2 Eigenanalysis of dual-branch MIMO Ricean systems

The impact of eigencharacteristics on MIMO performance has become evident from the previous section and has been widely recognised over the last years as well. For instance, the eigenvalues of $\mathbf{HH}^H$ reflect the power of each multiplexed data stream and therefore are inherently related to MIMO capacity [5, 6] and further constitute a metric of multipath richness [180]. For this reason, the main objective herein is the determination of the eigenvalue profile which includes among others the marginal eigenvalue and condition number distributions.

5.2.1 Eigenvalue statistics

Since the introduction of MIMO technology, an extensive amount of research effort has been devoted to the study of eigenvalue statistics (see [6, 44, 181–184] among others) which govern a variety of MIMO features spanning from SM ability to diversity order and error performance [185–188]. Apart from the eigenvalue statistics, an equally important metric is the condition number commonly defined as the ratio of the largest to the smallest eigenvalue. In the MIMO context, the condition number indicates the multipath richness of the channel [189] and it has also been shown to drastically affect the detection performance in SM systems [190, 191]. Hence, a detailed knowledge of the eigenvalue as well as of the condition number statistics is highly desirable since it will facilitate the efficient characterisation of the promising MIMO technology and the design of future communication networks.

All the above cited papers make use of random matrix theory and particularly of the theory of random complex Wishart matrices, established by the pioneering work of James [192]. In the usual scenario of Rayleigh fading the channel matrix entries have zero mean and, consequently, the tractable class of central (zero-mean) Wishart matrices comes up for which all ordered joint/marginal eigenvalue CDFs and PDFs are known in closed form (see for instance [193] and references therein). On the other hand, the presence of the specular component in Ricean channels violates the zero-mean condition but despite their practical relevance few results have been documented on the eigenvalue statistics of Ricean channels. This fact can be attributed to the difficulty in manipulating hypergeometric functions with two matrix arguments of non-central Wishart matrices compared to the one matrix argument of central Wishart matrices [192]. For example, following the fundamental guidelines introduced by Khatri [194], the PDF and CDF of the largest eigenvalue of an arbitrary size non-central Wishart matrix were derived in [187] and thereafter were used to analyse the performance of maximal ratio combining systems. Likewise, the marginal PDF of an unordered eigenvalue was derived in [195] along with the ergodic mutual information in explicit form. On the other hand, based on the joint eigenvalue distributions, different insightful results have been reported in the literature. To be more precise, the authors in [196] explored the moment generating function of capacity whereas in [197] the main focus was on the higher-order moments of capacity. Also, in [198] tight upper and lower bounds on the ergodic capacity of correlated MIMO Ricean channels were presented. For the dual case under consideration, exact density and distribution capacity functions for rank-1 MIMO Ricean channels were derived in [199], through the unordered joint eigenvalue PDF.

To the best of the author's knowledge, the first investigations dealing with the ordered marginal distributions of the smallest and largest eigenvalues of MIMO Ricean channels were separately addressed in [200], [185] and [201]. The former proposed the use of invariant polynomials which, in the author's opinion, made the overall analysis excessively complicated and further it merely considered the marginal CDFs; what's more, the distribution of the smallest eigenvalue was given in an integral non-analytical form. In [185], much simpler CDF expressions were expressed but, at the same time, the PDF densities were modelled via asymptotic first-order expansions which are, by definition, accurate only when the eigenvalues tend to zero. The latter paper recently studied the marginal eigenvalue PDFs, starting from the joint eigenvalue PDF, but the derivation of final closed-form expressions, which the authors acknowledge as quite involved, was beyond the scope of the paper. Summarising, it appears that no tractable closed-form formulae for the ordered marginal eigenvalue PDFs are available in the literature. For the rest of this chapter, the symbol $\sim \mathcal{CN}(\mathbf{X}, \mathbf{Y})$ will stand for a complex normally distributed matrix with mean $\mathbf{X}$ and covariance $\mathbf{Y}$. The entries of an $(m \times n)$ matrix $\mathbf{X}$ are denoted as $\{\mathbf{X}\}_{i,j}$ where $i = 1, \ldots, m$ and $j = 1, \ldots, n$ and the all-zero $(m \times n)$ matrix as $\mathbf{0}_{m \times n}$.

5.2.1.1 Review of dual non-central Wishart matrices

When a dual Ricean system is assumed, the (2×2) complex normal random matrix $\mathbf{H}$ is distributed according to $\mathbf{H} \sim \mathcal{CN}(\mathbf{M}, \mathbf{\Sigma} \otimes \mathbf{I}_2)$. The matrix $\mathbf{\Sigma} = \sigma^2 \mathbf{I}_2$ is the correlation matrix containing the variances σ^2 of the entries of $\mathbf{H}$ on its main diagonal. The instantaneous MIMO correlation matrix is defined as $\widetilde{\mathbf{W}} = \mathbf{H}\mathbf{H}^H$ and is said to follow the complex non-central Wishart distribution with two degrees of freedom and non-centrality matrix $\mathbf{\Omega} = \mathbf{\Sigma}^{-1}\mathbf{M}\mathbf{M}^H$, commonly denoted as $\widetilde{\mathbf{W}} \sim \mathcal{CW}_2(2, \mathbf{\Sigma}, \mathbf{\Omega})$[2]. Let's now consider a scaled version of $\widetilde{\mathbf{W}}$, that is $\mathbf{W} = \mathbf{\Sigma}^{-1}\widetilde{\mathbf{W}}$. Since $\mathbf{W}$ is a (2×2) Hermitian matrix, it has two real ordered eigenvalues $w_1 > w_2 > 0$, whose joint PDF is given by [192]

$$f(w_1, w_2) = \exp\left[-\sum_{i=1}^{2}(\lambda_i + w_i)\right] {}_0\widetilde{F}_1\left(2; \boldsymbol{\lambda}, \mathbf{w}\right)(w_1 - w_2)^2 \tag{5.20}$$

where $\boldsymbol{\lambda} = (\lambda_1, \lambda_2)$ contains the real ordered eigenvalues of $\mathbf{\Omega}$ and, in turn, $\mathbf{w} = (w_1, w_2)$ while ${}_0\widetilde{F}_1(.;.,.)$ is the complex hypergeometric function of two matrix arguments. A convenient version of ${}_0\widetilde{F}_1\left(2; \boldsymbol{\lambda}, \mathbf{w}\right)$ for the case of two transmit and two receive antenna elements

[2] It should be noted that if $\mathbf{M} = \mathbf{0}_{2\times 2}$ so that $\mathbf{\Omega} = \mathbf{0}_{2\times 2}$, a complex central Wishart matrix is obtained, i.e. $\widetilde{\mathbf{W}} \sim \mathcal{CW}_2(2, \mathbf{\Sigma})$.

was given by Gross and Richards [202] as

$$ {}_0\widetilde{F}_1\left(2;\boldsymbol{\lambda},\mathbf{w}\right)=\frac{\det\left({}_0F_1\left(1;w_i\lambda_j\right)\right)}{(\lambda_1-\lambda_2)(w_1-w_2)} \tag{5.21} $$

with ${}_0F_1(s+1;x)$ being the classical hypergeometric function [203]

$$ {}_0F_1(s+1;x)=s!x^{-s/2}I_s\left(2\sqrt{x}\right). \tag{5.22} $$

Regarding the statistical characteristics of $\mathbf{H}$ in (5.1), it can be inferred that $\mathbf{M}=\sqrt{\frac{K}{K+1}}\mathbf{H}_{\mathrm{L}}$ while $\mathbf{\Sigma}=\frac{1}{K+1}\mathbf{I}_2$. Then, it is trivial to show that the Wishart matrix $\widetilde{\mathbf{W}}=\mathbf{H}\mathbf{H}^H$ follows the distribution $\widetilde{\mathbf{W}}\sim\mathcal{CW}_2\left(2,\frac{1}{K+1}\mathbf{I}_2,K\mathbf{H}_{\mathrm{L}}\mathbf{H}_{\mathrm{L}}^H\right)$ and in turn the associated LoS version of interest $\mathbf{W}=(K+1)\widetilde{\mathbf{W}}$.

5.2.1.2 Marginal eigenvalue PDFs

In this section, the marginal PDFs of the smallest and largest eigenvalue of dual non-central Wishart matrices are derived. The starting point of the following analysis is the work presented in [185] where the marginal CDFs of all ordered eigenvalues of random size complex non-central Wishart matrices were derived. These explicit results apply for non-centrality matrices of arbitrary rank and are rewritten herein for the ease of the reader. The following mathematical derivation is exclusively performed in the matrix domain and, consequently, the eigenvalue PDFs cannot be simply obtained after differentiating the CDFs. More interestingly, it is shown the derived formulae, which are given in matrix form as well, can be efficiently evaluated and easily programmed thanks to the compact matrix sizes. To begin with, in the general case of a $(m\times n)$ MIMO system with $m\leq n$, the marginal CDF of the smallest eigenvalue w_n of $\mathbf{W}$ is [185]

$$ F_{w_n}(x)=1-\frac{\det\left(\mathbf{\Phi}(x)\right)}{\det\left(\mathbf{\Phi}(0)\right)},\ \ x>0. \tag{5.23} $$

The entries of the matrix $\mathbf{\Phi}(x)$ are succinctly given by

$$ \left\{\mathbf{\Phi}(x)\right\}_{i,j}=Q_{m+n-2i+1,m+n}\left(\sqrt{2\lambda_j},\sqrt{2x}\right) \tag{5.24} $$

where $Q_{p,q}(y,z)$ is the Nutall Q-function, originally defined in [205, Eq. (86)] according to

$$ Q_{p,q}(y,z)=\int_z^\infty x^p\exp\left[-\frac{x^2+y^2}{2}\right]I_q(yx)dx. \tag{5.25} $$

The CDF of the largest eigenvalue w_1 of $\mathbf{W}$ reads as

$$F_{w_1}(x) = \frac{\det\left(\mathbf{\Xi}(x)\right)}{\det\left(\mathbf{\Phi}(0)\right)}, \;\; x > 0. \tag{5.26}$$

Likewise, the entries of the matrix $\mathbf{\Xi}(x)$ are

$$\begin{aligned} \left\{\mathbf{\Xi}(x)\right\}_{i,j} &= Q_{m+n-2i+1,m+n}\left(\sqrt{2\lambda_j}, 0\right) \\ &\quad -Q_{m+n-2i+1,m+n}\left(\sqrt{2\lambda_j}, \sqrt{2x}\right). \end{aligned} \tag{5.27}$$

When $m = n = 2$, the following simplified expression for the entries of $\mathbf{\Phi}(x)$ is obtained (proof given in Appendix A.1)

$$\left\{\mathbf{\Phi}(x)\right\}_{i,j} = \begin{cases} \left(2\lambda_j + 2\right) Q\left(\sqrt{2\lambda_j}, \sqrt{2x}\right) + \sqrt{2x}\exp\left[-\left(\lambda_j + x\right)\right] & \\ \quad \times \left\{ \underbrace{\sqrt{2\lambda_j} I_1\left(2\sqrt{\lambda_j x}\right) + \sqrt{2x} I_0\left(2\sqrt{\lambda_j x}\right)}_{A(x)} \right\}, & \text{for } i = 1 \\ Q\left(\sqrt{2\lambda_j}, \sqrt{2x}\right), & \text{for } i = 2 \end{cases} \tag{5.28}$$

where the Marcum-Q function is defined as $Q(a,b) = \int_b^\infty x \exp\left[-\frac{a^2+x^2}{2}\right] I_0(ax)dx$. Please note that similar simplified expressions for the marginal eigenvalue CDFs have been investigated in [204], though the authors evaluated the Nutall-Q as an infinite series of polynomial terms which introduce higher computational requirements. The marginal PDF is now given by

$$f_{w_2}(w_2) = -\frac{\det\left(\mathbf{\Phi}(w_2)\right)}{\det\left(\mathbf{\Phi}(0)\right)} \mathrm{tr}\left(\mathbf{\Phi}^{-1}(w_2)\mathbf{\Psi}(w_2)\right) \mathbf{U}(w_2). \tag{5.29}$$

In the above equation, $\mathbf{U}(\cdot)$ is the unit step function while the entries of the (2×2) matrix $\mathbf{\Psi}(w_2)$ contain the derivatives of $\left\{\mathbf{\Phi}(x)\right\}_{i,j}$ with respect to x and are given by

$$\left\{\mathbf{\Psi}(w_2)\right\}_{i,j} = e^{-(\lambda_j + w_2)} \begin{cases} -\left(1+\lambda_j\right) I_0\left(2\sqrt{\lambda_j w_2}\right) + \frac{1-2w_2}{\sqrt{2w_2}} A(w_2) & \\ +2\sqrt{\lambda_j w_2} I_1\left(2\sqrt{\lambda_j w_2}\right) + \lambda_j I_2\left(2\sqrt{\lambda_j w_2}\right), & \text{for } i = 1 \\ -I_0\left(2\sqrt{\lambda_j w_2}\right), & \text{for } i = 2. \end{cases} \tag{5.30}$$

The marginal CDF of the largest eigenvalue w_1 can again be extracted from [185, Theorem 2],

based on [185, Eq. (20)], as

$$F_{w_1}(x) = \frac{\det\left(\boldsymbol{\Xi}(x)\right)}{\det\left(\boldsymbol{\Phi}(0)\right)}, \quad x > 0 \tag{5.31}$$

with the entries of the matrix $\boldsymbol{\Xi}(x)$ being (please see again Appendix A.1)

$$\left\{\boldsymbol{\Xi}(x)\right\}_{i,j} = \begin{cases} (2\lambda_j + 2)\, Q\left(\sqrt{2\lambda_j}, 0\right) - \left\{\boldsymbol{\Phi}(x)\right\}_{i,j}, & \text{for } i = 1 \\ Q\left(\sqrt{2\lambda_j}, 0\right) - Q\left(\sqrt{2\lambda_j}, \sqrt{2x}\right), & \text{for } i = 2. \end{cases} \tag{5.32}$$

In a similar manner, we can obtain the marginal PDF of w_1 as

$$f_{w_1}(w_1) = \frac{\det\left(\boldsymbol{\Xi}(w_1)\right)}{\det\left(\boldsymbol{\Phi}(0)\right)} \mathrm{tr}\left(-\boldsymbol{\Xi}^{-1}(w_1)\boldsymbol{\Psi}(w_1)\right) \mathbf{U}(w_1). \tag{5.33}$$

The proof is given in Appendix A.2. Clearly, the PDFs of both eigenvalues have been expressed as the product of exponentials with modified Bessel functions of the first kind and Marcum-Q functions which can be easily applied to the performance analysis of MIMO systems.

5.2.2 Condition number statistics

The distribution of the condition number is now explored and closed-form formulae for its PDF and CDF are introduced as a weighted sum of polynomials. While the seminal work of Edelman [206] revealed the significant importance of the condition number as a metric of the matrix ill-condition, it was limited to the case of (2×2) central Wishart matrices with unit variance. The work presented by Ratnarajah *et al.* [207] extended these results to account for matrices of random size and with arbitrary variance but still did not allow for non-zero mean Wishart matrices. It is also worth noting an interesting approach to model the temporal transition probabilities of the condition number using a finite-state Markov process [208]; more interestingly, it was shown that the CDF of the logarithm of the condition number can be very well approximated via a gamma variable. Yet, the analysis was again limited to Rayleigh-fading MIMO channels. This implies that the contribution of this section can be regarded as a broader framework of the above cited papers [206–208].

Generally speaking, the condition number is a metric of the channel rank or, in other words, of how invertible a given matrix is; a condition number close to one indicates a well-conditioned matrix with almost equal eigenvalues. On the contrary, as the condition number gets larger the matrix rank drops and eventually degenerates into a rank-1 matrix. Its importance in the area of

MIMO communications has been demonstrated in [189–191] among others. In the considered case, the condition number of the scaled MIMO correlation matrix $\mathbf{W}$ can be expressed as

$$z = \frac{w_1}{w_2} \geq 1. \tag{5.34}$$

From an information theory point of view, the impact of the condition number on MIMO capacity can be seen in the following equation, which returns the instantaneous channel capacity assuming CSI at the Rx and no knowledge at the Tx[3] [5]

$$\begin{aligned} C &= \log_2\left(\left(1+\frac{w_1}{\alpha}\right)\left(1+\frac{w_2}{\alpha}\right)\right) &(5.35)\\ &= \log_2\left(\left(1+\frac{zw_2}{\alpha}\right)\left(1+\frac{w_2}{\alpha}\right)\right) &(5.36)\end{aligned}$$

where $\alpha = 2(1+K)/\rho$. From (5.36), it is evident that there is no analytical one-to-one mapping between MIMO capacity and the condition number. However, their inter-dependency can be numerically evaluated; in Fig. 5.6 this inter-dependency is illustrated for an SNR of 20 dB[4]. This graph verifies the notion that high-rank channels, or low condition numbers, yield high capacities and vice-versa. From the previous discussion it is apparent how essential the determination of the statistical characteristics of the condition number is; ultimately, the SM performance of MIMO channels could be analytically predicted and appropriate space-time codes could be designed. In order to get a deeper understanding, the density and distribution functions of the condition number are now studied for two different cases; the distinction is based on the associated LoS eigenvalues and, in particular, on whether these are identical.

5.2.2.1 Case 1 ($\lambda_1 \neq \lambda_2$)

This first category represents any conventional MIMO configuration, with no constraint on the rank of the LoS channel matrix, that offers two distinct non-zero LoS eigenvalues $\lambda_1 > \lambda_2$. It is shown that the PDF of z, $f_z(z)$, can then be expressed as a weighted summation of polynomials given by

$$f_z(z) = \frac{e^{-(\lambda_1+\lambda_2)}(z-1)}{\lambda_1-\lambda_2}\sum_{k=0}^{\infty}\sum_{n=0}^{\infty}\frac{\Gamma(k+n+3)z^k}{(k!n!)^2(z+1)^{k+n+3}}\left[\lambda_1^k\lambda_2^n-\lambda_2^k\lambda_1^n\right] \tag{5.37}$$

[3] Please note that this capacity formula relies on an equal-power transmission policy where the Tx splits the power uniformly across all subchannels. This scheme, though not optimal, has been shown to be robust for maximising the capacity of the worst fading correlation matrix, or the so-called "maxmin" property [196].

[4] A more detailed discussion on the simulation settings is provided in Section 5.2.3.

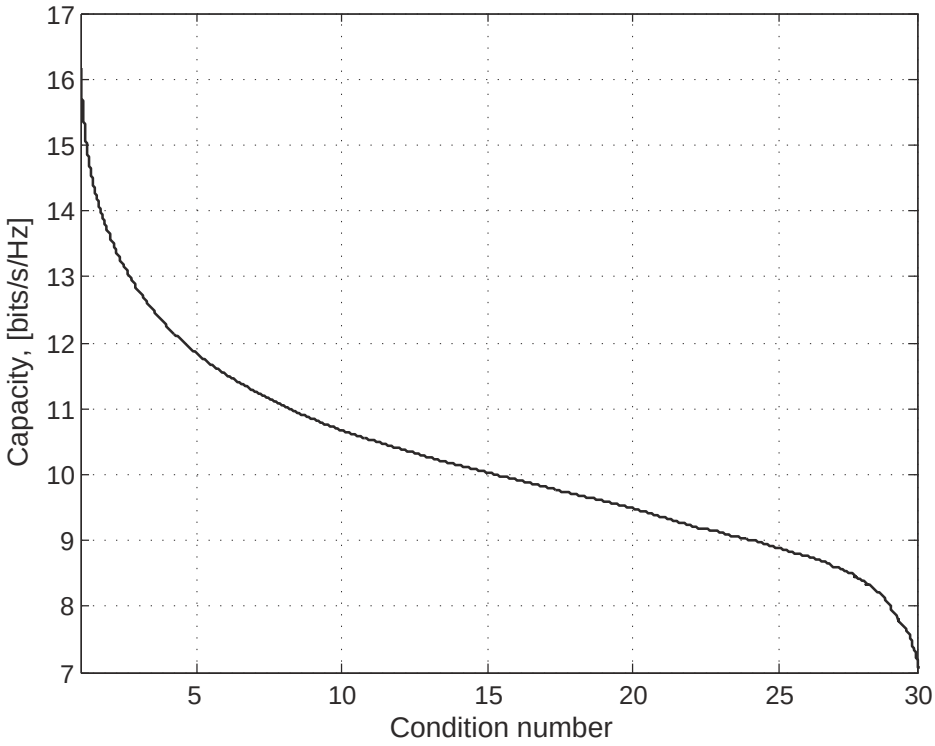

Figure 5.6: *Capacity evolution as a function of the condition number ($\rho = 20$ dB, $K = 5$ dB).*

with the Gamma function being rewritten for the case of an integer index as $\Gamma(n) = (n-1)!$. A detailed proof is given in Appendix A.3. In order to reduce the high computational complexity inserted by the infinite double summation of the above equation, only a truncated subset of terms may be considered according to

$$f_z(z) \approx \frac{e^{-(\lambda_1+\lambda_2)}(z-1)}{\lambda_1-\lambda_2} \sum_{k=0}^{K_s} \sum_{n=0}^{N_s} \frac{\Gamma(k+n+3)z^k}{(k!n!)^2(z+1)^{k+n+3}} \left[\lambda_1^k \lambda_2^n - \lambda_2^k \lambda_1^n\right]. \tag{5.38}$$

The values of K_s and N_s are chosen so that a further increase in the number of coefficients holds negligible impact on the final outcome (less than 0.5% between consecutive steps). It was empirically found that to fulfill this prerequisite with the minimum number of terms, K_s and N_s should be set to the same value. In fact, by adopting this approach the asymptotic result is approximated well with $K_s = N_s = 20$. This observation is verified in Fig. 5.7, where the evolution of the double summation against the number of terms K_s, N_s is depicted, for four arbitrary values of z.

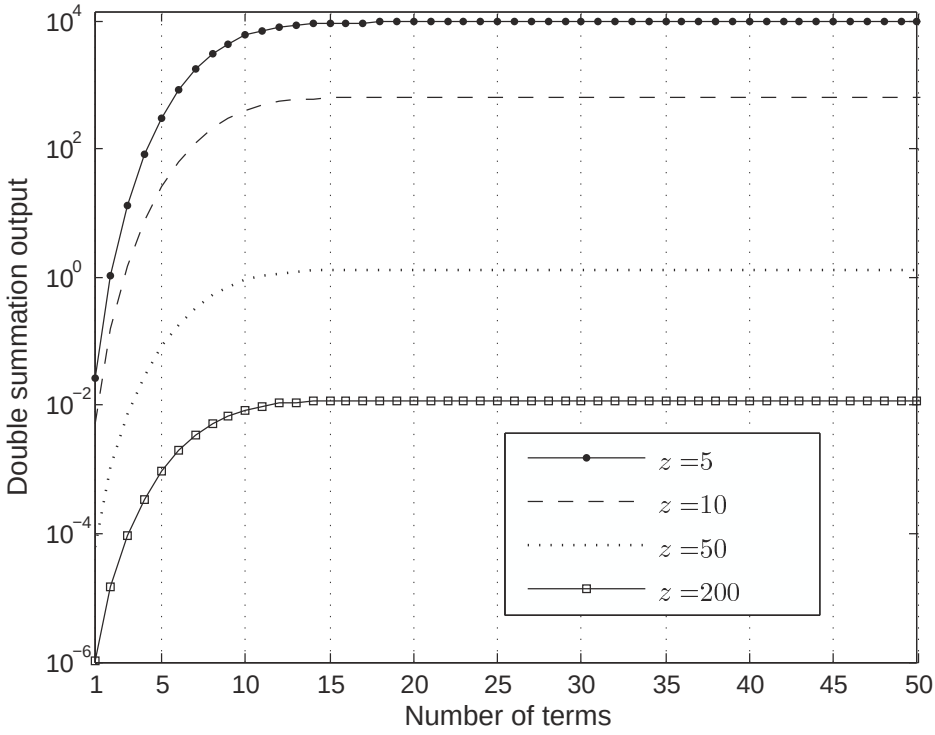

Figure 5.7: *Convergence of the double summation in (5.38) for four different values of the condition number z.*

The corresponding CDF of z, $F_z(x)$, is related to the PDF via the well known relationship

$$F_z(x) = \int_1^x f_z(z)dz \tag{5.39}$$

since by definition $z \geq 1$. By substituting (5.37) into (5.39) and taking into account the Dominated Convergence Theorem which states that the summation and integration can be interchanged, the following equation is obtained after some basic algebraic manipulations

$$F_z(x) = \frac{e^{-(\lambda_1+\lambda_2)}}{\lambda_1-\lambda_2}\sum_{k=0}^{\infty}\sum_{n=0}^{\infty}\frac{\Gamma(k+n+3)}{(k!n!)^2}\left[\lambda_1^k\lambda_2^n-\lambda_2^k\lambda_1^n\right]$$
$$\times\left\{\int_0^x\frac{z^{k+1}}{(z+1)^{k+n+3}}-\int_0^1\frac{z^{k+1}}{(z+1)^{k+n+3}}-\int_0^x\frac{z^k}{(z+1)^{k+n+3}}+\int_0^1\frac{z^k}{(z+1)^{k+n+3}}\right\} \tag{5.40}$$

For the integrals involved in (5.40), a tractable representation in terms of scalar hypergeometric

functions is available in [203, Eq. (3.194)]

$$\int_0^u \frac{t^\mu}{(1+bt)^\nu} dt = \frac{u^{\mu+1}}{\mu+1} {}_2F_1(\nu, \mu+1; \mu+2; -bu) \tag{5.41}$$

where ${}_2F_1(\alpha, \beta; \gamma; u)$ is the classical Gaussian hypergeometric function defined in [203, Eq. (9.14)]. The CDF of the condition number eventually becomes

$$\begin{aligned} F_z(x) = \frac{e^{-(\lambda_1+\lambda_2)}}{\lambda_1-\lambda_2} \sum_{k=0}^{\infty}\sum_{n=0}^{\infty} \frac{\Gamma(k+n+3)}{(k!n!)^2} \left[\lambda_1^k \lambda_2^n - \lambda_2^k \lambda_1^n\right] \\ \times \left\{ I_1^{k+1,k+n+3}(x) - I_1^{k,k+n+3}(x) \right\} \end{aligned} \tag{5.42}$$

where

$$\begin{aligned} I_1^{a,b}(y) &= \left(\frac{y^{a+1}}{a+1}\right) {}_2F_1(b, a+1; a+2; -y) \\ &- \left(\frac{1}{a+1}\right) {}_2F_1\left(b, a+1; a+2; -1\right). \end{aligned} \tag{5.43}$$

5.2.2.2 Case 2 $(\lambda_1 = \lambda_2)$

As was reported in Section 5.1, this is a special class of specifically designed LoS configurations with extensive practical interest since it offers two equal eigenvalues and thus delivers high capacities in the presence of strong deterministic components. In the case of equal eigenvalues though, the $(\lambda_1 - \lambda_2)$ term in the denominator of (5.21) becomes zero making the analysis invalid; in order to circumvent the division by zero *de l'Hôpital's* rule is employed to get a solution for the limit $(\lambda_1 \to \lambda_2)$. Following this approach, the ordered eigenvalue distribution $f(w_1, w_2)$ becomes [201]

$$\begin{aligned} f(w_1, w_2) = \lambda_1^{-1/2} e^{-2\lambda_1} (w_1 - w_2) e^{-(w_1+w_2)} \\ \times \left(\sqrt{w_1} I_1\left(2\sqrt{\lambda_1 w_1}\right) I_0\left(2\sqrt{\lambda_1 w_2}\right) \right. \\ \left. - \sqrt{w_2} I_1\left(2\sqrt{\lambda_1 w_2}\right) I_0\left(2\sqrt{\lambda_1 w_1}\right) \right). \end{aligned} \tag{5.44}$$

In Appendix A.3, it is shown that the PDF of the condition number has the form

$$f_z(z) = e^{-2\lambda_1}(z-1) \sum_{k=0}^{\infty}\sum_{n=0}^{\infty} \frac{\Gamma(k+n+4)}{(k!n!)^2 (k+1)(z+1)^{k+n+4}} \left(z^{k+1} - z^n\right). \tag{5.45}$$

The similarity between the infinite double summations involved in (5.37) and (5.45) is apparent and hence the finite subset approximation can be again used. In this case, a similar convergence check, as the one performed for (5.38), revealed that the choice $K_s = N_s = 15$ approximates the asymptotic solution reasonably well. As far as the condition number CDF is concerned, the concept for deriving an analytical expression is exactly the same as in (5.39)–(5.43). Thus, it is straightforward to show that for the case of equal LoS eigenvalues the condition number cumulative density reads as

$$F_z(x) = e^{-2\lambda_1} \sum_{k=0}^{\infty} \sum_{n=0}^{\infty} \frac{\Gamma(k+n+4)}{(k!n!)^2(k+1)} \times \Big\{ I_1^{k+2,k+n+4}(x) - I_1^{n+1,k+n+4}(x) - I_1^{k+1,k+n+4}(x) + I_1^{n,k+n+4}(x) \Big\}. \tag{5.46}$$

5.2.3 Numerical results

In this section, the theoretical analysis presented in Sections 5.2.1 and 5.2.2 is validated through a set of simulations. In order to allow the formulation of a general framework, a suboptimum HR configuration is used henceforth but all the presented results are readily extensible to the ideal case of equal eigenvalues. Referring back to (5.17) and Fig. 5.2, the inter-element spacings may be expressed as

$$s_1 = s_2 = \sqrt{\frac{\lambda(D+\delta d)}{2\cos^2\theta}} \tag{5.47}$$

where δd is the deviation from the optimum solution. The simulation settings for the LoS channel component are $\{d_{11} = d_{2,2} = D = 5.3852 \text{ m}\}$ and $\{d_{12} = 5.25 \text{ m}, d_{21} = 5.53 \text{ m}\}$. The spatial deviation δd is assumed to be -0.3852 m and the carrier frequency 5.9 GHz. The LoS matrix component then becomes

$$\mathbf{H}_{\text{L}}^{subopt} = \begin{bmatrix} 0.8384 + j0.5451 & 0.9411 + j0.3380 \\ -0.5123 - j0.8588 & 0.8384 + j0.5451 \end{bmatrix}. \tag{5.48}$$

Assuming a Ricean-K factor of 5 dB, the eigenvalues of $\mathbf{\Omega}^{subopt}$ can be easily computed and thereafter concatenated into the vector $\boldsymbol{\lambda} = (7.0336, 5.6155)$. After generating 50,000 random Monte-Carlo realisations of the channel matrix $\mathbf{H}$ according to (5.1), the accuracy of the analytical marginal eigenvalue CDFs/PDFs is respectively demonstrated in Figs. 5.8(a) and 5.8(b).

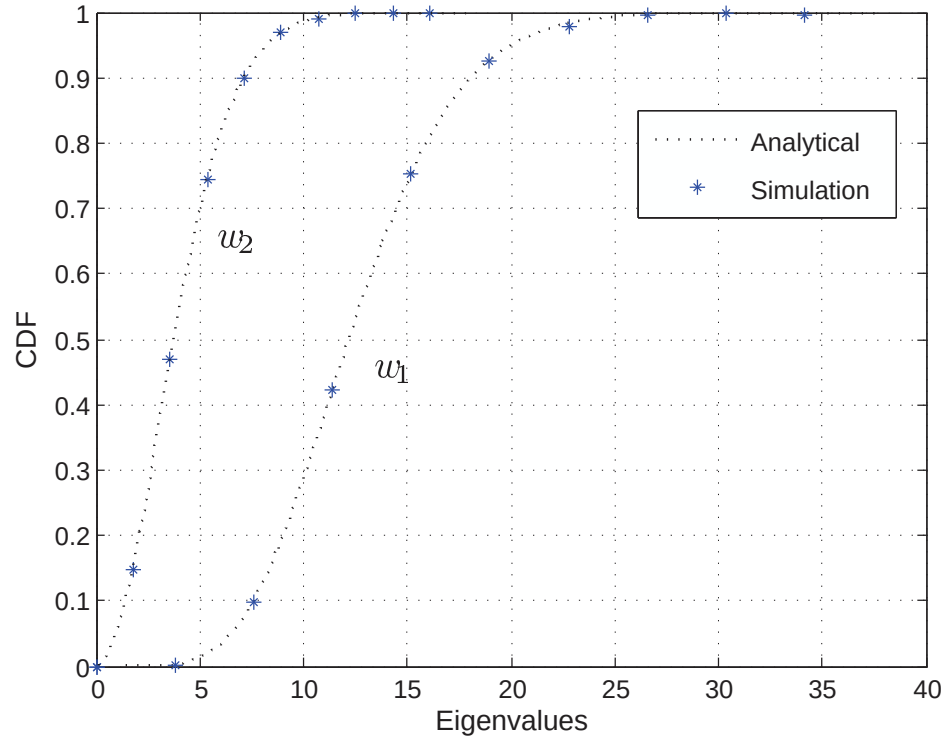

(a) Marginal eigenvalue CDFs.

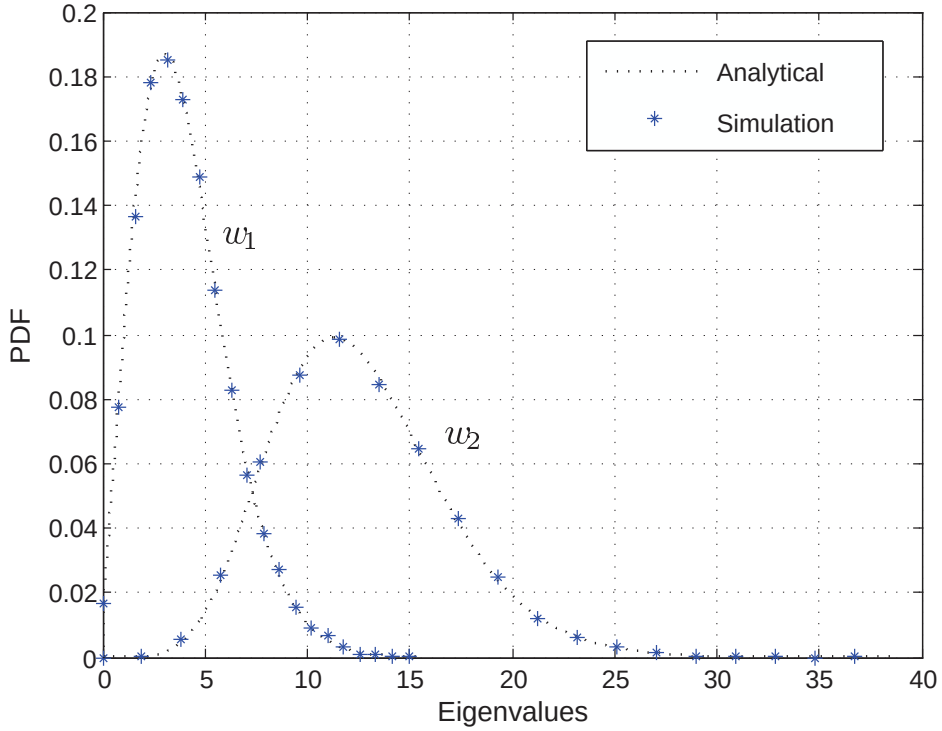

(b) Marginal eigenvalue PDFs.

Figure 5.8: *Marginal eigenvalue CDFs and PDFs of a dual non-central Wishart matrix.*

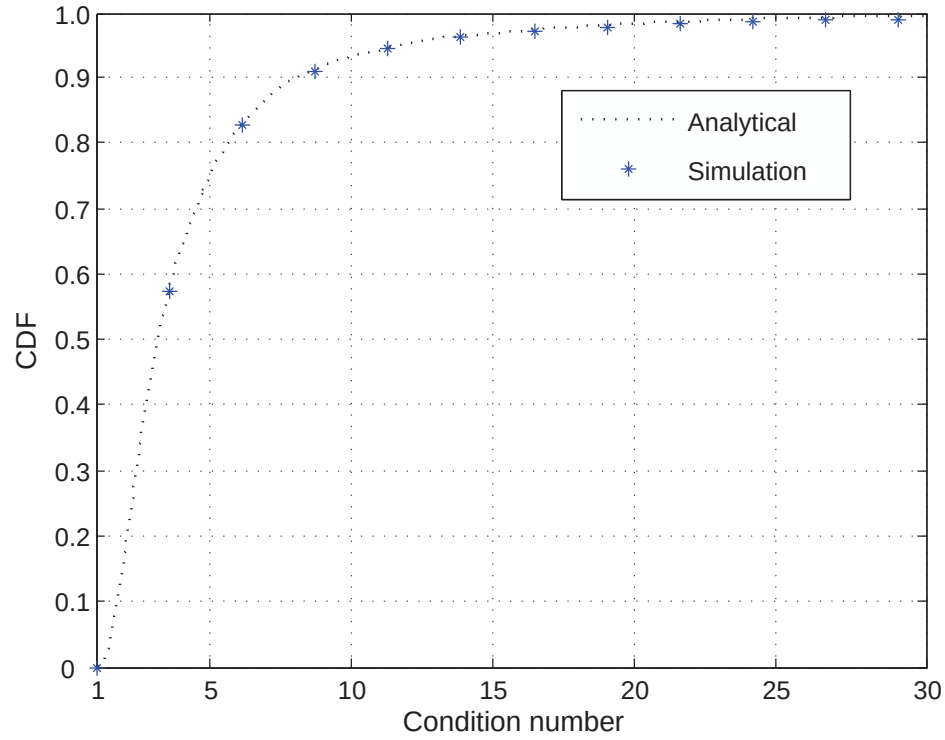

(a) CDF of the condition number.

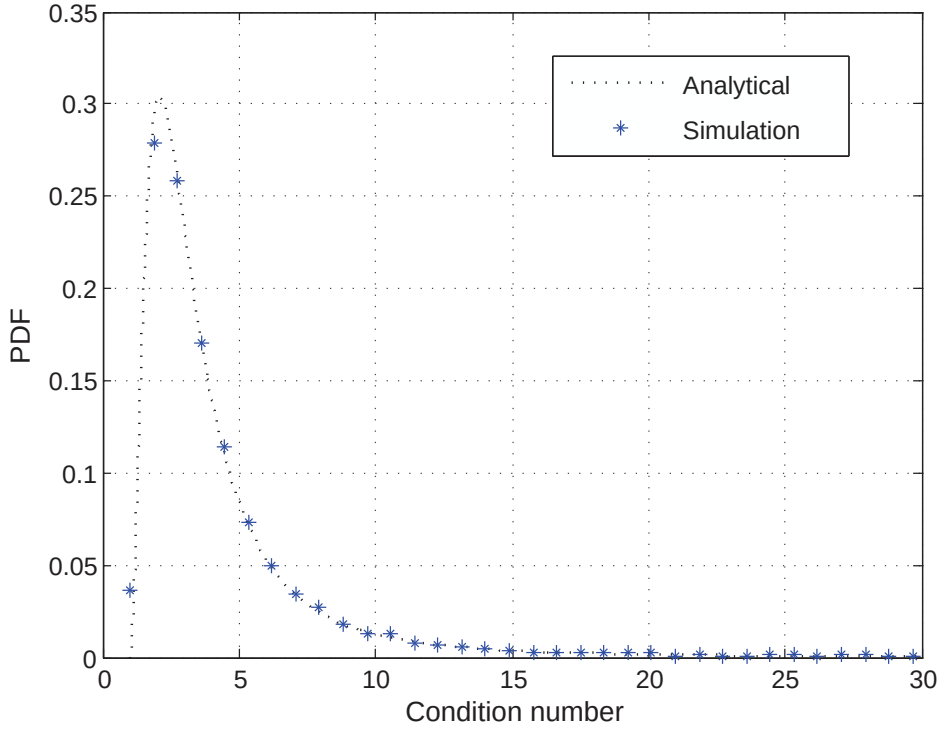

(b) PDF of the condition number.

Figure 5.9: *Condition number CDF and PDF of a dual non-central Wishart matrix.*

The analytical curves, as obtained from (5.23), (5.31) and (5.29), (5.33) respectively, are overlaid with the simulator outputs with the theoretical and simulation results being in remarkable agreement for both cases. Similarly, the quality of the analytical expressions for the condition number (5.38) and (5.42) is investigated in Figs. 5.9(a) and 5.9(b) where once more the agreement between simulation and theory is excellent.

5.3 Adaptive detection for SM-MIMO systems

In this section, a potential practical application of the previous mathematical derivations is proposed, by means of an AD suitable for SM systems. The main motivation for suggesting such a scheme is to reduce the implementation cost of MIMO detectors within most testbeds. We recall that the optimal detector for SM MIMO systems is the ML detector which minimises the error probability when all data vectors are equally likely but, at the same time, is computationally prohibitive [127]. One way to alleviate the excessive complexity of ML detectors is to settle for sphere decoding techniques, such as the Finke-Post algorithm proposed in [209], whose complexity, under certain assumptions, is polynomial in the problem size. In [210], it was shown that when the SNR is high the expected number of operations required by the sphere decoder is roughly cubic in the number of transmit antennas for a small problem size. However, the authors in [211] proved that for any arbitrarily fixed SNR the overall complexity of sphere decoders does not grow as a polynomial function of the problem size but as an exponential function instead. What's more, when ill-conditioned channels occur, the computational complexity of sphere decoding schemes increases to a significant extent [190]. On the other hand, different suboptimal techniques exist which span from the linear ZF detector to nonlinear techniques such as Ordered Successive Interference Cancellation (OSIC) [212]; the former is the simplest detection technique but causes a systematic performance degradation and further is unable to exploit all of the available diversity. Its main disadvantage lies in its poor performance when channels with large condition numbers occur.

From the previous discussion, it is evident that an AD which could switch between a ML and a ZF scheme, depending on the instantaneous channel conditions, is of vital importance since it will allow the efficient integration of MIMO systems into practical applications by simplifying their feasibility. A similar concept of adaptive MIMO transmission has been investigated by various research groups during the last years (the interested readers are referred to [213–215] among others) and essentially goes back to the fundamental diversity-multiplexing trade-

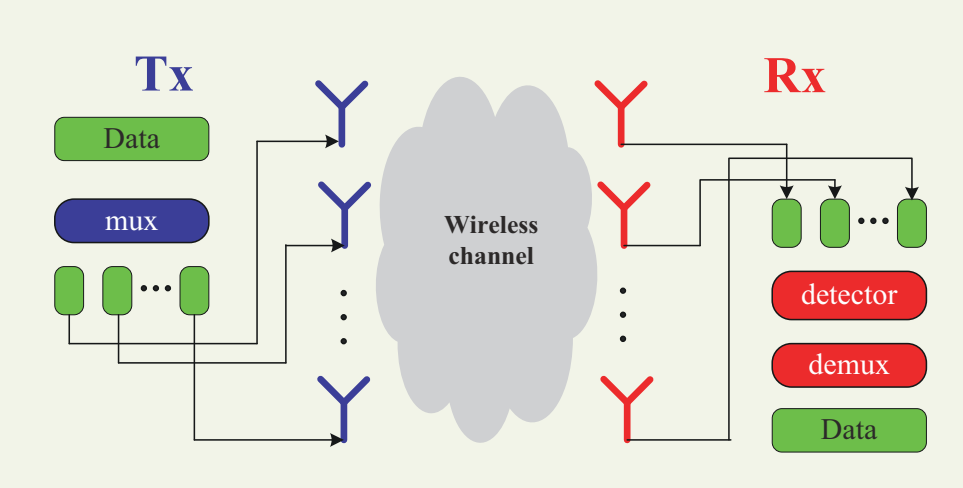

Figure 5.10: *A general SM-MIMO system.*

off [42]. As far as the author's knowledge goes, the first MIMO adaptive scheme for the receive side was recently presented in [216]. The authors however considered merely a Rayleigh channel, which leads to central complex Wishart matrices, and in this light the formulation of a generalized framework is not possible. The proposed scheme relaxes the assumption of Rayleigh fading to account for the commonly experienced LoS propagation and, consequently, embodies the model of [216] as a special case.

5.3.1 Detection schemes for SM systems

In this section the two reference detection schemes, namely ZF and ML detectors, are reviewed and thereafter the concept of the novel AD is explored. All the following investigations are based on a SM-MIMO transmission scheme, such as the widely employed V-BLAST [212], in which the data is divided into a number of N blocks, equal to the number of transmit elements, that are then simultaneously emitted (see Fig. 5.10). At the Rx, the main goal is to differentiate the data blocks originating from each of the transmit elements so that the transmitted signals are efficiently recovered. This differentiation is made possible due to the (ideally) unique spatial signature acquired by each data block as a result of the propagation path from the Tx to the Rx.

5.3.1.1 ZF detection

The simplest linear MIMO detector is the ZF receiver, where the received signal vector $\mathbf{y}$ is multiplied by the Moore-Penrose pseudoinverse $\mathbf{H}^{\dagger}$ of the channel matrix $\mathbf{H}$ to obtain an estimated transmit signal vector $\hat{\mathbf{x}}_{\text{ZF}}$ as follows

$$\hat{\mathbf{x}}_{\text{ZF}} = \mathbf{H}^{\dagger}\mathbf{H}\mathbf{x} + \mathbf{H}^{\dagger}\mathbf{n}. \tag{5.49}$$

The computational complexity of ZF includes an exhaustive search through the Q symbols in the constellation of the modulation technique for N times and thus it is of the order of $O(QN)$. However, the low complexity of the ZF receiver comes at the expense of noise amplification which induces irreducible errors. In fact, as the number of transmit and receive antennas grows with no bound, the noise amplification tends to infinity [217].

5.3.1.2 ML detection

An alternative detector is the optimal ML detector which remains robust and yields the best performance among all detection techniques [127]. Assuming equally likely, temporally uncoded transmit symbols, this receiver chooses the vector $\mathbf{t}$ that solves the following expression

$$\hat{\mathbf{x}}_{\text{ML}} = \arg\min_{\mathbf{t}} \|\mathbf{y} - \mathbf{H}\mathbf{t}\|_F^2 . \tag{5.50}$$

The optimisation is performed through an exhaustive search over all possible vector symbols. This implies that the complexity of the ML detector grows exponentially with the number of transmit antennas i.e. $O(Q^N)$, making the scheme infeasible for large antenna configurations and constellation sizes.

5.3.1.3 Adaptive detection

Given the aforementioned deficiencies of both detection strategies, the need of a detector which can adaptively switch between them in order to enhance the error performance and minimise the computational cost is strengthened. The AD uses ZF when the condition number is below a predefined threshold defined and ML detection otherwise. The key idea is to employ the ZF detector only for well-conditioned channels (low condition numbers) and let the ML deal with

the ill-conditioned channels (high condition numbers). Statistically speaking,

$$\hat{\mathbf{x}}_{\text{AD}} = \begin{cases} \hat{\mathbf{x}}_{\text{ZF}} & \text{if } z \leq \kappa \\ \hat{\mathbf{x}}_{\text{ML}} & \text{if } z > \kappa. \end{cases} \tag{5.51}$$

The threshold κ affects the complexity of the proposed scheme; for $\kappa = 1$, we get $\hat{\mathbf{x}}_{\text{AD}} = \hat{\mathbf{x}}_{\text{ML}}$ and complexity equals that of ML detection whereas for $\kappa \to \infty$ we have $\hat{\mathbf{x}}_{\text{AD}} = \hat{\mathbf{x}}_{\text{ZF}}$. In general, the probability of ZF calls is Prob $\{z \leq \kappa\} \equiv F_z(\kappa) = p_\kappa$ and therefore the average AD complexity g becomes

$$g = \underbrace{p_\kappa Q N}_{\text{ZF calls}} + \underbrace{(1-p_\kappa)Q^N}_{\text{ML calls}}, \;\; 0 \leq p_\kappa \leq 1. \tag{5.52}$$

The percentage of complexity reduction, compared to that of the ML detector, is

$$\frac{Q^N - g}{Q^N} = p_\kappa \left(1 - \frac{N}{Q^{N-1}}\right). \tag{5.53}$$

An illustrative graph, indicating the significant complexity advantage by employing the AD for a fixed number of transmit elements ($N = 2$), can be seen in Fig. 5.11. Obviously, the reduction is more pronounced for greater sizes of the symbol alphabet and higher number of ZF calls. As an example, for the commonly employed 16-QAM modulation and for $p_\kappa = 0.6$, the complexity is reduced by more than 52%.

5.3.2 AD performance evaluation

The AD performance is now investigated for two different geometrical LoS models, namely the suboptimum HR configuration $\mathbf{H}_{\text{L}}^{subopt}$ presented in Section 5.2.3 and the conventional LR configuration $\mathbf{H}_{\text{L}}^{conv}$ given in Section 5.1.2.2 with antenna spacings of 0.5λ. The K-factor was again set to 5 dB and therefore the eigenvalues of the latter configuration $\mathbf{\Omega}^{conv}$ become $\boldsymbol{\lambda}' = (12.649, 0.0001)$ thereby indicating the matrix ill-condition. For both geometrical models under investigation, 50,000 random Monte-Carlo realisations of the channel matrix $\mathbf{H}$ are generated according to (5.1) and a 16-QAM modulation scheme is employed. From Fig. 5.6, it is inferred that when $\kappa \leq 6.46$ the instantaneous capacity of the HR channel is greater than 11.4 bits/s/Hz (Rayleigh capacity). On this basis, a lower threshold of $\kappa = 5$ has been adopted as a reasonable indicator of the channel rank and multipath richness. In Fig. 5.12, the BER curves are depicted for three different detection schemes, namely ZF, ML and the proposed AD.

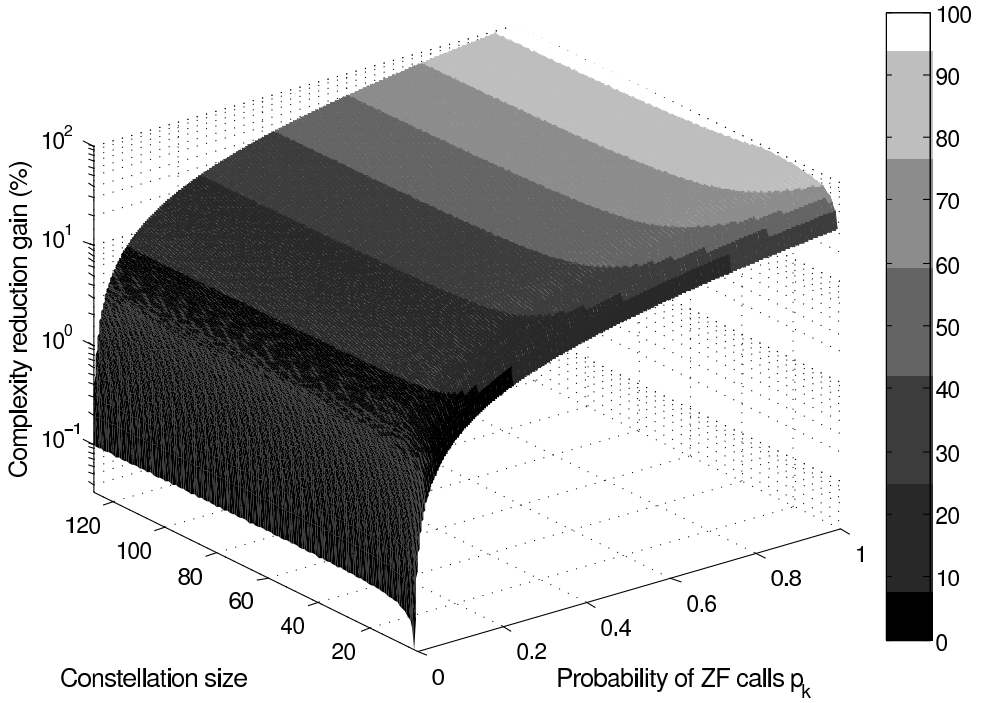

Figure 5.11: *Percentage of complexity reduction of the AD as a function of constellation size and probability of ZF calls (two transmit antennas).*

As expected, higher K-factors lead to significant performance enhancement for arrays designed following the suboptimum HR model. On the other hand, for low values of K-factor (below 0 dB) the channel approaches the i.i.d. Rayleigh channel characteristics which corresponds to a rich-scattering environment; in this region, the BER curves are approximately identical in both systems and the benefits of LoS-optimised arrays are minimised. In order to get a better understanding, the main AD performance characteristics are tabulated in Table 5.1 where the radically different trends of the two configurations are readily observable. The application of the detection scheme has a noticeable impact only on the HR channel; in fact, a significant percentage of ZF calls occur for all values of the K-factor with a consequent complexity reduction of up to 83.35%. The reader can also acknowledge the steady increase of p_κ as K gets higher since the channel becomes full rank and delivers two approximately equal eigenvalues. In the LR case, p_κ is always below 29.43% and further is inversely proportional to the K-factor. This phenomenon can be attributed to the ill-condition of conventional architectures which degenerate eventually into a rank-1 channel due to the increased dependence of the LoS rays' phases. Consequently, for $K \geq 5$ dB the number of ZF calls is too low to exploit the adaptivity benefits and a complexity identical to that of a ML detector inevitably takes place.

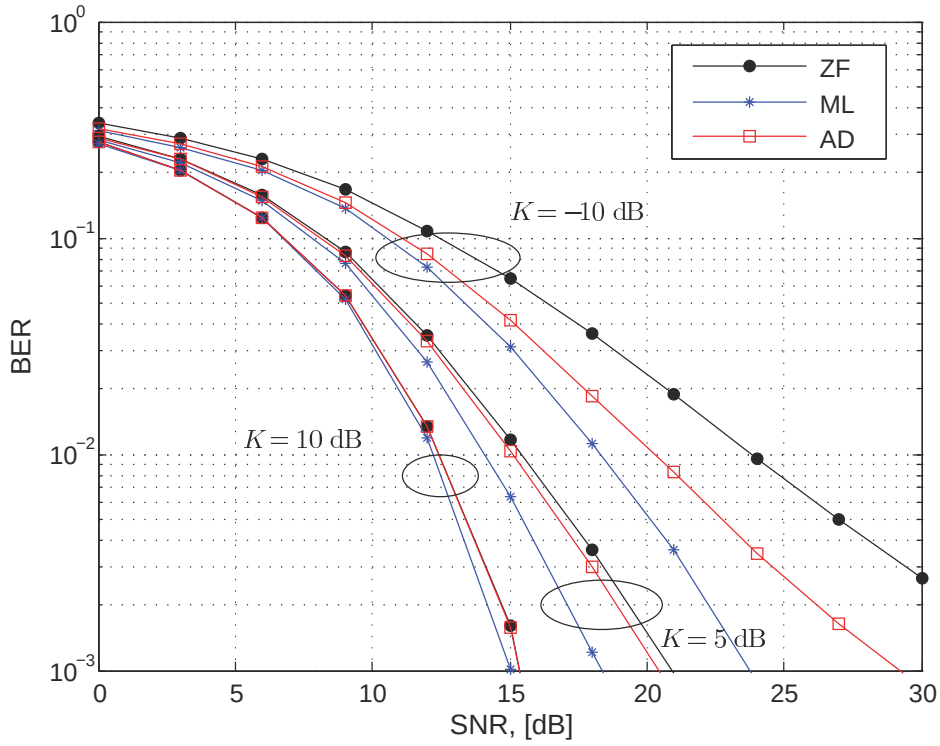

(a) Suboptimum HR LoS channel.

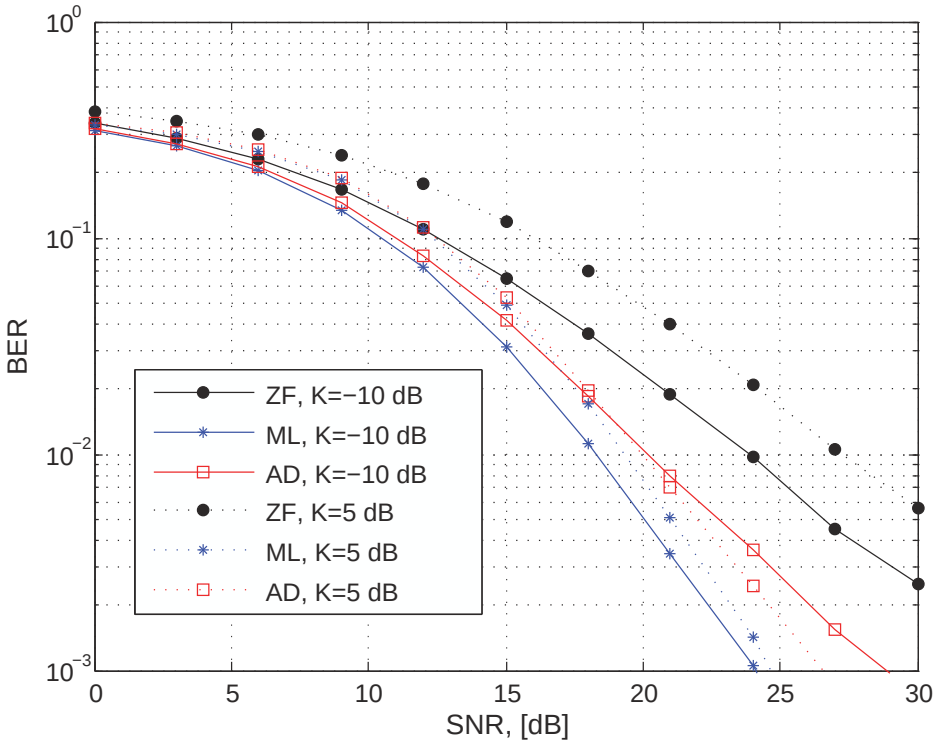

(b) Conventional LR LoS channel.

Figure 5.12: *BER curves for three different detection strategies (16-QAM modulation).*

K-factor	Suboptimum HR LoS channel			Conventional LR LoS channel		
	Analytical prob., p_κ	Simulated prob., p_κ	Compl. reduction	Analytical prob., p_κ	Simulated prob., p_κ	Compl. reduction
$K = -10$ dB	0.2992	0.3150	26.18%	0.2943	0.3132	25.75%
$K = -5$ dB	0.3203	0.3380	28.02%	0.2801	0.3002	24.51%
$K = 0$ dB	0.4372	0.4403	38.25%	0.2052	0.2241	17.95%
$K = 5$ dB	0.7499	0.7501	65.61%	0.0536	0.064	4.69%
$K = 10$ dB	0.9526	0.9620	83.35%	-	-	-

Table 5.1: *AD performance characteristics for two different LoS channel models as a function of the K-factor.*

5.4 Conclusions

In this chapter, the case of short-range propagation was considered where a non-fading component dominates the wireless channel. Contrary to the common belief, LoS MIMO channels are not always rank deficient; in fact, they can deliver capacities much higher than Rayleigh (rich scattering) channels do, with appropriate positioning of the antenna arrays. A tractable criterion to achieve subchannel orthogonality was devised for the case of dual-branch VTR MIMO systems with the proposed optimised configuration remaining robust even when large displacements occur. The beneficial effects of the K-factor were verified and it was concluded that the presence of strong specular components stabilises the link and makes the proposed configuration outperform the conventional architectures used nowadays in wireless communications.

The eigenstatistics of the above mentioned dual systems were subsequently analytically assessed with the derived closed-form formulae being validated through Monte-Carlo trials. In general, the eigenvalue and condition number statistics are very useful tools for determining numerous MIMO characteristics, ranging from SM ability and ergodic capacity to symbol error and detection performance. To further indicate the usefulness of this statistical analysis, an AD was developed whose kernel was a hard-decision condition number-based criterion. The dramatic decrease in terms of complexity, compared to the sophisticated ML detector, makes this adaptive scheme applicable to the majority of modern practical receivers. For LoS-optimised architectures, the attained performance was shown to be reasonably good especially for high values of the K-factor. On the contrary, the scheme's advantages diminish when it is applied to conventional antenna configurations since the channel matrix is inherently rank deficient and therefore yields a deteriorating performance with the increasing K-factor.

Chapter 6
Novel capacity upper bound for dual-branch MIMO Ricean systems

One of the most interesting topics in the theoretical analysis of wireless networks, is the determination of upper capacity bounds or, in other words, of the maximum achievable error-free data rate. In this chapter, a novel analytical upper bound on the ergodic capacity of dual-branch MIMO Ricean systems is derived based on a fundamental power constraint. The main advantages of the proposed bound are its low complexity and the fact that is applicable for arbitrary rank of the LoS component and system SNR. The mathematical formulations presented hereafter are using elements of non-central complex Wishart matrices and non-central complex quadratic forms. A comprehensive insight into the tightness of the bound is also provided where it is demonstrated that as the SNR tends to zero the bound becomes asymptotically tight; at high SNRs, the offset between empirical capacity and the proposed bound is analytically computed which implies that an explicit asymptotic capacity expression can ultimately be obtained. The remainder of the chapter is organised as follows: In Section 6.1, a detailed literature review is performed with the open problems and the chapter contributions being highlighted. In Section 6.2, some basic definitions related to quadratic forms are given along with the double-sided correlated MIMO Ricean channel model used throughout the chapter. Section 6.3 presents new upper capacity bounds for different categories of MIMO systems. In Section 6.4, the tightness of the novel bounds is explored while the numerical results are given in Section 6.5. Finally, Section 6.6 concludes the chapter and summarises the key findings.

6.1 Relations to previous and concurrent work

Taking into account the tractability in manipulating hypergeometric functions with only one matrix argument, it becomes more than expected that the majority of related studies documented in literature consider the common case of Rayleigh fading. For Rayleigh fading conditions, a plethora of results dealing with capacity bounds is available for various scenarios, spanning

from uncorrelated fading to double-sided spatial correlation (see for instance [5, 6, 218–220] and references therein among others). On the other hand, significantly fewer publications focusing on MIMO Ricean channels have been reported with the most important being found in [195, 196, 198, 221–232]. More specifically, in [221] the distribution of the ergodic capacity for i.i.d. rank-1 Ricean fading channels was explored at the high-SNR regime. In [195], explicit closed-form expressions for the ergodic capacity were presented via infinite series while in [196], capacity statistics (mean and second-order moment) were expressed in integral form for arbitrary rank of the mean channel matrix. An interesting approach is reported in [222] where upper and lower numerical bounds were derived for the i.i.d. case, assuming that the Tx has knowledge of statistical properties of the fading process but not of the instantaneous CSI. The first analytical bounds on MIMO Ricean capacity can be found in [223–225], where the assumption of uncorrelated fading at both ends was adopted. In [226, 227], these results were extended to account for spatial correlation at a single end of the MIMO link. The more general case of double-sided spatial correlation was addressed in [228, 229], using elements of quadratic form theory. The main characteristic of the above cited papers ([223–229]) though, is that they are limited to the case of rank-1 LoS matrices. As mentioned before, while this condition may occur quite often in reality, as a result of the excessive correlation of the LoS' rays phases, at the same time is not sufficiently general since it limits the applications of MIMO technology to conventional configurations.

To the best of the author's knowledge, the derivation of capacity bounds in the general case of arbitrary-rank mean matrices, has been separately assessed in [230], [231] and [198]. The former paper proposed a very tight lower bound on the ergodic capacity of semi-correlated MIMO Ricean channels after decomposing the channel correlation matrix into non-central Wishart submatrices and thereafter applying the bounding technique originally proposed in [220]. In [231], the authors relied on the expected values of elementary functions of complex non-central Wishart matrices to come up with an efficient capacity upper bound of semi-correlated MIMO Ricean channels. The latter paper represents so far the more general approach in the associated area since it derives several lower and upper bounds assuming all different types of spatial correlation. However, the paper's general upper bound is given as an infinite summation of Hayakawa polynomials of one matrix argument, which the authors acknowledge as quite involved and computationally inefficient. It is also worth mentioning the work presented by Lozano *et al.* [232], who considered the high-SNR capacity offsets in order to establish the key effect of the so-called power offset on MIMO performance. To sum up, it appears that no

tractable analytical results exist in the literature for the upper bound of double-sided correlated MIMO systems in Ricean fading with arbitrary-rank of the deterministic component.

On these grounds, in the present chapter, using some recent results on the theory of Wishart matrices and quadratic forms, a novel and efficient upper bound on the ergodic capacity of dual-branch MIMO systems is firstly derived based on a fundamental power constraint. In order to formulate a broad framework, the effects of spatial correlation are considered at both ends and, more importantly, the rank of the mean channel matrix is allowed to be arbitrary. In fact, the following analysis is carried out for both conventional LR and optimised HR configurations, as initially defined in Chapter 5. The tightness of the bound is also investigated in detail and it is clearly shown that as the SNR tends to zero the bound becomes asymptotically tight while, at infinitely high SNRs, the offset from true capacity is analytically determined as well.

6.2 Multivariate statistics definitions and channel model

Let's assume that the $(m \times n)$ complex matrix $\mathbf{X}$, with $m \leq n$, is distributed according to $\mathbf{X} \sim \mathcal{CN}_{m,n}(\mathbf{M}, \mathbf{\Sigma} \otimes \mathbf{\Psi})$, where $\mathbf{\Sigma} \in \mathbb{C}^{m \times m}$ and $\mathbf{\Psi} \in \mathbb{C}^{n \times n}$ are positive definite Hermitian matrices. Then, the matrix $\mathbf{Q} = \mathbf{X}\mathbf{\Lambda}\mathbf{X}^H$, with $\mathbf{\Lambda} \in \mathbb{C}^{n \times n}$, is said to be a non-central matrix-variate quadratic form denoted as $\mathbf{Q} \sim \mathcal{CQ}_{m,n}(\mathbf{A}, \mathbf{\Sigma}, \mathbf{\Psi}, \mathbf{M})$. In [198] and [228], the PDF of $\mathbf{Q}$ was expressed through complex Hayakawa polynomials of two matrix arguments which are very difficult to calculate numerically. A more tractable version of the associated PDF as a product of hypergeometric functions, can be found in [233, Eq. (5)]. Please note that non-central quadratic forms degenerate into non-central Wishart matrices when $\mathbf{\Psi} = \mathbf{I}_n$ and when either $\mathbf{\Lambda} = \mathbf{I}_n$ or $\mathbf{\Lambda}$ is idempotent with rank $R \geq m$ [198, 234]. The following theorem returns the υth moment of the determinant of (2×2) complex quadratic forms. Please note that hereafter the symbols $\det$ and $|\cdot|$ will be interchangeably used to denote the determinant operator. Finally, $\mathrm{etr}(\cdot)$ is a shorthand notation for $\exp(\mathrm{tr}(\cdot))$.

Theorem 1: Let $\mathbf{Q} \sim \mathcal{CQ}_{2,2}(\mathbf{I}_2, \mathbf{\Sigma}, \mathbf{\Psi}, \mathbf{M})$. Then, the υth moment of its determinant $|\mathbf{Q}|$ is given by

$$E\left[|\mathbf{Q}|^{\upsilon}\right] = |\mathbf{\Sigma}\mathbf{\Psi}|^{\upsilon} \left[\frac{\tilde{\Gamma}_2(\upsilon+2)}{\tilde{\Gamma}_2(2)}\right] {}_1\widetilde{F}_1\left(-\upsilon; 2; -\mathbf{\Theta}\right) \tag{6.1}$$

where $\mathbf{\Theta} = \mathbf{\Psi}^{-1}\bar{\mathbf{M}}\bar{\mathbf{M}}^H$ and $\bar{\mathbf{M}} = \mathbf{\Sigma}^{-1/2}\mathbf{M}$.

Proof: The proof begins by expressing the determinant of $\mathbf{Q} \sim \mathcal{CQ}_{2,2}(\mathbf{I}_2, \mathbf{\Sigma}, \mathbf{\Psi}, \mathbf{M})$ as

$$\begin{aligned} E\left[\det\left(\mathbf{Q}\right)^{\upsilon}\right] &= E\left[\det\left(\mathbf{X}\mathbf{X}^H\right)^{\upsilon}\right] \\ &= E\left[\det\left(\mathbf{\Sigma}^{1/2}\bar{\mathbf{X}}\bar{\mathbf{X}}^H\mathbf{\Sigma}^{1/2}\right)^{\upsilon}\right] \\ &= \det\left(\mathbf{\Sigma}\right)^{\upsilon} E\left[\det\left(\bar{\mathbf{X}}\bar{\mathbf{X}}^H\right)^{\upsilon}\right] \end{aligned} \tag{6.2}$$

where the complex normal matrix $\bar{\mathbf{X}}$ is distributed according to

$$\mathbf{X} \sim \mathcal{CN}_{2,2}(\bar{\mathbf{M}}, \mathbf{I}_2 \otimes \mathbf{\Psi}). \tag{6.3}$$

Using a result from [228] through the aid of the Cauchy-Binet formula, it can be shown that

$$\bar{\mathbf{X}}^H\bar{\mathbf{X}} \sim \mathcal{CW}_2(2, \mathbf{\Psi}, \mathbf{\Theta}) \tag{6.4}$$

and the expectation of the determinant in (6.2) can now be evaluated through [198, Theorem 1] to obtain

$$E\left[\det\left(\bar{\mathbf{X}}\bar{\mathbf{X}}^H\right)^{\upsilon}\right] = \det\left(\mathbf{\Psi}\right)^{\upsilon}\left[\frac{\tilde{\Gamma}_2(\upsilon+2)}{\tilde{\Gamma}_2(2)}\right]\mathrm{etr}(\mathbf{\Theta})_1\widetilde{F}_1\left(\upsilon+2; 2; \mathbf{\Theta}\right) \tag{6.5}$$

where the following property for the determinant of the product of square matrices has been used

$$\det\left(\mathbf{C}\mathbf{D}\right) = \det\left(\mathbf{D}\mathbf{C}\right). \tag{6.6}$$

The proof concludes after introducing the well known Kummer relation for hypergeometric functions of one matrix argument [235]

$${}_1\widetilde{F}_1\left(a; b; \mathbf{S}\right) = \mathrm{etr}(\mathbf{S})_1\widetilde{F}_1\left(b-a; b; -\mathbf{S}\right). \tag{6.7}$$

It should be pointed out that the above theorem is applicable only to (2×2) quadratic forms since for matrix sizes of $(m \times n)$, a finite summation over a collection of $\binom{n}{m}$ subsets needs to take place. The interested readers are referred to [228] for a detailed discussion. A simplified formula can now be obtained for the first-order moment of the determinant after applying the determinant representation of the hypergeometric function.

Corollary 1: For $\upsilon = 1$, (6.1) reduces to

$$E\left[|\mathbf{Q}|\right] = 2|\mathbf{\Sigma\Psi}|\left(1 + \frac{1}{2}\mathrm{tr}(\mathbf{\Theta}) + \frac{1}{2}\det\left(\mathbf{\Theta}\right)\right). \tag{6.8}$$

Proof: The authors in [198] showed that for any square matrix $\mathbf{B} \in \mathbb{C}^{m\times m}$, its hypergeometric function ${}_1\widetilde{F}_1\left(c; d; \mathbf{B}\right)$ can be expressed according to

$${}_1\widetilde{F}_1\left(c; d; \mathbf{B}\right) = \frac{\det\left({}_1\widetilde{F}_1\left(c-m+j; d-m+j; b_i\right) b_i^{j-1}\right)}{\prod_{i<j}(b_j - b_i)} \tag{6.9}$$

where $b_1, b_2, \ldots, b_m$ is the set of non-zero eigenvalues of $\mathbf{B}$. After taking into account the following properties for the scalar hypergeometric functions

$$\begin{aligned} {}_1\widetilde{F}_1(-2, 1; z) &= 1 - 2z + \frac{1}{2}z^2 & (6.10)\\ {}_1\widetilde{F}_1(-1, 2; z) &= 1 - \frac{1}{2}z^2 & (6.11) \end{aligned}$$

it is trivial to show that for the dual case under consideration

$${}_1\widetilde{F}_1\left(-1; 2; -\mathbf{\Theta}\right) = \frac{1}{2}\left(2 + \theta_1 + \theta_2 + \theta_1\theta_2\right) \tag{6.12}$$

where θ_1, θ_2 are the eigenvalues of $\mathbf{\Theta}$. The proof concludes after recalling that the sum and product of the eigenvalues return the trace and the determinant of a matrix, respectively. It is noteworthy that the same result can be drawn if we represent the hypergeometric function ${}_1\widetilde{F}_1\left(-1; 2; -\mathbf{\Theta}\right)$ via its zonal polynomials, as originally proposed in [234] and amended for the MIMO case in [231, Appendix I].

With regard to the MIMO channel model under consideration, the effects of spatial correlation at both ends can be easily incorporated into the i.i.d. Ricean model given in (5.1). To be more precise, the MIMO transfer channel matrix can now be rewritten according to

$$\mathbf{H} = \sqrt{\frac{K}{K+1}}\mathbf{H}_{\mathrm{L}} + \sqrt{\frac{1}{K+1}}\mathbf{R}_r^{1/2}\mathbf{H}_{\mathrm{W}}\mathbf{R}_t^{1/2}. \tag{6.13}$$

As was highlighted in Chapter 2, this Kronecker-type of modelling is inherently simple and sufficiently accurate when a small number of antenna is used [96]. Most importantly, it is the most common correlation structure model used in the vast majority of related publications [198,

220, 231]. Clearly, the channel matrix is distributed according to

$$\mathbf{H} \sim \mathcal{CN}_{2,2}\left(\sqrt{K/(K+1)}\mathbf{H}_{\mathrm{L}}, (K+1)^{-1}\mathbf{R}_r \otimes \mathbf{R}_t\right). \tag{6.14}$$

It should be noted that for optimised configurations the effects of spatial correlation are rather weak due to the increased antenna spacings. However, in the following analysis the presence of correlation is considered for the fairness of comparison with conventional configurations (more details are given in Section 6.5).

6.3 Ergodic capacity upper bounds

In this section, novel expressions for the upper bound of ergodic capacity based on a power constraint are derived. Let's assume firstly that the Rx has perfect CSI while the Tx knows neither the statistics nor the instantaneous CSI; then the uniform-power allocation ergodic capacity reads [5, 6]

$$\overline{C} \;=\; E\left[\log_2\left(\det\left(\mathbf{I}_2 + \frac{\rho}{2}\mathbf{H}\mathbf{H}^H\right)\right)\right]. \tag{6.15}$$

6.3.1 Double-sided correlated Ricean and Rayleigh fading

In the general case of double-sided correlated Ricean fading, where the channel matrix is distributed according to (6.14), the MIMO correlation matrix $\widetilde{\mathbf{W}} = \mathbf{H}\mathbf{H}^H$ exhibits non-central quadratic form distribution with the following properties

$$\widetilde{\mathbf{W}} \sim \mathcal{CQ}_{2,2}\left(\mathbf{I}_2, \mathbf{R}_r/(K+1), \mathbf{R}_t, \sqrt{K/(K+1)}\mathbf{H}_{\mathrm{L}}\right). \tag{6.16}$$

The following theorem returns an upper bound on the ergodic capacity of a double-sided correlated dual MIMO Ricean system.

Theorem 2: The ergodic capacity in bits/s/Hz of a (2×2) double-sided correlated MIMO Ricean channel with mean matrix $\sqrt{\frac{K}{K+1}}\mathbf{H}_{\mathrm{L}}$, receive correlation matrix $(K+1)^{-1}\mathbf{R}_r$ and transmit correlation matrix $\mathbf{R}_t$ is analytically upper bounded by

$$\overline{C} \leq \log_2\left(1 + 2\rho + \frac{\gamma\rho^2}{2}\right) \tag{6.17}$$

where the parameter γ is given as

$$\gamma = (K+1)^{-2}|\mathbf{R}_r||\mathbf{R}_t|\left(1+\frac{1}{2}\mathrm{tr}(\mathbf{\Theta})+\frac{1}{2}\det\left(\mathbf{\Theta}\right)\right) \tag{6.18}$$

with

$$\mathbf{\Theta} \;=\; K\mathbf{R}_t^{-1}\mathbf{R}_r^{-1/2}\mathbf{H}_{\mathrm{L}}{\mathbf{H}_{\mathrm{L}}}^H\left(\mathbf{R}_r^{-1/2}\right)^H. \tag{6.19}$$

Proof: An alternative way to express the ergodic MIMO capacity is through the real positive eigenvalues $\widetilde{w}_1, \widetilde{w}_2$ of $\widetilde{\mathbf{W}}$ which, in practice, represent the power carried by each spatial sub-channel. Then, (2.16) can be rewritten as

$$\overline{C} = E\left[\log_2\left(1+\frac{\rho}{2}\widetilde{w}_1\right)\left(1+\frac{\rho}{2}\widetilde{w}_2\right)\right]. \tag{6.20}$$

Expanding (2.17), to get

$$\overline{C} = E\left[\log_2\left(1+\frac{\rho}{2}(\widetilde{w}_1+\widetilde{w}_2)+\frac{\rho^2}{4}\det\left(\widetilde{\mathbf{W}}\right)\right)\right]. \tag{6.21}$$

Taking into account that $\log(\cdot)$ is a concave function and making use of the Jensen's inequality the following result is obtained

$$\begin{aligned}\overline{C} \;&\leq\; \log_2\left(1+\frac{\rho}{2}E\left[\widetilde{w}_1+\widetilde{w}_2\right]+\frac{\rho^2}{4}E\left[\det\left(\widetilde{\mathbf{W}}\right)\right]\right)\\ &=\; \log_2\left(1+2\rho+\frac{\rho^2}{4}E\left[\det\left(\widetilde{\mathbf{W}}\right)\right]\right).\end{aligned} \tag{6.22}$$

The second line follows from the widely used power constraint

$$E\left[\|\mathbf{H}\|_F^2\right] = 4 \tag{6.23}$$

or equivalently,

$$E\left[\mathrm{tr}\left(\mathbf{H}\mathbf{H}^H\right)\right] = E\left[\mathrm{tr}\left(\widetilde{\mathbf{W}}\right)\right] = E\left[\widetilde{w}_1+\widetilde{w}_2\right] = 4. \tag{6.24}$$

The upper bound in (6.17) follows immediately after introducing Corollary 1 and simplifying.

As was mentioned in Chapters 3 and 5, the key normalisation in (6.23) has been widely adopted into the capacity characterisation of MIMO systems [5, 6, 222, 231]. With regard to the novel upper bound derived in (6.17), two important remarks should be made. The first one is that the

bound is strictly applicable to dual-branch configurations since for larger MIMO setups we end up with a series of eigenvalue cross-products that are created after expanding (2.17). Secondly, by inspection of (6.17) it can be inferred that the proposed upper bound is rather simple as it just requires the computation of the elementary functions of three different deterministic matrices ($\mathbf{R}_r$, $\mathbf{R}_t$ and $\mathbf{\Theta}$) only once. Comparatively, the bound in [198, Eq. (66)] for arbitrary rank of the LoS component relies on an infinite summation of Hayakawa polynomials and therefore is hard to evaluate either analytically or numerically.

In the case of double-sided correlated Rayleigh fading ($K = 0$), the channel matrix is distributed according to $\mathbf{H} \sim \mathcal{CN}_{2,2}\left(\mathbf{0}_2, \mathbf{R}_r \otimes \mathbf{R}_t\right)$ and the upper bound in (6.17) reduces to

$$\overline{C} \leq \log_2\left(1 + 2\rho + \frac{\rho^2}{2}|\mathbf{R}_r\mathbf{R}_t|\right) \tag{6.25}$$

which is in perfect agreement with the bound derived in [219, Eq. (25)].

6.3.2 Uncorrelated Ricean and Rayleigh fading

For the sake of brevity, the case of single-side correlation is omitted in this chapter since the derivation is based on exactly the same concept as before. Therefore, let's now consider the special case of both ends exhibiting uncorrelated i.i.d. Ricean fading. Under these circumstances, the channel matrix is distributed according to

$$\mathbf{H} \sim \mathcal{CN}_{2,2}\left(\sqrt{\frac{K}{K+1}}\mathbf{H}_{\mathrm{L}}, \frac{1}{K+1}\mathbf{I}_2 \otimes \mathbf{I}_2\right). \tag{6.26}$$

Corollary 2: The ergodic capacity in bits/s/Hz of a (2×2) uncorrelated MIMO Ricean channel with mean matrix $\sqrt{\frac{K}{K+1}}\mathbf{H}_{\mathrm{L}}$ and receive correlation matrix $\mathbf{R}_r = \frac{1}{K+1}\mathbf{I}_2$ is analytically upper bounded by

$$\overline{C} \leq \log_2\left(1 + 2\rho + \frac{\beta\rho^2}{2}\right) \tag{6.27}$$

where $\beta = \left(1 + 2K + 0.5K^2 \det\left(\mathbf{T}\right)\right)/(K+1)^2$ and $\mathbf{T} = \mathbf{H}_{\mathrm{L}}\mathbf{H}_{\mathrm{L}}^H$.

Proof: This corollary is a consequence of (6.17) after taking into account that $\mathbf{\Theta} \equiv K\mathbf{T}$ for the case of uncorrelated fading at both ends. Furthermore, it holds that $\mathrm{tr}\left(K\mathbf{T}\right) = K\mathrm{tr}\left(\mathbf{T}\right)$ and given that the entries of the deterministic LoS component matrix are unit-amplitude complex exponentials, it is trivial to show that $\mathrm{tr}\left(\mathbf{T}\right) = 4$. Likewise, the determinant of $K\mathbf{T}$ may be

expressed as $\det(K\mathbf{T}) = K^2 \det(\mathbf{T})$ which concludes the proof. Note that, the upper bound in (6.27), depends only on $\mathbf{T}$ through the elementary symmetric polynomials of its eigenvalues. This is in agreement with the findings in [231].

The case of i.i.d. Rayleigh fading is obtained directly from (2.31), by setting $K = 0$ and $\mathbf{R}_r = \mathbf{R}_t = \mathbf{I}_2$. The upper bound in (6.27) then reduces to ($\beta = 1$)

$$\overline{C} \leq \log_2\left(1 + 2\rho + \frac{\rho^2}{2}\right) \tag{6.28}$$

which is identical with the results presented in [231, Eq. (5)], [218, Theorem 2] and [219, Eq. (22)].

6.4 Tightness of the upper bound

A crucial characteristic of all capacity bounds is their tightness, or in other words, the offset between the analytical bound and the empirical capacity. In general, the absolute error ϵ inserted by an upper bound U is given as $\epsilon = U - \overline{C}$. In this section, it is shown that the upper bound converges to the true capacity at low SNRs whereas at high SNRs, the offset from the true capacity is analytically determined. In the first case, the following corollary holds:

Corollary 3: The upper bound in (6.17) becomes asymptotically tight as the SNR ρ tends to zero.

Proof: The proof begins with further upper bounding the ergodic capacity in (6.17) according to

$$\overline{C} \leq \frac{1}{\ln 2}\left(2\rho + \frac{\gamma\rho^2}{2}\right) \tag{6.29}$$

where the logarithm property $\ln(1+x) \leq x$ has been used. Following [231] and [236], we can lower bound the ergodic capacity according to [236, Eq. (23)]

$$\begin{aligned}
\overline{C} &\geq E\left[\log_2\left(1 + \frac{\rho}{2}\|\mathbf{H}\|_F^2\right)\right] \\
&\geq \frac{\rho}{2\ln 2} E\left[\|\mathbf{H}\|_F^2\right] - \frac{1}{2\ln 2}\left(\frac{\rho}{2}\right)^2 E\left[\|\mathbf{H}\|_F^4\right] \\
&= \frac{2\rho}{\ln 2} - \frac{\rho^2}{8\ln 2} E\left[\|\mathbf{H}\|_F^4\right].
\end{aligned} \tag{6.30}$$

The second line follows from the property $\ln(1+x) \geq x - \frac{1}{2}x^2$. After subtracting (6.30) from (6.29), the absolute error ϵ of the proposed upper bound becomes

$$\epsilon = \frac{\rho^2}{2\ln 2}\left(\gamma + \frac{1}{4}E\left[\|\mathbf{H}\|_F^4\right]\right) \tag{6.31}$$

which asymptotically tends to zero as $\rho \to 0$.

Corollary 4: As the SNR $\rho \to \infty$, the absolute error inserted by the upper bound in (6.17) tends to

$$\epsilon = \log_2(2\gamma) - E\left[\log_2\left(\det\left(\widetilde{\mathbf{W}}\right)\right)\right]. \tag{6.32}$$

Proof: As $\rho \to \infty$, the upper bound U in (6.17), simplifies to

$$U \approx \log_2(2\gamma) + 2\log_2\left(\frac{\rho}{2}\right). \tag{6.33}$$

In (6.21), the quadratic term becomes significantly larger in the high SNR-regime and therefore the ergodic capacity may be approximated as

$$\begin{aligned}\overline{C} &\approx E\left[\log_2\left(\frac{\rho^2}{4}\det\left(\widetilde{\mathbf{W}}\right)\right)\right] \\ &= 2\log_2\left(\frac{\rho}{2}\right) + E\left[\log_2\left(\det\left(\widetilde{\mathbf{W}}\right)\right)\right].\end{aligned} \tag{6.34}$$

Subtracting (6.34) from (6.33), yields (6.32).

From (6.32), it is apparent that the bound's error is given in a non-analytical form; in this light, the crucial issue is to determine the expectation of the $\log\det$ function of a complex non-central quadratic matrix, which involves a nonlinear $\log$ function. Thus, the following theorem is introduced.

Theorem 3: Let's assume that $\widetilde{\mathbf{W}} \sim \mathcal{CQ}_{2,2}\left(\mathbf{I}_2, \mathbf{R}_r/(K+1), \mathbf{R}_t, \sqrt{K/(K+1)}\mathbf{H}_{\mathrm{L}}\right)$. Then the first-order moment of the logarithm of its determinant is given as

$$\begin{aligned}E\left[\log_2\left(\det\left(\widetilde{\mathbf{W}}\right)\right)\right] = \frac{1}{\ln 2}\Bigg[&\psi(1) + \psi(2) - 2\ln(K+1) + \ln|\mathbf{R}_r\mathbf{R}_t| \\ &- \frac{1}{\theta_1 - \theta_2}\left(\Lambda_1(\boldsymbol{\Theta}) + \Lambda_2(\boldsymbol{\Theta})\right)\Bigg]\end{aligned} \tag{6.35}$$

where θ_1, θ_2 are the eigenvalues of the matrix $\boldsymbol{\Theta}$ which was given in (6.19) while the well

known digamma functions $\psi(x)$ are defined as

$$\psi(x) \triangleq \frac{d}{dx} \ln \Gamma(x) = \frac{\Gamma'(x)}{\Gamma(x)}. \tag{6.36}$$

The polynomial terms $\Lambda_1(\mathbf{\Theta})$ and $\Lambda_2(\mathbf{\Theta})$ are essentially functions of the eigenvalues θ_1 and θ_2 and, in particular

$$\Lambda_1(\mathbf{\Theta}) = \theta_2 h_1(\theta_1) - h_2(\theta_1) \tag{6.37}$$

$$\Lambda_2(\mathbf{\Theta}) = h_2(\theta_2) - \theta_1 h_1(\theta_2) \tag{6.38}$$

where

$$h_1(x) = \sum_{k=0}^{\infty} \frac{\mathcal{P}(k,x)}{k} \tag{6.39}$$

$$h_2(x) = x \sum_{k=0}^{\infty} \frac{\mathcal{P}(k,x)}{k+1} \tag{6.40}$$

with $\mathcal{P}(a,x)$ being the regularised gamma function [237, 6.5.1].

$$\mathcal{P}(a,x) = \frac{1}{\Gamma(a)} \int_0^x t^{a-1} e^{-t} dt = \frac{\gamma(a,x)}{\Gamma(a)} \tag{6.41}$$

where $\gamma(a,x)$ is the lower incomplete gamma function.

Proof: The proof begins with the following key transformation

$$E\left[\ln x\right] = \frac{d}{d\upsilon} E\left[x^{\upsilon}\right]|_{\upsilon=0} \tag{6.42}$$

which holds since, by definition, $x^{\upsilon} = e^{\upsilon \ln x}$. By combining (6.42) and (6.1) and denoting

$$\zeta = E\left[\log_2\left(\det\left(\widetilde{\mathbf{W}}\right)\right)\right] = \frac{1}{\ln 2} E\left[\ln\left(\det\left(\widetilde{\mathbf{W}}\right)\right)\right] \tag{6.43}$$

we can directly get

$$\zeta = \frac{1}{\ln 2} \frac{d}{d\upsilon} \left\{ |(K+1)^{-1} \mathbf{R}_r \mathbf{R}_t|^{\upsilon} \left[\frac{\tilde{\Gamma}_2(\upsilon+2)}{\tilde{\Gamma}_2(2)}\right] {}_1\widetilde{F}_1\left(-\upsilon; 2; -\mathbf{\Theta}\right) \right\} \Bigg|_{\upsilon=0}. \tag{6.44}$$

It can be easily observed that the above differentiation consists of three multiplicative terms. Treating each one separately due to the chain rule, it is trivial to show that the first term results

in $\ln|\mathbf{R}_r\mathbf{R}_t| - 2\ln(K+1)$. The second one, may be rearranged according to

$$\begin{aligned}\frac{d}{d\upsilon}\left\{\frac{\tilde{\Gamma}_2(\upsilon+2)}{\tilde{\Gamma}_2(2)}\right\}\Bigg|_{\upsilon=0} &= \frac{\tilde{\Gamma}_2(\upsilon+2)}{\tilde{\Gamma}_2(2)}\,\frac{d}{d\upsilon}\left\{\ln\left(\tilde{\Gamma}_2(\upsilon+2)\right)\right\}\Bigg|_{\upsilon=0} \\ &= \frac{d}{d\upsilon}\left\{\sum_{i=1}^{2}\ln\left(\Gamma(\upsilon+2-i+1)\right)\right\}\Bigg|_{\upsilon=0} \end{aligned} \tag{6.45}$$

which, after invoking the definition of digamma functions (6.36), readily yields $\psi(1)+\psi(2)$. Focusing now on the last term, we get

$$\begin{aligned}\frac{d}{d\upsilon}\left\{{}_1\widetilde{F}_1\left(-\upsilon;2;-\mathbf{\Theta}\right)\right\}\Bigg|_{\upsilon=0} &= \frac{d}{d\upsilon}\left\{\mathrm{etr}(-\mathbf{\Theta})\,{}_1\widetilde{F}_1\left(\upsilon+2;\upsilon+2;\mathbf{\Theta}\right)\right\}\Bigg|_{\upsilon=0} \\ &= \frac{\frac{d}{d\upsilon}\,{}_1\widetilde{F}_1\left(\upsilon+2;\upsilon;\mathbf{\Theta}\right)\Big|_{\upsilon=0}}{{}_1\widetilde{F}_1\left(\upsilon;\upsilon;\mathbf{\Theta}\right)}. \end{aligned} \tag{6.46}$$

where the second line follows from the property ${}_1\widetilde{F}_1\left(\alpha;\alpha;x\right)=\exp(x)$. The proof concludes after introducing a very useful result from [198, Appendix II] for the nominator in the above equation. Substituting (6.45) and (6.46) into (6.44) and simplifying yields (6.35).

Please note that the derivation of the formula (6.35) relies, without loss of generality, on the assumption of two non-zero eigenvalues of the matrix $\mathbf{\Theta}$. For the case of rank-1 matrices, a similar analysis should be followed; this is however beyond the scope of this chapter and the interested readers are referred to [198] for a detailed discussion. Evidently, after replacing (6.35) into (6.32), we can obtain an analytical formula for the bound's offset at high SNRs, for the general case of double-sided correlated Ricean fading. In addition, this result can be further used to deduce exact capacity expressions in the high-SNR regime. When the channel exhibits i.i.d. Ricean fading and both ends are employed with optimally designed arrays as discussed in Section 5.1, the LoS component yields two equal eigenvalues and thus, the following corollary should be introduced.

Corollary 5: As the SNR $\rho\to\infty$, the absolute error inserted by the upper bound for the case of i.i.d. Ricean fading and optimised LoS configurations tends to

$$\begin{aligned}\epsilon = \log_2(2\beta) - \frac{1}{\ln 2}\Bigg[&\psi(1)+\psi(2)-2\ln(K+1) \\ &+\sum_{k=1}^{\infty}\frac{(2k+1)\gamma(k,\lambda_1)-\lambda_1 e^{-\lambda_1}\lambda_1^{k-1}}{(k+1)!}\Bigg]\end{aligned} \tag{6.47}$$

where $\lambda_1 = \lambda_2$ represents any of the two equal eigenvalues of $\mathbf{\Omega} \equiv K\mathbf{T}$.

Proof: The proof starts by noting that for i.i.d. Ricean fading $\mathbf{\Theta}$ should be replaced by $\mathbf{\Omega} \equiv K\mathbf{T}$ in all manipulations. Further, in the specific case of optimised configurations, the equality of eigenvalues leads to a division by zero in (6.35). In order to circumvent this singularity, *de l'Hôpital's* rule is used to get a solution at the limit $(\lambda_1 \to \lambda_2)$. In particular, the last term in (6.35) can be rewritten as

$$\xi = \lim_{\varepsilon \to 0} \left[\frac{d}{d\varepsilon} \left(\lambda_1 h_1(\lambda_1 + \varepsilon) - h_2(\lambda_1 + \varepsilon) \right) - h_1(\lambda_1) \right]. \tag{6.48}$$

Taking into account that

$$\frac{d}{dx}\mathcal{P}(a,x) = \frac{e^{-x}x^{a-1}}{\Gamma(a)} \tag{6.49}$$

and after some algebraic manipulations we end up with

$$\lim_{\varepsilon \to 0} \frac{d}{d\varepsilon} h_1(\lambda_1 + \varepsilon) = \sum_{k=1}^{\infty} \frac{e^{-\lambda_1}\lambda_1^{k-1}}{k\Gamma(k)} \tag{6.50}$$

$$\lim_{\varepsilon \to 0} \frac{d}{d\varepsilon} h_2(\lambda_1 + \varepsilon) = \sum_{k=1}^{\infty} \frac{e^{-\lambda_1}\lambda_1^{k-1}}{(k+1)\Gamma(k)} + \frac{h_2(\lambda_1)}{\lambda_1}. \tag{6.51}$$

Substituting (6.50)–(6.51) into (6.48),

$$\begin{aligned} \xi &= h_1(\omega) + \frac{h_2(\omega)}{\omega} - \omega e^{-\omega} \sum_{k=1}^{\infty} \frac{\omega^{k-1}}{k(k+1)\Gamma(k)} \\ &= \sum_{k=1}^{\infty} \frac{(2k+1)\gamma(k,\omega) - \omega e^{-\omega}\omega^{k-1}}{k(k+1)\Gamma(k)}. \end{aligned} \tag{6.52}$$

Recalling that for integer n, $\Gamma(n) = (n-1)!$, (6.47) is finally obtained.

6.5 Numerical results

In this section, the theoretical analysis presented in Sections 6.3 and 6.4 is validated through a set of Monte-Carlo simulations. Using exactly the same set of simulations as in Section 5.1.2, i.e. $D_{opt} = 5.3852$ m and $\theta_{opt} = 21.80°$, we examine both an optimised and conventional configuration, whose LoS matrix components are respectively taken through (5.18) and (5.19). Throughout the simulations, the constant correlation model is adopted thanks to its inherent simplicity. The entries of $\mathbf{R}_r$ and $\mathbf{R}_t$ in (2.31) can be modelled as $\{\mathbf{R}_r\}_{i,j} = (\delta_R)^{|i-j|}$ and,

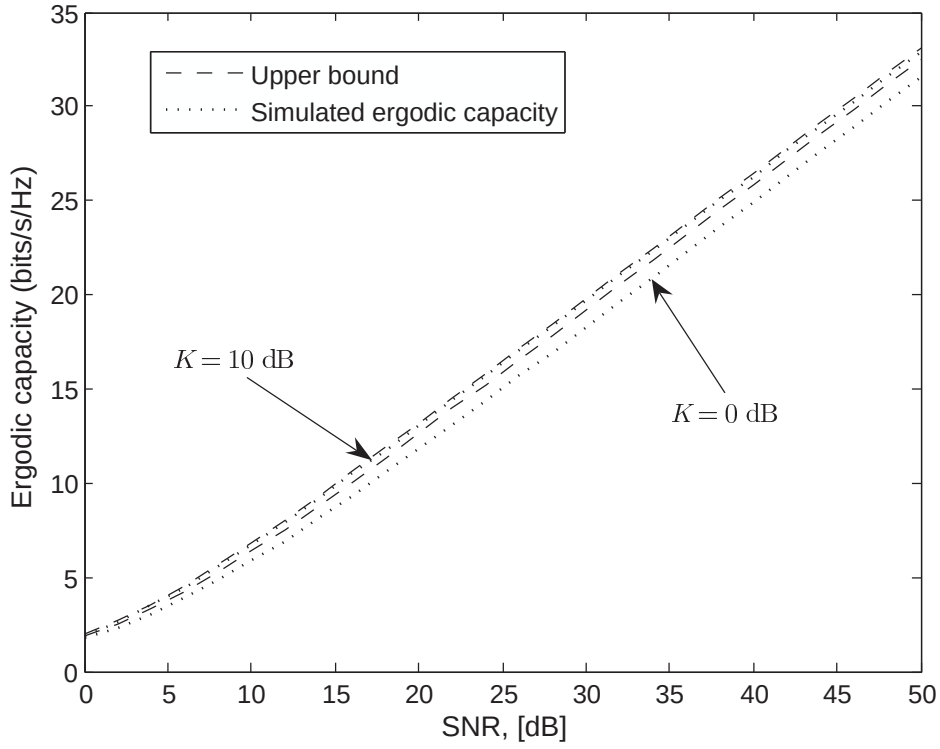

(a) Optimised configuration.

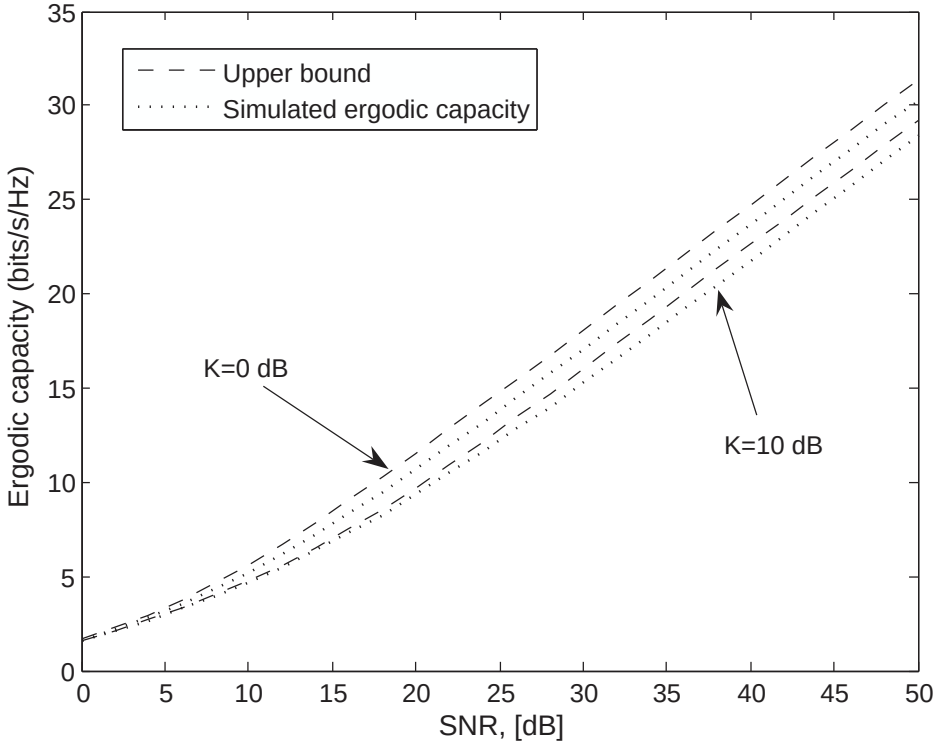

(b) Conventional configuration.

Figure 6.1: *Upper bound and ergodic capacity as a function of the SNR ($\delta_R = 0.2$, $\delta_T = 0.5$).*

in analogy, $\{\mathbf{R}_t\}_{i,j} = (\delta_T)^{|i-j|}$, where $\delta_R, \delta_T \in [0, 1)$. After generating 50,000 Monte-Carlo realizations of the channel matrix according to (2.31) and setting $\delta_R = 0.2$ and $\delta_T = 0.5$, the proposed bound in (6.17) is firstly evaluated against the SNR for different values of K. From Figs. 6.1(a) and 6.1(b), it can be easily seen that the bound is remarkably tight for the optimised configuration and, likewise, performs satisfactorily for conventional configurations. Moreover, at low SNRs both bounds converge asymptotically to the empirical values of ergodic capacity. Generally speaking, the bound becomes tighter as the K-factor increases and SNR decreases which is line with the conclusions drawn in [227, 229, 231]. Once more, the superiority of optimised configurations in the presence of strong deterministic components is indisputable.

As a next step, the effects of the K-factor on the performance of the proposed bound are investigated in Fig. 6.2, where it is again apparent that both bounds become tighter with an increasing K-factor. For Rayleigh-fading conditions though, or $K \leq 0$ dB, the achieved tightness is degraded and, under these circumstances, it is sensible to use more efficient bounds which are inherently tied to Rayleigh channels, like the ones presented in [218–220].

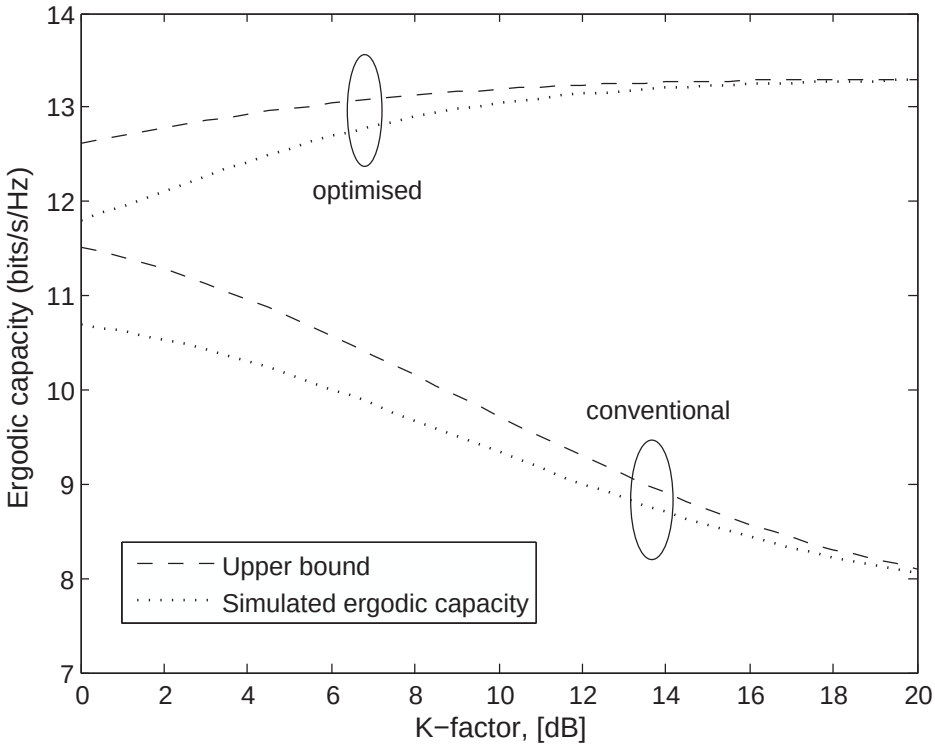

Figure 6.2: *Upper bound and ergodic capacity as a function of the K-factor ($\delta_R = 0.2$, $\delta_T = 0.5$ and $\rho = 20$ dB).*

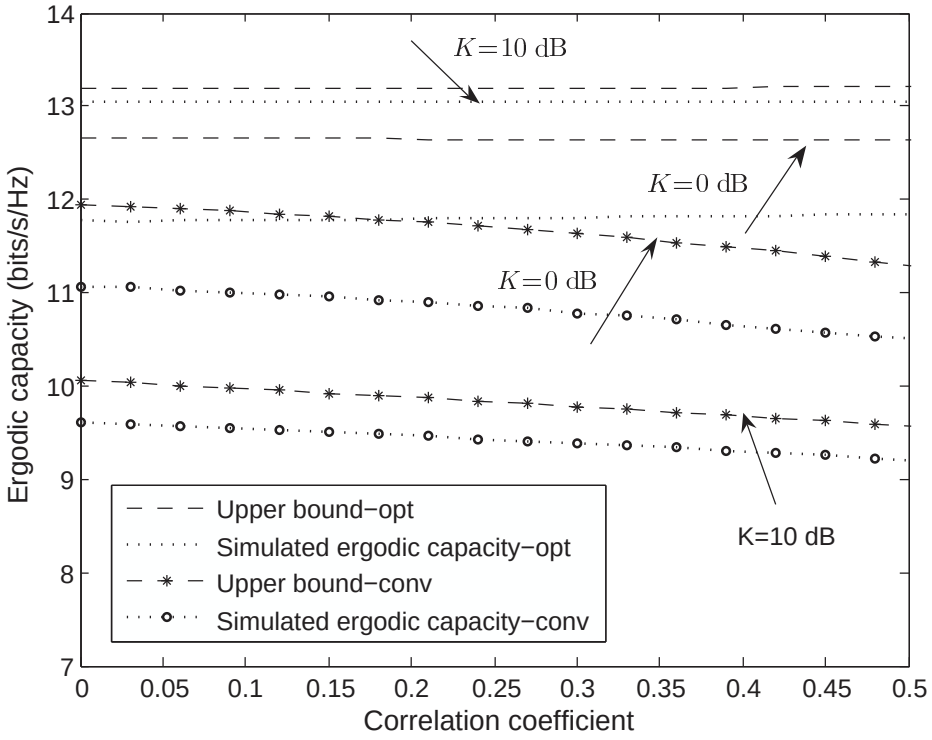

Figure 6.3: *Upper bound and ergodic capacity as a function of the correlation coefficients δ_R and δ_T ($\rho = 20$ dB).*

In Fig. 6.3, the relationship between practical values of spatial correlation and MIMO capacity is addressed. Clearly, the effects of correlation on ergodic capacity become less significant (smaller dynamic range) as the K-factor gets higher for both configurations under investigation, i.e. high K-factors provide robustness against spatial correlation. As expected, the large inter-element spacings make the optimised setup remain unaffected by the level of correlation; hence, it offers almost the same ergodic capacity regardless of the values of δ_R and δ_T. The conventional configuration, however, suffers from spatial correlation with the ergodic capacity decreasing as correlation gets higher. Intuitively, the tightness of the corresponding bound is relatively improved in the high-correlation regime. Please note that this outcome is in agreement with the results initially given in [219, 229, 231].

The absolute error inserted by the proposed bound is now tested against the system SNR and K-factor. The obtained surf plots are depicted in Figs. 6.4(a) and 6.4(b). The main difference between the two error distributions lies in the high-SNR/high-K-factor region. More specifically, when $\rho \geq 20$ dB the bound's error associated with optimised configurations decreases rapidly when $K \geq 5$ dB, whereas that of conventional configurations remains relatively unaf-

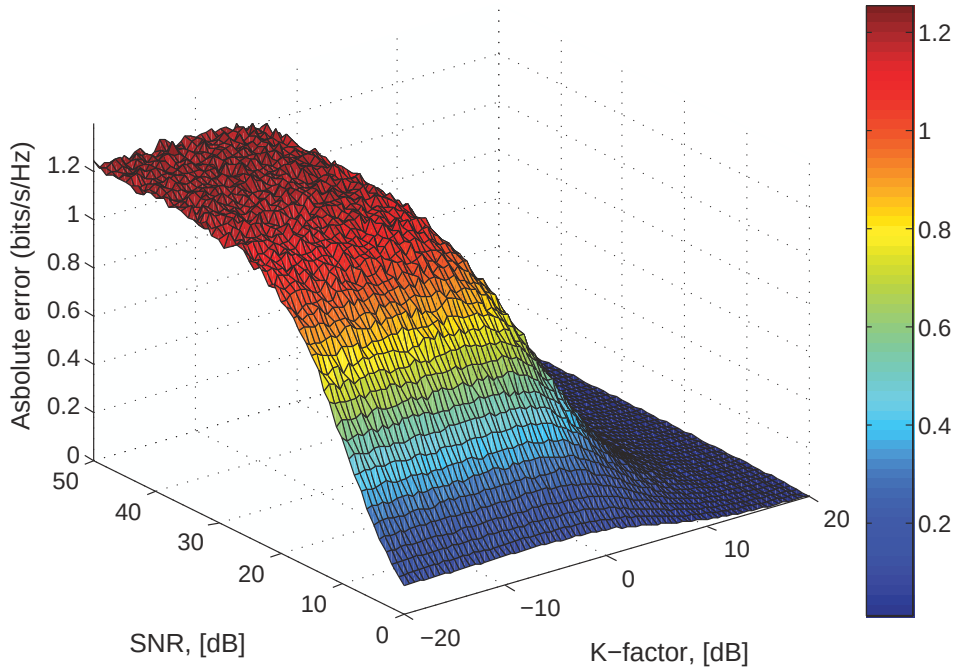

(a) Optimised configuration.

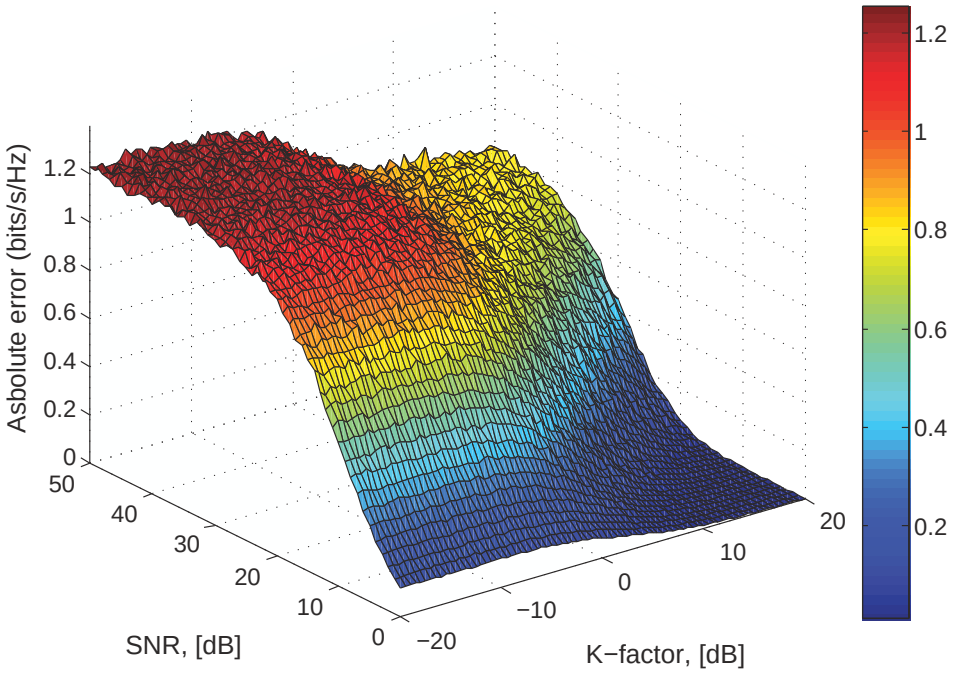

(b) Conventional configuration.

Figure 6.4: *Absolute error of the upper bound as a function of the SNR and K-factor ($\delta_R = 0.2$ and $\delta_T = 0.5$).*

fected. This is a result of the diminishing SNR effects on the ergodic capacity of LoS-optimised, as the K-factor gets higher. In other words, when $K \geq 5$ dB MIMO capacity approaches its maximal value and, consequently, the absolute error tends to decrease, regardless of the system SNR.

At the last stage of the evaluation process, the high-SNR deviation between the ergodic capacity and the proposed upper bound is considered, using the analytical formulae derived in (6.32) and (6.47). In Fig. 6.5, the analytical curves are overlaid with the outputs of a Monte-Carlo simulator with the match being remarkably good, thereby validating the accuracy of the above presented theoretical analysis. The error associated with optimised configurations is constantly lower than that of conventional ones, as a result of the rank-deficiency of the former. What's more, it appears that the latter error has a much smaller dynamic range revealing that a high K-factor does not have an extensive impact on its value. On the other hand, the bound for the optimised configuration yields an enhanced tightness as K increases and under strong Ricean conditions, the corresponding offset is minimised.

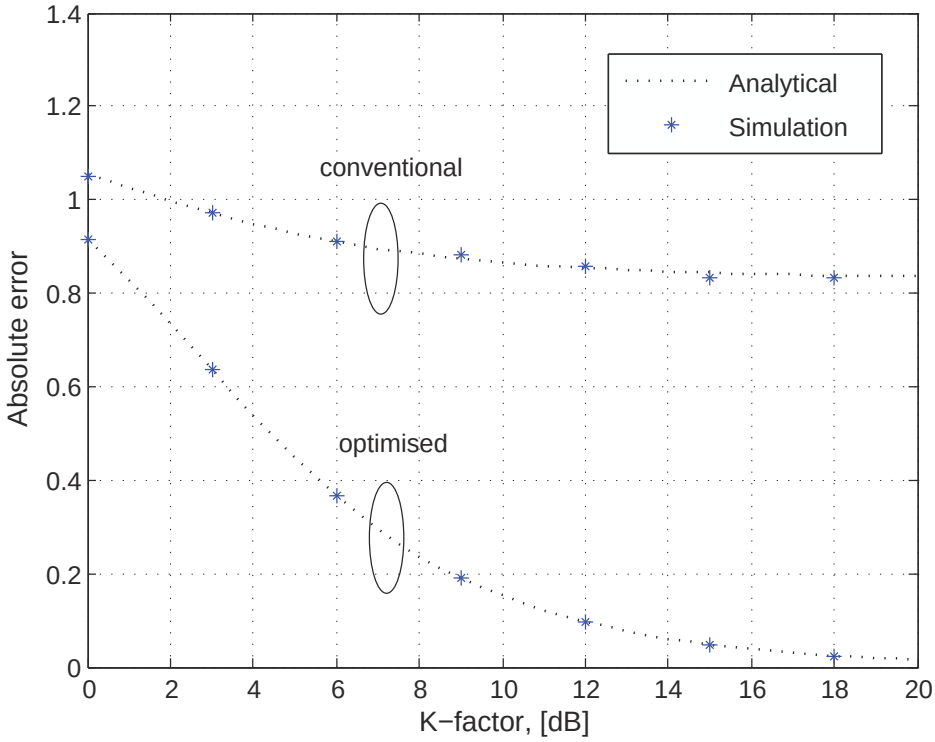

Figure 6.5: *Analytical and simulated absolute error of the upper bound in the high-SNR regime as a function of the K-factor ($\delta_R = 0.2$ and $\delta_T = 0.5$).*

6.6 Summary

In this chapter, the main purpose has been the derivation of a tractable upper bound for the ergodic capacity of dual-branch MIMO Ricean systems with the key concept originating from a widely used power constraint. The first empirical bound depends on the expected value of the determinant of either a non-central quadratic form (double-sided correlated Ricean fading) or non-central Wishart matrix (single-sided correlated and uncorrelated Ricean fading). For this reason, the determinant expectation had to be analytically defined by introducing the determinant representation of hypergeometric functions of one matrix argument. By doing so, the derived analytical bound becomes remarkably simple as it depends only on the elementary symmetric functions of, at most, three deterministic matrices and hence can be very efficiently evaluated. Apart from its inherent simplicity, another advantage of this novel bound is the fact that it is not confined to the common case of rank-1 deterministic LoS components. The simulation results demonstrated that the bound is sufficiently tight for optimised configurations and marginally looser for the conventional setups. The tightness of the bound was finally assessed in the low and high-SNR regions; in the former, the bound becomes asymptotically tight (absolute error tends to zero) whereas in the latter the bound's offset tends to a constant value that was analytically determined and validated through Monte-Carlo trials.

Chapter 7
Conclusions

This thesis has covered a wide range of areas related to modern MIMO wireless communications. It has been shown that its contributions are of both theoretical and practical interest and serve as a good starting point for additional research. In this concluding chapter, all the key findings from different chapters are summarised and several future research routes are suggested.

7.1 Summary of results

In Chapter 3, the Nakagami fading model is developed upon the eigendecomposition of the full spatial MIMO correlation matrix $\mathbf{R_H}$ using the data collected at a 5.2 GHz carrier frequency. The reason behind choosing the Nakagami-m distribution to model the eigenmodes' envelope variations can be attributed to its inherent flexibility that makes it exhibit the best statistical fit with the raw data. Although the computer generation of independent Nakagami-m deviates is broadly viewed as a trivial task, the reality is different; to be more precise, none of the the available known techniques is applicable for any arbitrary values of the shape parameters (m and Ω) or on their whole range. Hence, there was a motivation to introduce a novel rejection-based technique which fulfils both prerequisites and yields a satisfactory efficiency. The goodness of the proposed channel model is tested and compared with that of the Weichselberger and VCR models; the comparative results demonstrate the superiority of the Nakagami fading model from both information theory and error performance perspectives. The performance enhancement over the sophisticated Weichselberger model was found to be 2.2 dB in the case of ergodic and outage capacity and 3 dB in the case of BER mismatch. The VCR model, on the other hand, is unable to capture the spatial activity with accuracy due to the artificial generation of MPCs and, as a result, it systematically overestimates most channel characteristics. As was conjectured in Chapter 3, the Nakagami fading model is particularly important for 5-GHz band WLAN systems as well as for MIMO computer simulations, construction of optimum spatial filtering and design of space-time codes.

Apart from modelling the wireless channel, its characterisation is essential for understanding the spatio-temporal structure of the channel transfer matrix and ultimately predicting the performance of MIMO systems through the radio channel conditions. Intuitively, the extraction of multipath characteristics dictates the development of multi-dimensional channel parameter estimation algorithms; for this reason, in Chapter 4 the 3D FD-SAGE algorithm is introduced that, contrary to most array processing algorithms such as ESPRIT, Unitary ESPRIT and RMUSIC, can be directly applied to any arbitrary antenna geometry provided that the array response is known a priori. The scheme yields a remarkable robustness in a synthetic environment when used in conjunction with the SIC technique. The latter is also incorporated within the initialisation stage to detect the number of dominant MPCs since it poses no restrictions on the model order whereas most of the information theoretic criteria do. Using the same set of measured data as before, the performance of a real-time indoor MIMO channel is investigated in the double directional domain. It is found that the dependency of the two domains grows when a LoS is present or when the Tx faces the Rx and the distance between them is low (OLoS propagation). On the other hand, at NLoS Rx locations the azimuth dispersion gets larger since it benefits from the complex propagation paths' interactions and, in turn, the correlation between the angular domains falls off. It is worth mentioning that the average values tabulated in Table 4.4 serve as a good reference point for the planning of future indoor WLANs.

While the first part of the thesis is focused on indoor channels, the second part is purely devoted to short-range communications where the presence of a deterministic component violates the assumption of Rayleigh fading and the channel entries are Ricean distributed. Under these circumstances, it is widely believed that the beneficial effects of multipath propagation are diminished due to the high level of spatial correlation. However, with appropriate positioning of the antenna elements, the presence of a free-space component seems to strengthen the link so that it delivers high throughput. To this end, in Chapter 5 a 2D maximum capacity criterion is derived for the special case of two-element ULAs at both ends, as a function of the separation distance between the two arrays, their orientations and inter-element spacings on each array. This simplified criterion can be used as a guideline for designing LoS-optimised MIMO systems which can achieve higher capacity than that predicted for an i.i.d. Rayleigh MIMO channel.

Aside from this design methodology, a detailed eigenanalysis of dual-branch MIMO Ricean systems is performed using elements of random matrix theory. The marginal PDF and CDF distributions of the eigenvalues as well as of the condition number are deduced in closed-form

and validated via simulations. These formulae can aid the prediction of the most significant MIMO features, namely the SM ability, ergodic and outage capacity and finally the symbol error and detection performance. As a potential application of the above mentioned theoretical analysis, an AD is proposed so that the high cost and complexity of ML-based receivers is reduced. The scheme offers an extensive complexity reduction along with a satisfactory BER performance even when applied to suboptimum LoS configurations.

In Chapter 6, a tractable analytical upper bound on the ergodic capacity of dual MIMO Ricean systems is derived which, contrary to the majority of similar works documented in literature, is applicable for arbitrary rank of the mean channel matrix. In fact, the bound is evaluated for both a conventional rank-1 and optimal configurations with two equal LoS eigenvalues. In order to allow the formulation of a broad framework, the effects of spatial correlation at both ends are taken into account as well; by doing so, the derived results have not only a higher usability but also include previously published works as special cases. The asymptotic tightness of the bound is also explored where it is shown that as the SNR tends to zero the bound becomes asymptotically tight while it tends to a constant, that is analytically determined, for infinitely high SNRs.

7.2 Future research areas

There are several areas of this thesis that can be expanded at a future stage and some of these are being outlined below:

- In Chapter 3, the author showed the very good match of the Nakagami-m distribution with the indoor measured data. Due to time limitations, only a limited amount of data could be acquired and processed. Additional MIMO measurement trials to further characterise indoor channels in various propagation conditions would lead to greater confidence of the model. Another attractive research area is to extend the model to the wideband case thereby making it appropriate for the investigation of MIMO-OFDM systems. Further, it is quite challenging to explore whether different distributions can offer the same, or even a better, fit with the eigenmodes' envelope distributions. A strong candidate is the Weibull distribution [238] which has been proved to exhibit good fit to experimental fading measurements, for both indoor [239, 240], and outdoor environments [241, 242], and further includes the Rayleigh distribution as a special case.

- Another possible topic to be addressed is the asymptotic error performance of the SAGE algorithm and particularly the determination of the CR lower bound of the estimators. Unfortunately, due to time constraints, the author could not explore the interesting theory of point estimation; as a general rule whatsoever, the Fisher information matrix has firstly to be computed along with the log-likelihood function of the signal model [243] and thereafter the procedure described in [151] should be followed. The algorithm can also be extended to higher dimensions in order to embody the polarisation and Doppler information. From a comparative point of view, the application of the gradient-based ML RIMAX algorithm on the measured data is expected to increase the convergence speed compared to the coordinate-wise search strategy of the SAGE algorithm and further aid the detection of diffuse scattering contributions (see Section 4.6).

- One of the most interesting topics for future research, is the conduction of the first-ever VTR MIMO campaign at the standardised ITS frequency of 5.9 GHz. It is an indisputable fact that this campaign could serve as a very useful starting point for assessing the channel statistics in the joint spatio-temporal-Doppler domain under practical conditions. Nevertheless, the ultimate goal remains the development of new sophisticated channel models based on measurement data which will enrich our understanding of the emerging short-range MIMO communications in fast-varying environments.

- In Chapter 5, the main focus was on dual MIMO Ricean systems with two transmit and receive antennas since, as it was pointed out, these configurations are of high practical relevance thanks to their low setup size and implementation cost. While the criterion derived for maximum MIMO capacity (5.17) retains its straightforward form for a higher number of antennas according to [178], the same does not hold true for the eigenvalue and condition number statistics. Under these circumstances, the simplified relationships for dual systems (5.20), (5.21) and thereof become invalid; as was underlined in Section 5.2.1, the marginal eigenvalue CDF densities for an arbitrary size Wishart matrix can be found in [185]. The estimation, however, of the condition number distributions dictates among others the extraction of the joint density $f(w_1, w_n)$ (assuming a $(m \times n)$ MIMO system with $m \leq n$) which is a non-trivial task. Briefly stated, an appropriate transformation of variables followed by a $n-1$ integrations over all eigenvalue baselines have to take place. The interested reader is referred to [192, Eq. (102)] for additional information on the joint eigenvalue PDF of random size complex Wishart matrices.

- Likewise, the derivation of the upper bound in Chapter 6 is tied to these specific configurations due to the eigenvalue cross-products that are created after expanding the key capacity-eigenvalues relationship (2.17). In any case though, it would be really interesting to expand the semi-correlated analysis of [231], which is entirely based on the elementary functions of the channel correlation matrix, to allow for double-sided correlation. This can be achieved by decomposing the associated matrix into a series of weighted submatrices and thereafter applying some of the results on the moments of elementary functions of quadratic forms, recently presented in [198, 228].

Appendix A
Analytical derivations of eigenvalue and condition number distributions

A.1 Proofs of (5.28) and (5.32)

By inspection, it is noticed that the sum of the two indices of the Nutall-Q function in (5.24) is always odd. In such a case, one can express the Nutall-Q in terms of only a Marcum-Q function and a finite weighted sum of modified Bessel functions, using a result from [244]. Replacing the values $m = n = 2$ and $i = 1$ into [244, Eq. (13)], we get

$$Q_{0+2\cdot 1+1,0}\left(a,b\right) = 2^1 1! L_1^0\left(-\frac{a^2}{2}\right) Q_{0+1}\left(a,b\right) + \exp\left[-\frac{a^2+b^2}{2}\right]$$
$$\times\left\{2^1 1!\left(L_1^0\left(-\frac{a^2}{2}\right) - L_0^0\left(-\frac{a^2}{2}\right)\right)\frac{b}{a} I_1(ab) + bP_{1,1}(b^2) I_0(ab)\right\} \tag{A.1}$$

where, for the sake of simplicity, the same notation has been used as in [244]. This means that $L_k^n(x)$ is the generalized k-th order Laguerre polynomial [244, Eq. (14)] and $P_{k,l}(x)$ is a polynomial of order $k-l$ in x defined in [244, Eq. (10)]. By observing that $L_0^n(x) = 1$, $L_1^0(x) = 1-x$ and $P_{1,1}(x) = 1$, the key equation (5.28) is derived in a straightforward manner. The result in (5.32) can be readily obtained after following the same procedure.

A.2 Proofs of (5.29)–(5.33)

The derivation process relies on the classical formula for the derivative of a determinant, that is [245]

$$\frac{d}{dt}\det\left(\mathbf{B}(t)\right) = \det\left(\mathbf{B}(t)\right)\mathrm{tr}\left(\mathbf{B}^{-1}(t)\frac{d}{dt}\mathbf{B}(t)\right). \tag{A.2}$$

The above relationship is now applied to (5.23) which immediately yields (5.29); the use of the step function guarantees the positivity of the considered eigenvalue. At a next stage, the entries of the matrix $\mathbf{\Phi}(x)$ need to be differentiated with respect to x. The partial derivative of

a Marcum-Q function $Q(a,b)$ with respect to b was derived in [246] as

$$\frac{\partial Q(a,b)}{\partial b} = -bI_0(ab)\exp\left[-\frac{a^2+b^2}{2}\right] \tag{A.3}$$

that gives

$$\frac{\partial Q\left(\sqrt{2\lambda_j},\sqrt{2x}\right)}{\partial x} = -I_0(2\sqrt{\lambda_j x})\exp\left[-(\lambda_j+x)\right]. \tag{A.4}$$

The fundamental formulae for the derivatives of modified Bessel functions are also being used

$$\frac{\partial I_q(z)}{\partial z} = \frac{1}{2}\left(I_{q-1}(z)+I_{q+1}(z)\right) \tag{A.5}$$

$$\frac{\partial I_0(z)}{\partial z} = I_1(z). \tag{A.6}$$

Combining (A.3)–(A.6) with (5.28) and after some manipulations, it is trivial to calculate the entries of $\mathbf{\Psi}(w_2)$. The result for the largest eigenvalue is readily obtained after following the same procedure for the entries of $\mathbf{\Xi}(x)$.

A.3 Proofs of (5.37) and (5.45)

Starting with the joint eigenvalue PDF $f(w_1,w_2)$, the following transformation of variables is applied to estimate the marginal PDF of the condition number $z = w_1/w_2$ [123, Eq. (6.43)]

$$f_z(z) = \int_0^\infty w_2 f(zw_2,w_2)dw_2. \tag{A.7}$$

By substituting (5.20) into (A.7), the integral becomes

$$f_z(z) = e^{-(\lambda_1+\lambda_2)}(z-1)^2\int_0^\infty w_2^3 e^{-w_2(z+1)}{}_0\widetilde{F}_1\left(2;\boldsymbol{\lambda},\mathbf{w}'\right)dw_2 \tag{A.8}$$

where $\mathbf{w}' = (zw_2,w_2)$. If (5.21) is introduced in the analysis, the following relationship is obtained

$${}_0\widetilde{F}_1\left(2;\boldsymbol{\lambda},\mathbf{w}'\right) = \frac{\det\left({}_0F_1\left(1;w_i'\lambda_j\right)\right)}{w_2(\lambda_1-\lambda_2)(z-1)} \tag{A.9}$$

which leads to a simplified version of (A.8)

$$f_z(z) = \frac{e^{-(\lambda_1+\lambda_2)}(z-1)}{\lambda_1-\lambda_2}\int_0^\infty w_2^2 e^{-w_2(z+1)}\det\left({}_0F_1\left(1;w_i'\lambda_j\right)\right)dw_2. \tag{A.10}$$

For the dual case, (5.22) reduces to

$$ {}_0F_1(1;x) = I_0\left(2\sqrt{x}\right) \tag{A.11} $$

and therefore

$$ f_z(z) = \frac{e^{-(\lambda_1+\lambda_2)}(z-1)}{\lambda_1-\lambda_2} \int_0^\infty w_2^2 e^{-w_2(z+1)} \det\left(I_0\left(2\sqrt{w_i'\lambda_j}\right)\right) dw_2 \tag{A.12} $$

or

$$ \begin{aligned} f_z(z) = \frac{e^{-(\lambda_1+\lambda_2)}(z-1)}{\lambda_1-\lambda_2} \times \Bigg[& \int_0^\infty w_2^2 e^{-w_2(z+1)} I_0\left(2\sqrt{zw_2\lambda_1}\right) I_0\left(2\sqrt{w_2\lambda_2}\right) dw_2 \\ & - \int_0^\infty w_2^2 e^{-w_2(z+1)} I_0\left(2\sqrt{zw_2\lambda_2}\right) I_0\left(2\sqrt{w_2\lambda_1}\right) dw_2 \Bigg]. \end{aligned} \tag{A.13} $$

To the best of the author's knowledge, there is no analytical solution for the integrals involved in (A.13); in light of this fact, the zeroth-order modified Bessel function is expressed as an infinite sum of powers according to

$$ I_0(x) = \sum_{k=0}^{\infty} \left(\frac{1}{k!}\right)^2 \left(\frac{x}{2}\right)^{2k} \tag{A.14} $$

which results in

$$ \begin{aligned} f_z(z) = \frac{e^{-(\lambda_1+\lambda_2)}(z-1)}{\lambda_1-\lambda_2} \times \Bigg[& \int_0^\infty w_2^2 e^{-w_2(z+1)} \sum_{k=0}^{\infty}\sum_{n=0}^{\infty} \frac{(\lambda_1 z)^k \lambda_2^n w_2^{k+n}}{(k!n!)^2} dw_2 \\ & - \int_0^\infty w_2^2 e^{-w_2(z+1)} \sum_{k=0}^{\infty}\sum_{n=0}^{\infty} \frac{(\lambda_2 z)^k \lambda_1^n w_2^{k+n}}{(k!n!)^2} \Bigg]. \end{aligned} \tag{A.15} $$

The summation is directly interchanged with the integration and taking into account the following straightforward formula

$$ \int_0^\infty x^p e^{-ax} dx = \frac{\Gamma(p+1)}{a^{p+1}} \tag{A.16} $$

the proof of (5.37) is concluded.

The derivation of (5.45) represents essentially an extension to the analysis presented above. To be more precise, by combining (5.44) with (A.7) we get

$$f_z(z) = \lambda_1^{-1/2} e^{-2\lambda_1}(z-1) \times \left[\int_0^\infty \sqrt{z} w_2^{5/2} e^{-w_2(z+1)} I_1\left(2\sqrt{z\lambda_1 w_2}\right) I_0\left(2\sqrt{\lambda_1 w_2}\right) dw_2 \right.$$
$$\left. - \int_0^\infty w_2^{5/2} e^{-w_2(z+1)} I_1\left(2\sqrt{\lambda_1 w_2}\right) I_0\left(2\sqrt{z\lambda_1 w_2}\right) dw_2 \right]. \tag{A.17}$$

Once more, the infinite series representation of a first-order modified Bessel function of the first kind is adopted according to

$$\begin{aligned} I_1(x) &= \frac{x}{2} \sum_{k=0}^{\infty} \frac{1}{k!\Gamma(k+2)} \left(\frac{x}{2}\right)^{2k} \\ &= \frac{x}{2} \sum_{k=0}^{\infty} \frac{1}{k!^2(k+1)} \left(\frac{x}{2}\right)^{2k}. \end{aligned} \tag{A.18}$$

Substituting (A.14) and (A.18) into (A.17) one can obtain

$$\begin{aligned} f_z(z) &= \lambda_1^{-1/2} e^{-2\lambda_1}(z-1) \left[\int_0^\infty z w_2^{5/2} e^{-w_2(z+1)} \sqrt{\lambda_1 w_2} \sum_{k=0}^{\infty} \sum_{n=0}^{\infty} \frac{z^k \left(\lambda_1 w_2\right)^{k+n}}{(k!n!)^2(k+1)} dw_2 \right. \\ &\quad \left. - \int_0^\infty w_2^{5/2} e^{-w_2(z+1)} \sqrt{\lambda_1 w_2} \sum_{k=0}^{\infty} \sum_{n=0}^{\infty} \frac{z^n \left(\lambda_1 w_2\right)^{k+n}}{(k!n!)^2(k+1)} dw_2 \right] \end{aligned} \tag{A.19}$$

which after making use of (A.16) and some trivial manipulations returns (5.45).

Appendix B
Original publications

B.1 Journal papers

[J1] **M. Matthaiou**, Y. Kopsinis, D. I. Laurenson, and A. M. Sayeed, "Novel ergodic capacity upper bound for dual-branch MIMO Ricean systems," *submitted to IEEE Transactions on Communications*, August 2008.

[J2] †**M. Matthaiou**, D. I. Laurenson, and C. -X. Wang, "On analytical derivations of the condition number distributions of dual non-central Wishart matrices," *IEEE Transactions on Wireless Communications*, accepted for publication, October 2008.

[J3] **M. Matthaiou**, D. I. Laurenson, and J. S. Thompson, "Detailed characterisation of an indoor MIMO channel in the double directional spatial domain," *in press IET Microwaves, Antennas & Propagation*, 2008.

[J4] **M. Matthaiou**, N. Razavi-Ghods, D. I. Laurenson, and S. Salous, "Dual frequency MIMO measurements in the 2.26-2.5 GHz band," *John Wiley's Special Issue on Wireless Communications and Mobile Computing*, vol. 8, no. 5, pp. 607–614, June 2008 **(invited paper)**.

[J5] †**M. Matthaiou**, D. I. Laurenson, and J. S. Thompson, "A MIMO channel model based on the Nakagami-faded spatial eigenmodes," *IEEE Transactions on Antennas and Propagation*, vol. 56, no. 5, pp. 1494–1497, May 2008.

[J6] †**M. Matthaiou** and D. I. Laurenson, "Rejection method for generating Nakagami-m independent deviates," *IET Electronics Letters*, vol. 43, no. 25, pp. 1474–1475, December 2007.

†These papers are reprinted in this appendix.

B.2 Conference papers

[C1] †**M. Matthaiou**, D. I. Laurenson, and C. -X. Wang, "Reduced complexity detection for Ricean MIMO channels based on condition number thresholding," in *Proc. IEEE International Wireless Communications and Mobile Computing Conference (IWCMC)*, Crete, Greece, August 2008, pp. 988–993.

[C2] **M. Matthaiou**, D. I. Laurenson, and C. -X. Wang, "Capacity study of vehicle-to-roadside MIMO channels with a line-of-sight component," in *Proc. IEEE Wireless Communications and Networking Conference (WCNC)*, Las Vegas, USA, March 2008, pp. 775–779.

[C3] **M. Matthaiou**, N. Razavi-Ghods, D. I. Laurenson, and S. Salous, "An insight into the estimation of MIMO propagation parameters using the SAGE algorithm," in *Proc. IEEE European Conference on Antennas and Propagation (EuCAP)*, Edinburgh, U.K., November 2007 **(invited paper)**.

[C4] **M. Matthaiou**, D. I. Laurenson, and J. S. Thompson, "Stochastic modelling of MIMO channels using the spatial eigenmodes," in *Proc. IET Seminar on Smart Antennas and Cooperative Communications*, London, U.K., October 2007.

[C5] **M. Matthaiou**, D. I. Laurenson, N. Razavi-Ghods, and S. Salous, "Characterization of an indoor MIMO channel in frequency domain using the 3D-SAGE algorithm," in *Proc. IEEE International Conference on Communications (ICC)*, Glasgow, U.K., June 2007, pp. 5868–5872.

[C6] **M. Matthaiou**, N. Razavi-Ghods, D. I. Laurenson, and S. Salous, "Frequency correlation of an indoor MIMO channel," in *Proc. IEEE European Conference on Antennas and Propagation (EuCAP)*, Nice, France, June 2006.

[C7] **M. Matthaiou**, D. I. Laurenson, N. Razavi-Ghods, and S. Salous, "Dual frequency MIMO measurements in the 2.26-2.5 GHz band," in *Proc. IEEE International Symposium on Wireless Communication Systems (ISWCS)*, Valencia, Spain, September 2006, pp. 612–615.

On Analytical Derivations of the Condition Number Distributions of Dual Non-Central Wishart Matrices

Michail Matthaiou, *Member, IEEE,* David I. Laurenson, *Member, IEEE,*
and Cheng-Xiang Wang, *Member, IEEE*

***Abstract*—In this paper, we explore the statistical characterization of Multiple-Input Multiple-Output (MIMO) channel correlation matrices with the main focus being on their condition number statistics. More specifically, novel expressions are derived for the probability density function (PDF) and cumulative distribution function (CDF) of the MIMO condition number. Contrary to the majority of related studies, where only the common case of Rayleigh fading was considered, our investigation is extended to account for the generalized case of Ricean fading where a deterministic Line-of-Sight (LoS) component exists in the communication link. The overall analysis is based on the principles of random matrix theory and particularly of dual complex non-central Wishart matrices; the latter represent a practical class of MIMO systems, namely dual-branch systems which are equipped with two transmit and receive antenna elements. All the derived formulae are validated through extensive simulations with the attained accuracy being remarkably good.**

***Index Terms*—MIMO systems, non-central Wishart matrices, condition number, Ricean fading.**

I. Introduction

IT is an indisputable fact that, nowadays, Multiple-Input Multiple-Output (MIMO) systems are considered as a hot topic in the area of wireless communications. The pioneering works of Foschini [1] and Telatar [2] demonstrated the extensive performance enhancement when multiple antenna elements are used at both ends of a radio link. While a considerable amount of research effort has been devoted to the study of MIMO technology, there are still some open aspects that have not been addressed. One of the most interesting topics is the eigenanalysis of the MIMO correlation matrix and especially the statistical determination of its condition number, commonly defined as the ratio of the largest to the smallest eigenvalue. In the MIMO context, the condition number indicates the multipath richness of the channel [3] and has also been shown to drastically affect the detection and error performance in spatial multiplexing (SM) systems [4], [5]. Hence, a detailed knowledge of the condition number statistics is highly desirable since it will shed some light into the efficient characterization of the promising MIMO technology. We point out that throughout the paper our main interest lies in *dual-branch* (or simply *dual*) MIMO configurations, which are expected to be employed in the majority of future practical systems (e.g. hand-held devices), thanks to their small size and low complexity/implementation cost.

In order to conduct the above mentioned analysis, we have resorted to the use of complex Wishart matrices which have recently attracted considerable interest following the rapid development of MIMO systems. Most studies dealing with the application of Wishart matrix theory on MIMO systems elaborate on the common case of a rich scattering environment where no Line-of-Sight (LoS) component is present and the inter-element spacings are assumed to be sufficiently high; under these conditions, the entries of the channel matrix exhibit uncorrelated Rayleigh fading [1], [2], [6] and in practice we end up with the simplified case of complex central (zero-mean) Wishart matrices. The presence of a specular wavefront or a strong direct component though, violates the assumption of Rayleigh fading and the channel is said to be Ricean distributed instead. Surprisingly, despite their practical relevance, few results have been reported focusing on the eigenstatistics of Ricean channels. This fact can be attributed to the difficulty in manipulating hypergeometric functions with two matrix arguments of non-central Wishart matrices compared to the one matrix argument of central Wishart matrices [7].

With regard to the condition number statistics, we primarily recall the seminal work of Edelman [8] which revealed the vital importance of the condition number as a metric of the matrix ill-condition. However, his analysis was limited to the case of (2×2) central Wishart matrices with unit variance where the generalized work of Ratnarajah *et al.* [9] accounted for matrices of random size and with arbitrary variance. An interesting approach to model the temporal transition probabilities of the condition number using a finite-state Markov process can be found in [10]; more importantly, it was shown that the CDF of the logarithm of the condition number can be approximated particularly well via a gamma variable. Yet, all the above cited papers ([8]–[10]) were limited to Rayleigh-fading MIMO channels while the extension to Ricean-fading channels remains an open problem. On this basis, in the present study we explore the statistics of the condition number of a dual non-central Wishart matrix and introduce closed-form formulae for its PDF and CDF as weighted sums of polynomials. For the sake of completeness, two different cases are assessed with the classification being based on the

Manuscript received July 2, 2008; revised October 11, 2008; accepted October 23, 2008. The associate editor coordinating the review of this paper and approving it for publication was Dr. Huaiyu Dai.

M. Matthaiou was with the Institute for Digital Communications, The University of Edinburgh, U.K. He is now with the Institute for Circuit Theory and Signal Processing, Technische Universität München, Arcistrasse 21, 80333, Munich, Germany (email: matthaiou@nws.ei.tum.de).

D. I. Laurenson is with the Institute for Digital Communications, Joint Research Institute for Signal and Image Processing, The University of Edinburgh, EH9 3JL, Edinburgh, U.K. (e-mail: Dave.Laurenson@ed.ac.uk).

C. -X. Wang is with the Joint Research Institute for Signal and Image Processing, School of Engineering and Physical Sciences, Heriot-Watt University, EH14 4AS, Edinburgh, U.K. (e-mail: Cheng-Xiang.Wang@hw.ac.uk).

eigenvalues of the LoS matrix component (distinct or equal). As potential applications of our theoretical analysis, we can expect that it can facilitate the prediction of capacity and link-level performance of MIMO channels as well as the design of space-time codes and MIMO simulations.

The remainder of the paper is organized as follows: In Section II, the fundamental properties of the theory of Wishart matrices are outlined. In Section III, new expressions for the condition number distributions are derived. In Section IV, the underlying MIMO Ricean channel model used throughout the paper is discussed followed by the numerical results as obtained by Monte-Carlo simulations. Finally, Section V concludes the paper and summarizes the key findings.

A note on notation: We use upper and lower case boldfaces to denote matrices and vectors, respectively while $\mathbb{C}$ will denote the set of complex-valued numbers. The nomenclature $\sim \mathcal{CN}(\mathbf{X}, \mathbf{Y})$ stands for a complex normally distributed matrix with mean $\mathbf{X}$ and covariance $\mathbf{Y}$. An $(n \times n)$ identity matrix is expressed as $\mathbf{I}_n$ while the all-zero $(n \times m)$ matrix as $\mathbf{0}_{n\times m}$. The symbols $(\cdot)^H$ and $(\cdot)^{-1}$ correspond to Hermitian transposition and matrix inversion whereas $\otimes$ is the Kronecker product. Finally, $\det(\cdot)$ and $\|\cdot\|_F$ respectively return the matrix determinant and Frobenius norm.

II. Non-Central Wishart Matrices

As was previously highlighted, we are particularly interested in dual complex non-central Wishart matrices. In such a case, a (2×2) complex normal random matrix $\mathbf{H}$ is considered which is distributed according to $\mathbf{H} \sim \mathcal{CN}(\mathbf{M}, \mathbf{\Sigma} \otimes \mathbf{I}_2)$. The matrix $\mathbf{\Sigma} = \sigma^2\mathbf{I}_2$ is the correlation matrix containing the variances σ^2 of the entries of $\mathbf{H}$ on its main diagonal. The so-called instantaneous MIMO correlation matrix is defined as $\widetilde{\mathbf{W}} = \mathbf{H}\mathbf{H}^H$ and is said to follow the complex non-central Wishart distribution with two degrees of freedom and non-centrality matrix $\mathbf{\Omega} = \mathbf{\Sigma}^{-1}\mathbf{M}\mathbf{M}^H$, commonly denoted as $\widetilde{\mathbf{W}} \sim \mathcal{CW}_2(2, \mathbf{\Sigma}, \mathbf{\Omega})$[1].

We now consider a scaled version of $\widetilde{\mathbf{W}}$, that is $\mathbf{W} = \mathbf{\Sigma}^{-1}\widetilde{\mathbf{W}}$. Since $\mathbf{W}$ is a (2×2) Hermitian matrix, it has two real ordered eigenvalues $w_1 > w_2 > 0$, whose joint PDF is

$$f(w_1, w_2) = \exp\left[-\sum_{i=1}^{2}(\lambda_i + w_i)\right] {}_0\widetilde{F}_1\left(2; \boldsymbol{\lambda}, \mathbf{w}\right)(w_1 - w_2)^2 \tag{1}$$

where $\boldsymbol{\lambda} = (\lambda_1, \lambda_2)$ contains the real ordered eigenvalues of $\mathbf{\Omega}$ and, in turn, $\mathbf{w} = (w_1, w_2)$; moreover, ${}_0\widetilde{F}_1(.;.,.)$ is the complex hypergeometric function of two matrix arguments [7]. A convenient version of ${}_0\widetilde{F}_1\left(2; \boldsymbol{\lambda}, \mathbf{w}\right)$ for the dual case was given by Gross and Richards [11] as

$${}_0\widetilde{F}_1\left(2; \boldsymbol{\lambda}, \mathbf{w}\right) = \frac{\det\left({}_0F_1\left(1; w_i\lambda_j\right)\right)}{(\lambda_1 - \lambda_2)(w_1 - w_2)} \tag{2}$$

with $I_q(\cdot)$ denoting the qth order modified Bessel function of the first kind and ${}_0F_1(s+1; x)$ is the classical hypergeometric function [12]

$${}_0F_1(s+1; x) = s!x^{-s/2}I_s\left(2\sqrt{x}\right). \tag{3}$$

[1]It should be noted that if $\mathbf{M} = \mathbf{0}_{2\times 2}$ so that $\mathbf{\Omega} = \mathbf{0}_{2\times 2}$, a complex central Wishart matrix is obtained, expressed as $\widetilde{\mathbf{W}} \sim \mathcal{CW}_2(2, \mathbf{\Sigma})$.

III. Statistics of the Condition Number of $\mathbf{W}$

It is well established that the condition number is a metric of the channel rank or of how invertible a given matrix is; a condition number close to one indicates a well-conditioned matrix with almost equal eigenvalues. As the condition number gets larger though, the matrix rank drops and eventually degenerates into a rank-one matrix. Its importance in the area of MIMO communications has been demonstrated in [3]–[5] among others. In the considered case, the condition number of the scaled MIMO correlation matrix $\mathbf{W}$ becomes

$$z = \frac{w_1}{w_2} \geq 1. \tag{4}$$

From an information theory point of view, the impact of the condition number on MIMO capacity can be seen in (5), which returns the instantaneous channel capacity (in bits/s/Hz) assuming perfect channel knowledge at the Rx and no knowledge at the Tx and uniform power allocation [1]

$$\begin{aligned} C &= \log_2\left(\det\left(\mathbf{I}_2 + \frac{\rho}{2}\mathbf{H}\mathbf{H}^H\right)\right) \\ &= \log_2\left(\left(1 + \frac{zw_2}{\alpha}\right)\left(1 + \frac{w_2}{\alpha}\right)\right) \end{aligned} \tag{5}$$

where ρ is the system Signal-to-Noise ratio (SNR) and $\alpha = 2(1 + K)/\rho$. The symbol K stands for the the Ricean K-factor, normally expressing the ratio of the free-space signal power to the power of the scattered waves. From (5), it is evident that there is no analytical one-to-one mapping between MIMO capacity and the condition number. However, their inter-dependency can be numerically evaluated; in Fig. 1, this inter-dependency is illustrated for an SNR of 20 dB[2].

This graph verifies the notion that high-rank channels, or low condition numbers, yield high capacities and vice-versa. To get a deeper understanding, the density and distribution functions of the condition number are now studied for two different cases; the distinction is based on the associated LoS eigenvalues and, in particular, on whether these are identical.

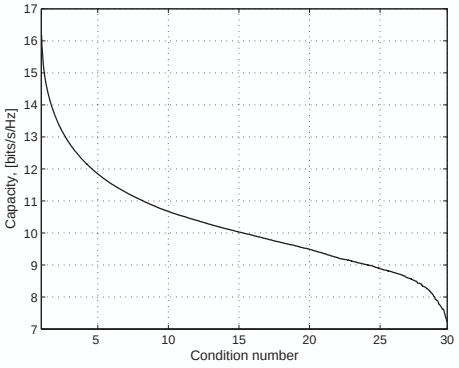

Fig. 1. Capacity evolution as a function of the condition number (SNR = 20 dB).

[2]A more detailed discussion on the simulation settings is provided in Section IV.

1) Case 1 ($\lambda_1 \neq \lambda_2$)*:* We firstly consider the common case of two distinct non-zero LoS eigenvalues $\lambda_1 > \lambda_2$ which reflects any conventional MIMO configuration with no constraint on the rank of the LoS channel matrix. We can show that the PDF of z, $f_z(z)$, can then be expressed as a weighted summation of polynomials given by

$$f_z(z) = \frac{e^{-(\lambda_1+\lambda_2)}(z-1)}{\lambda_1-\lambda_2} \sum_{k=0}^{\infty}\sum_{n=0}^{\infty} \frac{\Gamma(k+n+3)z^k}{(k!n!)^2(z+1)^{k+n+3}} \times \left[\lambda_1^k\lambda_2^n - \lambda_2^k\lambda_1^n\right] \quad (6)$$

with $\Gamma(n)$ denoting the Gamma function which, for the case of an integer index, can be rewritten as $\Gamma(n) = (n-1)!$. The full proof of (6) is provided in Appendix A.

In order to reduce the high computational complexity inserted by the infinite double summation of the above equation, a truncated finite subset of terms may be considered as

$$f_z(z) \approx \frac{e^{-(\lambda_1+\lambda_2)}(z-1)}{\lambda_1-\lambda_2} \sum_{k=0}^{K_s}\sum_{n=0}^{N_s} \frac{\Gamma(k+n+3)z^k}{(k!n!)^2(z+1)^{k+n+3}} \times \left[\lambda_1^k\lambda_2^n - \lambda_2^k\lambda_1^n\right]. \quad (7)$$

The values of K_s and N_s are chosen so that a further increase in the number of coefficients holds negligible impact on the final outcome (less than 0.5% between consecutive steps). It was empirically found that to fulfill this prerequisite with the minimum number of terms, K_s and N_s should be set to the same value. In fact, by adopting this approach the asymptotic result is approximated well with $K_s = N_s = 20$. This observation is verified in Fig. 2, where the evolution of the double summation against the number of terms K_s, N_s is depicted, for four arbitrary values of z.

The corresponding CDF of z, $F_z(x)$, can then be deduced by the PDF as

$$F_z(x) = \int_1^x f_z(z)dz. \quad (8)$$

By substituting (6) into (8) and taking into account the Dominated Convergence Theorem which states that summation and integration can be interchanged, Eq. (9) at the top of the next page is obtained after some basic algebraic manipulations. For the integrals involved in (9), a tractable representation in terms of scalar hypergeometric functions is available in [12, Eq. (3.194)]

$$\int_0^u \frac{t^\mu}{(1+bt)^\nu}dt = \frac{u^{\mu+1}}{\mu+1}{}_2F_1(\nu, \mu+1; \mu+2; -bu) \quad (10)$$

where ${}_2F_1(\alpha, \beta; \gamma; u)$ is the classical Gaussian hypergeometric function defined in [12, Eq. (9.14)]. The CDF of the condition number eventually becomes

$$F_z(x) = \frac{e^{-(\lambda_1+\lambda_2)}}{\lambda_1-\lambda_2} \sum_{k=0}^{\infty}\sum_{n=0}^{\infty} \frac{\Gamma(k+n+3)}{(k!n!)^2}\left[\lambda_1^k\lambda_2^n - \lambda_2^k\lambda_1^n\right] \times \left\{I_1^{k+1,k+n+3}(x) - I_1^{k,k+n+3}(x)\right\} \quad (11)$$

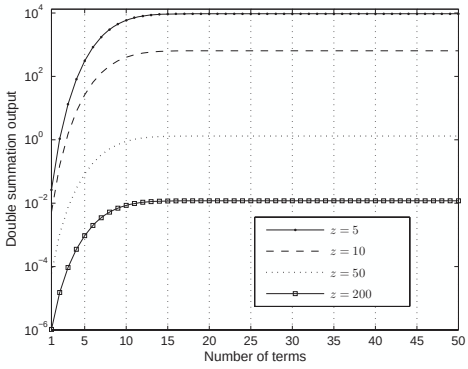

Fig. 2. Convergence of the double summation in (6) for four different values of z.

where

$$I_1^{a,b}(y) = \left(\frac{y^{a+1}}{a+1}\right){}_2F_1(b, a+1; a+2; -y) - \left(\frac{1}{a+1}\right){}_2F_1(b, a+1; a+2; -1). \quad (12)$$

2) Case 2 ($\lambda_1 = \lambda_2$)*:* This is a special class of specifically designed full-rank LoS configurations with extensive practical interest since it offers two equal eigenvalues and thus delivers high capacities in the presence of strong direct components. This is achieved with appropriate positioning of the antenna elements at both ends of the link so that subchannel orthogonality is attained [13]–[15]. This phenomenon is contrary to the common belief that LoS channels represent a hindrance in the area of MIMO communication since they are usually rank-deficient and therefore have only one non-zero eigenvalue. In the case of equal eigenvalues though, the $(\lambda_1 - \lambda_2)$ term in the denominator of (2) becomes zero making the analysis invalid; in order to circumvent this singularity we employ *de l'Hôpital's* rule to get a solution for the limit $(\lambda_1 \to \lambda_2)$. Then, the ordered eigenvalue distribution $f(w_1, w_2)$ becomes [13]

$$f(w_1, w_2) = \lambda_1^{-1/2}e^{-2\lambda_1}(w_1 - w_2)e^{-(w_1+w_2)} \times \left(\sqrt{w_1}I_1\left(2\sqrt{\lambda_1 w_1}\right) I_0\left(2\sqrt{\lambda_1 w_2}\right) - \sqrt{w_2}I_1\left(2\sqrt{\lambda_1 w_2}\right) I_0\left(2\sqrt{\lambda_1 w_1}\right)\right). \quad (13)$$

In Appendix B, it is shown that the PDF of the condition number has the following form

$$f_z(z) = e^{-2\lambda_1}(z-1)\sum_{k=0}^{\infty}\sum_{n=0}^{\infty} \frac{\Gamma(k+n+4)}{(k!n!)^2(k+1)(z+1)^{k+n+4}} \times \left(z^{k+1} - z^n\right). \quad (14)$$

The similarity between the infinite double summations involved in (6) and (14) is apparent and hence the finite subset approximation can be used again. In this case, a similar

$$F_z(x) = \frac{e^{-(\lambda_1+\lambda_2)}}{\lambda_1-\lambda_2}\sum_{k=0}^{\infty}\sum_{n=0}^{\infty}\frac{\Gamma(k+n+3)}{(k!n!)^2}\left[\lambda_1^k\lambda_2^n-\lambda_2^k\lambda_1^n\right] \times\left\{\int_0^x\frac{z^{k+1}}{(z+1)^{k+n+3}}-\int_0^1\frac{z^{k+1}}{(z+1)^{k+n+3}}-\int_0^x\frac{z^k}{(z+1)^{k+n+3}}+\int_0^1\frac{z^k}{(z+1)^{k+n+3}}\right\}. \quad (9)$$

convergence check, as the one performed for (7), revealed that the choice $K_s = N_s = 15$ approximates the asymptotic solution reasonably well. As far as the condition number CDF is concerned, the concept for deriving an analytical expression is exactly the same as in (8)–(12). Thus, it is trivial to show that for the case of equal LoS eigenvalues the condition number CDF is

$$F_z(x) = e^{-2\lambda_1}\sum_{k=0}^{\infty}\sum_{n=0}^{\infty}\frac{\Gamma(k+n+4)}{(k!n!)^2(k+1)}\times\left\{I_1^{k+2,k+n+4}(x) - I_1^{n+1,k+n+4}(x) - I_1^{k+1,k+n+4}(x) + I_1^{n,k+n+4}(x)\right\}. \quad (15)$$

IV. MIMO Channel Model and Numerical Results

The underlying MIMO channel model is now presented for the case of LoS propagation. For an uncorrelated fading scenario, the channel transfer function matrix $\mathbf{H} \in \mathbb{C}^{2\times 2}$ consists of a spatially deterministic component $\mathbf{H}_{\mathrm{L}}$ and a randomly distributed component $\mathbf{H}_{\mathrm{W}}$ which accounts for the scattered signals. Then, the channel model is

$$\mathbf{H} = \sqrt{\frac{K}{K+1}}\mathbf{H}_{\mathrm{L}} + \sqrt{\frac{1}{K+1}}\mathbf{H}_{\mathrm{W}}. \quad (16)$$

A common policy in the analysis of MIMO systems is to normalize the entries of $\mathbf{H}$ so that they have unity energy on average and the mean SNR is independent of the channel matrix. For this reason, $\mathbf{H}_{\mathrm{W}}$ is modeled as a Rayleigh distributed matrix with independent and identically distributed (i.i.d.) circular symmetric zero-mean complex Gaussian variables with unity variance. With regard to the free-space LoS component $\mathbf{H}_{\mathrm{L}}$, its entries can be expressed as $e^{-jkd_{m,n}}/d_{m,n}$, where $k = 2\pi/\lambda$ is the wavenumber corresponding to the carrier wavelength λ and $d_{m,n}$ is the distance between a receive element $m \in \{1,2\}$ and a transmit element $n \in \{1,2\}$. Please note that we have assumed, without loss of generality, isotropic radiators. Regarding the statistical characteristics of $\mathbf{H}$, it can be inferred that $\mathbf{M} = \sqrt{\frac{K}{K+1}}\mathbf{H}_{\mathrm{L}}$ while $\mathbf{\Sigma} = \frac{1}{K+1}\mathbf{I}_2$. Then, it is trivial to show that the Wishart matrix $\widetilde{\mathbf{W}} = \mathbf{H}\mathbf{H}^H$ follows the distribution $\widetilde{\mathbf{W}} \sim \mathcal{CW}_2\left(2, \frac{1}{K+1}\mathbf{I}_2, K\mathbf{H}_{\mathrm{L}}\mathbf{H}_{\mathrm{L}}^H\right)$ and the associated LoS version of interest $\mathbf{W} = (K+1)\widetilde{\mathbf{W}}$.

We can now validate the theoretical analysis presented in Section III through a set of simulations. For the sake of brevity, we consider the more general case of unequal LoS eigenvalues but all the presented results are readily extensible to the case of full-rank LoS configurations. Due to space limitations, we directly consider the LoS suboptimum configuration, as originally given by the authors in [16, Eq. 20], with

$$\mathbf{H}_{\mathrm{L}} = \begin{bmatrix} 0.8384 + j0.5451 & 0.9411 + j0.3380 \\ -0.5123 - j0.8588 & 0.8384 + j0.5451 \end{bmatrix}. \quad (17)$$

This matrix intuitively satisfies the power constraint, i.e. $\|\mathbf{H}_{\mathrm{L}}\|_F^2 = 4$. After generating 50,000 random Monte-Carlo realizations of the channel matrix $\mathbf{H}$ according to (16) and setting the K-factor equal to 5 dB, the ordered eigenvalues of $\mathbf{\Omega}$ were easily computed and thereafter concatenated into the vector $\boldsymbol{\lambda} = (7.0336, 5.6155)$. As a main step of the performance evaluation process, the analytical expressions derived for the statistics of the condition number are validated. In Figs. 3(a) and 3(b), the closed-form relationships (6) and (11) are respectively tested, where it is easily seen that theoretical and simulation results are in remarkable agreement for both cases.

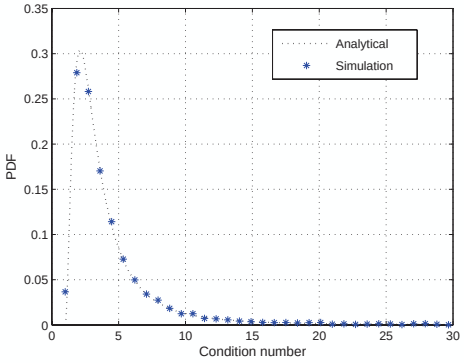

(a) PDF of the condition number.

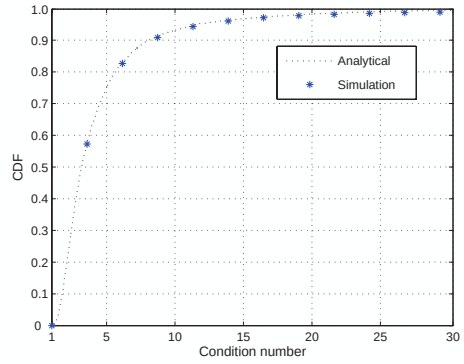

(b) CDF of the condition number.

Fig. 3. Condition number PDF and CDF of a dual complex non-central Wishart matrix.

From inspection of Fig. 1 and Fig. 3, we can also conjecture that for a relatively high percentage of realizations the proposed architecture yields large capacities and outperforms the common i.i.d. Rayleigh system which offers an ergodic capacity of 11.4 bits/s/Hz for the same operating SNR. This observation is consistent with the results presented in [13]–[15] where different optimized architectures were proposed for the case of near-field LoS propagation.

V. Conclusion

In the present contribution, a detailed statistical eigenanalysis of dual-branch MIMO systems has been performed. In detail, we derived the PDF and CDF of the condition number of a dual complex non-central Wishart matrix. This class of matrices has an increasing practical interest since it corresponds to compact MIMO systems with two antenna elements at both ends. The statistics of the condition number were thoroughly explored for a conventional as well as a specifically designed full-rank configuration with equal LoS eigenvalues. All theoretical formulae were tested against the outputs of a Monte-Carlo simulator and it was shown that the match between theory and simulation is excellent. It should be emphasized that all the analytical results presented in this paper can be easily evaluated since the overall complexity burden was kept as low as possible. More importantly, they constitute the basis of the statistical assessment of Ricean MIMO channels and further are very useful tools for determining numerous MIMO characteristics, spanning SM ability to symbol error and detection performance.

Appendix A
Derivation of the PDF of the Condition Number of $\mathbf{W}$ ($\lambda_1 \neq \lambda_2$)

Starting with the joint eigenvalue PDF $f(w_1, w_2)$, we apply the following transformation of variables to estimate the marginal pdf of the condition number $z = w_1/w_2$

$$f_z(z) = \int_0^\infty w_2 f(z w_2, w_2) dw_2. \tag{18}$$

By substituting (1) into (18), the integral becomes

$$f_z(z) = \frac{e^{-(\lambda_1+\lambda_2)}(z-1)}{\lambda_1 - \lambda_2} \int_0^\infty w_2^2 e^{-w_2(z+1)} \, {}_0\widetilde{F}_1\left(2; \boldsymbol{\lambda}, \mathbf{w}'\right) dw_2 \tag{19}$$

where $\mathbf{w}' = (z w_2, w_2)$. If (2) is introduced in our analysis, the following relationship is obtained

$${}_0\widetilde{F}_1\left(2; \boldsymbol{\lambda}, \mathbf{w}'\right) = \frac{\det\left({}_0F_1\left(1; w_i'\lambda_j\right)\right)}{w_2(\lambda_1 - \lambda_2)(z-1)} \tag{20}$$

which leads to a simplified version of (19)

$$f_z(z) = \frac{e^{-(\lambda_1+\lambda_2)}(z-1)}{\lambda_1 - \lambda_2} \int_0^\infty w_2^2 e^{-w_2(z+1)} \det\left({}_0F_1\left(1; w_i'\lambda_j\right)\right) dw_2. \tag{21}$$

For the dual case, (3) reduces to ${}_0F_1(1; x) = I_0\left(2\sqrt{x}\right)$; thus,

$$f_z(z) = \frac{e^{-(\lambda_1+\lambda_2)}(z-1)}{\lambda_1 - \lambda_2} \int_0^\infty w_2^2 e^{-w_2(z+1)} \det\left(I_0\left(2\sqrt{w_i'\lambda_j}\right)\right) dw_2. \tag{22}$$

We can now evaluate (22) as shown in (23) in the next page. To the best of our knowledge, there is no analytical solution for the integrals in (23); in this light, we express the zeroth-order modified Bessel function as an infinite sum of powers according to

$$I_0(x) = \sum_{k=0}^{\infty} \left(\frac{1}{k!}\right)^2 \left(\frac{x}{2}\right)^{2k}. \tag{24}$$

Inserting (24) into (23) and taking into account the following straightforward formula

$$\int_0^\infty x^p e^{-ax} dx = \frac{\Gamma(p+1)}{a^{p+1}} \tag{25}$$

we conclude the proof of (6).

Appendix B
Derivation of the PDF of the Condition Number of $\mathbf{W}$ ($\lambda_1 = \lambda_2$)

The derivation presented herein represents essentially an extension to the analysis of the previous section. To be more precise, by combining (13) with (18) we get (26) at the top of the next page.

Once more, the infinite series representation of a first-order modified Bessel function of the first kind is used according to

$$\begin{aligned} I_1(x) &= \frac{x}{2} \sum_{k=0}^{\infty} \frac{1}{k!\Gamma(k+2)} \left(\frac{x}{2}\right)^{2k} \\ &= \frac{x}{2} \sum_{k=0}^{\infty} \frac{1}{k!^2(k+1)} \left(\frac{x}{2}\right)^{2k}. \end{aligned} \tag{27}$$

After substituting (24) and (27) into (26) and making use of (25), we can directly obtain (14).

References

[1] G. J. Foschini, "Layered space-time architecture for wireless communications in a fading environment when using multiple antennas," *Bell Labs Technical Journal*, vol. 1, no. 2, pp. 41–59, Autumn 1996.

[2] I. E. Telatar, "Capacity of multi-antenna Gaussian channels," *ATT-Bell Labs Internal Technical Memorandum*, June 1995.

[3] V. Erceg, P. Soma, D. S. Baum, and A. J. Paulraj, "Capacity obtained from multiple-input multiple-output channel measurements in fixed wireless environments at 2.5 GHz," in *Proc. International Conference on Communications (ICC)*, vol. 1, New York, USA, May 2002, pp. 396–400.

[4] H. Artes, D. Seethaler, and F. Hlawatsch, "Efficient detection algorithms for MIMO channels: A geometrical approach to approximate ML detection," *IEEE Transactions on Signal Processing*, vol. 51, no. 11, pp. 2808–2820, November 2003.

[5] D. Wubben, R. Bohnke, V. Kuhn, and K. D. Kammeyer, "MMSE-based lattice-reduction for near-ML detection of MIMO systems," in *Proc. ITG Workshop on Smart Antennas*, Munich, Germany, March 2004, pp. 106–113.

[6] Ö. Oyman, R. U. Nabar, H. Bölcskei, and A. J. Paulraj, "Characterizing the statistical properties of mutual information in MIMO channels," *IEEE Transactions on Signal Processing*, vol. 51, no. 11, pp. 2784–2795, November 2003.

[7] A. T. James, "Distributions of matrix variates and latent roots derived from normal samples," *Annals of Mathematical Statistics*, vol. 35, no. 2, pp. 475–501, June 1964.

[8] A. Edelman, *Eigenvalues and condition numbers of random matrices*, Ph.D dissertation, MIT, Cambridge, MA, May 1989.

[9] T. Ratnarajah, R. Vaillancourt, and M. Alvo, "Eigenvalues and condition numbers of complex random matrices," *SIAM Journal on Matrix Analysis and Applications*, vol. 26, no. 2, pp. 441–456, January 2005.

$$f_z(z) = \frac{e^{-(\lambda_1+\lambda_2)}(z-1)}{\lambda_1-\lambda_2} \times \left[\int_0^\infty w_2^2 e^{-w_2(z+1)} I_0\left(2\sqrt{zw_2\lambda_1}\right) I_0\left(2\sqrt{w_2\lambda_2}\right) dw_2 - \int_0^\infty w_2^2 e^{-w_2(z+1)} I_0\left(2\sqrt{zw_2\lambda_2}\right) I_0\left(2\sqrt{w_2\lambda_1}\right) dw_2 \right]. \quad (23)$$

$$f_z(z) = \lambda_1^{-1/2} e^{-2\lambda_1}(z-1) \times \left[\int_0^\infty \sqrt{z} w_2^{5/2} e^{-w_2(z+1)} I_1\left(2\sqrt{z\lambda_1 w_2}\right) I_0\left(2\sqrt{\lambda_1 w_2}\right) dw_2 - \int_0^\infty w_2^{5/2} e^{-w_2(z+1)} I_1\left(2\sqrt{\lambda_1 w_2}\right) I_0\left(2\sqrt{z\lambda_1 w_2}\right) dw_2 \right]. \quad (26)$$

[10] P. -H. Kuo, P. J. Smith, and L. M. Garth, "A Markov model for MIMO channel condition number with application to dual-mode antenna selection," in *Proc. Vehicular Technology Conference (VTC)*, Dublin, Ireland, April 2007, pp. 471–475.

[11] K. I. Gross and D. S. Richards, "Total positivity, spherical series, and hypergeometric functions of matrix argument," *Journal on Approximation Theory*, vol. 59, no. 2, pp. 224–246, 1989.

[12] I. S. Gradshteyn and I. M. Ryzhik, *Table of Integrals, Series, and Products*, Sixth ed. Academic Press, San Diego, 2000.

[13] F. Bøhagen, P. Orten, G. E. Øien, and S. de la Kethulle de Ryhove, "Exact capacity expressions for dual-branch Ricean MIMO systems," *in press IEEE Transactions on Communications.*

[14] F. Bøhagen, P. Orten, and G. E. Øien, "Design of capacity-optimal high-rank line-of-sight MIMO channels," *IEEE Transactions on Wireless Communications*, vol. 6, no. 4, pp. 1420– 1425, April 2007.

[15] M. Matthaiou, D. I. Laurenson, and C. -X. Wang, "Capacity study of vehicle-to-roadside MIMO channels with a line-of-sight component," in *Proc. Wireless Communications and Networking Conference (WCNC)*, Las Vegas, USA, March 2008, pp. 775–779.

[16] —, "Reduced complexity detection for Ricean MIMO channels based on condition number thresholding," in *Proc. International Wireless Communications and Mobile Computing Conference (IWCMC)*, Crete, Greece, August 2008, pp. 988–993.

to the ideal behavior. The termination of the antenna will result in ringing behavior that should be smoothed by an appropriate loading scheme. A partially focused monocone antenna would provide an omnidirectional radiator with the properties of (6), while a partially focused TEM horn would provide one with more gain. The antenna designed by Ameya, *et al.*, seems to accomplish this task by tapering the impedance of the printed monocone.

VI. Conclusion

In this paper we have presented requirements for an UWB antenna that can provide a dispersionless channel when used as both the transmit and receive antenna. The desired antenna would need to closely approximate an ideal, pulsed line source and would radiate a waveform that approximates a half derivative of the applied voltage. We demonstrated that such a waveform could be generated by a current source that is spatially limited by a Gaussian waveform.

Creating an antenna that produces such a pulse is a challenge. We provided a concept that might lead to such an antenna. By noting that a focused aperture antenna radiates a derivative of the applied voltage and a completely unfocused aperture radiates a replica of the applied voltage [4], it was hypothesized that an antenna that is focused in elevation but unfocused in azimuth would create the desired waveform, at least in the vicinity of the antenna. Further analysis of the proposed strategy is warranted. However, recent experimental results using printed monopole antennas seem to indicate that the desired goal can be achieved, at least over a limited range of frequencies [9].

Acknowledgment

The author is grateful to C. J. Buchenauer for numerous fruitful discussions about the concepts presented in this paper, and would like to thank R. Ziolkowski for his comments on the early versions of this manuscript.

References

[1] Z. N. Chen, X. H. Wu, H. F. Li, N. Yang, and M. Y. W. Chia, "Considertations for source pulses and antennas in UWB radio systems," *IEEE Trans. Antennas Propag.*, vol. 52, pp. 1739–1748, Jul. 2004.

[2] T. K. Sarkar, S. Burintramara, N. Yilmazer, S. Hwang, Y. Zhang, A. De, and M. Salazar-Palma, "A discussion about some of the principles/practices of wireless communication under a Maxwellian framework," *IEEE Trans. Antennas Propag.*, vol. 54, pp. 3727–3745, Dec. 2006.

[3] J. R. Andrews, "UWB signal sources, antennas and propagation," Application Note AN-14a, Picosecond Pulse Lab,. Boulder, CO, Aug. 2003 [Online]. Available: http://www.picosecond.com/objects/AN-14a.pdf/

[4] C. J. Buchenauer, J. S. Tyo, and J. S. H. Schoenberg, "Antennas and electric field sensors for ultra-wideband transient measurements: Applications and methods," in *Ultra-Wideband, Short-Pulse Electromagnetics 3*, C. E. Baum, L. Carin, and A. P. Stone, Eds. New York: Plenum, 1997, pp. 405–421.

[5] C. E. Baum, "General properties of antennas," in *Sensor and Simulation Notes #330*. Albuquerque, NM: Phillips Laboratory, 1991.

[6] M. Kanda, "The effects of resitive loading of TEM horns," *IEEE Trans. Electromagn. Compat.*, vol. 24, pp. 245–255, May 1982.

[7] C. E. Baum, E. G. Farr, and D. V. Giri, "Review of impulse-radiating antennas," in *Review of Radio Science*, W. R. Stone, Ed. New York: Oxford Univ. Press, 1999, pp. 403–439.

[8] N. Engheta, "On fractional calculus and fractional multipoles in electromagnetism," *IEEE Trans. Antennas Propag.*, vol. 44, pp. 554–566, Apr. 1996.

[9] M. Ameya, M. Yamamoto, and T. Nojima, "An omnidirectional UWB printed dipole antenna with small waveform distortion," in *Proc. Progress In Electromagnetics Research Symp PIERS 2006*, Tokyo, Japan, Aug. 2006, p. 515.

A MIMO Channel Model Based on the Nakagami-Faded Spatial Eigenmodes

Michail Matthaiou, David I. Laurenson, and John S. Thompson

***Abstract*—We propose a stochastic model for multiple-input multiple-output (MIMO) communication systems based on the eigendecomposition of the spatial correlation matrix. It is shown that the channel matrix can be well modeled by the superposition of the spatial eigenmodes experiencing independent Nakagami-m fading. The proposed scheme is also compared with the existing correlation-based models using the data obtained from an indoor measurement campaign so that its performance is assessed in depth.**

***Index Terms*—Fading channels, multiple-input multiple-output (MIMO) systems, spatial correlation.**

I. Introduction

In recent years, the area of multiple-input multiple-output (MIMO) channel modeling has attracted considerable research interest since a reliable model can in principle predict the propagation mechanisms and ultimately make possible the integration of MIMO technology into real-time applications. On this basis, various stochastic modeling approaches have been proposed in the literature with a view to capturing the spatial behavior at both the transmitter (Tx) and the receiver (Rx).

More specifically, the so called "Kronecker model" [1] assumes that the spatial correlation properties at both ends of the link are separable which can result though in the multipath structure being rendered incorrectly. In other words, it enforces the joint angular power spectrum (APS) to be the product of the direction of arrival (DoA) and direction of departure (DoD) power spectra. The model may give accurate estimates when three or less antenna elements are employed but for larger arrays (and hence an improved angular resolution) its performance deteriorates significantly [2]. However, it has been extensively used for the theoretical analysis and simulations of MIMO systems thanks to its simplicity.

On the other hand, the so called "Weichselberger model" [3] alleviates the deficiencies of the Kronecker model by considering the joint correlation structure of both ends and consequently the average coupling between the spatial subchannels is effectively modeled. Although more robust than the Kronecker model with systems employing more than four antennas, it still falls short of precisely capturing all spatial activity [4], [5]. Yet, the multipath environment is occasionally not reproduced properly resulting in an inaccurate estimate of the joint APS.

In this letter, we present a full spatial correlation model which encompasses a generalized version of the aforementioned approaches and yields a better fit, in terms of statistical metrics, with the measured data. The common assumption of Rayleigh fading, which is often violated in measured channels, is relaxed by considering the more flexible Nakagami-m distribution in order to account for the presence of strong obstructed line-of-sight (LoS) components.

The letter is organized as follows: In Section II, we derive the proposed MIMO channel model in a straightforward manner. In Section III, an indoor MIMO measurement campaign is described. The statistical characteristics as well as the accuracy of the Nakagami-m

Manuscript received May 8, 2007; revised December 17, 2007.

The authors are with the Institute for Digital Communications, Joint Research Institute for Signal and Image Processing, School of Engineering and Electronics, The University of Edinburgh, EH9 3JL, Edinburgh, U.K. (e-mail: M.Matthaiou@ed.ac.uk).

Digital Object Identifier 10.1109/TAP.2008.922708

fading assigned to each eigenmode are addressed in Section IV. The performance of the stochastic model is evaluated in Section V using the measured data. Finally, Section VI summarizes the key findings.

II. MIMO Channel Model

For a flat-fading MIMO system equipped with N transmit and M receive antenna elements, the complex input-output relationship can be written for the discrete case as

$$\mathbf{y} = \mathbf{H}\mathbf{x} + \mathbf{n} \tag{1}$$

where $\mathbf{x} \in \mathbb{C}^{N\times 1}$ is the transmitted signal vector, $\mathbf{y} \in \mathbb{C}^{M\times 1}$ is the noise-corrupted received signal and $\mathbf{n} \in \mathbb{C}^{M\times 1}$ corresponds to the additive noise plus interference. The term $\mathbf{H} \in \mathbb{C}^{M\times N}$ is usually referred to as the channel transfer function matrix and contains the complex responses between all antenna pairs. The full spatial correlation matrix, describing the joint correlation properties of both link ends, is defined as [1]

$$\mathbf{R}_{\mathbf{H}} \triangleq E_{\mathbf{H}}\{\mathrm{vec}(\mathbf{H})\mathrm{vec}(\mathbf{H})^H\} \in \mathbb{C}^{MN\times MN} \tag{2}$$

where the vec$(\cdot)$ operator stacks the columns of a matrix into a vector and $(\cdot)^H$ is the Hermitian transposition. The eigendecomposition of $\mathbf{R}_{\mathbf{H}}$ into a sum of rank-one matrices yields

$$\mathbf{R}_{\mathbf{H}} = \sum_{k=1}^{MN} \lambda_k \mathbf{u}_k \mathbf{u}_k^H \tag{3}$$

where λ_k are the real non zero ordered eigenvalues ($\lambda_1 \geq \lambda_2 \geq \cdots \geq \lambda_{MN} \geq 0$) and $\mathbf{u}_k$ contain the corresponding eigenvectors which are by definition mutually orthogonal and have unit norm. We note that the number of non-zero eigenvalues determines the rank of $\mathbf{R}_{\mathbf{H}}$ which is upper bounded by MN. The eigenvector $\mathbf{u}_k$ can be reshaped column-wise into the matrix $\mathbf{U}_k = \mathrm{unvec}(\mathbf{u}_k) \in \mathbb{C}^{M\times N}$ which we will refer to hereafter as the k-th *eigenmode*. From a physical viewpoint, eigenvalues specify the degree of diversity offered by the channel while eigenmodes, commonly representing a linear combination of propagation paths, are indicative of the spatial multiplexing (SM) ability [3]. Likewise, the channel matrix can be modeled as

$$\mathbf{H}_{\mathrm{mod}} = \sum_{k=1}^{MN} g[k]\sqrt{\lambda_k}\mathbf{U}_k. \tag{4}$$

From (4), we readily infer that the probability density function (pdf) of $g[k]$ expresses the fading variations of the channel. In fact, the fading coefficients $g[k]$ are independent and identically distributed (i.i.d.) random variables satisfying the relationship $E_g\{g[m]g^*[n]\} = \delta_{mn}$, where δ_{mn} is the Kronecker delta function.[1] We underline the fact that the second-order moment of $g[k]$ is assumed to be the same for all k so that the eigenvalues λ_k reflect the power of each eigenmode.

III. Indoor Measurement Campaign

An indoor measurement campaign was carried out in the Electrical Engineering Building in Vienna University of Technology [6]. The measurements were conducted using the MEDAV RUSK ATM channel sounder which was probed at 193 equispaced frequency bins, covering 120 MHz of bandwidth, at a carrier frequency of 5.2 GHz. The Rx employed a uniform linear array (ULA) of eight vertically-polarized elements with an inter-element distance of 0.4λ which was fully calibrated in order to remove the undesired effects of mutual coupling and other array imperfections. At the Tx, an omnidirectional sleeve antenna was moved on a 10×20 rectangular grid with element spacings of 0.5λ. By considering a virtual eight-element ULA on each row, we end up with $13 \times 10 = 130$ spatial realizations of the 8×8 MIMO transfer matrix. Thus, a total set of $130 \times 193 = 25{,}090$ space and frequency realizations per measurement scenario was obtained.

The Rx was placed at 24 locations in several offices while the Tx was fixed in a hallway. In order to capture the whole azimuth domain activity, the Rx was steered to three different directions (spaced by 120°), leading to the generation of 72 data sets, i.e., combinations of Rx positions and directions.

IV. Nakagami-M Fading Characteristics

Intuitively, the main concept behind the proposed model (4) originates from the well-known *Karhunen-Loeve transform* (KLT) which has been extensively used in numerous applications that range from image compression to seismology and computer graphics in order to decorrelate multi-element data based on the eigendecomposition of the correlation matrix [7]. The resulting uncorrelated eigenmodes are assigned a Nakagami-m fading process [8] which yields a satisfactory fit with real-time data for various measured channels (see [9] and references therein). The normalized Nakagami-m pdf of the fading envelope R is given by

$$f_R(r) = \frac{2}{\Gamma(m)} m^m r^{2m-1} e^{-mr^2}, \quad r \geq 0 \tag{5}$$

with $\Gamma(\cdot)$ expressing the gamma function. The Nakagami fading figure $m[k](1 \leq k \leq MN)$, which determines the severity of fading, is estimated directly from the measured data according to

$$\begin{aligned} m[k] &= \frac{E\left\{\left|\mathbf{u}_k^H \mathrm{vec}(\mathbf{H})\right|^2\right\}^2}{E\left\{\left\{\left|\mathbf{u}_k^H \mathrm{vec}(\mathbf{H})\right|^2 - E\left\{\left|\mathbf{u}_k^H \mathrm{vec}(\mathbf{H})\right|^2\right\}\right\}^2\right\}} \\ &= \frac{\lambda_k^2}{E\left\{\left\{\left|\mathbf{u}_k^H \mathrm{vec}(\mathbf{H})\right|^2 - \lambda_k\right\}^2\right\}} \geq \frac{1}{2}. \end{aligned} \tag{6}$$

In Fig. 1, we illustrate the cumulative distribution function (cdf) of a normalized measured fading envelope which indicates the excellent fit of the Nakagami-m distribution.

This aggregate statistical metric shows the poor match of the commonly used Rayleigh distribution while the Ricean distribution fits reasonably well, except in the tails of the measured data. Similar trends were observed at most of the considered cases. To further justify our choice, we have computed the mean squared error (MSE) of these three candidate cdf fits across the whole data set with the key characteristics being tabulated in Table I. The average and standard deviation measures indicate that the Nakagami-m fit yields a rather good accuracy and substantially outperforms the Rayleigh fit by an order of one magnitude while it remains robust and experiences the lowest maximum MSE. On the basis of which model best fits the measured data set, we notice the smallest MSE to occur at 72.40% of the cases when a Nakagami-m fit is employed thereby confirming its improved performance compared to the other two reference distributions (right-hand column of Table I). For the generation of the uncorrelated Nakagami-m

[1]It is trivial to check the validity of (4) by calculating the spatial correlation matrix according to (2).

TABLE I
MSE CHARACTERISTICS OF THREE CDF FITTING DISTRIBUTIONS

	average MSE	std. deviation MSE	minimum MSE	maximum MSE	smallest MSE
Rayleigh	2.38×10^{-4}	1.72×10^{-3}	5.59×10^{-7}	5.32×10^{-2}	5.79 (%)
Ricean	4.95×10^{-5}	1.28×10^{-4}	5.53×10^{-7}	4.72×10^{-3}	21.81 (%)
Nakagami-m	3.81×10^{-5}	1.23×10^{-4}	4.65×10^{-7}	4.18×10^{-3}	72.40 (%)

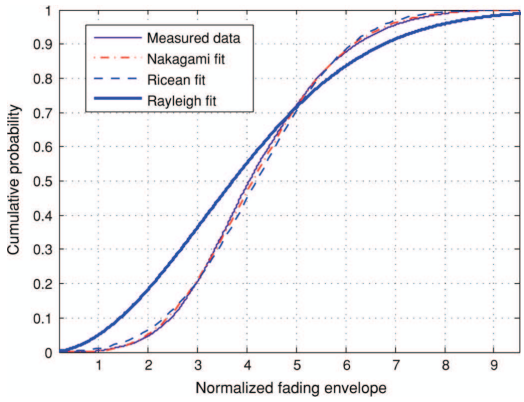

Fig. 1. Cdf of a normalized measured envelope in comparison with Nakagami-m, Ricean and Rayleigh distributions.

envelope variates we adopt the *rejection/acceptance method* proposed in [10] which is accurate and computationally efficient for arbitrary values of m. Then, the spatial fading coefficients may be expressed as $g[k] = R[k]\exp(j\phi[k])$, where $\phi[k]$ is a random phase distributed uniformly in $[0, 2\pi)$. The uniform phase assumption was found to be valid even for large values of the m-factor (i.e., non-Rayleigh conditions) and thanks to its intrinsic simplicity was incorporated throughout our analysis.

V. MIMO CHANNEL MODEL VALIDATION

The proposed model is assessed by means of the mutual information and the link-level performance using a minimum mean squared error (MMSE) detector which can minimize the overall error caused by noise and mutual interference. Firstly, we compute the measured correlation matrix, using all space and frequency realizations, and thereafter the matrix is decomposed in order to obtain the spatial eigenmodes; as a next step 25,090 synthetic channel realizations are generated according to (4) and hence the measured and simulated ensembles are the same. In order to remove the path-loss effects, both ensembles are normalized so that the constraint $E\{\|\mathbf{H}\|_F^2\} = MN$ is fulfilled, where $\|\cdot\|_F$ corresponds to the Frobenius norm.

Assuming perfect channel state information (CSI) at the Rx but no knowledge at the Tx, the average mutual information (ergodic channel capacity) is given by

$$I = E\left\{\log_2\left(\det\left(\mathbf{I}_M + \frac{\rho}{N}\mathbf{H}\mathbf{H}^H\right)\right)\right\}, \quad \text{(bits/s/Hz)} \quad (7)$$

where $\mathbf{I}_M$ is the $M \times M$ identity matrix and ρ denotes the system signal-to-noise ratio (SNR) per receiver branch [11]. The latter was set equal to 20 dB[2] while the expectation operation was performed on either the measured data or the fading realizations of $g[k]$. In Fig. 2, two different models are compared, namely the Nakagami and the Weichselberger models; the modeled capacity is plotted against the measured capacity for each of the 72 scenarios under investigation. The Kronecker model is not included in our comparison since it is a special case of the Weichselberger model and yields an inferior performance for the great majority of cases [3]–[5].

From this figure, we observe that the proposed model holds a smaller modeling error than the Weichselberger model, whose mismatch increases with decreasing mutual information, for all the scenarios under investigation; in particular, a 2.2 dB improvement was achieved in the MSE from -9.72 to -11.93 dB. Additional study revealed that the Weichselberger's accuracy diminishes when the outage mutual information is considered, resulting in an overestimation of the diversity level; this is consistent with the results presented in [4], [5]. The good fit of the Nakagami model can be partially attributed to the presence of strong obstructed LoS components at the majority of Rx locations due to its inherent higher flexibility compared to the more restricted Rayleigh and Ricean distributions. In other words, for the corresponding eigenmodes $m > 1$ and therefore the fluctuations of the signal strength reduce compared to Rayleigh fading.

The link-level performance is evaluated by considering a SM scheme, namely linear MMSE detection. The uncoded transmitted signal is modulated using BPSK modulation. For these specifications, the estimated transmit signal vector $\hat{\mathbf{x}}$ is [12]

$$\hat{\mathbf{x}} = \widetilde{\mathbf{W}} \cdot \mathbf{y}, \text{ where } \widetilde{\mathbf{W}} = \arg\min_{\mathbf{W}} E\{\|\mathbf{W}\mathbf{y} - \mathbf{x}\|^2\} \quad (8)$$

and thus the following closed-form expression is finally obtained

$$\hat{\mathbf{x}} = \mathbf{H}^H(\mathbf{H}\mathbf{H}^H + N_0\mathbf{I}_M)^{-1} \cdot \mathbf{y} \quad (9)$$

with N_0 expressing the noise power. Due to space constraints, we directly focus on the *BER mismatch* at a target SNR of 20 dB against the Nakagami m-factor of the dominant eigenmode (cf. Fig. 3). In general, the BER mismatch is defined as the difference between the measured and the modeled BER at a target SNR. The distribution of the m values validates clearly the assumption of Nakagami fading while we notice a significant portion of them well beyond the typical unity value. The proposed model holds again a superior performance for the vast majority of measured scenarios (68 out of 72 scenarios); in fact, its BER estimators deviate by up to 11% while the Weichselberger's by up to 20% and the MSEs (for the same target SNR) are 2. 24 $\times 10^{-5}$ and 4.47 $\times 10^{-5}$ respectively, expressing a 3 dB improvement. It is noteworthy that the relative difference of estimators is higher when more than one eigenmodes experience purely Nakagami fading ($m > 2$).

The only disadvantage of the proposed scheme lies in its increased complexity burden which is generally a crucial issue that affects the choice of the most appropriate channel model. While the Kronecker

[2]This value is chosen so that the system SNR is well below the measured SNR which lies in the region 55-60 dB after averaging the channel response across 128 temporal snapshots.

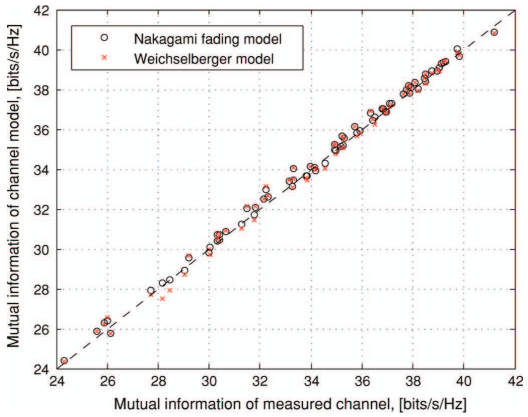

Fig. 2. Mutual information for two different channel models versus measured mutual information. The dashed line corresponds to the points of no modeling error.

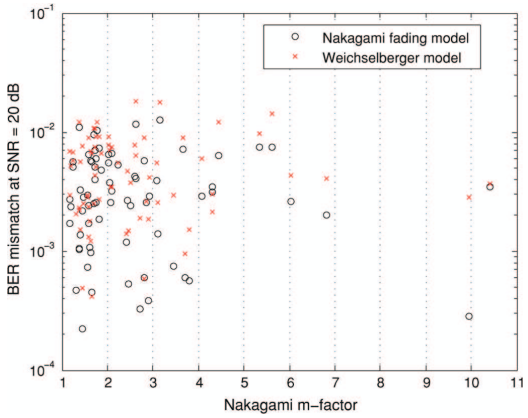

Fig. 3. BER mismatch at a target SNR of 20 dB against the Nakagami $\boldsymbol{m}$-factor of the dominant eigenmode.

and the Weichselberger models require respectively $M^2 + N^2 = 128$ and $MN + M(M-1) + N(N-1) = 176$ real parameters to be specified, the complexity order of our scheme is equal to that of the full correlation model, i.e., $(MN)^2 = 4096$. This implies that for practical systems of interest the complexity increase is modest; further, in terms of processing time an increase of 45% was observed on a 3.2 GHz Pentium, making the model rather appealing when an enhanced accuracy is desired.

VI. Conclusion

In this letter, a stochastic channel model has been presented with a view to the decomposition of the spatial correlation matrix. The Nakagami-m fading approach yields a satisfactory performance since in the majority of measured locations the presence of strong obstructed LoS components violates the common assumption of Rayleigh fading conditions. It is shown that the proposed model outperforms the sophisticated Weichselberger model in terms of both information theory (mutual information) and link-level performance (BER). The scheme can be regarded as a framework for describing different channels operating at the 5 GHz frequency band, e.g., Wireless Local Area Networks (WLANs), fixed wireless and peer-to-peer communications. It can also be used as a tractable tool for the simulation of MIMO systems, design of space-time codes and construction of spatial filtering at both ends.

Acknowledgment

The authors would like to thank Dr. M. Herdin, formerly of TU Vienna, for providing them with access to the results of propagation measurements carried out in Vienna. They would also like to acknowledge the support of the Scottish Funding Council for the Joint Research Institute with the Heriot-Watt University which is a part of the Edinburgh Research Partnership.

References

[1] J. P. Kermoal, L. Schumacher, K. I. Pedersen, P. E. Mogensen, and F. Frederiksen, "A stochastic MIMO radio channel model with experimental validation," *IEEE J. Sel. Areas Commun.*, vol. 20, pp. 1211–1226, Aug. 2002.

[2] H. Özcelik, M. Herdin, W. Weichselberger, J. Wallace, and E. Bonek, "Deficiencies of "Kronecker" MIMO radio channel model," *IEE Electron. Lett.*, vol. 39, no. 16, pp. 1209–1210, Aug. 2003.

[3] W. Weichselberger, "Spatial structure of multiple antenna radio channels: a signal processing viewpoint," Ph.D. dissertation, Technical Univ. Vienna, Austria, Dec. 2003.

[4] H. Özcelik, N. Czink, and E. Bonek, "What makes a good MIMO channel model?," in *Proc. VTC 2005*, May 2005, vol. 1, pp. 156–160.

[5] H. Özcelik, "Indoor MIMO channel models," Ph.D. dissertation , Technical Univ. Vienna, Austria, Dec. 2004.

[6] M. Herdin, H. Özcelik, H. Hofstetter, and E. Bonek, "Variation of measured indoor MIMO capacity with receive direction and position at 5.2 GHz," *IEE Electron. Lett.*, vol. 38, no. 21, pp. 1283–1285, Oct. 2002.

[7] S. Theodoridis and K. Koutroumbas, *Pattern Recognition*, 2nd ed. New York: Academic Press, 2003.

[8] M. Nakagami, W. C. Hoffman, Ed., "The $\boldsymbol{m}$-distribution—A general formula of intensity distribution of rapid fading," in *Statistical Methods in Radio Wave Propagation*, Oxford, U.K., 1960, pp. 3–36.

[9] P. J. Crepeau, "Uncoded and coded performance of MFSK and DPSK in Nakagami fading channels," *IEEE Trans. Commun.*, vol. 40, pp. 487–493, Mar. 1992.

[10] L. Cao and N. C. Beaulieu, "A simple efficient method for generating independent Nakagami-$\boldsymbol{m}$ fading samples," *Proc. VTC 2005*, pp. 44–47, Jun. 2005.

[11] G. Foschini and M. Gans, "On limits of wireless communication in a fading environment when using multiple antennas," *Wireless Pers. Commun.*, vol. 6, no. 3, pp. 311–335, Feb. 1998.

[12] S. Haykin, *Adaptive Filter Theory*, 4th ed. Englewood Cliffs, NJ: Prentice Hall, 2001.

Rejection method for generating Nakagami-*m* independent deviates

M. Matthaiou and D.I. Laurenson

The Nakagami-*m* distribution has gained considerable research interest in the area of wireless communications thanks to its good fit to empirical fading data. A simple scheme for the generation of independent Nakagami-*m* random variables (RVs) is presented and compared with the existing methods available in the literature.

Introduction: It is well established that the Nakagami-*m* distribution [1] yields a satisfactory fit with measured fading data over a wide range of frequency bands [2]. The Nakagami-*m* probability density function (PDF) of the signal's envelope r is given by the formula

$$f(x) = \frac{2}{\Gamma(m)}\left(\frac{m}{\Omega}\right)^m x^{2m-1} e^{-mx^2/\Omega} \qquad x \geq 0, \quad m \geq 0.5, \quad \Omega \geq 0 \tag{1}$$

where $\Gamma(.)$ expresses the gamma function, $m = E^2(x^2)/\mathrm{var}(x^2)$ is the shape parameter, determining the severity of fading, and $\Omega = \mathrm{E}(x^2)$. The generation of independent Nakagami-*m* RVs can provide an insight into the characterisation of practical diverse systems operating in slowly varying Nakagami-*m* fading environments. Surprisingly, to the best of the authors' knowledge, few results have been reported dealing with the computer simulation of independent Nakagami-*m* fading [3–5]. The so called 'brute method' [3], which considers the square root of a sum of squares of n zero-mean identically distributed Gaussian random variables, leads to a Nakagami distribution with $m = n/2$; however, this scheme is limited to integer and half-integer values of m. The authors in [4] showed that the product of a square-root beta process and a complex Gaussian process holds an accurate model but similarly is valid only for values of $m < 1$. The inverse method proposed in [5] is sufficiently accurate for arbitrary values of m but requires the computation of a different set of coefficients for each m value.

In this Letter, we present a novel technique for generating independent Nakagami-*m* samples based on the rejection method [6]. A similar approach has been recently addressed in [7] but lacks a uniform approach for the whole range of m values. In particular, the authors suggest the use of either the folded-Gaussian ($0.5 \leq m \leq 1.0$) or the Gaussian ($m \geq 1.0$) PDFs as hat functions, resulting in the achieved efficiency being strongly dependent on the corresponding interval (65.75 and 66.67% respectively), with the option to select different constants (which are determined empirically) to improve efficiency for particular ranges of m (see Tables 1 and 2 in [7]). This was achieved by applying the rejection scheme only in the confined region $0 \leq x \leq 4\,\Omega$. In light of this fact, a simple uniform technique, without any constraints on the range of random values, is proposed herein, which alleviates the deficiencies of the aforementioned schemes and yields an excellent accuracy.

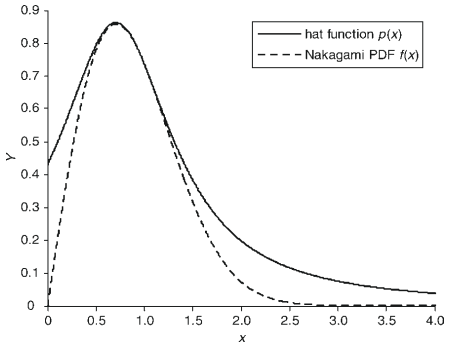

Fig. 1 *Rejection method for generating random Nakagami-m deviates using inverse polynomial function*

Rejection method: The rejection method relies on the selection of a comparison function (usually referred to as the hat function) $p(x)$ that has finite area and satisfies the inequality $p(x) \geq f(x)$, where $f(x)$ is the original PDF. We propose the use of a second-order inverse polynomial function which can be expressed as

$$p(x) = \frac{A\sqrt{\Omega}}{\Omega - B\sqrt{\Omega}x + x^2} \geq f(x) \tag{2}$$

An illustrative graph of the two functions under investigation is shown in Fig. 1. Taking into account that the maxima of (1) and (2) should coincide, it is trivial to show that $B = 2\sqrt{(2m-1)/2m}$. The scaling factor, A, is set such that the curves intersect at a single point, $x = x_{\max}$, without crossing. Thus

$$A = \frac{\Omega - B\sqrt{\Omega}x_{\max} + x_{\max}^2}{\sqrt{\Omega}} f(x_{\max}) \tag{3}$$

Solving $x \xrightarrow{\lim} x_{\max}\ d/dx(p(x) - f(x)) = 0$ gives one real positive solution at $x_{\max} = \sqrt{\Omega}$, which, when substituted into (3), yields

$$A = (2 - B)\frac{2m^m}{\Gamma(m)} e^{-m} \tag{4}$$

To generate independent samples from (2) we employ the widely known inverse method [6]; firstly, the indefinite integral $\int p(x)dx$ of (2) is computed, leading to the closed-form function

$$t = \frac{2A\tan^{-1}\left(\dfrac{\dfrac{2x}{\sqrt{\Omega}} - B}{\sqrt{4 - B^2}}\right)}{\sqrt{4 - B^2}} \tag{5}$$

A random sample of x is generated via the inverse function of (5)

$$x = \frac{\sqrt{\Omega}}{2}\left(\sqrt{4 - B^2}\tan\left(\frac{t\sqrt{4 - B^2}}{2A}\right) + B\right) \tag{6}$$

where t is a RV distributed uniformly in the range

$$\left[\frac{2A\tan^{-1}\left(\dfrac{-B}{\sqrt{4 - B^2}}\right)}{\sqrt{4 - B^2}}, \frac{A\pi}{\sqrt{4 - B^2}}\right]$$

It is worth noting that the above limits express, respectively, the minimum and maximum of (5) and define also the efficiency of the rejection method; in fact, their difference represents the area below $p(x)$. The generated sample x is accepted or rejected as a deviate based on the difference between (1) and (2). A detailed description of this well known algorithm can be found in [6].

Performance evaluation: By generating 2^{20} random x samples using (6) we were able to study the algorithm's performance in depth. Fig. 2 shows the theoretical and simulated Nakagami-*m* PDFs for $\Omega = 1$; it can be clearly seen that the achieved accuracy is noticeably high for all values of m, validating the choice of the rejection scheme as a powerful and straightforward technique for generating random deviates. A further study revealed that the maximum-likelihood (ML) estimators for the two shape parameters of the Nakagami PDF (Ω and m) give excellent agreement with theoretical values.

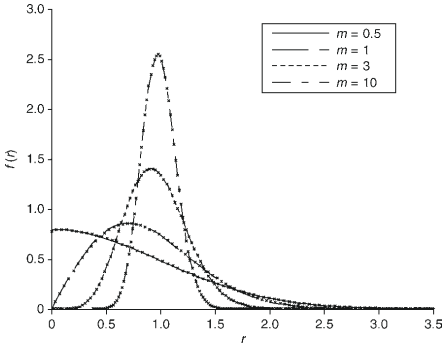

Fig. 2 *Theoretical and simulated Nakagami-m PDFs for arbitrary values of m (Ω = 1)*

—— theoretical curve
x simulated curve

Efficiency: It can be easily inferred that the method's efficiency is directly related to the m value. For high values of m, the tails of (1) decay slower than those of (2) and therefore the achieved efficiency decreases. In any case though, the efficiency in the common range of interest ($0.5 \leq m \leq 2.5$) lies above 65% (see Fig. 3).

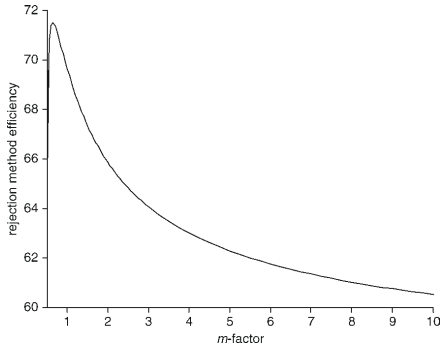

Fig. 3 *Efficiency of rejection method against m factor*

Conclusions: The generation of independent Nakagami-m deviates has been addressed by means of the rejection scheme based on an inverse polynomial function. It has been shown that the method can be easily applied for all values of the m parameter, yielding a high accuracy along with a satisfactory efficiency.

25 May 2007
Electronics Letters online no: 20071547
doi: 10.1049/el:20071547

M. Matthaiou and D.I. Laurenson (*Institute for Digital Communications, Joint Research Institute for Signal and Image Processing, School of Engineering and Electronics, University of Edinburgh, Edinburgh EH9 3JL, United Kingdom*)

E-mail: m.matthaiou@ed.ac.uk

References

1 Nakagami, M.: 'The m-distribution–a general formula of intensity distribution of rapid fading', *in* Hoffman, W.C. (Ed.): 'Statistical methods in radio wave propagation' (Oxford, UK, 1960, pp. 3–36)
2 Crepeau, P.J.: 'Uncoded and coded performance of MFSK and DPSK in Nakagami fading channels', *IEEE Trans. Commun.*, 1992, **40**, pp. 487–493
3 Proakis, J.G.: 'Digital communications' (McGraw-Hill, New York, USA, 1995, 3rd Edn.)
4 Yip, K.W., and Ng, T.S.: 'An efficient model for Nakagami-m fading channels, $m < 1$', *IEEE Trans. Commun.*, 2000, **48**, pp. 214–221
5 Beaulieu, N.C., and Cheng, C.: 'An efficient procedure for Nakagami-m fading simulation'. Global Telecommunications Conf., 2001, pp. 3336–3340
6 Papoulis, A., and Pillai, S.U.: 'Probability random variables and stochastic processes' (McGraw-Hill, Boston, USA, 2002, 4th Edn.)
7 Cao, L., and Beaulieu, N.C.: 'A simple efficient method for generating independent Nakagami-m fading samples'. Int. Conf. on Communications, Korea, May 2005, Vol. 1, pp. 44–47

Reduced Complexity Detection for Ricean MIMO Channels Based on Condition Number Thresholding

Michail Matthaiou*, David I. Laurenson*, and Cheng-Xiang Wang†
*Institute for Digital Communications, Joint Research Institute for Signal and Image Processing,
School of Engineering and Electronics, The University of Edinburgh,
Mayfield Road, EH9 3JL, Edinburgh, U.K.
Email: {M.Matthaiou, Dave.Laurenson}@ed.ac.uk
†Joint Research Institute for Signal and Image Processing,
School of Engineering and Physical Sciences, Heriot-Watt University,
EH14 4AS, Edinburgh, U.K.
Email: Cheng-Xiang.Wang@hw.ac.uk

***Abstract*—In this paper, a novel adaptive detection scheme for the case of Multiple-Input Multiple-Output (MIMO) Ricean channels with two transmit and receive antenna elements is presented. Our prime aim is to reduce the extensive complexity of Maximum-Likelihood (ML) detectors by developing an adaptive scheme which switches between a ML and a much simpler Zero-Forcing (ZF) detector depending on the instantaneous spatial conditions. The kernel of the adaptive detector (AD) is a hard-decision criterion based on the condition number of the MIMO correlation matrix. It is demonstrated that the proposed scheme offers a remarkable reduction in terms of complexity along with a satisfactory performance when specifically designed antenna arrays are employed.**

I. Introduction

The use of MIMO technology has become the new hot topic in wireless communications since the breakthrough works of Telatar [1] and Foschini [2] revealed the great advantages of employing multiple antennas at both the transmitter (Tx) and receiver (Rx). This technology can potentially enhance the reliability and speed of current and future wireless systems such as wireless local area networks (WLANs) or fourth generation cellular systems (4G). However, when it comes down to the feasibility of MIMO systems, a number of practical issues arises with the most prominent being the overall implementation complexity and cost.

Undoubtedly, the detection stage may be regarded as one of the most significant aspects in real-time applications. At this point, we recall that the optimal detector for spatial multiplexing (SM) MIMO systems is the ML detector which minimizes the error probability when all data vectors are equally likely but, at the same time, it is computationally prohibitive [3]. One way to alleviate this excessive complexity is to settle for sphere decoding techniques, such as the Finke-Post algorithm proposed in [4], whose complexity, under certain assumptions, is polynomial in the problem size. In [5], it was shown that when the Signal-to-Noise ratio (SNR) is high, the expected number of operations required by the sphere decoder is roughly cubic in the number of transmit antennas for a small problem size. However, the authors in [6] proved that for any arbitrarily fixed SNR, the overall complexity of sphere decoders does not grow as a polynomial function of the problem size but as an exponential function instead. What's more, when ill-conditioned channels occur, the computational complexity of sphere decoding schemes increases to a significant extent [7]. On the other hand, different suboptimal techniques exist which span from the linear ZF detector to nonlinear techniques such as Ordered Successive Interference Cancellation (OSIC) [8]; the former is the simplest detection technique but causes a systematic performance degradation and further is unable to exploit all of the available diversity. Its main disadvantage lies in its poor performance when channels with large condition numbers occur.

The previous discussion implies that an AD which could switch between a ML and a ZF scheme, depending on the instantaneous channel conditions, is of paramount interest since it will allow the efficient development of MIMO systems. In this paper, an AD is devised for the general case of Ricean MIMO channels where a dominant Line-of-Sight (LoS) component or a specular wavefront impinges on the receive array; we are particularly interested in the practical case of dual[1] Ricean MIMO systems. A similar concept of adaptive MIMO transmission has been investigated by various research groups during recent years (the interested readers are referred to [9]–[11] among others) and essentially goes back to the fundamental diversity-multiplexing tradeoff [12]. To the best of the authors' knowledge, the first MIMO adaptive scheme for the receive side was recently presented in [13]. The authors therein, however, considered only the common case of Rayleigh channels and hence the formulation of a generalized framework is infeasible; the proposed scheme relaxes the constraint of Rayleigh fading to account for the commonly experienced Ricean propagation and, consequently, it includes the model of [13] as a special case.

The hard-decision criterion for the adaptive switching relies on the condition number distribution whose exact determination requires knowledge of the theory of non-central complex

[1]Throughout the paper, the term dual will stand for MIMO systems with two transmit and two receive antenna elements.

Wishart matrices. On these grounds, we firstly derive a novel closed-form formula for the cumulative distribution function (CDF) of the MIMO condition number which is validated via Monte-Carlo simulations. It will also be shown that the AD preserves the robustness of the ML detector as well as the simplicity of the ZF detector and therefore can be easily implemented within most MIMO testbeds.

The remainder of the paper is organized as follows: In Section II, the preliminaries of the theory of Wishart matrices are outlined and a closed-form expression for the condition number CDF distribution is derived. In Section III, the underlying MIMO Ricean channel model used throughout the paper is presented. In Section IV, we briefly address the main characteristics of ZF and ML detections and subsequently those of the proposed adaptive scheme. In Section V, the validity of the analytical formula is tested and at a next stage we assess the performance of the AD for two different LoS geometrical configurations. Finally, Section VI concludes the paper and summarizes the key findings.

A note on notation: We use upper and lower case boldface to denote matrices and vectors, respectively while the symbol $\mathbb{C}$ denote the set of complex-valued numbers. The nomenclature $\sim \mathcal{CN}(\mathbf{X},\mathbf{Y})$ stands for a complex normally distributed matrix with mean $\mathbf{X}$ and covariance $\mathbf{Y}$. An $(n\times n)$ identity matrix is expressed as $\mathbf{I}_n$ while the all-zeros $(n\times m)$ matrix as $\mathbf{0}_{n\times m}$. The symbols $(\cdot)^H$ and $(\cdot)^{-1}$ correspond to Hermitian transposition and matrix inversion, respectively whereas $\otimes$ is the Kronecker product. Finally, $\det(\cdot)$ returns the determinant of a matrix.

II. Non-Central Wishart Matrices and Condition Number Distribution

As was previously mentioned, we are particularly interested in dual non-central Wishart matrices. In such a case, a (2×2) complex normal random matrix $\mathbf{H}$ is considered which is distributed according to $\mathbf{H}\sim\mathcal{CN}(\mathbf{M},\mathbf{\Sigma}\otimes\mathbf{I}_2)$. In general, $\mathbf{M}\neq\mathbf{0}_{2\times 2}$ whereas $\mathbf{\Sigma}=\sigma^2\mathbf{I}_2$ is the correlation matrix containing the variances σ^2 of the entries of $\mathbf{H}$ on its main diagonal. The so-called MIMO correlation matrix is defined as $\mathbf{W}=\mathbf{H}\mathbf{H}^H$ and is said to follow the complex non-central Wishart distribution with two degrees of freedom and non-centrality matrix $\mathbf{\Omega}=\mathbf{\Sigma}^{-1}\mathbf{M}\mathbf{M}^H$, commonly denoted as $\mathbf{W}\sim\mathcal{CW}_2(2,\mathbf{\Sigma},\mathbf{\Omega})$. It should be emphasized that if $\mathbf{M}=\mathbf{0}_{2\times 2}$, so that $\mathbf{\Omega}=\mathbf{0}_{2\times 2}$, a complex central Wishart matrix is eventually obtained, i.e. $\mathbf{W}\sim\mathcal{CW}_2(2,\mathbf{\Sigma})$.

We now consider a scaled version of $\mathbf{W}$, that is $\widetilde{\mathbf{W}}=\mathbf{\Sigma}^{-1}\mathbf{W}$. Since $\widetilde{\mathbf{W}}$ is a (2×2) Hermitian matrix, it has two real ordered eigenvalues $(w_1>w_2>0)$ where w_1 is the largest and w_2 the smallest eigenvalue, respectively; the joint eigenvalue PDF $f(w_1,w_2)$ is given by [14]

$$f(w_1,w_2)=\exp\left[-\sum_{i=1}^{2}(\lambda_i+w_i)\right]{}_0\widetilde{F}_1\left(2;\boldsymbol{\lambda},\mathbf{w}\right)(w_1-w_2)^2 \tag{1}$$

where $\boldsymbol{\lambda}=(\lambda_1,\lambda_2)$ contains the distinct real ordered eigenvalues of $\mathbf{\Omega}$ and, in turn, $\mathbf{w}=(w_1,w_2)$; furthermore, ${}_0\widetilde{F}_1(.;.,.)$ is the complex hypergeometric function of two matrix arguments. A convenient version of ${}_0\widetilde{F}_1\left(2;\boldsymbol{\lambda},\mathbf{w}\right)$ for the dual case was given by Gross and Richards [15] as

$${}_0\widetilde{F}_1\left(2;\boldsymbol{\lambda},\mathbf{w}\right)=\frac{\det\left({}_0F_1\left(1;w_i\lambda_j\right)\right)}{(\lambda_1-\lambda_2)(w_1-w_2)} \tag{2}$$

with $I_q(\cdot)$ denoting the q-th order modified Bessel function of the first kind and ${}_0F_1(s+1;x)$ is the hypergeometric function [16]

$${}_0F_1(s+1;x)=s!x^{-s/2}I_s\left(2\sqrt{x}\right). \tag{3}$$

From a mathematical point of view, the condition number z is defined as the ratio of the largest to the smallest eigenvalue and therefore

$$z=\frac{w_1}{w_2}\geq 1. \tag{4}$$

In [17], the authors showed that the probability density function (PDF) of z, $f_z(z)$, can be written as a weighted summation of polynomials according to (5), shown at the top of the next page. In (5), $\Gamma(n)$ denotes the Gamma function which, for the case of an integer index, can be rewritten as $\Gamma(n)=(n-1)!$. The corresponding CDF of z is then directly written as

$$F_z(x)=\int_1^x f_z(z)dz \tag{6}$$

or, equivalently

$$F_z(x)=\int_0^x f_z(z)dz-\int_0^1 f_z(z)dz. \tag{7}$$

By substituting (5) into (7) and taking into account the Dominated Convergence Theorem which suggests that the differentiation and integration can be interchanged we readily obtain (8). For the integrals involved in (8), a closed-form solution is available as [16, Eq. (3.194)]

$$\int_0^u\frac{t^\mu}{(1+bt)^\nu}dt=\frac{u^{\mu+1}}{\mu+1}{}_2F_1(\nu,\mu+1;\mu+2;-bu) \tag{10}$$

where ${}_2F_1(\alpha,\beta;\gamma;u)$ is the classical Gaussian hypergeometric function defined in [16, Eq. (9.14)]. We can finally write the CDF of the condition number according to (9), where

$$I_1^{k,n}(x)=\left(\frac{x^{k+2}}{k+2}\right){}_2F_1(k+n+3,k+2;k+3;-x)-\left(\frac{1}{k+2}\right){}_2F_1\left(k+n+3,k+2;k+3;-1\right) \tag{11}$$

and

$$I_2^{k,n}(x)=\left(\frac{x^{k+1}}{k+1}\right){}_2F_1(k+n+3,k+1;k+2;-x)-\left(\frac{1}{k+1}\right){}_2F_1(k+n+3,k+1;k+2;-1). \tag{12}$$

Clearly, we have expressed the condition number distribution as a weighted summation of Gaussian hypergeometric functions which can be efficiently evaluated and easily programmed.

$$f_z(z) = \frac{e^{-(\lambda_1+\lambda_2)}(z-1)}{\lambda_1-\lambda_2} \sum_{k=0}^{\infty}\sum_{n=0}^{\infty} \frac{\Gamma(k+n+3)z^k}{(k!n!)^2(z+1)^{k+n+3}} \left[\lambda_1^k\lambda_2^n - \lambda_2^k\lambda_1^n\right] \tag{5}$$

$$\begin{aligned} F_z(x) \quad &= \frac{e^{-(\lambda_1+\lambda_2)}}{\lambda_1-\lambda_2} \sum_{k=0}^{\infty}\sum_{n=0}^{\infty} \frac{\Gamma(k+n+3)}{(k!n!)^2} \left[\lambda_1^k\lambda_2^n - \lambda_2^k\lambda_1^n\right] \\ &\times \left\{ \int_0^x \frac{z^{k+1}}{(z+1)^{k+n+3}} - \int_0^1 \frac{z^{k+1}}{(z+1)^{k+n+3}} - \int_0^x \frac{z^k}{(z+1)^{k+n+3}} + \int_0^1 \frac{z^k}{(z+1)^{k+n+3}} \right\} \end{aligned} \tag{8}$$

$$F_z(x) = \frac{e^{-(\lambda_1+\lambda_2)}}{\lambda_1-\lambda_2} \sum_{k=0}^{\infty}\sum_{n=0}^{\infty} \frac{\Gamma(k+n+3)}{(k!n!)^2} \left[\lambda_1^k\lambda_2^n - \lambda_2^k\lambda_1^n\right] \left\{ I_1^{k,n}(x) - I_2^{k,n}(x) \right\} \tag{9}$$

III. MIMO Channel Model

In this section, the underlying MIMO channel model is discussed for the case of LoS propagation. We consider a memoryless, flat-fading MIMO system equipped with two elements at both the Tx and the Rx. The complex input-output relationship can be written for the discrete case as

$$\mathbf{y} = \mathbf{H}\mathbf{x} + \mathbf{n} \tag{13}$$

where $\mathbf{x} \in \mathbb{C}^{2\times 1}$ is the transmitted signal vector, $\mathbf{y} \in \mathbb{C}^{2\times 1}$ is the noise-corrupted received signal and $\mathbf{n} \in \mathbb{C}^{2\times 1}$ corresponds to the additive noise plus interference term. Moreover, the term $\mathbf{H} \in \mathbb{C}^{2\times 2}$ is referred to as the channel transfer function matrix and contains the complex responses between all antenna pairs.

In the case of Ricean fading, the channel matrix consists of a spatially deterministic specular component $\mathbf{H}_{\mathrm{L}}$ and a randomly distributed component $\mathbf{H}_{\mathrm{W}}$ which accounts for the scattered signals. Then, the channel model reads as [18]

$$\mathbf{H} = \sqrt{\frac{K}{K+1}}\mathbf{H}_{\mathrm{L}} + \sqrt{\frac{1}{K+1}}\mathbf{H}_{\mathrm{W}} \tag{14}$$

where K denotes the Ricean K-factor expressing the ratio of the free-space signal power to the power of the scattered waves. The entries of $\mathbf{H}_{\mathrm{W}}$ are assumed to be independent and identically distributed (i.i.d.) circular symmetric complex Gaussian variables with zero mean and unity variance so that their amplitudes follow the well-known Rayleigh distribution. As far as the LoS component $\mathbf{H}_{\mathrm{L}}$ is concerned, when the distance between the Tx and the Rx is small or the array size is large, its entries represent spherical wavefronts in the near-field region. Without loss of generality, we assume isotropic radiators and the complex responses are of the form $e^{-jkd_{m,n}}/d_{m,n}$, where $k = 2\pi/\lambda$ is the wavenumber corresponding to the carrier wavelength λ and $d_{m,n}$ is the distance between a receive element $m \in \{1,2\}$ and a transmit element $n \in \{1,2\}$.

Regarding the statistical characteristics of $\mathbf{H}$, it can be inferred that $\mathbf{M} = \sqrt{\frac{K}{K+1}}\mathbf{H}_{\mathrm{L}}$ while $\mathbf{\Sigma} = \frac{1}{K+1}\mathbf{I}_2$. Then, it is trivial to show that the Wishart matrix $\mathbf{W} = \mathbf{H}\mathbf{H}^H$ follows the distribution $\mathbf{W} \sim \mathcal{CW}_2\left(2, \frac{1}{K+1}\mathbf{I}_2, K\mathbf{H}_{\mathrm{L}}\mathbf{H}_{\mathrm{L}}^H\right)$ and in turn the associated LoS version of interest $\widetilde{\mathbf{W}} = (K+1)\mathbf{W}$.

IV. Detection Schemes For SM Systems

In this section we review the two reference detection schemes, namely ZF and ML detectors, and explore the concept of the novel adaptive detection strategy. All the following investigations are based on a SM-MIMO transmission scheme, such as the widely employed V-BLAST [8], in which the data is divided into a number of N_t blocks (equal to the number of transmit elements) that are then simultaneously emitted. At the Rx, the main goal is to differentiate the data blocks originating from each of the transmit elements so that the transmitted signals are efficiently recovered.

A. ZF detection

The simplest linear MIMO detector is the ZF receiver, where the received signal vector $\mathbf{y}$ is multiplied by the Moore-Penrose pseudoinverse $\mathbf{H}^{\dagger}$ of the channel matrix $\mathbf{H}$ to obtain an estimated transmit signal vector $\hat{\mathbf{x}}_{\mathrm{ZF}}$ as follows

$$\hat{\mathbf{x}}_{\mathrm{ZF}} = \mathbf{H}^{\dagger}\mathbf{H}\mathbf{x} + \mathbf{H}^{\dagger}\mathbf{n}. \tag{15}$$

The computational complexity of ZF includes an exhaustive search through the Q symbols in the constellation of the modulation technique for N_t times and thus it is of the order of $O(QN_t)$. However, the low complexity of the ZF receiver comes at the expense of noise amplification which induces irreducible errors. In fact, as the number of transmit and receive antennas grows with no bound, the noise amplification tends to infinity [19].

B. ML detection

On the other end, the optimal ML detector resides which remains robust and yields the best performance among all detection techniques [3]. Assuming equally likely, temporally uncoded transmit symbols, this receiver chooses the vector $\mathbf{t}$ that solves the following expression

$$\hat{\mathbf{x}}_{\mathrm{ML}} = \arg\min_{\mathbf{t}} \|\mathbf{y} - \mathbf{H}\mathbf{t}\|_F^2 . \tag{16}$$

The optimization is performed through an exhaustive search over all possible vector symbols. This implies that the complexity of the ML detector grows exponentially with the number of transmit antennas i.e. $O(Q^{N_t})$, making the scheme infeasible for large antenna setups and constellation sizes.

C. Adaptive detection

Given the deficiencies of both detection strategies, we herein propose a novel detector which can adaptively switch between them in order to enhance the error performance and minimize the computational cost. The AD uses ZF when the condition number is below a predefined threshold defined and ML detection otherwise. The key notion is to employ the ZF detector only for well-conditioned channels (low condition numbers) and let the ML deal with the ill-conditioned channels (high condition numbers). We can then write

$$\hat{\mathbf{x}}_{\text{AD}} = \begin{cases} \hat{\mathbf{x}}_{\text{ZF}} & \text{if } z \leq \kappa \\ \hat{\mathbf{x}}_{\text{ML}} & \text{if } z > \kappa. \end{cases} \tag{17}$$

The threshold κ affects the complexity of the proposed scheme; for $\kappa = 1$ we get $\hat{\mathbf{x}}_{\text{AD}} = \hat{\mathbf{x}}_{\text{ML}}$ and complexity equals that of ML detection whereas for $\kappa \to \infty$ we have $\hat{\mathbf{x}}_{\text{AD}} = \hat{\mathbf{x}}_{\text{ZF}}$. In general, the probability of ZF calls is $\text{Prob}\{z \leq \kappa\} \equiv F_z(\kappa) = p_\kappa$ and therefore the average AD complexity g becomes

$$g = \underbrace{p_\kappa Q N_t}_{\text{ZF calls}} + \underbrace{(1-p_\kappa)Q^{N_t}}_{\text{ML calls}}, \quad 0 \leq p_\kappa \leq 1. \tag{18}$$

The percentage of complexity reduction, compared to that of the ML detector, is

$$\frac{Q^{N_t} - g}{Q^{N_t}} = p_\kappa \left(1 - \frac{N_t}{Q^{N_t - 1}}\right). \tag{19}$$

Evidently, the reduction is more pronounced for greater sizes of the symbol alphabet and a higher number of ZF calls.

V. Simulation Results

In this section, the theoretical analysis presented in Section II is validated through a set of simulations and subsequently the link-level performance of the AD is assessed in terms of complexity and bit-error-rate (BER). In order to get a deeper insight, we explore two different geometrical models for the LoS component.

In particular, the first model belongs in the family of high-rank (HR) configurations which, contrary to the common belief, can deliver high MIMO capacities in the presence of strong LoS components (large K-factors). This is achieved by appropriate positioning of the antenna elements at both ends so that subchannel orthogonality is attained, or, the eigenvalues of $\mathbf{\Omega}$ become equal. In such a case though, the $(\lambda_1 - \lambda_2)$ term in the denominator of (2) becomes zero making the analysis invalid (division by zero). In this light, we consider a suboptimum HR LoS channel model in order to guarantee that $\lambda_1 \neq \lambda_2$; the LoS matrix component then reads [17]

$$\mathbf{H}_{\text{L}} = \begin{bmatrix} 0.8384 + j0.5451 & 0.9411 + j0.3380 \\ -0.5123 - j0.8588 & 0.8384 + j0.5451 \end{bmatrix} \tag{20}$$

Assuming a Ricean-K factor of 5 dB, the eigenvalues of $\mathbf{\Omega}$ can be easily computed and thereafter concatenated into the vector $\boldsymbol{\lambda} = (7.0336, 5.6155)$. The second model is a conventional architecture whose deterministic matrix reads

$$\mathbf{H}'_{\text{L}} = \begin{bmatrix} 0.8384 + j0.5451 & 0.9411 + j0.3380 \\ -0.5123 - j0.8588 & 0.8384 + j0.5451 \end{bmatrix} \tag{21}$$

and, likewise, $\boldsymbol{\lambda}' = (12.649, 0.0001)$. For both geometrical models under investigation, 50,000 random Monte-Carlo realizations of the channel matrix $\mathbf{H}$ were generated according to (14). In Fig. 1, the simulated CDF curves of the condition number are overlaid with the analytical results returned by (9).

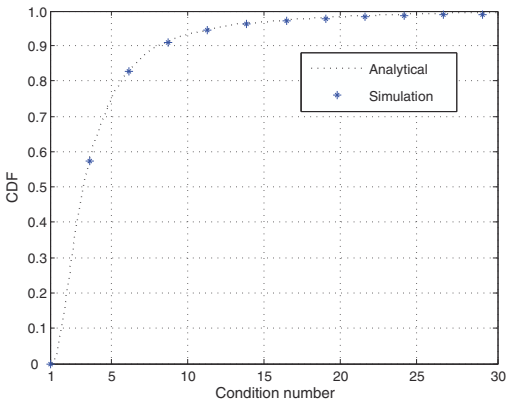

(a) HR LoS channel.

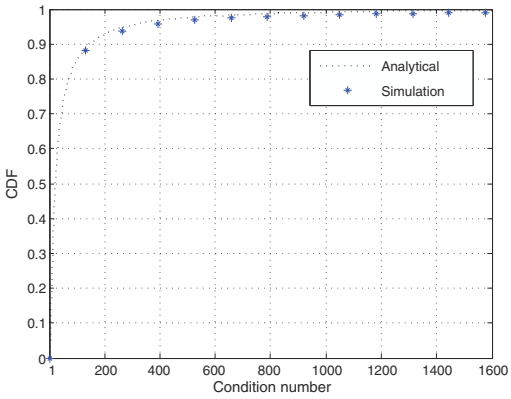

(b) LR LoS channel.

Fig. 1. Simulated and analytical CDFs of the condition number z of two Ricean MIMO channel models ($K = 5$ dB).

The match between the simulated and theoretical results is excellent in both cases, thereby indicating the validity of the derived formulae. We also point out that for the HR model a significant percentage of realizations is close to unity

(well-conditioned channels) while, in contrary, the LR model systematically yields a rather high condition number.

The next stage of our investigation comprises the assessment of the AD advantages assuming a 16-QAM modulation type. In [17], we found that when $\kappa \leq 6.46$ the instantaneous capacity of the HR channel is greater than the ergodic capacity of a common (2×2) i.i.d. Rayleigh channel and hence we have adopted a threshold of $\kappa = 5$ as a reasonable indicator of the channel rank and multipath richness. In Fig. 2, the BER curves are depicted for three different detection schemes, namely ZF, ML and the proposed AD. As anticipated, higher K-factors lead to significant performance enhancement for arrays designed following the suboptimum HR model. On the other hand, for low values of K-factor (below 0 dB) the channel approaches the i.i.d. Rayleigh channel characteristics which corresponds to a rich-scattering environment; in this region, the BER curves are approximately identical in both systems and the benefits of LoS-optimized arrays are minimized. In the limit ($K \to \infty$ dB) the LoS component vanishes and we end up with a pure i.i.d Rayleigh channel where all multipath components have equal amplitudes.

In order to get a better understanding, the main AD performance characteristics are tabulated in Table I where the radically different trends of the two configurations are readily observable. More specifically, the application of the detection scheme has a noticeable impact on the HR channel; in fact, a significant percentage of ZF calls occur for all values of the K-factor with a consequent complexity reduction of up to 83.35%. We also observe a steady increase of p_κ as K gets higher since the channel becomes full rank and delivers two approximately equal eigenvalues. In the LR case p_κ is always below 29.43% and further is inversely proportional to the K-factor. This phenomenon can be attributed to the ill-condition of conventional architectures which degenerate eventually into a rank-one channel due to the linear dependence of the LoS rays' phases (higher spatial correlation). Consequently, for $K \geq 5$ dB the number of ZF calls is too low to exploit the adaptivity benefits and a complexity identical to that of a ML detector inevitably takes place.

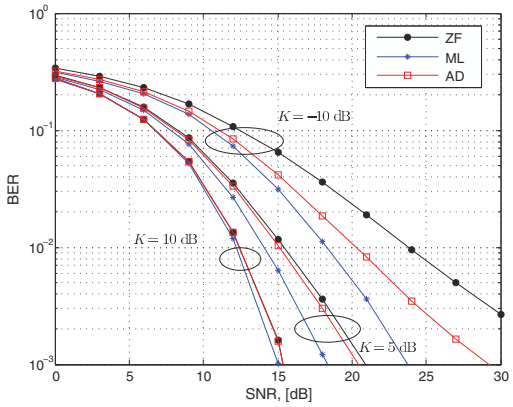

(a) Suboptimum HR LoS channel.

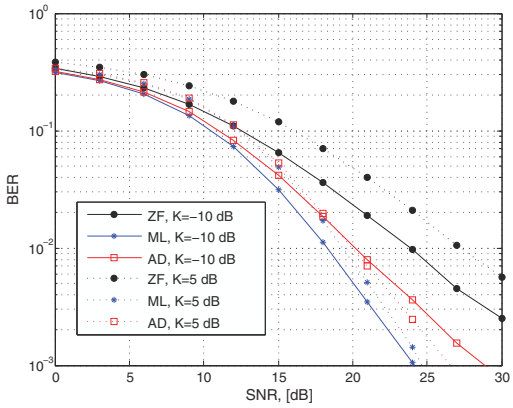

(b) Conventional LR LoS channel.

Fig. 2. BER curves for three different detection strategies based on a 16-QAM modulation.

VI. Conclusion

In the present contribution, the potential of developing an AD relying on the condition number of the MIMO correlation matrix, has been investigated. On this basis, we firstly derived a closed-form formula for the CDF of the condition number of dual non-central complex Wishart matrices as a weighted summation of Gaussian hypergeometric functions. The analytical CDF expression was firstly validated through extensive Monte-Carlo simulations where it was clearly demonstrated that the match between theory and simulation is very good. At a next stage, the distribution of the condition number was used to construct the hard-decision criterion of the proposed AD which is appealing not only from a theoretical but also from a practical perspective; most importantly, the dramatic decrease in terms of complexity, compared to the sophisticated ML detector, makes the model applicable to the majority of modern practical receivers. Further, when the antenna elements are positioned in such a way to guarantee subchannel orthogonality, the attained performance was shown to be reasonably good, especially for high values of the K-factor. On the contrary, the scheme advantages diminish when it is applied to a conventional antenna configuration since the channel matrix is inherently rank deficient and therefore yields a deteriorating performance with the increasing Ricean K-factor.

Acknowledgments

The authors would like to thank Dr. Ioannis Sarris, formerly of Bristol University, for his valuable help and stimulating technical discussions during the first stage of our work. They would also like to acknowledge the support of the Scottish Funding Council in the Joint Research Institute for Signal and Image Processing with Heriot-Watt University which is a part of the Edinburgh Research Partnership.

TABLE I
AD PERFORMANCE CHARACTERISTICS FOR TWO DIFFERENT LOS CHANNEL MODELS AS A FUNCTION OF THE K-FACTOR.

	Suboptimum HR LoS channel model			LR LoS channel model		
K–factor	Analyt. p_κ	Simul. p_κ	Compl. reduction	Analyt. p_κ	Simul. p_κ	Compl. reduction
$K = -10$ dB	0.2992	0.3150	26.18%	0.2943	0.3132	25.75%
$K = -5$ dB	0.3203	0.3380	28.02%	0.2801	0.3002	24.51%
$K = 0$ dB	0.4372	0.4403	38.25%	0.2052	0.2241	17.95%
$K = 5$ dB	0.7499	0.7501	65.61%	0.0536	0.064	4.69%
$K = 10$ dB	0.9526	0.9620	83.35%	-	-	-

REFERENCES

[1] I. E. Telatar, "Capacity of multi-antenna Gaussian channels," *ATT-Bell Labs Internal Technical Memorandum*, June 1995.

[2] G. J. Foschini, "Layered space-time architecture for wireless communications in a fading environment when using multiple antennas," *Bell Labs Technical Journal*, vol. 1, no. 2, pp. 41–59, Autumn 1996.

[3] R. N. A. Paulraj and D. Gore, *Introduction to Space-Time Wireless Communications*, Cambridge University Press, U.K. , 2003.

[4] U. Fincke and M. Phost, "Improved methods for calculating vectors of short length in a lattice, including a complexity analysis," *Mathematics of Computation*, vol. 44, pp. 463–471, April 1985.

[5] B. Hassibi and H. Vikalo, "On the sphere-decoding algorithm I. Expected complexity," *IEEE Transactions on Signal Processing*, vol. 53, no. 8, pp. 2806–2818, August 2005.

[6] J. Jalden and B. Ottersten, "On the complexity of sphere decoding in digital communications," *IEEE Transactions on Signal Processing*, vol. 53, no. 4, pp. 1474–1484, April 2005.

[7] H. Artes, D. Seethaler, and F. Hlawatsch, "Efficient detection algorithms for MIMO channels: A geometrical approach to approximate ML Detection," *IEEE Transactions on Signal Processing*, vol. 51, no. 11, pp. 2808–2820, November 2003.

[8] G. Golden, G. J. Foschini, R. Valenzuela, and P. Wolniasky, "Detection algorithm and initial laboratory results using the V-BLAST space-time communication architecture," *IEE Electronics Letters*, vol. 35, pp. 14–15, 1999.

[9] R. W. Heath and A. J. Paulraj, "Switching between diversity and multiplexing in MIMO systems," *IEEE Transactions on Communications*, vol. 53, no. 6, pp. 962–968, June 2005.

[10] A. Forenza, M. R. McKay, A. Pandharipande, R. W. Heath, and I. B. Collings, "Adaptive MIMO transmission for exploiting the capacity of spatially correlated channels," *IEEE Transactions on Vehicular Technology*, vol. 56, no. 2, pp. 619–630, March 2007.

[11] A. Forenza, M. R. McKay, I. B. Collings and R. W. Heath, "Switching between OSTBC and spatial multiplexing with linear receivers in spatially correlated MIMO channels," in *Proc. Vehicular Technology Conference (VTC)*, Melbourne, Australia, May 2006, pp. 1387–1391.

[12] L. Zheng and D. Tse, "Diversity and multiplexing: A fundamental tradeoff in multiple-antenna channels," *IEEE Transactions on Information Theory*, vol. 49, no. 5, pp. 1073–1096, May 2003.

[13] J. Maurer, G. Matz, and D. Seethaler, "Low-complexity and full-diversity MIMO detection based on condition number thresholding," in *Proc. Acoustics, Speech and Signal Processing Conference (ICASSP)*, vol. 3, Honolulu, Hawaii, April 2007, pp. 61–64.

[14] A. T. James, "Distributions of matrix variates and latent roots derived from normal samples," *Ann. Math. Stat.*, vol. 35, no. 2, pp. 475–501, June 1964.

[15] K. I. Gross and D. S. Richards, "Total positivity, spherical series, and hypergeometric functions of matrix argument," *Journal on Approximation Theory*, vol. 59, no. 2, pp. 224–246, 1989.

[16] I. S. Gradshteyn and I. M. Ryzhik, *Table of Integrals, Series, and Products*, Academic Press, Sixth ed., San Diego, 2000.

[17] M. Matthaiou, D. I. Laurenson, and C. -X. Wang, "On analytical derivations of the eigenvalue and condition number distributions of dual non-central Wishart matrices," submitted to *IEEE Transactions on Wireless Communications*, March 2008.

[18] F. Rashid-Farrokhi, A. Lozano, G. J. Foschini, and R. Valenzuela, "Spectral efficiency of wireless systems with multiple transmit and receive antennas," in *Proc. International Symposium on Personal, Indoor and Mobile Radio Communications (PIMRC)*, vol. 1, London, U.K., September 2000, pp. 373–377.

[19] R. Bohnke, D. Wubben, V. Kuhn, and K. -D. Kammeyer, "Reduced complexity MMSE detection for BLAST architectures," in *Proc. Global Telecommunications Conference (GLOBECOM)*, vol. 4, San Francisco, USA, December 2003, pp. 2258–2262.

[20] I. Sarris and A. R. Nix, "Design and performance assessment of high-capacity MIMO architectures in the presence of a line-of-sight component," *IEEE Transactions on Vehicular Technology*, vol. 56, no. 4, pp. 2194–2202, July 2007.

[21] M. Matthaiou, D. I. Laurenson, and C. -X. Wang, "Capacity study of vehicle-to-roadside MIMO channels with a line-of-sight component," in *Proc. Wireless Communications and Networking Conference (WCNC)*, Las Vegas, USA, March 2008, pp. 775–779.

References

[1] A. Ihler, "Kernel density estimation toolbox for MATLAB" [Online]. Available to download at `http://ssg.mit.edu/ihler/code/kde.shtml`.

[2] C. E. Shannon, "A mathematical theory of communications," *Bell Systems Technical Journal*, vol. 27, 1948.

[3] S. K. Yong and C. C. Chong, "An overview of multi-gigabit wireless through millimeter wave technology: Potentials and technical challenges," *EURASIP Journal on Wireless Communications and Networking*, vol. 2007, pp. 1–10.

[4] B. Razavi, "Gadgets gab at 60 GHz," *IEEE Spectrum*, vol. 45, no. 2, pp. 46–58, February 2008.

[5] G. J. Foschini, "Layered space-time architecture for wireless communications in a fading environment when using multiple antennas," *Bell Labs Technical Journal*, vol. 1, no. 2, pp. 41–59, Autumn 1996.

[6] I. E. Telatar, "Capacity of multiantenna Gaussian channels," *ATT-Bell Labs Internal Technical Memorandum*, June 1995.

[7] IEEE 802.11 Working Group, "Part 11: Wireless LAN medium access control (MAC) and physical layer (PHY) specifications: High speed physical layer in the 5 GHz band," IEEE P802.11a/D7.0, August 1999.

[8] IEEE 802.11n Working Group, "Draft amendment to wireless LAN medium access control (MAC) and physical layer (PHY) specifications: Enhancements for higher throughput," IEEE P802.11n/D3.02, January 2008.

[9] IEEE 802.16e Working group, "Local and metropolitan networks–Part 16: Air interface for fixed broadband wireless access systems, Amendment 2: Physical and medium access control layers for combined fixed and mobile operation in licensed bands and corrigendum," December 2005.

[10] IEEE 802.16-2004 Working group, "Local and metropolitan networks–Part 16: Air interface for fixed broadband wireless access systems," October 2004.

[11] Z. Abichar, P. Yanlin, and J. M. Chang, "WiMAX: The emergence of wireless broadband," *IEEE IT Professional*, vol. 8, no. 4, pp. 44–48, August 2006.

[12] IEEE 802.11p Working Group, "Draft amendment to wireless LAN medium access control (MAC) and physical layer (PHY) specifications: Wireless access in vehicular environments," IEEE P802.11p/D2.01, March 2007.

[13] J. Yin, T. ElBatt, G. Yeung, B. Ryu, and S. Habermas, "Performance evaluation of safety applications over DSRC vehicular ad hoc networks," in *Proc. of ACM International Workshop on Vehicular Ad hoc Networks (VANET)*, Philadelphia, USA, October 2004, pp. 1–9.

[14] M. Peden *et al.*, "World report on road traffic injury prevention," World Health Organisation report, 2004.

[15] S. Biswas, R. Tatchikou, and F. Dion, "Vehicle-to-vehicle wireless communication protocols for enhancing highway traffic safety," *IEEE Communications Magazine*, vol. 44, no. 1, pp. 74–82, January 2006.

[16] `http://www.cvisproject.org/`.

[17] M. Matthaiou, D. I. Laurenson, and J. S. Thompson, "A MIMO channel model based on the Nakagami-faded spatial eigenmodes," *IEEE Transactions on Antennas and Propagation*, vol. 56, no. 5, pp. 1494–1497, May 2008.

[18] M. Matthaiou, D. I. Laurenson, and J. S. Thompson, "Stochastic modelling of MIMO channels using the spatial eigenmodes," in *Proc. IET Seminar on Smart Antennas and Cooperative Communications*, London, U.K., October 2007.

[19] M. Matthaiou and D. I. Laurenson, "Rejection method for generating Nakagami-m independent deviates," *IET Electronics Letters*, vol. 43, no. 25, pp. 1474–1475, December 2007.

[20] M. Matthaiou, N. Razavi-Ghods, D. I. Laurenson, and S. Salous, "Characterization of an indoor MIMO channel in frequency domain using the 3D-SAGE algorithm," in *Proc. International Conference on Communications (ICC)*, Glasgow, U.K., June 2007, pp. 5868–5872.

[21] M. Matthaiou, D. I. Laurenson, and J. S. Thompson, "Detailed characterisation of an indoor MIMO channel in the double directional spatial domain," *in press IET Microwaves, Antennas & Propagation*, 2008.

[22] M. Matthaiou, D. I. Laurenson, and C. -X. Wang, "Capacity study of vehicle-to-roadside MIMO channels with a line-of-sight component," in *Proc. Wireless Communications and Networking Conference (WCNC)*, Las Vegas, USA, March 2008, pp. 775–779.

[23] M. Matthaiou, D. I. Laurenson, and C. -X. Wang, "On analytical derivations of the condition number distributions of dual non-central Wishart matrices," *IEEE Transactions on Wireless Communications*, accepted for publication, October 2008.

[24] M. Matthaiou, D. I. Laurenson, and C. -X. Wang, "Reduced complexity detection for Ricean MIMO channels based on condition number thresholding," in *Proc. International Wireless Communications and Mobile Computing Conference (IWCMC)*, Crete, Greece, August 2008, pp. 988–993.

[25] M. Matthaiou, Y. Kopsinis, D. I. Laurenson, and A. M. Sayeed, "Novel ergodic capacity upper bound of dual-branch MIMO Ricean systems," *submitted to IEEE Transactions on Communications*, August 2008.

[26] M. Steinbauer, "A comprehensive transmission and channel model for directional radio channels," in *COST 259 TD (98) 027*, Bern, Switzerland, 1998.

[27] L. P. Rice, "Radio transmission into buildings at 35 and 150 MHz," *Bell Systems Technical Journal*, vol. 38, no. 1, pp. 197–210, 1959.

[28] D. Molkdar, "Review on radio propagation into and within buildings," *IEE Proceedings on Microwaves, Antennas and Propagation*, vol. 138, no. 1, pp. 61–73, February 1991.

[29] J. B. Andersen, T. S. Rappaport, and S. Yoshida, "Propagation measurements and models for wireless communications channels," *IEEE Communications Magazine*, pp. 42-49, January 1995.

[30] S. R. Saunders, *Antennas and Propagation for Wireless Communication Systems*, John Wiley & Sons Ltd., West Sussex, U.K., 1999.

[31] B. Sclar, "Rayleigh fading channels in mobile digital communications systems Part I: Characterization," *IEEE Communications Magazine*, vol. 35, no. 7, pp. 90–100, July 1997.

[32] P. Smulders and L. M. Correia, "Characterization of propagation in 60 GHz radio channels," *Electronics and Communication Engineering Journal*, vol. 9, no. 2, pp. 73–80, April 1997.

[33] G. Y. Delisle, J. P. Lefevre, M. Lecours, and J. Y. Chouinard, "Propagation loss prediction: A comparative study with application to the mobile radio channel," *IEEE Transactions on Vehicular Technology*, vol. 34, no. 2, pp. 86–96, 1986.

[34] V. S. Abhayawardhana, I. J. Wassell, D. Crosby, M. P. Sellars, and M. G. Brown, "Comparison of empirical propagation path loss models for fixed wireless access systems," in *Proc. Vehicular Technology Conference (VTC)*, vol. 1, Stockholm, Sweden, 2005, pp. 73–77.

[35] M. C. Vanderveen, *Estimation of Parametric Channel Models in Wireless Communications*, Ph.D. dissertation, Stanford University, Stanford, USA, December 1977.

[36] J. G. Proakis, *Digital Communications*, McGraw-Hill Ed., 1995.

[37] M. Nakagami, "The m-distribution-A general formula of intensity distribution of rapid fading," *Statistical Methods in Radio Wave Propagation*, W. C. Hoffman Ed., pp. 3–36, Oxford, U.K., 1960.

[38] W. R. Braun and U. Dersh, "A physical mobile radio channel," *IEEE Transactions on Vehicular Technology* vol. 40, pp. 472–482, May 1991.

[39] P. J. Crepeau, "Uncoded and coded performance of MFSK and DPSK in Nakagami fading channels," *IEEE Transactions on Communications*, vol. 40, no. 3, pp. 487–493, March 1992.

[40] J. Winters, "On the capacity of radio communication systems with diversity in a Rayleigh fading environment," *IEEE Journal on Selected Areas in Communications*, vol. 5, no. 5, pp. 871–878, June 1987.

[41] A. Paulraj and T. Kailath, "U. S. Patent #5345599: Increasing capacity in wireless broadcast systems using distributed transmission/directional reception (DTDR)," September 1994.

[42] L. Zheng and D. N. C. Tse, "Diversity and multiplexing: A fundamental tradeoff in multiple-antenna channels," *IEEE Transactions on Information Theory*, vol. 49, no. 5, pp. 1073–1096, May 2003.

[43] W. Weichselberger, *Spatial Structure of Multiple Antenna Radio Channels: A Signal Processing Viewpoint*, Ph.D. dissertation, Technical University of Vienna, December 2003.

[44] M. Debbah and R. Müller, "MIMO channel modelling and the principle of maximum entropy," *IEEE Transactions on Information Theory*, vol. 51, no. 5, pp. 1667–1690, May 2005.

[45] R. G. Gallager, *Information Theory and Reliable Communications*, Wiley, 1968.

[46] A. Goldsmith, S. A. Jafar, N. Jindal, and S. Vishwanath, "Capacity limits of MIMO channels," *IEEE Journal on Selected Areas in Communications*, vol. 21, no. 5, pp. 684–702, June 2003.

[47] A. Medles, S. Visuri, and D. T. M. Slock, "On MIMO capacity for various types of partial channel knowledge at the transmitter," in *Proc. Information Theory Workshop (ITW)*, Sophia Antipolis, France, 2003, pp. 99–102.

[48] M. Steinbauer, A. F. Molisch, and E. Bonek, "The double directional radio channel," *IEEE Antennas and Propagation Magazine*, vol. 43, no. 4, pp. 51–53, August 2001.

[49] H. Özcelik, *Indoor MIMO channel models*, Ph.D. dissertation, Technical University of Vienna, December 2004.

[50] P. Almers *et al.*, "Survey of channel and radio propagation models for wireless MIMO systems," *EURASIP Journal on Wireless Communications and Networking*, pp. 1–19, vol. 2007.

[51] R. B. Ertel, P. Cardieri, K. W. Sowerby, T. S. Rappaport, and J. H. Reed, "Overview of spatial channel models for antenna array communication systems," *IEEE Personal Communications Magazine*, pp. 10–22, 1998.

[52] G. Athanasiadou, A. R. Nix, and J. P. McGeehan, "A microcellular ray-tracing propagation model and evaluation of its narrow-band and wide-band predictions," *IEEE Journal on Selected Areas in Communications*, vol. 18, no. 3, pp. 322–335, March 2000.

[53] J. Ling, D. Chizhik, and R. Valenzuela, "Predicting multi-element receive and transmit array capacity outdoors with ray tracing," in *Proc. Vehicular Technology Conference (VTC)*, vol. 1, Rhodes, Greece, May 2001, pp. 392–394.

[54] A. F. Molisch, A. Kuchar, J. Laurilla, K. Hugl, and R. Schmalenberger, "Geometry-based directional model for mobile radio channels-principles and implementation," *European Transactions on Telecommunications*, vol. 14, no. 4, pp. 351–359, 2003.

[55] W. C. Y. Lee, "Effects of correlation between two mobile base-station antennas," *IEEE Transactions on Communications*, vol. 21, pp. 1214–1224, November 1973.

[56] S. P. Stapleton, X. Carbo, and T. McKeen, "Tracking and diversity for a mobile communications base station array antenna," in *Proc. Vehicular Technology Conference (VTC)*, Atlanta, USA, 1996, pp. 1695–1699.

[57] S. P. Stapleton, X. Carbo, and T. McKeen, "Spatial channel simulator for phased arrays," in *Proc. Vehicular Technology Conference (VTC)*, 1994, pp. 1789–1792.

[58] A. Abdi and M. Kaveh, "A space-time correlation model for multielement antenna systems in mobile fading channels," *IEEE Journal on Selected Areas in Communications*, vol. 20, no. 3, pp. 550–560, April 2002.

[59] D. S. Shiu, G. J. Foschini, M. J. Gans, and J. M. Kahn, "Fading correlation and its effects on the capacity of multielement antenna systems," *IEEE Transactions on Communications*, vol. 48, no. 3, pp. 502–513, March 2000.

[60] M. Patzold and B. O. Hogstad, "A space-time channel simulator for MIMO channels based on the geometrical one-ring scattering model," *Wireless Communications and Mobile Computing, Special Issue on Multiple-Input Multiple-Output (MIMO) Communications*, vol. 4, no. 7, pp. 727–737, November 2004.

[61] X. Cheng, C. -X. Wang, and D. I. Laurenson, "A generic space-time-frequency correlation model and its corresponding simulation model for narrowband MIMO channels," in *Proc. European Conference on Antennas and Propagation (EuCAP)*, Edinburgh, U.K., November 2007.

[62] M. Patzold and B. O. Hogstad, "A wideband space-time MIMO channel simulator based on the geometrical one-ring model," in *Proc. Vehicular Technology Conference (VTC)*, Montreal, Canada, September 2006, pp. 1–6.

[63] J. W. C. Jakes, *Microwave Mobile Communications*, IEEE Press Piscataway, USA, 1974.

[64] P. Petrus, J. H. Reed, and T. S. Rappaport, "Effects of directional antennas at the base station on the Doppler spectrum," *IEEE Communications Letters*, vol. 1, pp. 40–42, March 1997.

[65] T. C. Fulghum, K. J. Molnar, and A. Del-Hallen, "The Jakes fading model for antenna arrays incorporating azimuth spread," *IEEE Transactions on Vehicular Technology*, vol. 51, no. 5, pp. 968–977, September 2002.

[66] P. Petrus, J. H. Reed, and T. S. Rappaport, "Geometrical-based statistical macrocell channel model for mobile environments," *IEEE Transactions on Communications*, vol. 50, no. 3, pp. 494–502, March 2002.

[67] J. Laurila, A. F. Molisch, and E. Bonek, "Influence of the scatterer distribution on power delay profiles and azimuthal power spectra of mobile radio channels," in *Proc. International Symposium on Spread Spectrum Techniques and Applications (ISSSTA)*, vol. 1, Sun City, South Africa, September 1998, pp. 267–271.

[68] J. Fuhl, A. F. Molisch, and E. Bonek, "Unified channel model for mobile radio systems with smart antennas," *IEE Proceedings in Radar, Sonar and Navigation*, vol. 145, no. 1, pp. 32–41, February 1998.

[69] J. C. Liberti and T. S. Rappaport, "A geometrically based model for line of sight multipath radio channels," in *Proc. Vehicular Technology Conference (VTC)*, Atlanta, USA, April 1996, pp. 844-848.

[70] M. Patzold and N. Youssef, "Modelling and simulation of directional-selective and frequency-selective mobile radio channels," *Urban & Fisher Verlag International Journal of Electronics and Communications*, vol. AEU-55, no. 6, pp. 433–442, November 2001.

[71] M. Patzold and B. O. Hogstad, "A wideband MIMO channel model derived from the geometric elliptical scattering model," in *Proc. International Symposium on Wireless Communication Systems (ISWCS)*, Valencia, Spain, September 2006, pp. 138–143.

[72] T. Zwick, C. Fischer, and W. Wiesbeck, "A stochastic multipath channel model including path directions for indoor environments," *IEEE Journal on Selected Areas in Communications*, vol. 20, no. 6, pp. 1178–1192, August 2002.

[73] A. S. Akki and P. Haber, "A statistical model of mobile-to-mobile land communication channel," *IEEE Transactions on Vehicular Technology*, vol. 35, no. 1, pp. 2–7, February 1986.

[74] A. S. Akki, "Statistical properties of mobile-to-mobile land communication channel," *IEEE Transactions on Vehicular Technology*, vol. 43, no. 4, pp. 826–831, November 1994.

[75] G. J. Byers and F. Takawira, "Spatially and temporally correlated MIMO channels: Modeling and capacity analysis," *IEEE Transactions on Vehicular Technology*, vol. 53, no. 3, pp. 634–643, May 2004.

[76] M. Patzold, B. O. Hogstad, N. Youssef, and D. Kim, "A MIMO mobile-to-mobile channel model: Part I-the reference model," in *Proc. International Symposium on Personal, Indoor and Mobile Radio Communications (PIMRC)*, Germany, September 2005, pp. 573–578.

[77] X. Cheng, C. -X. Wang, D. I. Laurenson, H. -H. Chen, and A. V. Vasilakos, "Space-time-frequency characterization of non-isotropic MIMO mobile-to-mobile multicarrier Ricean fading channels," in *Proc. International Wireless Communications and Mobile Computing Conference (IWCMC)*, Crete, Greece, August 2008, pp. 994–999.

[78] X. Cheng, C. -X. Wang, D. I. Laurenson, H. -H. Chen, and A. V. Vasilakos, "A generic geometrical-based MIMO mobile-to-mobile channel model," in *Proc. International Wireless Communications and Mobile Computing Conference (IWCMC)*, Crete, Greece, August 2008, pp. 1000–1005.

[79] M. Toeltsch, J. Laurila, A. F. Molisch, K. Kalliola, P. Vainikainen, and E. Bonek, "Statistical characterization of urban mobile radio channels," *IEEE Journal on Selected Areas in Communications*, vol. 20, no. 3, pp. 539–549, April 2002.

[80] A. F. Molisch, "A generic model for the MIMO wireless propagation channels in macro- and microcells," *IEEE Transactions on Signal Processing*, vol. 52, no. 1, pp. 61–71, January 2004.

[81] L. Correia, ed., *COST 259 final report: Wireless Flexible Personalised Communications*, New York: John Wiley & Sons, Chistester, U.K., 2001.

[82] C. Oestges and B. Clerckx, *MIMO Wireless Communications: From Real-World Propagation to Space-Time Coding*, Elsevier Ltd., 2007.

[83] A. A. M. Saleh and R. A. Valenzuela, "A statistical model for indoor multipath propagation," *IEEE Journal on Selected Areas in Communications*, vol. 5, no. 2, pp. 128–137, February 1987.

[84] Q. H. Spencer, B. D. Jeffs, M. A. Jensen, and A. L. Swindlehurst, "Modeling the statistical time and angle of arrival characteristics of an indoor multipath channel," *IEEE Journal on Selected Areas in Communications*, vol. 18, no. 3, pp. 347–359, March 2000.

[85] C. C. Chong, C. M. Tan, D. I. Laurenson, S. McLaughlin, M. A. Beach, and A. R. Nix, "A new wideband spatio-temporal channel model for 5-GHz band WLAN systems," *IEEE Journal on Selected Areas in Communications*, vol. 21, no. 2, pp. 139–150, February 2003.

[86] J. W. Wallace and M. A. Jensen, "Modeling the indoor MIMO wireless channel," *IEEE Transactions on Antennas and Propagation*, vol. 50, no. 5, pp. 591–599, May 2002.

[87] K. H. Li, M. A. Ingram, and A. V. Ngygen, "Impact of clustering in statistical indoor propagation models on link capacity," *IEEE Transactions on Communications*, vol. 50, no. 4, pp. 521–523, April 2002.

[88] N. Czink, X. Yin, H. Özcelik, M. Herdin, E. Bonek, and B. Fleury, "Cluster characteristics in a MIMO indoor propagation environment," *IEEE Transactions on Wireless Communications*, vol. 6, no. 4, pp. 1465–1475, April 2007.

[89] N. Czink, E. Bonek, L. Hentila, P. Kyosti, J. P. Nuutinen, and J. Ylitalo, "The interdependence of cluster parameters in MIMO channel modeling," in *Proc. European Conference on Antennas and Propagation (EuCAP)*, Nice, France, November 2006.

[90] N. Czink and X. Yin, "Estimation of cluster angular spread in MIMO indoor environments," in *Proc. International Workshop on Signal Processing for Wireless Communications (SPWC)*, London, U.K., 2005.

[91] H. Hofstetter, A. F. Molisch, and N. Czink, "A twin-cluster MIMO channel model," in *Proc. European Conference on Antennas and Propagation (EuCAP)*, Nice, France, November 2006.

[92] T. Zwick, D. J. Cichon, and W. Wiesbeck, "Microwave propagation modelling in indoor environments," in *Proc. International Conference on Microwave und Optronics (MIOP)*, Sindelfingen, Germany, May 1995, pp. 629–633.

[93] T. Zwick, F. Demmerle, and W. Wiesbeck, "Comparison of channel impulse response measurements and calculations in indoor environments," in *Proc. International Antennas and Propagation Symposium (APS)*, Baltimore, USA, July 1996, pp. 1498–1501.

[94] J. P. Kermoal, L. Schumacher, K. I. Pedersen, P. E. Mogensen, and F. Frederiksen, "A stochastic MIMO radio channel model with experimental validation," *IEEE Journal on Selected Areas in Communications*, vol. 20, pp. 1211–1226, August 2002.

[95] F. Rashid-Farrokhi, A. Lozano, G. Foschini, and R. Valenzuela, "Spectral efficiency of wireless systems with multiple transmit and receive antennas," in *Proc. International Symposium on Personal, Indoor and Mobile Radio Communications (PIMRC)*, vol. 1, London, U.K., September 2000, pp. 373–377.

[96] K. Yu, M. Bengtsson, B. Ottersten, D. McNamara, P. Karlsson, and M. A. Beach, "Modeling of wideband MIMO radio channels based on NLoS indoor measurements," *IEEE Transactions on Vehicular Technology*, vol. 53, no. 3, pp. 655–665, May 2004.

[97] E. Bonek, H. Özcelik, M. Herdin, W. Weichselberger, and J. Wallace, "Deficiencies of a popular MIMO radio channel model," in *Proc. International Symposium on Wireless Personal Multimedia Communications (WPMC)*, Yokosuka, Japan, October 2003.

[98] H. Özcelik, N. Czink, and E. Bonek, "What makes a good MIMO channel model?," in *Proc. Vehicular Technology Conference (VTC)*, vol. 1, Stockholm, Sweden, 2005, pp. 156–160.

[99] W. Weichselberger, *Spatial Structure of Multiple Antenna Radio Channels: A Signal Processing Viewpoint*, Ph.D. dissertation, Technical University of Vienna, December 2003.

[100] N. Costa and S. Haykin, "A novel wideband MIMO channel model and experimental validation," *IEEE Transactions on Antennas and Propagation*, vol. 56, no. 2, pp. 550–562, February 2008.

[101] A. M. Sayeed, "Deconstructing multiantenna fading channels," *IEEE Transactions on Signal Processing*, vol. 50, no. 10, pp. 2563–2579, October 2002.

[102] K. Pensel and J. A. Nossek, "Uplink and downlink calibration of an antenna array in a mobile communication system," COST 259 Technical Document, in *TD(97)55*, Lisbon, Portugal, September 1997.

[103] A. G. Burr, "Capacity bounds and estimates for the finite-scatters MIMO wireless channel," *IEEE Journal on Selected Areas in Communications*, vol. 21, no. 5, pp. 812–818, June 2003.

[104] H. Steyskal and J. S. Herd, "Mutual coupling compensation in small array antennas," *IEEE Transactions on Antennas and Propagation*, vol. 38, no. 12, pp. 1971–1975, December 1990.

[105] D. Gesbert, H. Böelcskei, and A. Paulraj, "Outdoor MIMO wireless channels: Models and performance prediction," *IEEE Transactions on Communications*, vol. 50, no. 12, pp. 1926–1934, December 2002.

[106] D. Chizhik, G. Foschini, M. Gans, and R. Valenzuela, "Keyholes, correlations, and capacities of multielement transmit and receive antennas," *IEEE Transactions on Wireless Communications*, vol. 1, pp. 361–368, April 2002.

[107] Technical Specification Group Radio Access Networks, "Spatial channel model for multiple input multiple output (MIMO) simulations (Release 6)," Technical Report 3GPP TR. 25.996, V6.1.0., 3rd Generation Partnership Project, September 2003.

[108] 3GPP, R1-050586, "Wideband SCM," 2005.

[109] L. Schumacher, L. T. Berger, and J. Ramiro-Moreno, "Recent advances in propagation characterisation and multiple antenna processing in the 3GPP framework," in *Proc. General Assembly of International Union of Radio Science (URSI)*, Maastricht, The Netherlands, August 2002.

[110] C. -X. Wang, X. Hong, H. Wu, and W. Xu, "Spatial temporal correlation properties of the 3GPP spatial channel model and the Kronecker MIMO channel model," *EURASIP Journal on Wireless Communications and Networking*, vol. 2007, 9 pages, 2007.

[111] V. Erceg *et al.*, "TGn Channel Models," IEEE 802.11-03/940r4, May 2004, available at `http://www.wirelessworld.com/`.

[112] K. Yu, Q. Li, and M. Ho, "Measurement ivestigation of tap and cluster angular spreads at 5.2 GHz," *IEEE Transactions on Antennas and Propagation*, vol. 53, no. 7, pp. 2156–2160, July 2005.

[113] `http://www.ist-winner.org/`.

[114] D. S. Baum, J. Hansen, G. Del Galdo, M. Milojevic, J. Salo, and P. Kyösti, "An interim channel model for beyond-3G systems: Extending the 3GPP spatial channel model (SCM)," in *Proc. Vehicular Technology Conference (VTC)*, vol. 5, Stockholm, Sweden, May 2005, pp. 3132–3136.

[115] H. El-Sallabi, D. S. Baum, P. Zetterberg, P. Kyösti, T. Rautiainen, and C. Schneider, "Wideband spatial channel model for MIMO systems at 5 GHz in indoor and outdoor environments," in *Proc. Vehicular Technology Conference (VTC)*, vol. 6, Melbourne, Australia, May 2006, pp. 2916–2921.

[116] L. Correia, ed., *COST 273 final report: Towards Mobile Broadband Multimedia Networks, Models and tools for 4G*, Elsevier, 2006.

[117] A. F. Molisch, H. Asplund, R. Heddergott, M. Steinbauer, and T. Zwick, "The COST259 directional channel model-Part I: Overview and methodology," *IEEE Transactions on Wireless Communications*, vol. 5, no. 12, pp. 3421–3433, December 2006.

[118] `http://www.cost2100.org/`.

[119] A. Paier *et al.*, "Characterization of vehicle-to-vehicle radio channels from measurements at 5.2 GHz," *Springer Wireless Personal Communications*, June 2008.

[120] A. Paier *et al.*, "Car-to-car radio channel measurements at 5 GHz: Pathloss, power-delay profile, and delay-Doppler spectrum," in *Proc. International Symposium on Wireless Communication Systems (ISWCS)* Trondheim, Norway, October 2007.

[121] R. S. Thomä *et al.*, "Identification of time-variant directional mobile radio channels," *IEEE Transactions on Instrumentation and Measurement*, vol. 49, no. 2, pp. 357–364, April 2000.

[122] S. Theodoridis and K. Koutroumbas, *Pattern Recognition*, 2nd Edition, Academic Press, Inc., 2003.

[123] A. Papoulis and S. U. Pillai, *Probability, Random Variables and Stochastic Processes*, 4th ed. Boston, McGraw-Hill, 2002.

[124] K. W. Yip and T. S. Ng, "An efficient model for Nakagami-m fading channels, $m < 1$," *IEEE Transactions on Communications*, vol. 48, pp. 214–221, February 2000,

[125] N. C. Beaulieu and C. Cheng, "An efficient procedure for Nakagami-m fading simulation," in *Proc. Global Telecommunications Conference (CLOBECOM)*, Texas, USA, November 2001, pp. 3336–3340.

[126] L. Cao and N. C. Beaulieu, "A simple efficient method for generating independent Nakagami-m fading samples," in *Proc. International Conference on Communications (ICC)*, vol. 1, Korea, May 2005, pp. 44–47.

[127] A. Paulraj, R. Nabar, and D. Gore, *Introduction to Space-Time Wireless Communications*, Cambridge University Press, U.K., 2003.

[128] S. Haykin, *Adaptive Filter Theory*, Prentice Hall, 4th Edition, 2002.

[129] H. Krima and M. Viberg, "Two decades of array signal processing: The parametric approach," *IEEE Signal Processing Magazine*, vol. 13, pp. 67–94, 1996.

[130] M. S. Bartlett, "Smoothing periodograms for time series with continuous spectra," *Nature*, vol. 161, pp. 686–687, 1948.

[131] J. Capon, "High-resolution frequency-wavenumber spectrum analysis," *Proceedings of the IEEE*, vol. 57, no. 8, pp. 1408-1418, August 1969.

[132] R. O. Schmidt, "Multiple emitter location and signal parameter estimation," in *Proc. RADC Spectral Estimation Workshop*, Rome, NY, 1979.

[133] G. Bienvenu and L. Kopp, "Adaptivity to background noise spatial coherence for high resolution passive methods," in *Proc. International Conference on Acoustics, Speech and Signal Processing (ICASSP)*, Denver, USA, April 1980, pp 307–310.

[134] M. Kaveh and A. J. Barabell, "The statistical performance of the MUSIC and the minimum-norm algorithms in resolving plane waves in noise," *IEEE Transactions on Acoustics, Speech and Signal Processing*, vol. 24, no. 2, pp. 331–341, April 1986.

[135] T. J. Shan, M. Wax, and T. Kailath, "On spatial smoothing for direction-of-arrival estimation of coherent signals," *IEEE Transactions on Acoustics, Speech and Signal Processing*, vol. 33, no. 4, pp. 806–811, August 1985.

[136] S. U. Pillai and B. H. Kwon, "Forward/backward spatial smoothing techniques for coherent signal identification," *IEEE Transactions on Acoustics, Speech and Signal Processing*, vol. 37, no. 1, pp. 8–15, January 1989.

[137] A. Paulraj, R. Roy, and T. Kailath, "A subspace rotation approach to signal parameter estimation," *Proceedings of the IEEE*, pp. 1044–1045, July 1986.

[138] R. Roy and T. Kailath, "ESPRIT-estimation of signal parameters via rotational invariance techniques," *IEEE Transactions on Acoustics, Speech and Signal Processing*, vol. 37, no. 7, pp. 984–995, July 1989.

[139] M. Haardt and J. A. Nossek, "Unitary ESPRIT: How to obtain increased estimation accuracy with a reduced computational burden," *IEEE Transactions on Signal Processing*, vol. 43, no. 5, pp. 1232–1242, May 1995.

[140] A. J. Barabell, "Improving the resolution performance of eigenstructure-based direction finding algorithms," in *Proc. International Conference on Acoustics, Speech and Signal Processing (ICASSP)*, Boston, USA, 1983, pp. 336–339.

[141] F. Belloni, A. Richter, and V. Koivunen, "Extension of root-MUSIC to non-ULA array configurations," in *Proc. International Conference on Acoustics, Speech and Signal Processing (ICASSP)*, vol. 4, Toulouse, France, 2006, pp. 897–900.

[142] M. Pesavento, A. B. Gershman, and K. M. Wong, "Direction finding in partly-calibrated sensor arrays composed of multiple subarrays," *IEEE Transactions on Signal Processing*, vol. 50, no. 9, pp. 2103–2115, September 2002.

[143] C. M. S. See and A. B. Gershman, "Direction-of-arrival estimation in partly calibrated subarray-based sensor arrays in the presence of array and channel imperfections," *IEEE Transactions on Signal Processing*, vol. 52, no. 2, pp. 329–338, February 2004.

[144] S. A. Elkader, A. B. Gershman, and K. M. Wong, "Improving the robustness of the RARE algorithm against subarray orientation errors," in *Proc. International Conference on Acoustics, Speech, and Signal Processing (ICASSP)*, vol. 2, 2004, pp. 241–244.

[145] A. P. Dempster, N. M. Laird, and D. B. Rubin, "Maximum likelihood from incomplete data via the EM algorithm," *Journal of the Royal Statistical Society, Series B (Methodological)*, vol. 39, no. 1, pp. 1–38, 1977.

[146] J. A. Fessler and A. O. Hero, "Space-alternating generalized expectation-maximization algorithm," *IEEE Transactions on Signal Processing*, vol. 42, no. 10, pp. 2664–2677, October 1994.

[147] P.J. Chung and J. F. Böhme, "Comparative convergence analysis of EM and SAGE algorithms in DOA estimation," *IEEE Transactions on Signal Processing*, vol. 49, no. 12, pp. 2940–2949, December 2001.

[148] C. C. Chong, *Dynamic Directional Channel Model for Indoor Wireless Communications*, Ph.D. dissertation, The University of Edinburgh, September 2003.

[149] M. Feder and E. Weinstein, "Parameter estimation of superimposed signals using the EM algorithm," *IEEE Transactions on Acoustics, Speech and Signal Processing*, vol. 36, no. 4, pp. 477–489, April 1988.

[150] B. H. Fleury, D. Dahlhaus, R. Heddergott, and M. Tschudin, "Wideband angle of arrival estimation using the SAGE algorithm," in *Proc. International Symposium on Spread Spectrum Techniques and Applications (ISSSTA)*, Mainz, Germany, vol. 1, September 1996, pp. 79–85.

[151] B. H. Fleury, M. Tschudin, R. Heddergott, D. Dahlhaus, and K. I. Pedersen, "Channel parameter estimation in mobile radio environments using the SAGE algorithm," *IEEE Journal on Selected Areas in Communications*, vol. 17, no. 3, pp. 438–450, March 1999.

[152] B. H. Fleury, P. Jourdan, and A. Stucki, "High-resolution channel parameter estimation for MIMO applications using the SAGE algorithm," *International Zurich Seminar on Broadband Communications*, ETH Zurich, Switzerland, 2002, pp. 30-1–30-9.

[153] X. Yin, B. H. Fleury, P. Jourdan, and A. Stucki, "Polarisation estimation of individual propagation paths using the SAGE algorithm," in *Proc. International Symposium on Personal, Indoor and Mobile Radio Communication (PIMRC)*, Beijing, China, September 2003, pp. 1795–1799.

[154] C. C. Chong, D. I. Laurenson, C. M. Tan, S. McLaughlin, M. A. Beach, and A. R. Nix, "Joint detection-estimation of directional channel parameters using the 2-D frequency domain SAGE algorithm with serial interference cancellation," in *Proc. International Conference on Communications (ICC)*, vol. 2, New York, USA, April 2002, pp. 906–910.

[155] H. Akaike, "A new look at the statistical model identification," *IEEE Transactions on Automatic Control*, vol. 19, no. 6, pp. 716–723, December 1974.

[156] J. Rissanen, "Modeling by the shortest data description," *Automatica*, vol. 14, pp. 465–471, 1978.

[157] A. K. Jain and R. C. Dubes, *Algorithms for Clustering Data*, Prentice-Hall, Englewood Cliffs, New Jersey, USA, 1988.

[158] B. W. Silverman, *Density Estimation for Statistics and Data Analysis*, Chapman and Hall, London, U.K., 1986.

[159] P. Hall, S. J. Sheather, M. C. Jones, and J. S. Marron, "On optimal data-based bandwidth selection in kernel density estimation," *Biometrika*, vol. 78, no. 2, pp. 263–269, 1991.

[160] D. W. Scott, *Multivariate Density Estimation: Theory, Practice and Visualization*, John Wiley & Sons, Inc., New York, USA, 1992.

[161] K. I. Pedersen, P. E. Mogensen, and B. H. Fleury, "A stochastic model of the temporal and azimuthal dispersion seen at the base station in outdoor propagation environments," *IEEE Transactions on Vehicular Technology*, vol. 49, no. 2. pp. 437–447, March 2000.

[162] A. Algans, K. I. Pedersen, and P. E. Mogensen, "Experimental analysis of the joint statistical properties of azimuth spread, delay spread, and shadow fading," *IEEE Journal on Selected Areas in Communications*, vol. 20, no. 3, pp. 523–531, April 2002.

[163] S. E. Foo, C. M. Tan, and M. A. Beach, "Spatial temporal characterization of UTRA FDD channels at the user equipment," in *Proc. Vehicular Technology Conference (VTC)*, vol. 2, Jeju, Korea, April 2003, pp. 793–797.

[164] C. M. Tan, A. R. Nix, and M. A. Beach, "Dynamic spatial-temporal propagation measurement and super-resolution channel characterisation at 5.2 GHz in a corridor environment," in *Proc. Vehicular Technology Conference (VTC)*, Vancouver, Canada, September 2002, pp. 797–801.

[165] C. C. Chong, D. I. Laurenson and S. McLaughlin, "Spatio-temporal correlation properties for the 5.2-GHz indoor propagation environments," *IEEE Antennas and Wireless Propagation Letters*, vol. 2, no. 8, pp. 114–117, 2003.

[166] S. Wyne, N. Czink, J. Karedal, P. Almers, F. Tufvesson, and A. Molisch, "A cluster-based analysis of outdoor-to-indoor office MIMO measurements at 5.2 GHz," in *Proc. Vehicular Technology Conference (VTC)*, Montreal, Kanada, September 2006, pp. 1–5.

[167] C. M. Tan, *Multidimensional Channel Characterisation with Efficient High-Resolution Array Signal Processing Algorithms*, Ph.D. dissertation, University of Bristol, December 2004.

[168] M. Bengtsson and B. Volcker, "On the estimation of azimuth distributions and azimuth spectra," in *Proc. Vehicular Technology Conference (VTC)*, vol. 3, Atlantic City, USA, 2001, pp. 1612–1615.

[169] A. Richter and R. S. Thomä, "Joint maximum likelihood estimation of specular paths and distributed diffuse scattering," in *Proc. Vehicular Technology Conference (VTC)*, vol. 1, 2005, pp. 11–15.

[170] A. Richter, M. Landmann, and R. S. Thomä, "A gradient based method for maximum likelihood channel parameter estimation from multidimensional channel sounding measurement," in *Proc. General Assembly of the International Union of Radio Science (URSI)*, Maastricht, Netherlands, 2002.

[171] R. S. Thomä, M. Landmann, and A. Richter, "RIMAX-A maximum likelihood framework for parameter estimation in multidimensional channel sounding," in *Proc. International Symposium on Antennas and Propagation (ISAP)*, Sendai, Japan, August 2004, pp. 53–56.

[172] C. M. Tan, M. A. Beach, and A. R. Nix, "Enhanced-SAGE algorithm for use in distributed-source environments," *IEE Electronics Letters*, vol. 39, no. 8, pp. 697–698, April 2003.

[173] C. M. Tan, M. A. Beach, and A. R. Nix, "Multipath parameters estimation with a reduced complexity unitary-SAGE algorithm," *European Transactions on Telecommunications*, vol. 14, pp. 515–528, 2004.

[174] D. P. McNamara, M. A. Beach, P. N. Fletcher, and P. Karlsson, "Capacity variation of indoor multiple input multiple output (MIMO) channels," *IEE Electronics Letters*, vol. 36, no. 24, pp. 2037–2038, November 2000.

[175] L. Cottatelluci and M. Debbah, "On the capacity of MIMO Rice channels," in *Proc. Allerton Conference*, Illinois, USA, 2004.

[176] L. Cottatelluci and M. Debbah, "The effect of line of sight on the asymptotic capacity of MIMO systems," in *Proc. International Symposium on Information Theory (ISIT)*, Chicago, USA, 2004, p. 242.

[177] I. Sarris and A. R. Nix, "Design and performance assessment of high-capacity MIMO architectures in the presence of a line-of-sight component," *IEEE Transactions on Vehicular Technology*, vol. 56, no. 4, pp. 2194–2202, July 2007.

[178] I. Sarris and A. R. Nix, "Design and performance assessment of maximum capacity MIMO architectures in line-of-sight," *IEE Proceedings in Communications*, vol. 153, no. 4, pp. 482–488, August 2006.

[179] F. Bøhagen, P. Orten, and G. E. Øien, "Construction and capacity analysis of high-rank line-of-sight MIMO channels," in *Proc. IEEE Wireless Communications and Networking Conference (WCNC)*, March 2005, pp. 432–437.

[180] J. B. Andersen, "Multipath richness-a meaure of MIMO capacity, COST 259 Technical Document, in *TD(04)157*, Duisburg, Germany, September 2004.

[181] C. Martin and B. Ottersen, "Analytic approximations of eigenvalue moments and mean channel capacity for MIMO channels," in *Proc. International Conference on Acoustics, Speech and Signal Processing (ICASSP)*, May 2002, pp. III-2389–III-2392.

[182] C. Martin and B. Ottersen, "Asymptotic eigenvalue distributions and capacity for MIMO channels under correlated fading," *IEEE Transactions on Wireless Communications*, vol. 3, no. 4, pp.1350–1359, July 2004.

[183] M. Wennstrom, *On MIMO Systems and Adaptive Arrays for Wireless Communication: Analysis and Practical Issues*, Ph.D dissertation, Uppsalla University, 2002.

[184] R. K. Mallik, "The pseudo-Wishart distribution and its application to MIMO systems," *IEEE Transactions on Information Theory*, vol. 49, no. 10, pp. 2761–2769, October 2003.

[185] S. Jin, M. R. McKay, X. Gao, and I. B. Collings, "MIMO multichannel beamforming: SER and outage using new eigenvalue distribution of complex noncentral Wishart matrices," *IEEE Transactions on Communications*, vol. 56, no. 3, pp. 424–434, March 2008.

[186] L. M. Garth, P. J. Smith, and M. Shafi, "Exact symbol error probabilities for SVD transmission of BPSK data over fading channels," in *Proc. IEEE International Conference on Communications (ICC)*, vol. 4, Seoul, Korea, March 2005, pp. 2271–2276.

[187] M. Kang and M. -S. Alouini, "Largest eigenvalue of complex Wishart matrices and performance analysis of MIMO MRC systems," *IEEE Journal on Selected Areas in Communications*, vol. 21, no. 3, pp. 418–426, April 2003.

[188] I. Medvedev *et al.*, "Transmission strategies for high throughput MIMO OFDM communication," in *Proc. IEEE International Conference on Communications (ICC)*, vol. 4, 2005, pp. 2621–2625

[189] V. Erceg, P. Soma, D. S. Baum, and A. J. Paulraj, "Capacity obtained from multiple-input multiple-output channel measurements in fixed wireless environments at 2.5 GHz," in *Proc. International Conference on Communications (ICC)*, vol. 1, New York, USA, May 2002, pp. 396–400.

[190] H. Artes, D. Seethaler, and F. Hlawatsch, "Efficient detection algorithms for MIMO channels: A geometrical approach to approximate ML detection," *IEEE Transactions on Signal Processing*, vol. 51, no. 11, pp. 2808–2820, November. 2003.

[191] D. Wubben, R. Bohnke, V. Kuhn, and K. D. Kammeyer, "MMSE-based lattice-reduction for near-ML detection of MIMO systems," in *Proc. ITG/IEEE Workshop on Smart Antennas (WSA)*, Munich, Germany, March 2004, pp. 106–113.

[192] A. T. James, "Distributions of matrix variates and latent roots derived from normal samples," *Annals of Mathematical Statistics*, vol. 35, no. 2, pp. 475–501, June 1964.

[193] T. Ratnarajah, *Topics in complex random matrices and information theory*, Ph.D. dissertation, University of Ottawa, 2003.

[194] C. G. Khatri, "Non-central distributions of ith largest characteristic roots of three matrices concerning complex multivariate normal populations," *Annals of the Institute of Statistical Mathematics*, vol. 21, pp. 23-32, 1969.

[195] G. Alfano, A. Lozano, A. M. Tulino, and S. Verdú, "Mutual information and eigenvalue distribution of MIMO Ricean channels," in *Proc. International Symposium on Information Theory and Applications (ISITA)*, Parma, Italy, October 2004, pp. 1040–1045.

[196] M. Kang and M.-S. Alouini, "Capacity of MIMO Rician channels," *IEEE Transactions on Wireless Communications*, vol. 5, no. 1, pp. 112–122, January 2006.

[197] A. Maaref and S. Aissa, "Joint and marginal eigenvalue distributions of (non)central complex Wishart matrices and PDF-based approach for characterizing the capacity statistics of MIMO Ricean and Rayleigh fading channels," *IEEE Transactions on Wireless Communications*, vol. 6, no. 10, pp. 3607–3619, October 2007.

[198] M. R. McKay and I. Collings, "General capacity bounds for spatially correlated Rician MIMO channels," *IEEE Transactions on Information Theory*, vol. 51, no. 9, pp. 3121–3145, September 2005.

[199] P. Smith and L. Garth, "Exact capacity distribution for dual MIMO systems in Ricean fading," *IEEE Communications Letters*, vol. 8, no. 1, pp. 18–20, January 2004.

[200] T. Ratnarajah, R. Vaillancount, and M. Alvo, "Complex random matrices and Rician channel capacity," *Problems of Information Transmission*, vol. 41, no. 1, pp. 1–22, January 2005.

[201] F. Bøhagen, P. Orten, G. E. Øien, and S. de la Kethulle de Ryhove, "Exact capacity expressions for dual-branch Ricean MIMO systems," *in press IEEE Transactions on Communications*, 2008.

[202] K. I. Gross and D. S. Richards, "Total positivity, spherical series, and hypergeometric functions of matrix argument," *Journal on Approximation Theory*, vol. 59, no. 2, pp. 224–246, 1989.

[203] I. S. Gradshteyn and I. M. Ryzhik, *Table of Integrals, Series, and Products*, Sixth ed. Academic Press, San Diego, 2000.

[204] M. Charafeddine and A. Paulraj, "Simplified eigenvalues distributions of 2×2 complex noncentral Wishart," *Asilomar Conference on Signals, Systems, and Computers (ACSSC)*, Monterey, California, USA, November 2007.

[205] A. H. Nutall, "Some integrals involving the Q function," *Naval Underwater Systems Center, New London, Lab., New London, CT, 4297*, 1972.

[206] A. Edelman, *Eigenvalues and condition numbers of random matrices*, Ph.D. dissertation, MIT, Cambridge, MA, May 1989.

[207] T. Ratnarajah, R. Vaillancourt, and M. Alvo, "Eigenvalues and condition numbers of complex random matrices," *SIAM Journal on Matrix Analysis and Applications*, vol. 26, no. 2, pp. 441–456, 2005.

[208] P. -H. Kuo, P. J. Smith, and L. M. Garth, "A Markov model for MIMO channel condition number with application to dual-mode antenna selection," in *Proc. IEEE Vehicular Technology Conference (VTC*), Dublin, Ireland, April 2007, pp. 471–475.

[209] U. Fincke and M. Phost, "Improved methods for calculating vectors of short length in a lattice, including a complexity analysis," *Mathematics of Computation*, vol. 44, pp. 463–471, April 1985.

[210] B. Hassibi and H. Vikalo, "On the sphere-decoding algorithm I. Expected complexity," *IEEE Transactions on Signal Processing*, vol. 53, no. 8, pp. 2806–2818, August 2005.

[211] J. Jalden and B. Ottersten, "On the complexity of sphere decoding in digital communications," *IEEE Transactions on Signal Processing*, vol. 53, no. 4, pp. 1474–1484, April 2005.

[212] G. Golden, G. J. Foschini, R. Valenzuela, and P. Wolniasky, "Detection algorithm and initial laboratory results using the V-BLAST space-time communication architecture," *IEE Electronics Letters*, vol. 35, pp. 14–15, 1999.

[213] R. W. Health and A. J. Paulraj, "Switching between diversity and multiplexing in MIMO systems," *IEEE Transactions on Communications*, vol. 53, no. 6, pp. 962–968, June 2005.

[214] A. Forenza, M. R. McKay, A. Pandharipande, R. W. Health, and I. B. Collings, "Adaptive MIMO transmission for exploiting the capacity of spatially correlated channels," *IEEE Transactions on Vehicular Technology*, vol. 56, no. 2, pp. 619–630, March 2007.

[215] A. Forenza, M. R. McKay, I. B. Collings and R. W. Health, "Switching between OSTBC and spatial multiplexing with linear receivers in spatially correlated MIMO channels," in *Proc. Vehicular Technology Conference (VTC)*, Melbourne, Australia, May 2006, pp. 1387–1391.

[216] J. Maurer, G. Matz, and D. Seethaler, "Low-complexity and full-diversity MIMO detection based on condition number thresholding," in *Proc. Acoustics, Speech and Signal Processing Conference (ICASSP)*, vol. 3, Honolulu, Hawaii, April 2007, pp. 61–64.

[217] R. Bohnke, D. Wubben, V. Kuhn, and K. -D. Kammeyer, "Reduced complexity MMSE detection for BLAST architectures," in *Proc. Global Telecommunications Conference (GLOBECOM)*, vol. 4, San Francisco, USA, December 2003, pp. 2258–2262.

[218] A. Grant, "Rayleigh fading multi-antenna channels," *EURASIP Journal on Applied Signal Processing - Special Issue on Space-Time Coding - part I*, vol. 2002, no. 3, pp. 316–329, March 2002.

[219] H. Shin and J. H. Lee, "Capacity of multi-antenna fading channels: Spatial fading correlation, double scattering, and keyhole," *IEEE Transactions on Information Theory*, vol. 49, no. 10, pp. 2636–2647, October 2003.

[220] Q. T. Zhang, X. W. Cui and X. M. Li, "Very tight capacity bounds for MIMO-correlated Rayleigh-fading channels," *IEEE Transactions on Wireless Communications*, vol. 4, no. 2, pp. 681–688, March 2005.

[221] J. Hansen and H. Bölcskei, "A geometrical investigation of the rank-1 Ricean MIMO channel at high SNR," in *Proc. International Symposium on Information Theory (ISIT)*, Chigano, USA, June 2004, p. 64.

[222] S. K. Jayaweera and H. V. Poor, "On the capacity of multiple-antenna systems in Rician fading," *IEEE Transactions on Wireless Communications*, vol. 4, no. 3, pp. 1102–1111, May 2005.

[223] Y. -H. Kim and A. Lapidoth, "On the log determinant of non-central Wishart matrices," in *Proc. International Symposium on Information Theory (ISIT)*, Yokohama, Japan, June 2003, p. 54.

[224] S. Jin and X. Gao, "Tight lower bounds on the ergodic capacity of Ricean fading MIMO channels," in *Proc. International Conference on Communications (ICC)*, vol. 4, May 2005, pp. 2412–2416.

[225] S. Jin and X. Gao, "Tight upper bound on the ergodic capacity of the Rician fading MIMO channels," in *Proc. Wireless Communications and Networking Conference (WCNC)*, vol. 1, March 2005, pp. 402–407.

[226] M. R. McKay and I. B. Collings, "On the capacity of frequency-flat and frequency-selective Rician MIMO channels with single-sided correlation," *IEEE Transactions on Wireless Communications*, vol. 5, no. 8, pp. 2038–2043, August 2005.

[227] X. W. Cui, Q. T. Zhang, and Z. M. Feng, "Generic procedure for tightly bounding the capacity of MIMO correlated Rician fading channels," *IEEE Transactions on Communications*, vol. 53, no. 5, pp. 890–898, May 2005.

[228] M. R. McKay, P. J. Smith and I. B. Collings, "New properties of complex noncentral quadratic forms and bounds on MIMO mutual information," in *Proc. International Symposium on Information Theory (ISIT)*, Seatle, USA, July 2006, pp. 1209–1213.

[229] S. Jin, X. Gao and X. You, "On the ergodic capacity of rank-1 Ricean-fading MIMO channels," *IEEE Transactions on Information Theory*, vol. 53, no. 2, pp. 502–517, February 2007.

[230] M. R. McKay and I. B. Collings, "Improved general lower bound for spatially-correlated Rician MIMO capacity," *IEEE Communications Letters*, vol. 10, no. 3, pp. 162–164, March 2006.

[231] J. Salo, F. Mikas, and P. Vainikainen, "An upper bound on the ergodic mutual information in Rician fading MIMO channels," *IEEE Transactions on Wireless Communications*, vol. 5, no. 6, pp. 1415–1421, June 2006.

[232] A. Lozano, A. M. Tulino, and S. Verdù, "High-SNR power offset in multiantenna communication," *IEEE Transactions on Information Theory*, vol. 51, no. 12, pp. 4134–4151, December 2005.

[233] T. Ratnarajah, "Non-central quadratic forms on complex random matrices and applications," in *Proc. Workshop on Statistical Signal Processing (SSP)*, Bordeaux, France, July 2005.

[234] A. M. Mathai, *Jacobians of Matrix Transformations and Functions of Matrix Arguments*, Singapore: World Scientific, 1997.

[235] A. P. Prudnikov, Y. A. Bruchkov, and O. I. Marichev, *Integrals and Series*, vol. 3, Gordon and Breach Science Publishers, 1990.

[236] Ö. Oyman, R. Nabar, H. Bölcskei, and A. Paulraj, "Characterizing the statistical properties of mutual information in MIMO channels," *IEEE Transactions on Signal Processing*, vol. 51, no. 11, pp. 2782–2795, November 2003.

[237] M. Abramowitz and I. A. Stegun, *Handbook of Mathematical Functions With Formulas, Graphs, and Mathematical Tables*, New York: Dover, 1972.

[238] W. Weibull, "A statistical distribution function of wide applicability," *Journal of Applied Mechanics*, no. 27, pp. 291–297, 1951.

[239] H. Hashemi, "The indoor radio propagation channel," *Proc. of the IEEE*, vol. 81, no. 7, pp. 943–968, July 1993.

[240] F. Babich and G. Lombardi, "Statistical analysis and characterization of the indoor propagation channel," *IEEE Transactions on Communications*, vol. 48, no. 3, pp. 455–464, March 2000.

[241] N. S. Adawi *et al.*, "Coverage prediction for mobile radio systems operating in the 800/900 MHz frequency range," *IEEE Transactions on Vehicular Technology*, vol. 37, no. 1, pp. 3–72, February 1988.

[242] M. A. Taneda, J. Takada, and K. Araki, "A new approach to fading: Weibull model," in *Proc. International Symposium on Personal, Indoor and Mobile Radio Communications (PIMRC)*, Osaka, Japan, September 1999, pp. 711–715.

[243] E. L. Lehmann, *Theory of Point Estimation*, New York, Wiley, 1983.

[244] A. H. Nutall, "The Nutall Q function-Its relation to the Marcum Q function and its application in digital communication performance evaluation," *IEEE Transactions on Communications*, vol. 50, no. 11, pp. 1712–1715, November 2002.

[245] M. A. Golberg, "The derivative of a determinant," *American Mathematical Monthly*, vol. 79, pp. 1124–1126, December 1972.

[246] W. K. Pratt, "Partial derivatives of Marcum's Q Function," *Proc. of the IEEE*, pp. 1220–1221, July 1968.